Interplay of Microscopic symmetries and Entanglement in effective theories of correlated quantum matter

A Thesis

Submitted to the
Tata Institute of Fundamental Research, Mumbai
Subject Board of Physics
for the degree of Doctor of Philosophy

by

Ankush Chaubey

International Centre for Theoretical Sciences
Tata Institute of Fundamental Research
Bengaluru, India
February, 2026

DECLARATION

This thesis is a presentation of my original research work. Wherever contributions of others are involved, every effort is made to indicate this clearly, with due reference to the literature, and acknowledgement of collaborative research and discussions.

The work was done under the guidance of Professor Subhro Bhattacharjee at the International Centre for Theoretical Sciences, Tata Institute of Fundamental Research, Bengaluru.

Ankush Chaubey

In my capacity as supervisor of the candidate's thesis, I certify that the above statements are true to the best of my knowledge.

Subhro Bhattacharjee

Date: 12.02.2026

Acknowledgement

The journey of my PhD would not have been pleasant without the remarkable and inspiring company of people around me. Their presence made this journey truly joyful, and I will always cherish the memories created during this time. I think this is the best way I can express my gratitude towards them.

I would like to begin by thanking *Subhro* for his guidance and patience in working with me throughout these years. I am grateful to him for introducing me to fascinating problems in the world of condensed matter. I learned a lot from him through various discussions (although many times they converted into arguments). I also admire his support in non-academic matters.

I am also grateful to my collaborators *Sergej Moroz*, *Vijay Shenoy*, and *Krishnendu Sengupta*, with whom I have worked on various projects. I am especially grateful to *Sergej* for teaching me iDMRG and for the generous hospitality shown by him and *Diana* during my visits to Sweden. I would also like to thank my collaborators and friends, *Basudeb* and *Harsh*, working with them has always been a joy. I am equally grateful to *Stithadi Roy* and *Subroto Mukherjee* for kindly agreeing to be the members of my TMC committee. Special thanks to *Loga*, working on a project with him was a great learning experience. I would also like to acknowledge *Karlo Penc* and *Yasir Iqbal* for reviewing this thesis and for their insightful feedback.

I have always felt lucky to have delightful discussions with the members of the condensed matter group: *Abhishodh, Adhip, Arnab, Indrajit, Junaid, Krushna, Manish, Monica, Sibaram, Souvik, Sumukha and Swadesh*. A special thanks to *Alan* and *Rekha* for enlightening me with new ideas from their research. I will always be grateful to *Krushna, Souvik, Basudeb, and Harsh* for their help at different moments during my PhD. All the numerics I did during my PhD would not have been possible without the help of *Bikram*, *Bibek*, and *Tamoghna*. I will always appreciate their support.

I am grateful to have been part of office G-109, a room filled with laughter and humor, where I shared the space with wonderful officemates *Harshit*, *Aditya*, and *Sandeep*, along with an unofficial but permanent member, *Kunal*. It was a great experience to share the office with them. *Harshit*, who is also my batchmate, provided company that

made my journey of joining ICTS, through COVID and into the final years, much more enjoyable. I will always cherish the moments we shared, from making silly mistakes in the lab to playing badminton and having fun conversations over lunch and dinner. *Aditya*, who seems to know everything, was always a source of learning during our discussions. Conversations with *Sandeep* were always fun, especially when trying new things in numerics. I also greatly admire the many discussions I had with *Kunal*, from which I often learned a lot. Our office also had two visitors, *Prateek* and *Sparsh*. I will always miss those 3:00 PM chit-chats when *Prateek* used to come in the office with an apple. Those moments were always refreshing for me, and I truly enjoyed our conversations. As for *Sparsh*, I will always admire our serious discussions about life and other topics, even though I usually dislike taking things seriously.

I am grateful to other batchmates, *Shivam, Uddeepta, Souvik, Omkar, Bhanu, Mahaveer, Priyadarshi, Tuneer, Anup, Mukesh, Jigyasa, Umesh, and Sahil*, with whom I had enlightening discussions during coursework and projects. I will always admire the humor of *Shivam*. I am also grateful to *Bhanu* and *Mahaveer* for being wonderful company on morning runs. Special thanks to *Uddeepta* for being a wonderful company on badminton court and board games. I will always cherish all the moments spent with *Ashik*, *Akash*, *Shalabh*, and *Aditya Thorat* talking with them was always a pleasant experience. I will always miss the weekend morning tea marathons with *Ashik*, hopping between different tea shops and enjoying long gup-shups. The reels shared by *Akash* on Instagram were one of the main reasons I used it. I really enjoyed watching them and laughed a lot. Special thanks to *Naveen*, *Asrat*, and *Anurag*, who kindly helped me understand many concepts of QFT used in my research. Thanks to *Saumav* for enlightening me with many fascinating ideas in fluid dynamics.

I am also grateful to *Anushka, Aiswarya, Aniket, Abhinav, Atharva, Avi, Chandru, Diksha, Godwin, Irshad, Jyotirmoy, Kanak, Kaushtubh, Mayank, Mrinal, Neha, Nitesh, Priyanka, Rajarshi, Rahul, Rishabh, Ritwick, Seema, Sam, Santhiya, Shridhar, Shashank, Thanmayee, Varun and Vinay*, there presence made the last six years more pleasant. I will always admire the simplicity and humble behavior of *Saikat* and *Jitendra*.

I am also grateful to *Hemanta, Madhulika, Nidhi, Pavana, Raju, and Ramya* for their help during various academic and administrative tasks. Special thanks to *Suresh* and *Basavraj* for their assistance with transport and other emergency situations. I would also like to extend my heartfelt thanks to all the canteen staff, security guards and cleaning personnel, whose dedicated efforts ensured that I had a comfortable stay during the past six years.

Outside G-109 and ICTS, I was lucky to meet incredible people on the badminton court, including *Reuben, Jitesh, Soumyadeep, Rashmi, Debosmita, Shruti, Dhanashree, Jim,*

Rajesh, Ajay, Viraj, Bhushan, Ankur, Manjunath, Parul, Shanmugapriya and Advait, with them it was always fun to play and enjoy the game. I have always admired the creative thinking of *Reuben* and have often wished to developed a similar mindset myself. Apart from running and badminton, I was fortunate to go on treks, which would not have been possible without the company of *Ankur, Atharva, Basudeb, Bhanu, Harsh, Hemanta, Krushna, Kritika, Ramesh, and Uddeepta*, with them it became an enjoyable activity.

Towards the end of my PhD, I met *Sarvesh* and *Vinay* from INSTEM, talking to them was always fun.

I would also like to thank my friends from undergrad, *Asghar, Avesh, Brijesh, Praveen, Aman, Manoj, and Priyanuj*, with them I began my journey of exploring the field of physics.

I am also deeply grateful to my family for their constant support and patience throughout these years.

dedicated to my family and
to everyone who strives to bring a smile to the faces of others....

List of Figures

List of Tables

Contents

Abstract

Traditional framework based on spontaneous symmetry breaking is insufficient to describe novel phases such as quantum spin liquids, topological states, and non-Fermi liquids, which require understanding many-body entanglement and the non-trivial implementation of microscopic symmetries at low energies. This thesis addresses three particular examples of the above interplay. First, we study superconductivity of $J = 3/2$ electrons on honeycomb lattice in context of transition metal tri-halides in presence of strong spin-orbit coupling. We identify a host of novel superconductors that includes gapped, nodal, and pair-density-wave states. Second, we study Z_2 fractionalized fermionic systems, where the projective action of symmetries is crucial to identifying phases arising from frustration among fractionalized degrees of freedom. The interplay of frustration and emergent gauge structures leads to dimer models exhibiting both topologically ordered phases and dimer crystals, resulting in a rich phase diagram. Third, we develop a wavefunctional approach for correlated metallic phases that captures quantum fluctuations of the Fermi surface and describes both Fermi liquid and non-Fermi liquid phenomenology. Together, these studies demonstrate the interplay of symmetries and entanglement in correlated quantum matter.

Chapter 1

Introduction

"Discovery consists of seeing what everybody has seen, and thinking what nobody has thought."
- Albert Szent-Györgyi

From observations in everyday life, such as metals conducting electricity while insulators[1] do not, or sticking of a refrigerator magnet, to more exotic phases like superconductivity, all of these can arise from the interactions of electrons and ions. Over the years, the number of known phases has continued to increase, ranging from Kondo insulators [4] to quantum spin liquids [5] and recently discovered altermagnetism [6][2]. This leads to the question: *How can we understand these phases that arise from the interactions of such constituents at the macroscopic scale?*

Addressing this question is a central goal of many-body physics [7, 8], with well-known examples including superconductivity [9, 10], magnetism [11], the fractional quantum Hall effect [12, 13], and Bose–Einstein condensation [14]. Conventional examples include phases explained within the framework of spontaneous symmetry breaking (SSB) [15], such as charge-density waves [16] and BCS superconductivity [9, 17]. Beyond these lie topological phases [18], such as topological insulators [19] and the fractional quantum Hall effect [13], whose characterization crucially depends on many-body entanglement. More exotic phases, including strange metals [20], feature gapless bulk behavior, and their understanding continues to pose challenges in many-body physics.

To understand these phases, it is essential to identify the emergent degrees of freedom that arise from interactions among macroscopic numbers of electrons and ions. These lead to the realization of phases that are qualitatively distinct from the behavior of the individual constituents, as emphasized by Anderson: *"the whole is not only more than, but very different from, the sum of its parts"* [21]. Therefore, organizing principles are needed to explain such emergent phases. One of the organizing principles under which a large class of phases can be successfully described is the Landau–Ginzburg

[1] Leaving aside topological insulators.
[2] This list is not complete.

paradigm of symmetry breaking [15, 22]. However, other phases require a broader theoretical framework involving topology, gauge theory, fractionalization, and anomalies [23]. A natural starting point to derive these organizing principles is the identification of fundamental ingredients: the relevant degrees of freedom, the symmetries they respect, and the interactions among them, as encoded in the Hamiltonian. For illustration, let us consider a generic form of the Hamiltonian[3] [1]

$$H = \sum_{ij,\alpha,\beta} (t_{ij,\alpha\beta} c^{\dagger}_{i\alpha} c_{j\beta} + h.c.) + \lambda \sum_{i} \mathbf{L}_i \cdot \mathbf{S}_i + U \sum_{i} n_{i\alpha} n_{i\beta} + \mu \sum_{i,\alpha} n_{i\alpha} \tag{1.1}$$

Here, $c_{i\alpha}$ annihilates an electron at site i in orbital α, with the first term representing the electron hopping on a lattice. The electrons interact via an on-site Hubbard interaction of strength U, and there is also atomic spin-orbit coupling with strength λ, which entangles the spin $\mathbf{S}$ and the angular momentum $\mathbf{L}$ of the electron. A chemical potential term with coefficient μ fixes the filling. This defines the degrees of freedom and how they interact. Transformations that leave the Hamiltonian invariant constitute the symmetries of the system. The nature of the emergent phases depends on how

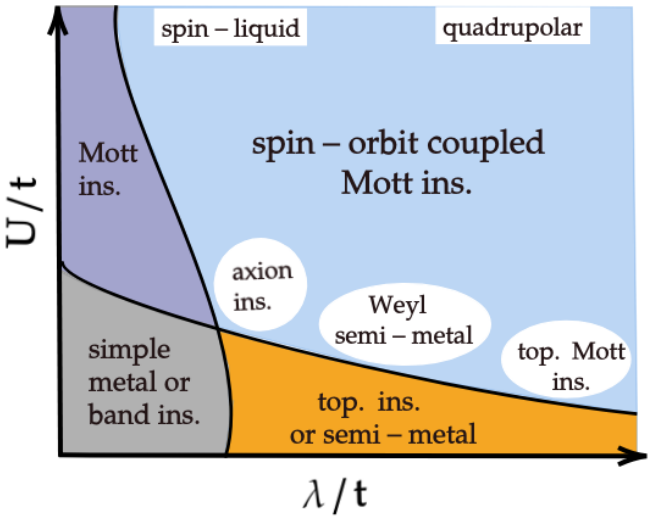

Figure 1.1: Redrawn from the paper *" Correlated quantum phenomena in the strong spin-orbit regime, "* [1]. Schematic Phase diagram as function of Spin-orbit coupling strength (λ) and Interaction strength (U) in Eq. 1.1.

the degrees of freedom interact. In this context, the relative strengths of these parameters determine the dominant interactions and, consequently, the realized phases. This is illustrated schematically in Fig. 1.1. Depending on the chemical potential, metallic,

[3]For simplification, we will focus only on the electron-electron interaction. Note that even for electrons, there can be other terms, such as Hund's coupling [24], but for this thesis, they are not relevant to the discussion.

semimetallic, or band insulating phases can emerge when hopping t dominates. Mott insulating phases arise when strong interactions localize electrons at appropriate fillings. Topological phases appear in the strong spin-orbit coupling limit. A rich variety of phases, such as axion insulators [25], topological insulators [19], Weyl semimetals [26–28], and quantum spin liquids [1, 29], can emerge in the regime where both interactions and spin-orbit coupling are significant and competing. These correspond to the blue region in the Fig. 1.1, covering the various mentioned phases.

This naturally raises the question of how to systematically understand such phases. One way is to broadly classify them according to the nature of their low energy excitations. Gapped phases lack propagating low energy degrees of freedom in the bulk, whereas gapless phases possess them [30]. Gapless phases can be further subdivided: semimetals exhibit a vanishing density of states (DoS) at low energies, while metals possess a finite DoS characterized by a Fermi surface. Further classification requires understanding the detailed nature of these low energy excitations. A more systematic and powerful approach is provided by field theory [8], which offers essential frameworks for capturing the low energy physics of different phases: Landau–Ginzburg theory for spontaneous symmetry broken phases [15, 22, 31], Chern-Simons theory for topological phases [32, 33], Fermi-liquid theory for metallic phases[4] [34–36], Bosonization for Tomonaga-Luttinger liquid phase in one dimension [2, 37] and relativistic theory of Dirac fermions for semimetallic phases [38–41].

However, identifying the field theory consists of two parts: first, deriving the field theory appropriate to the relevant energy scale; and second, characterizing the low-energy degrees of freedom, which are fields, by their transformation properties under the microscopic symmetries. This can be illustrated through the example of the transverse field Ising model on a D-dimensional cubic lattice,

$$H = -J \sum_{\langle ij \rangle} \tau_i^z \tau_j^z + \Gamma \sum_i \tau_i^x, \tag{1.2}$$

where τ_i^x and τ_i^z are Pauli matrices acting on the spin-$\frac{1}{2}$ degree of freedom at the ith site. This model exhibits ordered and disordered phases depending on the competition between the interaction strength J and the transverse field Γ. When the transverse field Γ dominates, the Ising spins are disordered, whereas for weak transverse fields, the Ising spins are in an ordered phase in which the Z_2 symmetry $\left(\tau_i^z \to \epsilon \tau_i^z \quad \forall i \text{ and } \epsilon = \pm 1\right)$ is spontaneously broken [42]. The low-energy transition between these phases is de-

[4] more specifically, weakly interacting short-range repulsive fermions at fractional filling with a Fermi surface

scribed by the scalar field theory [22]:

$$S[\phi] = \int d^{D+1}x \left((\partial_\mu \phi)^2 + m^2 \phi^2 + r\phi^4 \right). \tag{1.3}$$

The field ϕ captures order parameter fluctuations. While this theory successfully encodes the spontaneous breaking of Z_2 symmetry, it does not distinguish whether the ordered phase corresponds to ferromagnetic or antiferromagnetic order. Resolving this requires examining how the field ϕ transforms under lattice translations: for ferromagnetic order, the field maps onto itself ($\phi \to \phi$), whereas for antiferromagnetic order, it maps onto its negative ($\phi \to -\phi$). This example highlights the importance of understanding the implementation of microscopic symmetries in the low energy theory for the characterization of a phase.

The microscopic symmetries are embedded in the symmetries of the low energy theory. As the microscopic theory flows to the low energy scale under the renormalization group (RG), additional low energy symmetries (or IR symmetries with group G_{IR}) can emerge because operators that break them become irrelevant [43]. This induces an embedding of the microscopic symmetries (or UV symmetries with group G_{UV}) into the IR symmetry group G_{IR} via a group homomorphism from G_{UV} to G_{IR}, which need not be one-to-one or onto [44]. This can be understood from the example of the transverse field Ising model discussed earlier, where the low energy theory (Eq. 1.3) has continuous translation and rotation symmetry, whereas Eq. 1.2 has only the discrete rotation and translation symmetries of the underlying lattice. Other examples include graphene, where the low-energy description is given by a relativistic theory of Dirac fermions exhibiting emergent Lorentz symmetry. Additionally, the microscopic internal SU(2) spin rotation symmetry enlarges to an internal SU(4) symmetry [38]. This enhanced symmetry arises due to an emergent chiral SU(2) symmetry in the valley-subband sector. The covering group of this chiral SU(2) and the spin SU(2) symmetry forms the SU(4) group. Here also, lattice symmetries are embedded in the IR symmetries of the low energy theory (see [38, 40] for details).

Understanding the implementation of microscopic symmetries in the low energy theory becomes more important for strongly correlated systems, where the interplay of *interactions*, *symmetries*, and *entanglement* significantly alters the scope of electronic phases, including the nature of emergent degrees of freedom that characterize the low energy properties of such phases. This includes composite fermions in the fractional quantum Hall effect [12], spinons in quantum spin liquids [5], and Bogoliubov quasiparticles in superconductors [9, 31].

A central issue in such systems is understanding how microscopic symmetries are

realized at low energies, particularly when the quantum numbers of emergent degrees of freedom differ markedly from those of the underlying microscopic constituents. Two prominent platforms where such situations arise are systems with strong *spin-orbit coupling* (SOC) and those exhibiting *fractionalization*. SOC intertwines the real and spin spaces, leading to a nontrivial implementation of microscopic symmetries. On the other hand, fractionalization gives rise to emergent gauge structures in the theory, which allow for a projective implementation of microscopic symmetries, i.e., symmetry transformations accompanied by a gauge transformation [5, 8, 45]. Exploring these cases forms the focus of the first two parts of this thesis.

A further challenge arises in understanding strongly correlated phases with Fermi surfaces that cannot be recast in terms of weakly interacting quasiparticles, such as non-Fermi liquid (NFL) phases [46, 47], where Landau quasiparticles [35] do not exist. Even the fate of the IR fixed point for NFLs remains unsettled because the standard perturbative methods used to analyze interacting systems break down due to strong correlations and singular interactions near the Fermi surface [47, 48]. Addressing these challenges requires new ideas for understanding such phases. In the third part of the thesis, we address this question using trial wavefunctions.

This thesis will address these three key themes, which are discussed in detail in the following sections.

1.1 Superconductivity in Spin-Orbit Coupled System

As discussed before, Spin-Orbit coupling leads to the realization of a plethora of unconventional phases as shown in Fig. 1.1. It arises as a relativistic correction to the Schrödinger equation for an electron in an atom. It can be understood as the coupling between the electron's spin and the effective magnetic field it experiences in its rest frame due to its orbital motion around the nucleus [29]. It corresponds to the following term in the Hamiltonian [29],

$$H'_{SOC} = \sum_i \lambda \mathbf{L}_i \cdot \mathbf{S}_i \tag{1.4}$$

where λ corresponds to the spin-orbit coupling amplitude for the ith electron with orbital momentum $\mathbf{L}_i$ and spin $\mathbf{S}_i$. For a many-electron system, along with SOC, there is also interaction between electrons (as discussed in Eq. 1.1). The interplay of these two leads to the realization of exotic phases, as shown in Fig. 1.1. From a material perspective, SOC strength dominates for heavier elements, whereas electron-electron interaction dominates for lighter elements of the periodic table [1, 49]. In the first

part of this thesis, we focus on transition metal trihalides MX_3 (M = Zr, Hf and X = Cl,Br) [40, 50]. Here, M atoms in their d^1 configuration form a honeycomb lattice in the edge-sharing octahedral environment of halide ions. These systems provide a platform for Spin-Orbit coupling discussed in detail in [40]. The effective degree of freedom at every site corresponds to $j = 3/2$ orbitals arising because of SOC. The low energy theory for these systems is Dirac theory with internal SU(8) symmetry [40]. The multi-orbital setting with $j = 3/2$ orbitals at each lattice site, along with a large emergent symmetry group, provides avenues for realizing unconventional multiband superconductors in the presence of interactions. This can give rise to a variety of superconducting phases, such as multigapped [17], pair-density-wave (PDW) [51, 52], and nodal superconductors [53]. A distinctive feature of these multiband superconductors is that they provide a platform to study Leggett modes, which correspond to fluctuations of the relative phase between superconducting order parameters [54]. In the first part of the thesis, we will examine the superconducting phases that can be realized in these systems[5]. The nature of these phases can be understood by analyzing the transformation properties of superconducting order parameters[6] under the action of microscopic symmetries [38, 55]. In our investigation, we find *twelve* distinct superconducting phases, which divide into *four* singlets, *two* doublets, and *six* triplets under the action of microscopic symmetries [55]. *Eleven* of these superconductors are non-unitary (having multiple superconducting gaps) [17], including *five* that are gapless (nodal) superconductors, where the nodes are protected by lattice symmetries. The triplet superconductors result from finite-momentum pairing and form examples of pair-density wave superconductivity [56].

1.2 Z_2 Fractionalized Phases

Other platforms for realizing non-trivial implementations of microscopic symmetries arise through fractionalization [5,57,58]. In fractionalization, a physical degree of freedom is decomposed into more elementary objects, called partons [5]. A classic example is the one-dimensional Mott insulating phase of the Hubbard model, which can be described in terms of partons-spinons (carrying spin) and holons (carrying charge) [59]. Other examples include quantum spin liquid phases [5, 45, 60], the fractional quantum Hall effect [12], and orthogonal metals [61, 62]. Fractionalization naturally introduces a redundant transformation known as a gauge transformation. Under this transformation, the partons transform, while the original physical degree of free-

[5] Insulating phases are discussed in details in [40]

[6] We will be using the term superconducting bilinears in the later part of the thesis

dom remains invariant. As a consequence, microscopic symmetries are implemented projectively [5,8,45], that is, each symmetry operation is accompanied by an associated gauge transformation that preserves the Hamiltonian.

In the second part of the thesis, we focus on the case of Z_2 fractionalization of a spinless fermion c_i on the square lattice [61–63]. Here, the fermion fractionalizes into an Ising spin τ_i^x and a fermion f_i at the ith site [61], such that

$$c_i^\dagger = \tau_i^x f_i^\dagger \, .$$

In this representation, f_i carries the charge quantum number of c_i, whereas τ_i^x tracks the parity of fermionic occupancy at site i. Such fractionalization can give rise to exotic phases, such as orthogonal metals. These are non-Fermi liquid states in which the gauge-invariant fermion is gapped, yet transport persists via the fractionalized fermions [61, 62]. Both τ_i^x and f_i carry a Z_2 gauge charge. This corresponds to the local Z_2 gauge transformation $f_i \to \epsilon_i f_i$ and $\tau_i^x \to \epsilon_i \tau_i^x$, with $\epsilon_i = \pm 1$ and leaves the gauge-invariant fermion c_i unchanged. This leads to an emergent Z_2 gauge structure in the theory, with the Z_2 gauge field σ_{ij}^z residing on the lattice links.

The low energy effective theory for the fractionalized degrees of freedom, minimally coupled to Z_2 gauge fields (σ_{ij}^z) on the links, is governed by the following Hamiltonian (terms in red and blue) [61,64]:

$$\mathcal{H} = -J \sum_{\langle ij \rangle} \tau_i^x \sigma_{ij}^z \tau_j^x - \Gamma \sum_i \tau_i^z - t \sum_{\langle ij \rangle} f_i^\dagger \sigma_{ij}^z f_j - \mu \sum_i f_i^\dagger f_i - \kappa \sum_\square \prod_{\langle ij \rangle \in \square} \sigma_{ij}^z - h \sum_{\langle ij \rangle} \sigma_{ij}^x \quad (1.5)$$

with the Gauss's law given by

$$\prod_{j \in i} \sigma_{ij}^x = (-1)^{\frac{1-\tau_i^z}{2} + f_i^\dagger f_i}. \quad (1.6)$$

Here, (τ_i^x, τ_i^z) are the Pauli matrices acting on the spin-1/2 degree of freedom at the ith site and $(\sigma_{ij}^x, \sigma_{ij}^z)$ are the Pauli matrices acting on the spin-1/2 degree of freedom on the bonds of the lattice. In Eq. 1.5, the terms in black correspond to the Z_2 gauge theory describing the dynamics of the gauge field [65,66], where $\square$ represents an elementary plaquette of the square lattice, and in Eq. 1.6, the product runs over all sites j that are nearest neighbors of site i.

We studied this model where the Ising spins and fermions are frustrated due to a background π-flux from the emergent Z_2 gauge field on the links. This corresponds to the limit $\kappa \to -\infty$ and $h = 0$. For the Ising spins, the model reduces to a frustrated

transverse field Ising model, which exhibits an order-to-disorder transition described by the 3D XY^* universality class [67].

For the fermions, this corresponds to fermions hopping on a square lattice with π-flux per plaquette. The low energy theory at half-filling is described by a relativistic theory of Dirac fermions. Using a projective implementation of microscopic symmetries on the Dirac fermions and Ising soft modes, we investigated the fate of the fermions as the Ising spins transition from the ordered to the disordered phase. This forms the discussion of the second part of the thesis. Our analysis indicates that the fermions remain gapless throughout the transition from disorder to order. In the ordered phase of the Ising spins, the fermions form a semimetallic phase that breaks lattice symmetry, whereas in the disordered phase they realize an orthogonal semimetal phase [64].

The model can also be written in terms of gauge-invariant operators using the mapping $Z_{ij} = \tau_i^x \sigma_{ij}^z \tau_j^x$ and $X_{ij} = \sigma_{ij}^x$, together with Gauss's law [68, 69]:

$$\begin{aligned}\mathcal{H} = &-J \sum_{\langle ij \rangle} Z_{ij} - \Gamma \sum_i \left[\prod_{j \in i} X_{ij} \right] (-1)^{c_i^\dagger c_i} - t \sum_{\langle ij \rangle} c_i^\dagger Z_{ij} c_j - \mu \sum_i c_i^\dagger c_i \\ &- \kappa \sum_{\square} \prod_{\langle ij \rangle \in \square} Z_{ij} - h \sum_{\langle ij \rangle} X_{ij}. \end{aligned} \tag{1.7}$$

In the absence of fermions (at filling $\nu = 0$), the limit $\kappa \to -\infty$ and $h = 0$ corresponds to the odd toric code model in a Zeeman field [70]. At $\Gamma = 0$, the ground state configurations correspond to a dimer covering on the dual lattice, where each site of the dual lattice is connected to exactly one dimer [3]. The Γ term generates perturbatively the resonating term of the quantum dimer model [71], which stabilizes the columnar dimer ordering of dimers on the dual lattice. This ordering is also the ordered phase of the frustrated transverse field Ising model [3].

Adding the following potential term for the dimers,

$$+\frac{\Omega}{4} \sum_i \left((1 - Z_{i-\hat{x},i})(1 - Z_{i+\hat{x},i}) + (1 - Z_{i-\hat{y},i})(1 - Z_{i+\hat{y},i}) \right), \tag{1.8}$$

yields the quantum dimer model in the limit $\Omega/J \ll 1$ and $\Gamma/J \ll 1$, known as the Rokhsar–Kivelson Hamiltonian [71]. Varying Γ and Ω can drive transitions out of the dimer regime. For large Γ, a topologically ordered phase emerges [70], while for large Ω, a staggered phase appears [72, 73].

We analyzed the Hamiltonian in Eq. 1.7 in the absence of fermions, combined with the term in Eq. 1.8, which yields a rich phase diagram with three ordered phases: columnar, staggered, and topological ordered. These phases are separated by three

phase boundaries that possibly meet at a multicritical point. We will complete our discussion in the second part of the thesis by exploring this phase diagram.

1.3 Correlated Metals

As mentioned before, phases are broadly classified based on their spectra into gapped and gapless phases. Gapless phases, characterized by a finite DoS and a Fermi surface, continue to pose conceptual challenges for theorists. These phases possess extensive gapless modes, making them susceptible to external perturbations, yet they can still form stable phases of matter [48]. One well-understood example is that of weakly interacting, short-range repulsive fermions at fractional filling with a Fermi surface, commonly referred to as Fermi liquids. These phases are ubiquitous in nature, often persisting down to low temperatures, and are effectively described within Landau's quasiparticle framework [35]. In the Fermi liquid phase, low energy excitations near the Fermi surface can be adiabatically mapped onto those of non-interacting fermions with renormalized parameters, known as Landau quasiparticles [35]. Moreover, the renormalization group (RG) approach developed in Ref. [36, 74] demonstrates that forward-scattering interactions remain marginal at both tree and one-loop levels, consistent with Landau Fermi liquid theory. However, among all interaction channels, only the BCS interaction which is marginal at tree level, becomes relevant at one-loop when attractive, resulting in superconducting instability [30, 36], which was not captured within the original Landau Fermi liquid framework.

This RG framework provides a solid understanding of Fermi liquids; however, experiments (see reviews [47, 75]) have revealed gapless phases with a Fermi surface but no Landau quasiparticles. In addition, phases exhibiting seemingly disconnected Fermi arcs instead of closed Fermi surfaces have been observed in cuprates [76, 77]. Such phases lie beyond the Fermi liquid paradigm and are referred to as non-Fermi liquids (NFL). These can arise when Fermi surfaces are coupled to critical bosons corresponding to fluctuations of an order parameter or emergent gauge fields [47, 48]. Due to strong quantum fluctuations, a comprehensive understanding of NFL phases remains a significant challenge. NFL phases can exhibit scaling behavior distinct from Fermi liquids, due to which terms irrelevant in Fermi liquid theory may have nontrivial consequences for NFLs [30].

Understand them requires new approaches. We study trial ground-state wavefunctions capable of capturing the phenomenology of both Fermi liquid and non-Fermi liquid phases. Our method employs superposition of Fock space wavefunctions to analyze the ground-state properties of such correlated metals [78]. Through this super-

position, we describe fluctuations in the shape of the Fermi surface, which correspond to fluctuations in the single-particle occupancy $n_{\mathbf{k}}$, since $n_{\mathbf{k}}$ does not commute with the interacting Hamiltonian. Such fluctuations are key signatures of renormalization, or even vanishing, of the quasiparticle residue [34], thereby distinguishing Fermi liquids from non-Fermi liquids. The final part of this thesis aims to provide insights into trial ground states for such correlated metallic phases, capturing the phenomenology of both Fermi liquid and non-Fermi liquid regimes by incorporating quantum fluctuations in the shape of the Fermi surface.

1.4 Thesis Structure

This thesis is broadly divided into three parts. The first part, comprising Chapters 2 to 5, focuses on superconductivity in spin–orbit coupled systems. The second part, consisting of Chapter 6, addresses Z_2 fractionalized phases. The third part, Chapter 7, discusses the trial wavefunction approach for correlated metals. We will conclude our discussion in Chapter 8. A brief summary of the contents of each chapter is provided below.

Chapter 2 This chapter introduces the spin-orbit coupled system and the low energy theory developed in [40]. We begin with the SU(8) Dirac theory [40] and then cover the Nambu representation used to incorporate superconducting terms into the Hamiltonian. The chapter concludes with a brief review of the various superconducting phases.

Chapter 3 This chapter examines the implementation of microscopic symmetries in the low energy theory. We then explore the effects of short-range interactions. While the semimetal phase is perturbatively stable against weak interactions, strong interactions spontaneously break the symmetry, leading to the condensation of bilinears. We focus on bilinears that spontaneously break the U(1) symmetry and gap out the Dirac fermions. This analysis requires identifying all the mass terms in the Nambu basis. After determining these mass terms, we present a classification of the various superconducting phases based on their transformation properties under microscopic symmetries.

Chapter 4 This chapter provides a detailed discussion of lattice singlet and doublet superconductors. In total, we examine four singlet and two doublet superconducting phases. We analyze their spectra, time-reversal properties, and order-parameter man-

ifolds, along with their realizations on the lattice. These superconductors do not break translation symmetries.

Chapter 5 This chapter focuses in detail on lattice triplet superconductors. The triplet states considered not only break rotational symmetry but also break translational symmetry, corresponding to pair-density-wave (PDW) superconductors. All the superconductors studied in this chapter correspond to pair-density-wave superconductivity. We discuss similar details as in the previous chapter for singlet and doublet superconductors. Then, we conclude our discussion of the various superconducting phases (singlets, doublets and triplets) realized for spin–orbit coupled SU(8) Dirac fermions by summarizing our results in the summary section of this chapter.

Chapter 6 This chapter discusses the Z_2 fractionalization of spinless fermions where it fractionalizes into an Ising spin and a fermion. We examined the projective action of symmetries to identify the phases arising from frustration among the fractionalized degrees of freedom. After understanding these phases, we considered the same model at a different fermion filling, $\nu = 0$. This limit leaves a frustrated transverse-field Ising model of Ising spins, which, when supplemented with an additional term, provides an interpolation between the RK Hamiltonian and the Toric code. The second part of this chapter presents a detailed analysis of the phase diagram of this Hamiltonian.

Chapter 7 This chapter addresses the problem of strongly correlated metals with a Fermi surface, but from a different perspective. We focus on trial wavefunctions that can capture the known phenomenology of these phases. These trial wavefunctions are constructed as superpositions of states in the Fock space. To verify this approach, the chapter first discusses the exact diagonalization of interacting spinless fermions in one dimension in two different ways. Then, it presents a toy model where the ground state corresponds to a superposition of all states in the Fock space. Finally, in two dimensions, different trial wavefunctions are examined, and various correlators are computed in those states.

Chapter 8 We conclude our discussion of the three parts by summarizing the main findings of this thesis and providing perspectives for future directions.

Chapter 2

Superconductivity in Spin-orbit coupled SU(8) Dirac Semimetal

Chapters 2–5 are based on our work published in Ref. [55], carried out in collaboration with Basudeb Mondal, Vijay Shenoy, and Subhro Bhattacharjee. I am grateful to them for their guidance and support. The results presented in Appendix A.8 were produced by Vijay Shenoy.

2.1 Introduction

Superconductivity in Dirac systems (DSC) [39,41,79–83] is different from their conventional weak-coupling BCS counterparts (those arising from the instability of a Fermi surface [9]). Starting with the fact that the superconductivity in Dirac semi-metals occur at finite interaction strength [39, 79–84] as opposed to the conventional superconductors, the Dirac nature of the underlying fermions clearly distinguishes, among other things, the properties of superconducting junctions involving a DSC [85–88], from their BCS counterparts. Further, superconductors realized on the surface of the DSMs of topological insulators harbour a plethora of unconventional properties [88–91]. The nature of the superconductors realized in such Dirac systems is intricately related to the underlying symmetries [38]. Therefore, the possibility of realizing unconventional superconductivity in Dirac systems due to non-trivial implementation of microscopic symmetries arising from strong spin-orbit coupling offers an interesting direction of exploration apropos candidate materials [88, 90, 91].

The study of these materials, particularly the metallic halides (MX_3 with M=Zr, Hf and X=Cl, Br) indicates [40, 50] that strong spin-orbit coupling (SOC) can lead to a SU(8) Dirac semi-metal (DSM) in these layered honeycomb lattice materials with active $j = 3/2$ electrons at $1/4$th filling. The low-energy description of such a DSM is

captured by the free Dirac Hamiltonian [40]

$$H_D = -iv_F \int d^2\mathbf{x}\, \chi^\dagger(\mathbf{x}) \left[\bar{\boldsymbol{\alpha}} \cdot \boldsymbol{\partial}\right] \chi(\mathbf{x}) \tag{2.1}$$

where v_F is the Fermi-velocity, $\chi(\mathbf{x})$ is a 16-component Dirac spinor and $\bar{\boldsymbol{\alpha}} = (\bar{\alpha}_1, \bar{\alpha}_2)$ are two (16×16) anti-commuting Dirac matrices.

The above effective low-energy (IR) free theory has an enlarged global SU(8) symmetry, and the microscopic (UV) symmetries, including time reversal (TR), are embedded non-trivially on the low-energy fields due to the underlying SOC. A related outcome of the strong SOC is the position of the Dirac points in the Brillouin zone (BZ) – unlike monolayer graphene, where there are two in-equivalent Dirac cones at the BZ corners (the so-called $\mathbf{K}'$ and $\mathbf{K}$ points) [92] – here, there are four Dirac points: one at the BZ center (Γ) and three at the middle of BZ boundary (M) (see Fig. 2.1(b)). Under UV symmetries, these four Dirac valleys break up as a singlet (Γ) and a triplet (M_1, M_2, M_3) along with locking of the real and spin spaces. This results in a plethora of phases proximate to the DSM obtained by breaking the SU(8) and/or TR symmetry by partially/fully gaping out the Dirac fermions due to condensation of fermion bilinears of the form $\langle \chi^\dagger(\cdots)\chi \rangle \neq 0$ (where $(\cdots)$ is a 16×16 matrix that anti-commute with Dirac matrices $\bar{\alpha}_1$ and $\bar{\alpha}_2$ in Eq. 2.1). In particular, Ref. [40] analyzed 64 such bilinears comprised of the SU(8) singlet and the adjoint multiplet to obtain 24 distinct phases describing various charge/spin density waves as well as symmetry protected topological phases– all of which conserve the global U(1) symmetry

$$\chi \longmapsto e^{i\theta}\chi, \tag{2.2}$$

related to the electron charge conservation. Due to the distinction in the position (and number) of the Dirac valleys, the larger IR symmetry and the implementation of the UV symmetries, the resultant phases are quite different compared to monolayer graphene [38].

In this chapter, we explore the consequences of the above symmetry implementation in the SU(8) DSM to understand the nature of various superconducting instabilities that are naturally proximate to the SU(8) DSM and can be obtained at finite interaction strengths [39, 79–83]. Such superconductors (SCs) spontaneously break the above $U(1)$ symmetry via condensation of charge $2e$ Cooper pairs, *i.e.*, $\langle \chi^\dagger(\cdots)\chi^\dagger \rangle \neq 0$, where $(\cdots)$ denote an appropriate matrix that decides the pairing symmetry. On generic grounds [93], there are 16 different pairing channels for the $j = 3/2$ electrons with total angular momentum of each Cooper pair ranging from $J_T = 0$ (singlet) to $J_T = 3$ (septet) with the even (odd) J_T corresponding to spatial parity even (odd)

pairing (see Eq. 4.9). We show that the presence of many bands [10, 94–100] (resulting in different flavours of Dirac fermions) and spin-orbitally locked higher ($j = 3/2$) representation opens up the possibility to realize a new set of unconventional SCs via specific symmetry allowed combination of the larger number of available pairing channels for $j = 3/2$ electrons [93, 101] and characterize them systematically using space-group representations [10,38,99,100,102,103]. The present work, along with the study of the normal phases discussed in Ref. [40], provides a comprehensive catalog of phases proximate to SOC induced SU(8) DSM.

Due to the intertwining of the spin and real spaces by SOC, the irreducible representations of the superconducting order parameters have a mixed structure that generically results in the direction dependence of the angular momentum of the Cooper pairs. This locking of angular momentum with direction naturally gives rise to non-unitary SCs [95] with possible finite momentum pairing in the absence of magnetic order or external magnetic field. Indeed, the non-trivial interplay of the higher-dimensional spin representation and the superconducting pairing symmetry is central to the rich variety of SCs that can be realized in this system.

Our classification shows that there are 72 superconducting fermion bilinears that form real and imaginary components of 36 pairing amplitudes. This gives rise to 12 spin-orbit coupled SCs that are distinct from each other under microscopic symmetries – *four* singlets, *two* doublets and *six* triplets. Most of the SCs – including several singlet ones– are non-unitary and hence show a multi-gap structure. Five of these are nodal SCs (the smallest gap is zero), which are protected by some subgroup of the SU(8). For the other seven, we generically obtain gapped superconductivity except in some cases (such as the odd parity doublets, $\mathcal{E}_u$, in Sec. 4.2.1 and $\mathcal{T}_g$ and $\mathcal{T}_u$ triplets in Sec. 5.1), where the smaller of the two gaps collapses on sub-space of the superconducting order-parameter manifold, giving rise to nodal SCs. The SOC-mediated interlocking of the spin and real spaces is manifest in the structure of the Cooper-pair wave functions of the respective SCs, which also results in multi-gap structures and possible Leggett modes [104] – even for the singlets due to the higher $j = 3/2$ representation and SOC. Another reflection of the spin-orbital interlocking is seen in the variation of the multiple gaps as a function of the SC order-parameter space, including the collapse of the gap at isolated points or on extended order-parameter subspaces (only for triplets). Further, while the singlet and the doublet SCs result from zero momentum pairing, this is not the case for the triplets, which then give rise to pair density-wave (PDW) SCs.

In this chapter, we will review the theoretical framework of SU(8) Dirac fermions as discussed in [40]. We begin by outlining the construction and symmetry proper-

ties of the SU(8) Dirac semimetal. Following this, we explore the superconducting phases emergent in these Dirac fermions, introducing the Nambu representation that provides a comprehensive framework to encompass all possible superconducting instabilities. The chapter concludes with an overview summarizing the classification and characteristic features of the various superconducting instabilities that arise in the SU(8) Dirac semimetal.

2.2 SU(8) Dirac fermions on Honeycomb lattice.

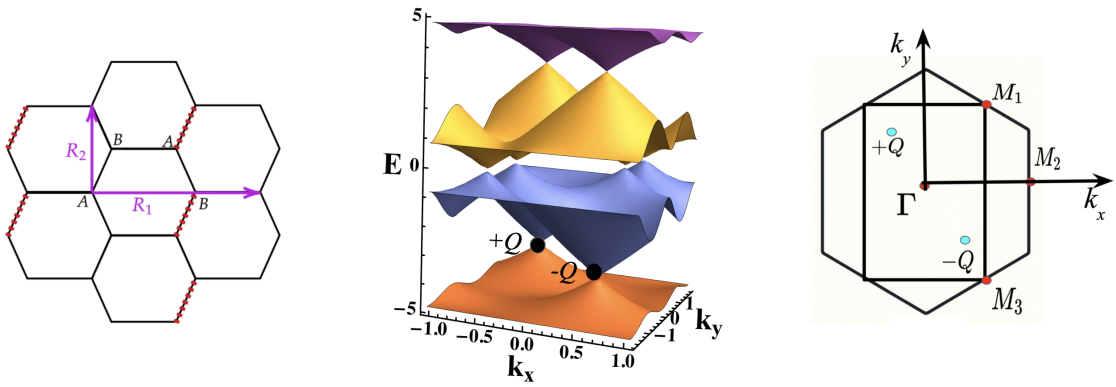

(a) **(b)** **(c)**

Figure 2.1: (a) Honeycomb lattice with a particular realization $\eta_{\mathbf{rr'}} = +(-1)$ on black(red) bonds that implements π-flux through each honeycomb plaquette. There are two choice of unit cell –(1) the *global basis* that uses the primitive 2-site unit cell of the honeycomb lattice consisting of (A, B) (Eq. 2.3), or (2) the *local basis* that has a 4-site unit cell (Eq. 2.5 with lattice vectors $(\mathbf{R_1}, \mathbf{R_2})$). (b) Band structure for the microscopic Hamiltonian Eq. 2.3 in local basis for the magnetic unit cell consisting of four sites. Each band is four-fold degenerate. For d_1 system, the lowest four bands are occupied with the chemical potential crossing the two Dirac points. (c) The primitive honeycomb BZ (Brown) with Dirac cones at Γ, M_1, M_2, M_3 points. For the local basis with a 4-site unit cell as shown in (a), we have a rectangular BZ (green) with Dirac cones as $\pm\mathbf{Q} = \pm[-\pi/6, \pi/2\sqrt{3}]$ points as shown in (b) [40].

We start by summarizing the essential microscopic details from Ref. [40] (using the same notations) leading to the low-energy Dirac theory of Eq. 2.1, which is realized in $j = 3/2$ SOC coupled honeycomb systems with d^1 electronic configuration in the nearest neighbor in-direct hopping model given by [40, 49, 50]

$$H = -\frac{t}{\sqrt{3}} \sum_{\langle \mathbf{rr'} \rangle} \Psi^\dagger(\mathbf{r}) \mathcal{U}^{global}_{\mathbf{rr'}} \Psi(\mathbf{r'}) + \text{h.c.}, \tag{2.3}$$

where

$$\Psi(\mathbf{r}) = [\Psi_{1/2}, \Psi_{-1/2}, \Psi_{3/2}, \Psi_{-3/2}]^T, \tag{2.4}$$

is the four-component electron annihilation operator corresponding to the $j = 3/2$ orbitals at the lattice site at $\mathbf{r}$ and $\mathcal{U}^{global}_{\mathbf{r}\mathbf{r}'}$ are 4×4 hopping matrices. Various lattice symmetries are indicated in Fig. 2.2. These, along with the time reversal (TR), $\mathbb{T}$ (with $\mathbb{T}^2 = -1$), generate the microscopic (UV) symmetry group of the system.

The directed product of the hopping matrices on the honeycomb plaquette, *i.e.*, $\prod_{\langle \mathbf{r}\mathbf{r}' \in \hexagon \rangle} \mathcal{U}^{global}_{\mathbf{r}\mathbf{r}'} = -\Sigma_0$ (with Σ_0 being the 4×4 identity matrix). This implies that the electrons have a SU(4) symmetry, which can be made manifest via a site-dependent unitary transformation on the atomic orbitals via

$$\phi'(\mathbf{r}) = g(\mathbf{r})^\dagger \Psi(\mathbf{r}), \tag{2.5}$$

where $g^\dagger(\mathbf{r})\, \mathcal{U}^{global}_{\mathbf{r}\mathbf{r}'}\, g(\mathbf{r}') = \eta_{\mathbf{r}\mathbf{r}'}\Sigma_0$, with $g(\mathbf{r})$ being a 4×4 unitary matrix at the lattice site $\mathbf{r}$, $\phi'(\mathbf{r})$ being fermion orbitals (flavours) in the *local basis*, and $\eta_{\mathbf{r}\mathbf{r}'} = \pm 1$ being an Ising gauge field. In this local basis, the problem reduces to four decoupled flavours (from the underlying SU(4) symmetry) of fermions hopping on the honeycomb lattice in π-flux, whence, choosing a suitable magnetic unit-cell (Fig. 2.1(a)), the band Hamiltonian is diagonalized to obtain two 4-fold (flavour) degenerate Dirac nodes/valleys at momenta $\pm\mathbf{Q}$, as shown in Fig. 2.1((b) and (c)). Expanding about the two valleys ($\pm$), we get the continuum Dirac Hamiltonian given by

$$H_D \;\; = -iv_F \sum_{f=1}^{4} \int d^2\mathbf{x}\; \chi_f^\dagger(\mathbf{x}) \left[\alpha_1 \partial_1 + \alpha_2 \partial_2\right] \chi_f(\mathbf{x}), \tag{2.6}$$

where there are four flavours (for $f = 1, 2, 3, 4$) of 4-component Dirac spinor, χ_f, *i.e.*,

$$\chi_f = \left(\chi_{f1+}, \chi_{f2+}, \chi_{f1-}, \chi_{f2-}\right)^T, \tag{2.7}$$

with the subscript $1(2)$ denoting the two bands that touch at each of the two Dirac valleys ($\pm$), in the local basis, and

$$\alpha_1 = \tau_3\sigma_1, \qquad \alpha_2 = \tau_0\sigma_2, \tag{2.8}$$

are the two anti-commuting Dirac matrices with τ_i, σ_i (for $i = 0, 1, 2, 3$) being 2×2 Identity and the Pauli matrices that act on the valley and band spaces, respectively.

This can be written in a more compact notation given in Eq. 2.1 with

$$\bar{\alpha}_i = \Sigma_0 \alpha_i \quad (i = 1, 2), \tag{2.9}$$

and

$$\chi = (\chi_1, \chi_2, \chi_3, \chi_4)^T, \tag{2.10}$$

being the 16-component spinor obtained by stacking the different flavours with Σ_0 acting in the flavour space.

The flavour SU(4) symmetry is manifest in the local basis and is generated by the fifteen Σ_i matrices (see Ref. [40] for their explicit form). In addition, the above free Dirac theory has an emergent SU(2) symmetry generated by

$$\{\tau_3\sigma_0/2, \tau_1\sigma_2/2, \tau_2\sigma_2/2\} \equiv \{\zeta_1, \zeta_2, \zeta_3\}/2, \tag{2.11}$$

such that it (Eq. 2.1) is invariant under the covering group of SU(4)$\otimes$SU(2), *i.e.*, SU(8) generated by [40]

$$\mathcal{P}_a = \Sigma_i \zeta_j. \tag{2.12}$$

It is useful to note that as discussed in Ref. [40], the above low-energy theory can also be derived in the *global basis* of Ψ (Eq. 2.3), using the 2-point honeycomb unit cell (Fig. 2.1). In this basis, the SU(4) symmetry is not manifest, and we get four bands (each two-fold Kramers degenerate) and have 4 Dirac points at 1/4th filling. The location of the four Dirac points in the global basis is also shown in Fig. 2.1, with one being located at the primitive BZ center (Γ point) while the other three being located at the three inequivalent mid-points of the BZ boundary– the so-called M points. The details are briefly discussed in Appendix A.1 for completeness, while further details are given in Ref. [40]. Throughout the chapter, we shall mostly work in the local basis unless explicitly stated. However, occasionally we shall refer to the global basis when it proves more insightful.

2.3 Superconductivity in Dirac fermions

The above free Dirac theory needs to be supplemented with short-range four-fermion interactions amongst the electrons of the generic form

$$H_{int} = \int d^2\mathbf{x} d^2\mathbf{x}' \; V_{ijkl} \; \chi_i^\dagger(\mathbf{x}) \chi_j^\dagger(\mathbf{x}') \chi_k(\mathbf{x}) \chi_l(\mathbf{x}'). \tag{2.13}$$

The Dirac semi-metal is perturbatively stable to such short-range four-fermion interaction [39, 79–83], but strong interaction generically leads to condensation of fermion bilinears, *i.e.*,

$$\langle \chi^\dagger_{f\tau\sigma}\chi_{f'\tau'\sigma'}\rangle \neq 0, \text{ or } \langle \chi_{f\tau\sigma}\chi_{f'\tau'\sigma'}\rangle \neq 0. \tag{2.14}$$

While condensation of both these sets of bilinears spontaneously break the symmetries of the free theory as well as possibly other microscopic symmetries with concomitant gaping out of all/fraction of the Dirac fermions, a major classifying difference between them is – the first set is electronic charge neutral and the second set carry charge $2e$.

The mean field Hamiltonian for both the normal and the superconductors is obtained by decoupling the four-fermion interactions in the different particle-hole and particle-particle channels, respectively, to obtain

$$H_{MF} = H_D + \tilde{\Delta}\int d^2\mathbf{x}\,[\chi^\dagger\,\tilde{m}\,\chi] + \Delta\int d^2\mathbf{x}\,[\chi^\dagger\, m\, (\chi^\dagger)^T] + \text{h.c.}, \tag{2.15}$$

with H_D is given by Eq. 2.1 or Eq. 2.6 and

$$\tilde{\Delta} = \langle \chi^\dagger \tilde{m} \chi\rangle\ ,\ \Delta = \langle \chi^T\, m^\dagger\, \chi\rangle\,, \tag{2.16}$$

where $\tilde{m}$ is a 16-dimensional Hermitian matrix and m is a 16-dimensional anti-symmetric matrix (see below). Further details for diagonalizing Eq. 2.15 are given in Appendix A.2.

2.3.1 Hamiltonian in Nambu basis

To study these orders, it is useful to use the Nambu spinor representation [38]. We define the 32-component Nambu spinor as

$$\chi_N(\mathbf{x}) = [\chi(\mathbf{x}), \chi^{\dagger T}(\mathbf{x})], \tag{2.17}$$

or equivalently in momentum space

$$\chi_N(\mathbf{q}) = [\chi(\mathbf{q}), \chi^{\dagger T}(-\mathbf{q})]. \tag{2.18}$$

Note that this is slightly different from the conventional Nambu spinor (Eq. A.5), where the TR partners are stacked [85, 87], as discussed in Appendix A.2. However, we find the representation in Eq. 2.17 more convenient to implement the symmetries in the present case. The transformation between the two bases is straightforward as discussed in Appendix A.2. The free Dirac Hamiltonian in Eq. 2.1 can then be written,

in momentum space, as

$$H_D = \frac{v_F}{2} \int \mathrm{d}^2\mathbf{q} \;\; \chi_N^\dagger(\mathbf{q}) \Big(\tilde{\alpha}_1 \, q_x + \tilde{\alpha}_2 \, q_y \Big) \chi_N(\mathbf{q}), \tag{2.19}$$

where, for the rest of the calculations, we set $v_F = 1$ and

$$\tilde{\alpha}_1 = \mu_0 \bar{\alpha}_1, \quad \tilde{\alpha}_2 = \mu_3 \bar{\alpha}_2. \tag{2.20}$$

Here, μ_0 is 2×2 the identity matrix, and μ_i for $i = 1, 2, 3$ are the Pauli matrices that act on the Nambu sector.

The mean-field Hamiltonian in Eq. 2.15 in the Nambu basis has the following form,

$$H_{MF} = H_D + \int d^2\mathbf{x} \, \left[\chi_N^\dagger \, M_{general} \, \chi_N \right]. \tag{2.21}$$

Here, H_D is given by Eq. 2.19 and $M_{general}$ is 32-dimensional Hermitian matrix which has the following generic form

$$M_{general} = \begin{bmatrix} M_{ph} & M_{pp} \\ M_{pp}^\dagger & -M_{ph}^T \end{bmatrix}, \tag{2.22}$$

where $M_{ph} (= M_{ph}^\dagger)$ and $M_{pp} (= -M_{pp}^T)$ are 16×16 matrices respectively in the particle-hole (normal) and particle-particle (superconducting) sectors. Note that the anti-symmetry of M_{pp} is due to fermionic statistics and ensuing Pauli exclusion principle [10] such that the mass matrix obeys

$$M_{general} = -(\mu_1 \, M_{general} \, \mu_1)^T. \tag{2.23}$$

Thus, to obtain the different masses, we consider all possible independent matrices $M_{general}$ which anti-commute with the matrices $\tilde{\alpha}_1$ and $\tilde{\alpha}_2$, and follow the above constraint (Eq. 2.23). To this end, we write

$$M_{general} = \mathcal{M}_{\alpha\beta\gamma\delta} X_{\alpha\beta\gamma\delta}, \tag{2.24}$$

where $\mathcal{M}$ is the amplitude and

$$X_{\alpha\beta\gamma\delta} = \mu_\alpha \Sigma_\beta \tau_\gamma \sigma_\delta, \tag{2.25}$$

forms the set of linearly independent 32-dimensional matrices formed from the matrices acting in the different spaces mentioned above. There are possible 1024 such $X_{\alpha\beta\gamma\delta}$ matrices, of which 256 anticommute with $\tilde{\alpha_1}$ and $\tilde{\alpha_2}$ (Eq. 2.20), and only 136 of them

are allowed by the antisymmetry constraint of Eq. 2.23. Out of these 136, 64 are normal masses of the form

$$\chi_N^\dagger(X_{0\beta\gamma\delta})\chi_N, \text{ and } \chi_N^\dagger(X_{3\beta\gamma\delta})\chi_N, \tag{2.26}$$

which correspond to the SU(8) singlet and the adjoint multiplet, whose properties were analyzed in Ref. [40].

The rest of the 72 matrices have a generic form of

$$\chi_N^\dagger(X_{1\beta\gamma\delta})\chi_N, \text{ and } \chi_N^\dagger(X_{2\beta\gamma\delta})\chi_N, \tag{2.27}$$

and correspond to U(1) breaking superconducting masses. In the rest of the work, we study the properties of these superconducting masses. Upon expanding the two expressions above, we have, in terms of the 16-component Dirac spinor (Eq. 2.10)

$$\begin{aligned}\chi_N^\dagger(X_{1\beta\gamma\delta})\chi_N &= \boldsymbol{\chi}^\dagger \left(\Sigma_\beta\tau_\gamma\sigma_\delta\right) (\boldsymbol{\chi}^\dagger)^T + \text{h.c.},\\ \chi_N^\dagger(X_{2\beta\gamma\delta})\chi_N &= -i\left(\boldsymbol{\chi}^\dagger \left(\Sigma_\beta\tau_\gamma\sigma_\delta\right) (\boldsymbol{\chi}^\dagger)^T\right) + \text{h.c.},\end{aligned} \tag{2.28}$$

where the constraint in Eq. 2.23 now demands that

$$\left(\Sigma_\beta\tau_\gamma\sigma_\delta\right)^T = -\Sigma_\beta\tau_\gamma\sigma_\delta, \tag{2.29}$$

i.e., they are anti-symmetric. Eq. 2.28 for the masses has a simple interpretation. In terms of Dirac spinor $\boldsymbol{\chi}$, there are 36 independent bilinears of the form $\boldsymbol{\chi}^T \left(\Sigma_\beta\tau_\gamma\sigma_\delta\right) \boldsymbol{\chi}$, which, when expressed in terms of the Nambu spinors, give the real and imaginary parts of the superconducting amplitude resulting in 72 superconducting masses with pairing amplitudes

$$\Delta_{\beta\gamma\delta} = \langle \boldsymbol{\chi}^T \left(\Sigma_\beta\tau_\gamma\sigma_\delta\right) \boldsymbol{\chi}\rangle. \tag{2.30}$$

Thus, in analogy with graphene [38, 105], the 136 bilinears break up as Irreps of SU(8) as

$$1 \oplus 63 \oplus 36 \oplus 36^* \tag{2.31}$$

where the 1 and 63 are the normal orders corresponding to SU(8) singlet and adjoint multiplet, respectively, while the 36 and 36^* correspond to real and imaginary components of the superconducting orders. The global symmetry of the free Dirac theory

and the constraints on the mass matrix (Ref. 2.23) become manifest in the Majorana representation of the χ fermions, as shown in Appendix A.3, which has a manifest SO(16) symmetry. The 136 masses then are given by the SO(16) singlet and the 135-dimensional symmetric rank-2 tensors (see Appendix A.3) [105]. Therefore, the Majorana representation naturally unifies the normal and the superconducting masses.

2.4 Overview of results

The SU(8) DSM described by Eq. 2.6 (or Eq. 2.1) is obtained in indirect hopping model of $j = 3/2$ electrons on honeycomb lattice at $1/4$th filling due to the two valleys leading to the 16-component Dirac fermions, χ (Eq. 2.10), in local basis or equivalently four 4-component Dirac fermions, χ_g (Eq. A.2), in global basis, as shown in Fig. 2.1. To analyze all the phases – both normal and superconducting – on equal footing, it is useful to describe the theory in terms of the Majorana representation whence the free Dirac theory has a manifest SO(16) symmetry (Appendix A.3), such that there are 136 fermion bilinears corresponding to masses for the fermions. These correspond to one SO(16) singlet and 135 symmetric rank-2 tensors. Out of the 136 bilinears, 64 correspond to normal (non-superconducting) masses that correspond to 24 phases studied recently in Ref. [40]. These break various microscopic symmetries and correspond to different symmetry broken as well as SPT phases. While the remaining 72 bilinears, the topic of the present work, correspond to various superconducting phases proximate to the SU(8) DSM.

These 72 bilinears correspond to the real and imaginary components of 36 superconducting pairing amplitudes, which, under microscopic symmetries, divide up to give 12 distinct SCs comprising up of four singlets ($\mathcal{A}$), four doublets ($\mathcal{E}$), and eight triplets ($\mathcal{T}$), and cataloged in Tables 2.1, 2.2 and 2.3. The details of the symmetry transformations for the superconducting bilinears are given in Appendix A.4. The further subdivision of the different Irreps is given by

- 4-singlets : $\mathcal{A}_{1g}^{I}, \mathcal{A}_{1g}^{II}, \mathcal{A}_{1u}, \mathcal{A}_{2u}$
- 2-doublets : $(3)\mathcal{E}_u, \mathcal{E}_g$
- 6-triplets : $\mathcal{T}_{1g}^{I}, \mathcal{T}_{1g}^{II}, \mathcal{T}_{1g}^{III}, (2)\mathcal{T}_{1u}, \mathcal{T}_{2g}, (2)\mathcal{T}_{2u}$.

where, similar to Ref. [40], we use the subscripts $1(2)$ and $g(u)$ to denote even (odd) under π-rotation ($\mathbf{C_2}'$) and inversion, $\mathbf{I}$, respectively (see Fig. 2.2). Note that the number within $()$ indicates the multiplicity of the Irreps. Particularly for doublet and triplet SCs, some of the Irreps with higher multiplicities (namely, $\mathcal{E}_u$, $\mathcal{T}_{1u}$ and $\mathcal{T}_{2u}$) do not give

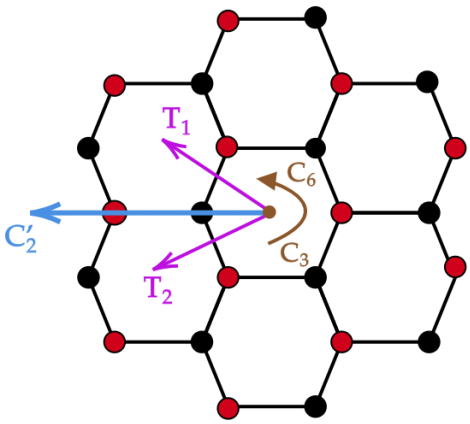

Figure 2.2: Lattice transformation: Here, the honeycomb lattice lies in a plane perpendicular to [111] planes in Cartesian coordinates (also discussed in Ref. [40, 106]). Transformation $\mathbf{C_2'}$ is the rotation by π amount about the axis shown in cyan. $\mathbf{T_1}, \mathbf{T_2}$ are translations by honeycomb lattice vectors. $\mathbf{C_6}(\mathbf{C_3})$ corresponds to rotation by $2\pi/6(2\pi/3)$ about the center of Honeycomb. $\sigma_\mathbf{h}$ is the reflection about the Honeycomb plane so that the combined transformation $\mathbf{S_6} = \mathbf{C_6}\sigma_\mathbf{h}$ is the symmetry of the lattice.

rise to distinct SCs. Out of the 12 different SCs listed above, 7(denoted in black colour) are gapped and 5 (in red) are gapless (nodal). Further, while the singlets are generically time-reversal (TR) invariant, the doublets and the triplets generically break it spontaneously. The above list of SCs realized in the $j = 3/2$ system, as described below, is much richer than their $j = 1/2$ counterparts – briefly summarized in Appendix A.8. Indeed, the $j = 1/2$ system realizes only five superconducting phases that have analogues in the $j = 3/2$ system.

The real and imaginary components of the $j = 3/2$ superconducting bilinears have a generic form

$$\langle \chi^\dagger (\Sigma_\beta \tau_\gamma \sigma_\delta)(\chi^\dagger)^T \rangle + \text{h.c.}, \; -i\langle \chi^\dagger (\Sigma_\beta \tau_\gamma \sigma_\delta)(\chi^\dagger)^T \rangle + \text{h.c.} \tag{2.32}$$

(as discussed in Eq. 2.28) where Σ_β are 4×4 matrices that act in the SU(4) flavour space and are of the same form as the matrices discussed in appendix C of [40], while, as mentioned before, τ_γ and σ_δ are Pauli matrices that act in the Dirac valley and band spaces, respectively.

Out of the four singlet SCs listed in Table 2.1, two belong to $\mathcal{A}_{1g}$, and the other two respectively to $\mathcal{A}_{1u}$ and $\mathcal{A}_{2u}$, comprising four different SCs. Notably, the first two even-parity pairings lead to distinct gapped SCs, even though they correspond to the same Irrep, $\mathcal{A}_{1g}$, and both are $j = 3/2$ singlets. They respectively correspond to on-site s-wave and next nearest neighbour (NNN) s-wave SCs, with the former being unitary and the latter being a rather rare example of a non-unitary singlet SC with a double

Irrep	Microscopic Symmetries Broken	$\Delta \cdot \Delta^\dagger$	Brief Description
$\mathcal{A}_{1g}^{I}$	None	U	Gapped. $j = 3/2$ singlet. On-site s-wave pairing. Possible inversion-odd Leggett mode. (Sec. 4.1.1)
$\mathcal{A}_{1g}^{II}$	None	N.U.	Double gap. $j = 3/2$ singlet. Extended s-wave (NNN pairing). (Sec. 4.1.1)
$\mathcal{A}_{1u}$	None	N.U.	Both gapped and gapless (nodal) branches of excitations with nodes at Γ-point protected by SO(4) symmetry. NNN pairing. Cooper pair wave function symmetric (anti-symmetric) in space (spin). (Sec. 4.1.2)
$\mathcal{A}_{2u}$	None	N.U.	Similar to $\mathcal{A}_{1u}$ but distinct irrep. (Sec. 4.1.2)

Table 2.1: Summary of the singlet SCs discussed in Sec. 4.1. NNN refers to next nearest neighbor. $g(u)$ denotes the Irrep is even (odd) under parity. U (N.U.) stands for unitary (non-unitary) pairing.

gap excitation spectrum (Fig. 4.1). The distinction arises due to the SU(4) flavour space structure. Interestingly, the unitary $\mathcal{A}_{1g}$ SC can be viewed as coexisting two s-wave condensates– one made up of pairing between $J_z = \pm 3/2$ orbitals and the other the same between the $J_z = \pm 1/2$ orbitals (Eq. 4.7) with a relative (inversion) symmetry enforced π-phase difference between the two condensates. This leads to a possibility of a gapped Leggett mode [104] that is odd under inversion. The two odd parity SCs, on the other hand, are both non-unitary with the smaller of the two gaps being zero, leading to nodal Bogoliubov excitations (Fig. 4.3) that are protected by an SO(4) subgroup. The mean field lattice Hamiltonians for the unitary (non-unitary) SCs have on-site (next nearest neighbour) pairings. Finally, even though none of the singlets break any microscopic symmetries, a linear superposition of any two of them generically breaks one or more symmetries. There are four doublets corresponding to two distinct non-unitary SCs summarized in Table 2.2– all with spin anti-symmetric pairing. The three odd parity doublet SCs (denoted as $\mathcal{E}_u^I, \mathcal{E}_u^{II}$ and $\mathcal{E}_u^{III}$ in Table 2.2) obtained from a combination of $J_T = 2$ ($m_T = 0, \pm 2$) angular momentum states, are adiabatically connected without breaking any microscopic symmetries (appendix A.6). Together, they give rise to a single non-unitary SC with two pairing gaps. On the TRI sub-manifold, the two gaps may coincide for some combination of pairings. At other combinations of pairing, generally breaking TR, the lower of the two gaps may vanish at isolated points on the order-parameter manifold giving rise to nodal SCs (Eq. 4.37) making

Irrep	Microscopic Symmetries Broken	Brief Description
$\mathcal{E}_u^I$, $\mathcal{E}_u^{II}$, and $\mathcal{E}_u^{III}$	$(\mathbf{C_2'}, \mathbf{C_3}, \mathbf{S_6}, \sigma_\mathbf{d})$	Staggered on-site pairing (Fig. 4.5) for $\mathcal{E}_u^I$ and NNN pairing for $\mathcal{E}_u^{II}$ and $\mathcal{E}_u^{III}$. Double gap. $\mathcal{E}_u^I$ reduces to a single gap in the TRI sub-manifold. For all doublets on isolated points in the TRB manifold, the lower of the two gaps becomes zero (Eq. 4.37), giving rise to a nodal SC. Order parameter manifold is $(S^1 \times S^2)/Z_2$, which reduces to $(S^1 \times S^1)/Z_2$ in the TRI sub-manifold. (Sec. 4.2.1)
$\mathcal{E}_g$	$(\mathbf{C_2'}, \mathbf{C_3}, \mathbf{S_6}, \sigma_\mathbf{d})$	Anisotropic NNN pairing (Fig. 4.7). Three gapped branches and one gapless branch of excitation, each 4-fold degenerate (Fig. 4.6(a)). The nodes are at the Γ-point and their degeneracy changes (Fig. 4.6(b)). (Sec. 4.2.2)

Table 2.2: Summary of the doublet SCs discussed in Sec. 4.2. TRI (TRB) stands for TR invariance (TR breaking). Note that doublets are generically non-unitary and break TR.

them rather unconventional where the direction of the superconducting order parameter can be changed in the order parameter manifold to obtain a gapped or a nodal SC. The truly gapless (nodal) SC is obtained from the pairing of the ($J_T = 0$) spin singlet; on the other hand, in the parity even $\mathcal{E}_g$ doublet, where the superconductivity originates from anisotropic NNN pairing as shown in Fig. 4.7. The excitation spectrum in this case (Fig. 4.6(a)) generically contains three four-fold degenerate gapped branches and one gapless nodal branch. The origin of the nodal branch can be traced to the Dirac node at the center of the BZ in the global basis (Appendix A.5) that is protected by a SO(4) subgroup. The order parameters for all the doublets generically span a $(S^1 \times S^2)/Z_2$ manifold, which reduces to $(S^1 \times S^1)/Z_2$ within the TRI sub-manifold. Lattice symmetries do allow (see for example Eqs. 4.39 and 4.40) energetic distinction between the TRB and TRI sub-manifolds leading to the possibility of obtaining unconventional vortices in the TRI manifold since $\pi_1\left(\frac{S^1 \times S^1}{Z_2}\right) = Z \times Z$ [17, 107, 108]. Finally, there are eight triplets giving rise to six distinct SCs summarized in Table 2.3. These SCs generically correspond to finite momentum pairing and hence break translation symmetry in addition to other point group symmetries, as well as TR. Hence, they generically correspond to pair-density-wave (PDW) SCs [56, 109, 110] with the order-

Irrep	Microscopic Symmetries Broken	Brief Description
$\mathcal{T}^{I}_{1g}$	$(\mathbf{T_1}, \mathbf{T_2}, \mathbf{C'_2}, \mathbf{C_3}, \mathbf{S_6}, \sigma_\mathbf{d})$	Two gaps which become equal in the TRI sub-manifold. On sections of TR breaking sub-manifold, the smallest gap goes to zero, leading to a nodal SC. Onsite finite momentum pairing with *stripy* pattern (Fig. 5.1). (Sec. 5.1.1).
$\mathcal{T}^{II}_{1g}$	$(\mathbf{T_1}, \mathbf{T_2}, \mathbf{C'_2}, \mathbf{C_3}, \mathbf{S_6}, \sigma_\mathbf{d})$	Very similar to the triplet above, but arises from flavour symmetric pairing and is a distinct SC. The *stripy* pairing is NNN (Fig. 5.2). (Sec. 5.1.1).
$\mathcal{T}^{III}_{1g}$	$(\mathbf{T_1}, \mathbf{T_2}, \mathbf{C'_2}, \mathbf{C_3}, \mathbf{S_6}, \sigma_\mathbf{d})$	Nodal SC with NNN finite momentum pairing (Fig. 5.5(b)). Dirac nodes at the Γ-point. Node degeneracy changes with the direction of the order parameter (Fig. 5.4). (Sec. 5.1.1).
$\mathcal{T}_{2g}$	$(\mathbf{T_1}, \mathbf{T_2}, \mathbf{C'_2}, \mathbf{C_3}, \mathbf{S_6}, \sigma_\mathbf{d})$	Multiply gapped (Fig. 5.6) with gapless nodes at M-points (Eq. 5.18), leading to a PDW SC obtained from NNN pairing (Fig. 5.7). (Sec. 5.1.2).
$\mathcal{T}^{I}_{2u}$ and $\mathcal{T}^{II}_{2u}$	$(\mathbf{T_1}, \mathbf{T_2}, \mathbf{C'_2}, \mathbf{C_3}, \mathbf{S_6}, \sigma_\mathbf{d})$	Multiple gaps, with the lowest gap reduced to zero on a sub-manifold of the order parameter space, giving rise to a nodal SC. Zero modes correspond to linear combinations of Dirac modes at different valleys. NNN finite momentum pairing (Fig. 5.10). (Sec. 5.1.3).The two triplets can be adiabatically connected without breaking further microscopic symmetries, so they are not distinct SCs.
$\mathcal{T}^{I}_{1u}$ and $\mathcal{T}^{II}_{1u}$	$(\mathbf{T_1}, \mathbf{T_2}, \mathbf{C'_2}, \mathbf{C_3}, \mathbf{S_6}, \sigma_\mathbf{d})$	Spectrum is similar to $\mathcal{T}^{I}_{2u}$ and $\mathcal{T}^{II}_{2u}$ triplet discussed above; two triplets represent the same SC. NNN finite momentum pairing (Fig. 5.10). (Sec. 5.1.4).

Table 2.3: Summary of the triplet SCs. Like the doublets, all the triplet SCs are generically non-unitary and break TR. Generically, the triplets have finite momentum pairing resulting in breaking of translation symmetries in the resultant pair density wave (PDW) SCs.

parameter manifold being $(S^1 \times CP^2)/Z_2$ [111,112] which reduces to $(S^1 \times S^2)/Z_2$ in the TR invariant sub-space. The associated Cooper-pair wave functions are formed by a mixture of $J_T = 1, 2$, and 3 sectors that are intricately interlocked with the real space directions. Although the three $\mathcal{T}_{1g}$ triplets (denoted by $\mathcal{T}_{1g}^{I}, \mathcal{T}_{1g}^{II}$ and $\mathcal{T}_{1g}^{III}$ in Table 2.3) belong to the same Irrep, they have somewhat different properties. Further, the TR invariant sub-manifolds of these three SCs cannot be adiabatically connected without breaking further lattice symmetries and/or TR. Finally, while the two of them are gapped, the third one is a nodal SC. Among the other three, the $\mathcal{T}_{2g}$ triplet is a nodal SC, while the other two ($\mathcal{T}_{1u}$ and $\mathcal{T}_{2u}$) are generically gapped, except at sub-parts of the order-parameter manifold when the smallest of the multiple gaps closes.

Chapter 3

Implementation of microscopic symmetries and classification of superconducting pairing

In this chapter, we will examine the classification of the 72 superconducting masses. We begin with a discussion of the microscopic symmetries. Then, we classify the masses under the action of the $U(4)$ symmetry in the flavor sector, and conclude the chapter with a discussion on the transformation properties of bilinears under microscopic symmetry.

3.1 Microscopic Symmetries

To classify the different SCs, it is useful to understand the transformations of the superconducting bilinears (Eq. 2.30) under the microscopic symmetries– lattice transformations and TR. This, of course, is related to the symmetry transformation of the Dirac fermions [40]. Due to the underlying SOC, the microscopic transformation leads to mixing of the SU(4) flavours. Here we summarize these transformations for completeness and refer the reader to Ref. [40] for further details.

The symmetry group of lattice transformations, $\mathbb{S}$, is generated by

$$\{\mathbf{T_1}, \mathbf{T_2}, \mathbf{C_3}, \mathbf{C_6}\sigma_\mathbf{h}, \mathbf{C_2'}, \sigma_\mathbf{d}, \mathbf{I}\}$$

where $\{\mathbf{T_1}, \mathbf{T_2}\}$ correspond to the lattice translations of honeycomb lattice, $\{\mathbf{C_2'}, \mathbf{C_3}, \mathbf{C_6}\}$ are two, three and six-fold lattice rotations and $\{\sigma_\mathbf{h}, \sigma_\mathbf{d}, \mathbf{I}\}$ are reflections and inversions as explained in Ref. [40] (also shown in fig. 2.2). Under the action of $\mathbb{S}$, the Dirac

spinors transform as

$$\chi(\mathbf{x}) \xrightarrow{\mathbb{S}} \Omega_{\mathbb{S}}\, \chi(\mathbb{S}^{-1}\mathbf{x}), \tag{3.1}$$

where $\Omega_{\mathbb{S}}$ is a 16×16 dimensional matrix representation of $\mathbb{S}$ whose explicit forms are given in Ref. [40]. This, for Nambu spinors, $\chi_N(\mathbf{x})$, leads to

$$\begin{aligned}\chi_N(\mathbf{x}) &\xrightarrow{\mathbb{S}} \left[\, \Omega_{\mathbb{S}}\, \chi(\mathbb{S}^{-1}\mathbf{x}),\ \left(\chi^\dagger(\mathbb{S}^{-1}\mathbf{x})\, \Omega_{\mathbb{S}}^\dagger\right)^T \,\right]^T \\ &= \frac{1}{2}\Big[\mu_0 \otimes (\Omega_{\mathbb{S}} + \Omega_{\mathbb{S}}^*) + \mu_3 \otimes (\Omega_{\mathbb{S}} - \Omega_{\mathbb{S}}^*)\Big]\chi_N(\mathbb{S}^{-1}\mathbf{x}).\end{aligned} \tag{3.2}$$

In addition, under the microscopic TR symmetry, the Dirac fermions transform such that $\mathrm{TR}^2 = -1$ with the detailed form of the transformation matrix also given in Ref. [40]. Finally, the microscopic charge conservation is described by Eq. 2.2.

3.2 Classification of Superconducting masses

Given the microscopic symmetries, we now turn to the classification of the superconducting masses. The resultant structure of the mass matrix is obtained by setting the normal masses to zero, whence Eq. 2.22 reduces to

$$\begin{aligned}M^{Sc} &= \begin{bmatrix} 0_{16\times16} & \Delta_{\beta\gamma\delta}(\Sigma_\beta\tau_\gamma\sigma_\delta) \\ \Delta^*_{\beta\gamma\delta}(\Sigma_\beta\tau_\gamma\sigma_\delta) & 0_{16\times16}\end{bmatrix} \\ &= \sum_{i=1}^{d} \begin{bmatrix} 0_{16\times16} & \Delta_i\tilde{\mathrm{M}}_i \\ \Delta_i^*\tilde{\mathrm{M}}_i & 0_{16\times16}\end{bmatrix},\end{aligned} \tag{3.3}$$

where $0_{16\times16}$ is the 16×16 zero matrix. The second expression concretely applies for an irreducible representation (Irrep) of dimension d, with pairing amplitude $\mathbf{\Delta} = (\Delta_1, \Delta_2, \cdots, \Delta_d)$, with Δ_i being complex numbers and $\tilde{M}_i$ denoting corresponding matrices which are given by particular combination of $\Sigma_\beta\tau_\gamma\sigma_\delta$ specific for the Irrep. For our case, $d \in \{1, 2, 3\}$, which corresponds to singlet, doublet and triplet representations, respectively.

At the outset, we would like to point out the broad classification of such masses under the microscopic TR symmetry. Under TR,

$$\tilde{M}_i \to \pm\tilde{M}_i \quad \forall\, i. \tag{3.4}$$

Now we can define

$$\mathrm{T}_i^+ = (\mu_1 + i\mu_2) \otimes \tilde{\mathrm{M}}_i \text{ and } \mathrm{T}_i^- = (\mu_1 - i\mu_2) \otimes \tilde{\mathrm{M}}_i \tag{3.5}$$

such that,

$$M^{Sc} = \sum_{i=1}^{d} (\Delta_i \mathrm{T}_i^+ + \Delta_i^* \mathrm{T}_i^-) = \sum_{i=1}^{d} |\Delta_i| (\mathrm{e}^{i\tilde{\delta}_i} \mathrm{T}_i^+ + \mathrm{e}^{-i\tilde{\delta}_i} \mathrm{T}_i^-). \tag{3.6}$$

Under charge U(1) (Eq. 2.2),

$$\chi_i \to \mathrm{e}^{i\theta} \chi_i,\ \mathrm{T}_i^+ \to \mathrm{e}^{-i2\theta} \mathrm{T}_i^+,\ \mathrm{T}_i^- \to \mathrm{e}^{i2\theta} \mathrm{T}_i^-. \tag{3.7}$$

Thus, if all the phases $\tilde{\delta}_i$ (in Eq. 3.6) for all the components in a particular Irrep are the same, then a uniform U(1) rotation can get rid of it. This is always possible for singlets ($d = 1$), but is generically not possible for doublets and triplets ($d = 2, 3$). Hence, while the former are TR symmetric, the latter generically break it. However, a linear combination of different singlets can break TR.

With this, we now turn to the complete classification of the SCs under the microscopic symmetries. To this end, we provide a two-step classification by first considering only the internal U(4) symmetry of the Dirac bilinears defined in Eq. 2.30 (the Nambu bilinears can be then obtained via Eq. 2.27) before taking on the full classification under the microscopic lattice symmetries.

3.2.1 Classification under U(4)

As mentioned before, the Hamiltonian in Eq. 2.1 has U(4) invariance, under which the Dirac bilinears in Eq. 2.30 that transform as

$$\chi^T \Sigma_\beta \tau_\gamma \sigma_\delta \chi \xrightarrow{U(4)} \chi^T \left(\Omega_U^{(f)}\right)^T \Sigma_\beta \Omega_U^{(f)} \otimes \tau_\gamma \sigma_\delta \chi. \tag{3.8}$$

Here, $\Omega_U^{(f)}$ is a 4×4 unitary matrix in flavour space as is evident from the superscript f. The Dirac bilinear in Eq. 3.8 transforms as a $4 \otimes 4$ representation of U(4) which is reduced to

$$4 \otimes 4 = 6 \oplus 10, \tag{3.9}$$

where 6 and 10 correspond to 6-dimensional anti-symmetric and 10-dimensional symmetric Irreps of U(4). The above U(4) transformations do not mix the two classes – the symmetric and anti-symmetric flavour matrices, Σ_β. Hence, we can classify the above

Irreps	Set of masses	Flavour Sector	Dimension
1	$\left(\mu_1\Sigma_i\tau_1\sigma_0\ ,\ \mu_2\Sigma^i\tau_1\sigma_0\right)$	$\Sigma_i \in \Sigma_{Asy}$	$(6,6)$
2	$\left(\mu_1\Sigma_i\tau_0\sigma_2\ ,\ \mu_2\Sigma^i\tau_0\sigma_2\right)$	$\Sigma_i \in \Sigma_{Sy}$	$(10,10)$
3	$\left(\mu_1\Sigma_i\tau_2\sigma_0\ ,\ \mu_2\Sigma^i\tau_2\sigma_0\right)$	$\Sigma_i \in \Sigma_{Sy}$	$(10,10)$
4	$\left(\mu_1\Sigma_i\tau_3\sigma_2,\ \mu_2\Sigma^i\tau_3\sigma_2\right)$	$\Sigma_i \in \Sigma_{Sy}$	$(10,10)$

Table 3.1: Classification under U(4) transformation

superconducting masses into two groups

$$\begin{aligned} \Sigma_\beta \in \Sigma_{Asy} \qquad & i.e.,\ \Sigma_\beta^T = -\Sigma_\beta, \\ \Sigma_\beta \in \Sigma_{sy} \qquad & i.e.,\ \Sigma_\beta^T = \Sigma_\beta. \end{aligned} \tag{3.10}$$

Eq. 2.29 now demands that the first class of flavour matrices in Eq. 3.10 can only occur in combination with $\tau_\gamma\sigma_\delta$ such that this combination of valley-band space matrices is symmetric (in addition to the constraints discussed above) and there is precisely one such combination, given by

$$\tau_1\sigma_0. \tag{3.11}$$

Similarly, for the second class of matrices in Eq. 3.10, $\tau_\gamma\sigma_\delta$ needs to be anti-symmetric, and there are three such combinations, given by

$$\tau_3\sigma_2,\ \tau_2\sigma_0,\ i\tau_0\sigma_2. \tag{3.12}$$

These are summarized in Table 3.2. Putting this back in the general form of the masses for the Nambu spinor consistent with Eq. 2.23, the 72 superconducting bilinears (Eq. 2.27) can then be classified into four groups as shown in Table 3.1.

3.2.2 Classification under lattice symmetries

The lattice symmetries, however, mix the flavour and the chiral spaces due to the SOC as realized in Ref. [40], such that the structure of the Irreps and hence the resultant symmetry breaking becomes more involved. In particular, under lattice symmetry $\mathbb{S}$, the Dirac bilinears transform as

$$\chi^T\,\Sigma_\beta\tau_\gamma\sigma_\delta\,\chi \quad \xrightarrow{\mathbb{S}} \chi^T\left[\left(\Omega_{\mathbb{S}}^{(f)}\right)^T\Sigma_\beta\Omega_{\mathbb{S}}^{(f)}\right]\otimes\left[\left(\Omega_{\mathbb{S}}^{(c)}\right)^T\tau_\gamma\sigma_\delta\Omega_{\mathbb{S}}^{(c)}\right]\chi, \tag{3.13}$$

Valley-Subband Sector	Irrep	Transposition
$\{\tau_1\sigma_0\}$	$\mathcal{A}_{1g}$	Symmetric
$\{\tau_3\sigma_2,\ \tau_2\sigma_0,\ i\,\tau_0\sigma_2\}$	$\mathcal{T}_{2g}$	Anti-symmetric

Table 3.2: Decomposition of chiral (valley and sub-band) sector under lattice symmetries.

where the superscripts f and c represent respectively the flavour and the valley-subband (chiral) spaces on which $\Omega_{\mathbb{S}}^{(f)}$ and $\Omega_{\mathbb{S}}^{(c)}$ act such that the transformation of the Dirac spinor under symmetry $\mathbb{S}$ is given by

$$\chi \to \Omega_{\mathbb{S}}^{(f)} \otimes \Omega_{\mathbb{S}}^{(c)}\, \chi. \tag{3.14}$$

This tensor product structure of the transformation matrices arises naturally from working in the local basis and is explicitly demonstrated in Ref. [40].

The four matrices (Eqs. 3.11 and 3.12) in the valley-band space break up into $1 \oplus 3$, as discussed above, to give

$$4 = \mathcal{A}_{1g} \oplus \mathcal{T}_{2g}. \tag{3.15}$$

Here, we use the same notation for the Irreps as introduced in Ref. [40] and summarized in Appendix A.4. The singlet is the symmetric matrix, and the triplet is composed of three anti-symmetric matrices and is summarized in Table 3.2 for easy reference.

For the 16 flavour matrices (Eq. 3.9), the six antisymmetric ones (Eq. 3.10), under lattice symmetries, break up into $1 \oplus 2 \oplus 3$ with

$$6 = \mathcal{A}_{1g} \oplus \mathcal{E}_u \oplus \mathcal{T}_{1g}, \tag{3.16}$$

as summarized in the first three rows of Table 3.3, while the 10 symmetric ones (Eq. 3.10) break up as $1 \oplus 3 \oplus 3 \oplus 3$, *i.e.*,

$$10 = \mathcal{A}_{2g} \oplus \mathcal{T}_{2g} \oplus \mathcal{T}_{1u} \oplus \mathcal{T}_{2u} \tag{3.17}$$

as denoted by the lower four rows of Table 3.3.

The full classification of the 36 superconducting bilinears for the Dirac fermions, $\chi^T \Sigma_\beta \tau_\gamma \sigma_\delta \chi$, can now be obtained by combining the representations of the flavour and the chiral sectors, similar to Ref. [40], but noting, as above, that only combinations of symmetric (anti-symmetric) flavour matrices are allowed with anti-symmetric (symmetric) chiral matrices.

Flavour Sector	Irrep	Transpose
$\{\Sigma_{13}\}$	$\mathcal{A}_{1g}$	AntiSym
$\{\Sigma_{24}, \Sigma_{25}\}$	$\mathcal{E}_u$	AntiSym
$\{\Sigma_1, \Sigma_3, i\,\Sigma_{45}\}$	$\mathcal{T}_{1g}$	AntiSym
$\{\Sigma_2\}$	$\mathcal{A}_{2g}$	Sym
$\{\Sigma_{32}, i\,\Sigma_0, \Sigma_{12}\}$	$\mathcal{T}_{2g}$	Sym
$\{\Sigma_{15},\ i(\frac{\sqrt{3}}{2}\Sigma_5 - \frac{1}{2}\Sigma_4),\ \frac{\sqrt{3}}{2}\Sigma_{34} - \frac{1}{2}\Sigma_{35}\}$	$\mathcal{T}_{1u}$	Sym
$\{\Sigma_{14},\ i(\frac{\sqrt{3}}{2}\Sigma_4 + \frac{1}{2}\Sigma_5),\ -\frac{\sqrt{3}}{2}\Sigma_{35} - \frac{1}{2}\Sigma_{34}\}$	$\mathcal{T}_{2u}$	Sym

Table 3.3: Decomposition of flavour space matrices under lattice symmetries. Anti-Sym(Sym) specifies if matrix is anti-symmetric(symmetric) under transposition (see Eq. 3.10 and Table 3.1).

Flavour anti-symmetric masses : There are six anti-symmetric Σ_β matrices (Table 3.3 and Eq. 3.16) which can only combine with the symmetric singlet of the chiral space to give

$$\mathcal{A}_{1g} \otimes \mathcal{A}_{1g} = \mathcal{A}_{1g}, \tag{3.18}$$
$$\mathcal{E}_u \otimes \mathcal{A}_{1g} = \mathcal{E}_u, \tag{3.19}$$
$$\mathcal{T}_{1g} \otimes \mathcal{A}_{1g} = \mathcal{T}_{1g}. \tag{3.20}$$

Flavour symmetric masses : Similarly, the 10 flavour symmetric matrices can only combine with the anti-symmetric chiral triplet to give a total of 30 flavour symmetric direct product matrices that are divided into three singlets, three doublets, and seven triplets, as shown below

$$\mathcal{A}_{2g} \otimes \mathcal{T}_{2g} = \mathcal{T}_{1g}, \tag{3.21}$$
$$\mathcal{T}_{2g} \otimes \mathcal{T}_{2g} = \mathcal{T}_{1g} \oplus \mathcal{T}_{2g} \oplus \mathcal{E}_g \oplus \mathcal{A}_{1g}, \tag{3.22}$$
$$\mathcal{T}_{1u} \otimes \mathcal{T}_{2g} = \mathcal{T}_{1u} \oplus \mathcal{T}_{2u} \oplus \mathcal{E}_u \oplus \mathcal{A}_{2u}, \tag{3.23}$$
$$\mathcal{T}_{2u} \otimes \mathcal{T}_{2g} = \mathcal{T}_{1u} \oplus \mathcal{T}_{2u} \oplus \mathcal{E}_u \oplus \mathcal{A}_{1u}. \tag{3.24}$$

Finally, turning to the Nambu bilinears (Eq. 2.27), it is clear that we have 72 superconducting masses that are formed out of the real and imaginary components of the above 36 bilinears as denoted in the Table. 3.1. This leads to the classification of the superconducting masses under microscopic symmetries and leads to

- 4-singlets : $(2)\mathcal{A}_{1g}, \mathcal{A}_{1u}, \mathcal{A}_{2u}$
- 4-doublets : $(3)\mathcal{E}_u, \mathcal{E}_g$
- 8-triplets : $(3)\mathcal{T}_{1g}, (2)\mathcal{T}_{1u}, \mathcal{T}_{2g}, (2)\mathcal{T}_{2u}$.

each of which can be TR even or odd, corresponding to the real and imaginary components of the pairing amplitude.

As remarked above, the two components of the singlet pairing can be combined along with charge $U(1)$ to give rise to four distinct TR even SCs. Further, while the $\mathcal{A}_{1u}$ and the $\mathcal{A}_{2u}$ singlets go to their negative under some point group transformation, this can be rectified via the U(1) phase and hence they do not break any microscopic symmetries. However, a linear combination of two singlets may break lattice and/or TR symmetries. The doublets and the triplets, on the other hand, generically break TR symmetry. While there are 12 of them, we find that some of the doublets and triplets can be adiabatically deformed into each other without breaking any further symmetries, thus leading to only 8 distinct SCs, as we shall discuss below. The above superconducting masses give rise to both gapped and gapless SCs, which we now discuss in detail. To this end, we divide the discussion into the singlet, doublet and triplet Irreps in the next two chapters.

It is useful to note the classification of SCs for a two-orbital per site, *i.e.*, an effective $j = 1/2$ system, instead of four (Eq. 2.4), on the honeycomb lattice with π-flux at $1/4$th filling. The resultant low-energy theory corresponds to a different representation of the microscopic symmetries, now acting on the $j = 1/2$ electrons. This is discussed in Appendix A.8 and leads to *five* SCs – two singlets, one doublet and two triplets. As is evident from the discussion presented in the section, the $j = 3/2$ system discussed in the main text realizes a myriad of new phases that are not realized by the $j = 1/2$ system.

Chapter 4

Singlet and Doublet Superconductors

After understanding the classification of superconducting phases, we now discuss each of these phases in detail. In this chapter, we first focus on the four singlet superconductors, followed by a discussion of the two doublet superconductors.

4.1 Singlet superconductors

As discussed below Eq. 3.3, for singlets we can always perform a U(1) transformation on the masses to make them TR symmetric, resulting in 4 different TR symmetric singlet SCs– two $\mathcal{A}_{1g}$, and one each of $\mathcal{A}_{1u}$ and $\mathcal{A}_{2u}$.

4.1.1 The two gapped $\mathcal{A}_{1g}$ singlets

The two $\mathcal{A}_{1g}$ singlets (we denote them as $\mathcal{A}_{1g}^{I}$ and $\mathcal{A}_{1g}^{II}$) arise respectively from Eqs. 3.18 and 3.22. These two singlets correspond to two different superconducting phases as they cannot be deformed into each other without closing the spectral gap for the Bogoliubov quasi-particles (see below) or breaking further symmetries.

The low-energy Hamiltonian in the presence of the two $\mathcal{A}_{1g}^{x}$ (x= I or II) masses is given by Eq. 2.21, with the form of the mass matrix given by Eq. 3.3 with $d = 1$. The $\mathcal{A}_{1g}^{I}$ singlet is particularly simple and arises from the direct product of the singlets in flavour and valley-subband sectors (see Eq. 3.18) such that

$$\text{Singlet} - \text{I} \; : \; \begin{array}{l} m^{\mathcal{A}_{1g}^{I}} = \Sigma_{13}\tau_1\sigma_0, \\ \Delta^{\mathcal{A}_{1g}^{I}} = \langle \chi^T m^{\mathcal{A}_{1g}^{I}} \chi \rangle. \end{array} \tag{4.1}$$

The $\mathcal{A}_{1g}^{II}$ singlet, on the other hand, arises from the direct product of triplets in the

flavour and valley-subband sectors as mentioned in Eq. 3.22 and this results in

$$\begin{aligned} & m^{\mathcal{A}_{1g}^{II}} = \frac{(\Sigma_0\tau_0\sigma_2+\Sigma_{12}\tau_3\sigma_2-\Sigma_{23}\tau_2\sigma_0)}{\sqrt{3}} \\ \text{Singlet}-\text{II} \ : & \\ & \Delta^{\mathcal{A}_{1g}^{II}} = \langle \chi^T \, m^{\mathcal{A}_{1g}^{II}} \chi \rangle \end{aligned} \tag{4.2}$$

Note that while both the masses are $\mathcal{A}_{1g}$ singlets, they are composed of different combinations of the flavour and chiral sectors, which lead to different consequences, with the first being unitary, while the second one a rather rare example of a non-unitary singlet SC, *i.e.*,

$$\left[\Delta^{\mathcal{A}_{1g}^{I}} m^{\mathcal{A}_{1g}^{I}}\right] \cdot \left[\Delta^{\mathcal{A}_{1g}^{I}} m^{\mathcal{A}_{1g}^{I}}\right]^\dagger = |\Delta^{\mathcal{A}_{1g}^{I}}|^2 \Sigma_0\tau_0\sigma_0, \tag{4.3}$$

and

$$\left[\Delta^{\mathcal{A}_{1g}^{II}} m^{\mathcal{A}_{1g}^{II}}\right] \cdot \left[\Delta^{\mathcal{A}_{1g}^{II}} m^{\mathcal{A}_{1g}^{II}}\right]^\dagger = |\Delta^{\mathcal{A}_{1g}^{II}}|^2 \left[\Sigma_0\zeta_0 + \frac{2}{3}(\Sigma_{12}\zeta_1 + \Sigma_{13}\zeta_2 - \Sigma_{23}\zeta_3)\right], \tag{4.4}$$

where $\zeta_0 = \tau_0\sigma_0$ and $\zeta_i (i = 1, 2, 3)$ are given in Eq. 2.11.

$\mathcal{A}_{1g}^{I}$ Singlet

Diagonalizing the mean field Hamiltonian (Eq. 2.21) for singlet-I (Eq. 4.1) provides two bands with gapped dispersion for the Bogoliubov quasi-particles of the form

$$E^{\pm}(q_x, q_y, \Delta^{\mathcal{A}_{1g}^{I}}) = \pm\sqrt{q_x^2 + q_y^2 + |\Delta^{\mathcal{A}_{1g}^{I}}|^2}, \tag{4.5}$$

where, as usual, $2|\Delta^{\mathcal{A}_{1g}^{I}}|$ is the gap in the spectrum. Each band is 16-fold degenerate. This single gap is a direct outcome of the unitary pairing (Eq. 4.3). Indeed, the SO(16) symmetry group (Eq. A.28) is broken down to SO(8) $\otimes$ SO(8) by the unitary pairing. The resultant SC vortex is featureless and is characterised by the usual homotopy classification $\pi_1(S^1) = Z$.

The above form of the pairing can be traced back to the lattice BCS Hamiltonian (in the global basis) of the form

$$H_{\mathcal{A}_I}^{global} = H + \sum_{\mathbf{r}} \left(\Delta_{lat}^{\mathcal{A}_{1g}^{I}}\right)^* \Psi^T(\mathbf{r}) \, \Sigma_{13} \, \Psi(\mathbf{r}) + \text{h.c.} \tag{4.6}$$

where H is given by Eq. 2.3 and $\Psi(\mathbf{r})$ corresponds to the $j = 3/2$ orbitals. Note that

the pairing is on-site, *i.e.*,

$$\left(\Delta_{lat}^{\mathcal{A}_{1g}^{I}}\right)^{*} = \langle \Psi^{\dagger}(\mathbf{r})\Sigma_{13}(\Psi^{\dagger}(\mathbf{r}))^{T}\rangle, \tag{4.7}$$

similar to the s-wave pairing. In particular, given the explicit form of

$$\Sigma_{13} = -\frac{7}{3}\left(J_y - \frac{4}{7}J_y^3\right) = \begin{pmatrix} 0 & -i & 0 & 0 \\ i & 0 & 0 & 0 \\ 0 & 0 & 0 & i \\ 0 & 0 & -i & 0 \end{pmatrix}, \tag{4.8}$$

it is clear that the form is reminiscent of a *spin singlet* type pairing within the $\pm 1/2$ and $\pm 3/2$ orbitals, respectively, with a relative π-phase. Indeed, the relative π-phase can be understood as a pairing in the spin-$3/2$ SU(2)-singlet sector. Note that in the local basis (Eq. 2.5), all the pairings transform as $3/2 \otimes 3/2$ representation [93] of the SU(2) generated by (J_x, J_y, J_z) [40] that is a subgroup of the flavour SU(4). Under spin SU(2), the decomposition has the well-known form

$$\frac{3}{2} \otimes \frac{3}{2} = 0 \oplus 1 \oplus 2 \oplus 3. \tag{4.9}$$

Thus, the total spin angular momentum of the Cooper pair can be $J_T = 0, 1, 2, 3$, with the magnetic quantum number, $m_T = -J_T, \cdots, J_T$. The black (red) colour corresponds to symmetric (anti-symmetric) representations, such that only anti-symmetric (symmetric) representations are allowed by the Pauli exclusion principle when the real-space part of the wave function is symmetric (anti-symmetric) under spatial inversion.

For the above on-site pairing, the spin part of the Cooper-pair wave function is given by the SU(2) singlet anti-symmetric wave-function [93]

$$|J_T = 0, m_T = 0\rangle = \frac{1}{2}\left(|3/2, -3/2\rangle - |-3/2, 3/2\rangle\right) - \frac{1}{2}\left(|1/2, -1/2\rangle - |-1/2, 1/2\rangle\right) \tag{4.10}$$

while its on-site spatial part is symmetric. The SU(2) singlet then demands the relative π phase for the above on-site s-wave SC. The statement becomes manifest in the local basis, whence, on using Eq. 2.5, the hopping term becomes diagonal while the pairing term remains unchanged, such that in the local basis there is pairing between the flavours (1,2) and (3,4), respectively, with a relative π-phase between the two sets of pairing terms. Due to the inter-twinning of real and spin spaces, the change of the relative phase from π leads to the mixing of the above singlet with the onsite $\mathcal{E}_u$ dou-

blet (corresponding to a part of the antisymmetric representation 2 in Eq. 4.9) studied in Section 4.2.1 resulting in breaking of inversion symmetry. This relative π-phase is therefore a direct outcome of the symmetry implementation. One can therefore conceive of fluctuations in relative phase that would correspond to an inversion-odd Leggett mode [1] [104]. Symmetry analysis shows that the gap of this Leggett mode appears to be driven by a quartic coupling with the $\mathcal{E}_u$ pairing field, raising the possibility of an undamped Leggett mode investigated in superconducting Dirac materials [113]. Clearly, such a Leggett mode is absent in the $j = 1/2$ counterpart (Appendix A.8).

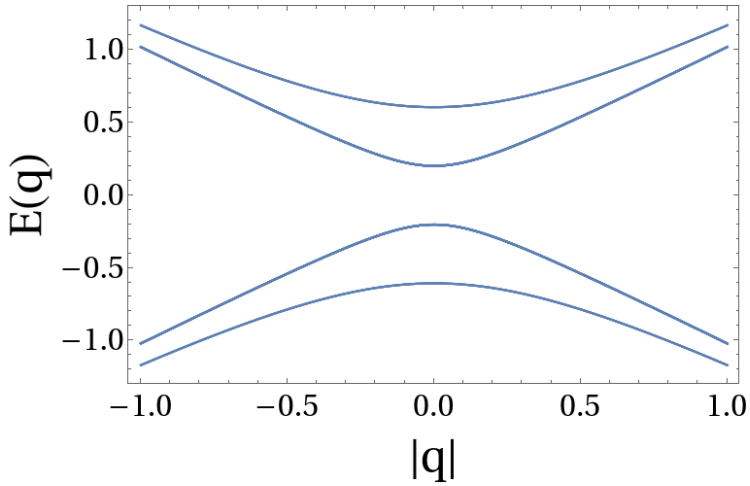

Figure 4.1: Spectrum for the non-unitary $\mathcal{A}_{1g}^{II}$ singlet (with $\Delta^{\mathcal{A}_{1g}^{II}} = 0.35$) around the Dirac points. Each of the uppermost and the lowermost bands is 4-fold degenerate, while each of the rest two is 12-fold degenerate. This degeneracy structure implies that the SO(16) symmetry of the free Hamiltonian breaks down into SO(2)⊗SO(2)⊗SO(6)⊗SO(6). Here, $|\mathbf{q}|$ is measured from the position of Dirac cones.

$\mathcal{A}_{1g}^{II}$ Singlet

The $\mathcal{A}_{1g}^{II}$ singlet originates from the direct product of $\mathcal{T}_{2g}$ lattice triplets in both the flavour and valley-subband sectors, as outlined in Eq. 3.22 and the corresponding pairing matrix is given in Eq. 4.2. Due to the non-unitary pairing (Eq. 4.4), the spectrum (Fig. 4.1) has a double gap structure, which can be checked by diagonalizing the mean-field Hamiltonian.

Similar to the first singlet discussed above, the low-energy Hamiltonian in the presence of this superconducting mass can be interpreted as the low-energy limit of a lat-

[1] The term "Leggett mode" refers to a collective excitation of a multicomponent superconducting order parameter, specifically an oscillation of the relative phase between different condensates (e.g., different bands, orbitals, or pairing channels).

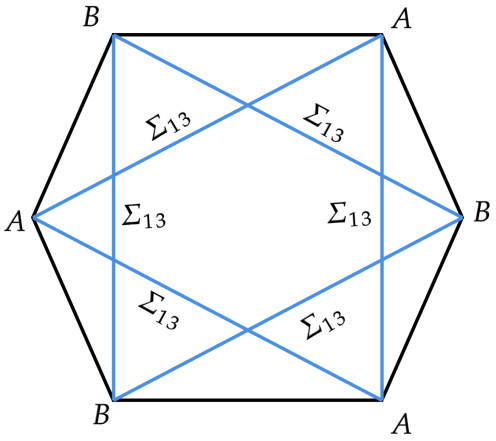

Figure 4.2: Schematic of the pairing in global basis for the $\mathcal{A}_{1g}^{II}$ singlet on the lattice (Eq. 4.2). The blue bonds represent SC pairing amplitudes on the NNN bonds with the pairing matrix being Σ_{13}.

tice BCS Hamiltonian (in the global basis) of the form

$$H_{\mathcal{A}_{II}}^{global} = H + \sum_{\langle\langle \mathbf{r}\mathbf{r}' \rangle\rangle} \left(\Delta_{lat}^{\mathcal{A}_{1g}^{II}}\right)^{*} \Psi^{T}(\mathbf{r})\, \Sigma_{13}\, \Psi(\mathbf{r}') + \text{h.c.} \tag{4.11}$$

where H is the free fermion Hamiltonian (Eq. 2.3) and the pairing matrix is given by Σ_{13}. However, unlike in the previous case (Eq. 4.11), the pairing is NNN, as pictorially shown in Fig. 4.2. Thus, while the spin part of the Cooper pair wave function is still given by Eq. 4.10, the spatial part is symmetric, with weights on the NNN sites, resulting in an extended s-wave SC.

Are the two $\mathcal{A}_{1g}$ superconductors distinct ?

Given that both the $\mathcal{A}_{1g}$ SCs discussed above belong to the same Irrep, it is useful to understand the sense in which they represent distinct SCs, if at all. Comparing the lattice Hamiltonians in Eqs. 4.6 and 4.11, it is clear that they respectively correspond to on-site $s-$wave and extended (NNN) s-wave SCs for the $j = 3/2$ electrons. However, while $\mathcal{A}_{1g}^{I}$ is unitary, $\mathcal{A}_{1g}^{II}$ is non-unitary as is evident from one and two gap spectra, respectively. This is because, in the global basis, the hopping Hamiltonian, H (Eq. 2.3), does not have the spin-rotation symmetry. Therefore, a simple one-parameter adiabatic interpolation between them fails and is interrupted by a gapless point, which is in accordance with the fact that there is an intermediate phase transition, since they break different flavour symmetries (Eq. 4.1 vs 4.2). Analyzing the pairing matrix in the local basis(Eq. 2.5) provides, $\mathcal{A}_{1g}^{I}$ singlet belongs to SU(2) singlet sector (0 in Eq.

4.9), while that of $\mathcal{A}_{1g}^{II}$ belongs to the symmetric representation of the SU(2) (1 and 3 Eq. 4.9). Based on this, we conclude that the two $\mathcal{A}_{1g}$ represent distinct SCs.

4.1.2 The Gapless Singlets : $\mathcal{A}_{1u}$ and $\mathcal{A}_{2u}$

The $\mathcal{A}_{2u}$ and the $\mathcal{A}_{1u}$ singlets arise from the decomposition in Eq. 3.23 and 3.24, respectively, and represent two distinct gapless SCs. Indeed, unlike the $\mathcal{A}_{1g}$s, both the $\mathcal{A}_{1u}$ and the $\mathcal{A}_{2u}$ exhibit gapless Bogoliubov spectrum (see Fig 4.3). For both the singlets, the SO(16) symmetry of the free Hamiltonian is broken down to SO(4)⊗SO(6)⊗SO(6). In the following, we first discuss the low-energy Hamiltonian along with a lattice realization for these masses and then provide an understanding of these gapless modes by analyzing these masses in the global basis. The low-energy Hamiltonian in the pres-

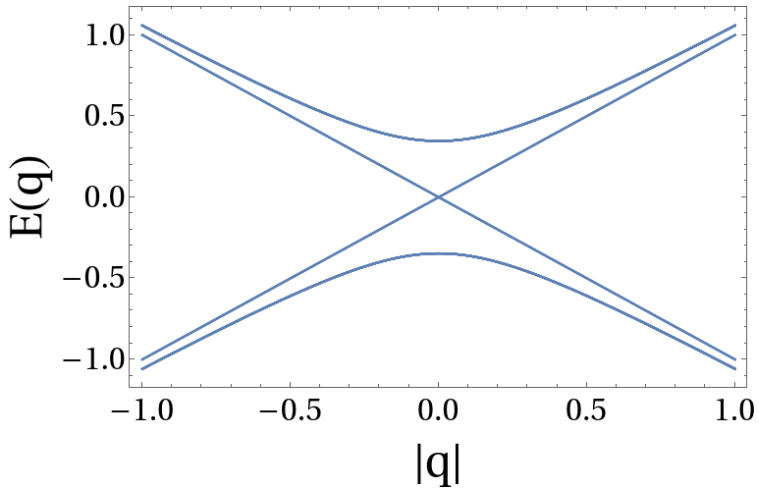

Figure 4.3: Dispersion for the $\mathcal{A}_{1u}$ and $\mathcal{A}_{2u}$ irreps (for $\Delta^{\mathcal{A}_{1u}} = 0.30$) around the Dirac points. The gapped bands are 12-fold degenerate, originating from Dirac nodes at M-points in the global basis, while the gapless 4-fold degenerate bands originate from the Γ-point (Eq. 4.18)

ence of these masses is given by Eq. 2.21. The corresponding mass matrix is given by Eq. 3.3 with $d = 1$ for the $\mathcal{A}_{1u}$ singlet with

$$m^{\mathcal{A}_{1u}} = \frac{1}{\sqrt{3}}\left(\frac{\sqrt{3}}{2}\Sigma_{35} + \frac{1}{2}\Sigma_{34}\right)\tau_3\sigma_2 + \frac{1}{\sqrt{3}}\left(\frac{\sqrt{3}}{2}\Sigma_4 + \frac{1}{2}\Sigma_5\right)\tau_0\sigma_2 + \frac{1}{\sqrt{3}}\Sigma_{14}\tau_2\sigma_0, \tag{4.12}$$

and

$$\Delta^{\mathcal{A}_{1u}} = \langle \chi^T\, m^{\mathcal{A}_{1u}}\, \chi \rangle, \tag{4.13}$$

such that the pairing is non-unitary, *i.e.*,

$$\left[\Delta^{\mathcal{A}_{1u}} m^{\mathcal{A}_{1u}}\right] \cdot \left[\Delta^{\mathcal{A}_{1u}} m^{\mathcal{A}_{1u}}\right]^{\dagger} = |\Delta^{\mathcal{A}_{1u}}|^2 \left[\Sigma_0\zeta_0 + \frac{1}{3}\left(\Sigma_{23}\zeta_3 - \Sigma_{12}\zeta_1 - \Sigma_{13}\zeta_2\right)\right]. \quad (4.14)$$

For the $\mathcal{A}_{2u}$ singlet, we similarly have an analogous mass matrix with

$$m^{\mathcal{A}_{2u}} = \frac{1}{\sqrt{3}}\left(\frac{\sqrt{3}}{2}\Sigma_{34} - \frac{1}{2}\Sigma_{35}\right)\tau_3\sigma_2 + \frac{1}{\sqrt{3}}\left(-\frac{\sqrt{3}}{2}\Sigma_5 + \frac{1}{2}\Sigma_4\right)\tau_0\sigma_2 - \frac{1}{\sqrt{3}}\Sigma_{15}\tau_2\sigma_0, \quad (4.15)$$

and

$$\Delta^{\mathcal{A}_{2u}} = \langle \chi^T m^{\mathcal{A}_{2u}} \chi \rangle. \quad (4.16)$$

Thus, the pairing in this case too is non-unitary, *i.e.*, $\left[\Delta^{\mathcal{A}_{2u}} m^{\mathcal{A}_{2u}}\right] \cdot \left[\Delta^{\mathcal{A}_{2u}} m^{\mathcal{A}_{2u}}\right]^{\dagger}$ has a form similar to Eq. 4.14. Thus, both the SCs have a double gap structure, with one of the gaps being exactly zero corresponding to four zero eigenvalues of the matrix on the right-hand-side of Eq. 4.14 (the other twelve eigenvalues are non-zero equal and hence give rise to 12 fold degenerate gapped excitations) and is evident from Fig. 4.3. This gapless structure becomes most transparent when the low-energy theory is written in the global basis (using the χ_g spinors defined in Eq. A.1). Note that in the global basis [40], there are four valleys (see Fig. 2.1)– one at Γ point and three at the three inequivalent $M \equiv (M_1, M_2, M_3)$ points– and each valley contributes a 4-component Dirac spinor as expressed in Eq. A.2. The corresponding Nambu spinor (in the global basis) is then given by

$$\chi_g^N = \left(\tilde{\chi}_{g\Gamma}, \tilde{\chi}_{g\Gamma}^{\dagger}, \tilde{\chi}_{gM_1}, \tilde{\chi}_{gM_1}^{\dagger}, \tilde{\chi}_{gM_2}, \tilde{\chi}_{gM_2}^{\dagger}, \tilde{\chi}_{gM_3}, \tilde{\chi}_{gM_3}^{\dagger}\right)^T. \quad (4.17)$$

In this basis the mass matrices (Eq. 3.3), $M_{global}^{\mathcal{A}_u}$, corresponding to the $\mathcal{A}_{1u}$ and the $\mathcal{A}_{2u}$ singlets have the generic form of

$$\left(\begin{array}{cc|cc|cc|cc}
0_{4\times4} & 0_{4\times4} & 0_{4\times4} & 0_{4\times4} & 0_{4\times4} & 0_{4\times4} & 0_{4\times4} & 0_{4\times4} \\
0_{4\times4} & 0_{4\times4} & 0_{4\times4} & 0_{4\times4} & 0_{4\times4} & 0_{4\times4} & 0_{4\times4} & 0_{4\times4} \\
\hline
0_{4\times4} & 0_{4\times4} & 0_{4\times4} & \mathcal{W}_1 & 0_{4\times4} & 0_{4\times4} & 0_{4\times4} & 0_{4\times4} \\
0_{4\times4} & 0_{4\times4} & \mathcal{W}_1^{\dagger} & 0_{4\times4} & 0_{4\times4} & 0_{4\times4} & 0_{4\times4} & 0_{4\times4} \\
\hline
0_{4\times4} & 0_{4\times4} & 0_{4\times4} & 0_{4\times4} & 0_{4\times4} & \mathcal{W}_2 & 0_{4\times4} & 0_{4\times4} \\
0_{4\times4} & 0_{4\times4} & 0_{4\times4} & 0_{4\times4} & \mathcal{W}_2^{\dagger} & 0_{4\times4} & 0_{4\times4} & 0_{4\times4} \\
\hline
0_{4\times4} & 0_{4\times4} & 0_{4\times4} & 0_{4\times4} & 0_{4\times4} & 0_{4\times4} & 0_{4\times4} & \mathcal{W}_3 \\
0_{4\times4} & 0_{4\times4} & 0_{4\times4} & 0_{4\times4} & 0_{4\times4} & 0_{4\times4} & \mathcal{W}_3^{\dagger} & 0_{4\times4}
\end{array}\right), \quad (4.18)$$

where $\mathcal{W}_i$ are 4×4 matrices which are essentially the pairing matrices for the χ_{gM_i} spinor (for $i = 1, 2, 3$). From the structure of the matrices, it is clear that the pairing is absent for the Dirac fermions $\chi_{g\Gamma}$, which then remains massless due to lattice symmetries as well as an emergent SO(4), similar to the protection of the Γ-DSM in Ref. [40], and is discussed in Appendix A.5. The SO(4) can either be broken via inducing spin-octupole Hall order [40] or admixing the above SC with the gapped $\mathcal{A}_{1g}$ singlet SC discussed above in Section 4.1.1.

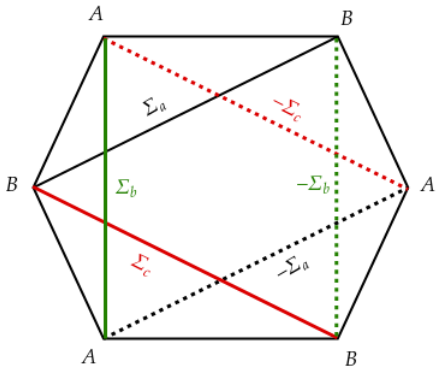

Figure 4.4: Schematic of the pairing for for $\mathcal{A}_{1u}$ and $\mathcal{A}_{2u}$ singlets the lattice BCS Model in global basis (Eq. 4.19). The connecting lines indicate NNN pairing amplitudes with their colours representing the pairing matrix. Solid(dashed) lines indicate the sign of the pairing term is positive(negative) with the matrices $(\Sigma_a, \Sigma_b, \Sigma_c)$ described in Eqs. 4.20 and 4.21 respectively for the two singlets.

The above low-energy forms of the two gapless SCs stem from a mean-field lattice Hamiltonian with NNN pairing, which, in the global basis (similar to Eq. 4.11), is given by

$$H^{global}_{\mathcal{A}_{1u(2u)}} = H + \sum_{\langle\langle \mathbf{r}\mathbf{r}' \rangle\rangle} \left[\left(\Delta^{\mathcal{A}_{1u(2u)}}_{lat} \right)^* \; \Psi^T(\mathbf{r}) \, \mathcal{X}_{\mathbf{r}\mathbf{r}'} \, \Psi(\mathbf{r}') + \text{h.c.} \right], \tag{4.19}$$

where $\mathcal{X}_{\mathbf{r}\mathbf{r}'}$ is the pairing matrix between the NNN sites at $\mathbf{r}$ and $\mathbf{r}'$ that are pictorially shown in Fig. 4.4, where Σ_a, Σ_b and Σ_c are the pairing matrices on the different NNN bonds. For the $\mathcal{A}_{1u}$ singlet, these paring matrices respectively are

$$-\frac{1}{2}(\Sigma_{24} + \sqrt{3}\Sigma_{25}), \;\; \Sigma_{24}, \;\; \frac{1}{2}(\sqrt{3}\Sigma_{25} - \Sigma_{24}), \tag{4.20}$$

while, for the $\mathcal{A}_{2u}$ singlet, they are

$$\frac{1}{2}(\Sigma_{25} - \sqrt{3}\Sigma_{24}), \;\; -\Sigma_{25}, \;\; \frac{1}{2}(\sqrt{3}\Sigma_{24} + \Sigma_{25}). \tag{4.21}$$

Each of the Cooper pair wave functions is symmetric in real space with weights at NNN sites, while the spin wave functions for the three bonds with $\Sigma_a, \Sigma_b, \Sigma_c$ (Fig. 4.4) are anti-symmetric and given by

$$|\Phi_a\rangle = \frac{1}{2}|J_T = 2, m_T = 0\rangle + \sqrt{\frac{3}{8}}|J_T = 2, m_T = 2\rangle - \sqrt{\frac{3}{8}}|J_T = 2, m_T = -2\rangle, \tag{4.22}$$

$$|\Phi_b\rangle = |J_T = 2, m_T = 0\rangle, \tag{4.23}$$

$$|\Phi_c\rangle = -\frac{1}{2}|J_T = 2, m_T = 0\rangle + \sqrt{\frac{3}{8}}|J_T = 2, m_T = 2\rangle - \sqrt{\frac{3}{8}}|J_T = 2, m_T = -2\rangle, \tag{4.24}$$

for $\mathcal{A}_{1u}$ and

$$|\Phi_a\rangle = \frac{\sqrt{3}}{2}|J_T = 2, m_T = 0\rangle + \sqrt{\frac{1}{8}}|J_T = 2, m_T = 2\rangle - \sqrt{\frac{1}{8}}|J_T = 2, m_T = -2\rangle \tag{4.25}$$

$$|\Phi_b\rangle = \frac{1}{\sqrt{2}}\left(|J_T = 2, m_T = 2\rangle - |J_T = 2, m_T = -2\rangle\right), \tag{4.26}$$

$$|\Phi_c\rangle = \frac{\sqrt{3}}{2}|J_T = 2, m_T = 0\rangle - \sqrt{\frac{1}{8}}|J_T = 2, m_T = 2\rangle + \sqrt{\frac{1}{8}}|J_T = 2, m_T = -2\rangle \tag{4.27}$$

for $\mathcal{A}_{2u}$.

Noticeably, while the spatial part of the wave-function is symmetric and as a result the spin-part is anti-symmetric, the structure of the latter depends on the actual direction of the bonds in the former (Fig. 4.4) in both the superconductors, due to the SOC, resulting in inversion odd SCs.

4.2 Doublet Superconductors

There are four doublet bilinears, one with the irrep $\mathcal{E}_g$ and three with $\mathcal{E}_u$, given in Eq. 3.19, 3.22, 3.23 and 3.24 respectively. The three $\mathcal{E}_u$ masses represent a single gapped SC, while the $\mathcal{E}_g$ doublet represents a nodal SC. In the following, we first discuss the three $\mathcal{E}_u$ doublets and then the $\mathcal{E}_g$ doublet.

4.2.1 The 3 $\mathcal{E}_u$ Doublets

The three $\mathcal{E}_u$ doublets, denoted as $\mathcal{E}_u^I, \mathcal{E}_u^{II}$ and $\mathcal{E}_u^{III}$, arise in Eq. 3.19, 3.23 and 3.24 respectively. The low-energy Hamiltonian in the presence of $\mathcal{E}_u^x$ (for $x = I, II, III$) doublet is given by Eq. 2.21 with the mass matrices, $M^{\mathcal{E}_u^x}$ of the form given by Eq. 3.3

with the mass matrices $m_1^{\mathcal{E}_u^x}$ and $m_2^{\mathcal{E}_u^x}$ given by

$$\mathcal{E}_u^I : \begin{cases} m_1^{\mathcal{E}_u^I} = \Sigma_{24}\tau_1\sigma_0 \\ m_2^{\mathcal{E}_u^I} = \Sigma_{25}\tau_1\sigma_0 \end{cases} \tag{4.28}$$

$$\mathcal{E}_u^{II} : \begin{cases} m_1^{\mathcal{E}_u^{II}} = \frac{1}{\sqrt{6}}(\frac{1}{2}\Sigma_{35} - \frac{\sqrt{3}}{2}\Sigma_{34})\tau_3\sigma_2 - \sqrt{\frac{2}{3}}\Sigma_{15}\tau_2\sigma_0 + \frac{1}{\sqrt{6}}(\frac{\sqrt{3}}{2}\Sigma_5 - \frac{1}{2}\Sigma_4)\tau_0\sigma_2 \\ m_2^{\mathcal{E}_u^{II}} = \frac{1}{\sqrt{2}}\frac{\Sigma_{35}-\sqrt{3}\Sigma_{34}}{2}\tau_3\sigma_2 - \frac{1}{\sqrt{2}}\frac{\sqrt{3}\Sigma_5-\Sigma_4}{2}\tau_0\sigma_2. \end{cases} \tag{4.29}$$

$$\mathcal{E}_u^{III} : \begin{cases} m_1^{\mathcal{E}_u^{III}} = -\frac{1}{\sqrt{6}}(\frac{1}{2}\Sigma_{34} + \frac{\sqrt{3}}{2}\Sigma_{35})\tau_3\sigma_2 + \sqrt{\frac{2}{3}}\Sigma_{14}\tau_2\sigma_0 - \frac{1}{\sqrt{6}}(\frac{\sqrt{3}}{2}\Sigma_4 + \frac{1}{2}\Sigma_5)\tau_0\sigma_2 \\ m_2^{\mathcal{E}_u^{III}} = \frac{1}{\sqrt{2}}\frac{\Sigma_{34}+\sqrt{3}\Sigma_{35}}{2}\tau_3\sigma_2 - \frac{1}{\sqrt{2}}\frac{\sqrt{3}\Sigma_4+\Sigma_5}{2}\tau_0\sigma_2. \end{cases} \tag{4.30}$$

The corresponding pairing amplitudes,

$$\Delta_i^{\mathcal{E}_u^x} = \langle \chi^T m_i^{\mathcal{E}_u^x} \chi \rangle \quad (i = 1, 2), \tag{4.31}$$

can be parametrised as

$$(\Delta_1^{\mathcal{E}_u^x}, \Delta_2^{\mathcal{E}_u^x}) = \Delta^{\mathcal{E}_u^x} e^{i\tilde{\phi}}(\cos\theta, \sin\theta e^{i\tilde{\gamma}}), \tag{4.32}$$

where $\Delta^{\mathcal{E}_u^x} = \sqrt{|\Delta_1^{\mathcal{E}_u^x}|^2 + |\Delta_2^{\mathcal{E}_u^x}|^2}$, $\tilde{\phi}, \tilde{\phi} + \tilde{\gamma} \in (0, 2\pi]$ are the phases of the superconducting amplitudes and $\theta = \tan^{-1}\left(|\Delta_2^{\mathcal{E}_u^x}|/|\Delta_1^{\mathcal{E}_u^x}|\right)$. For a general phase difference ($\tilde{\gamma} \neq 0$), the SC breaks the microscopic time-reversal symmetry as explained in Sec. 3.2.

All three doublets give rise to non-unitary SCs, and the details of the Bogoliubov spectrum depend on the values of the various parameters in the superconducting amplitude (Eq. 4.32). As mentioned earlier, these three $\mathcal{E}_u$ doublets represent a single superconducting phase. This can be demonstrated through a similar analysis as done in Sec. 4.1.1. We can find an adiabatic path between any two of them without closing the quasi-particle energy gap and without breaking further microscopic symmetries. Thus, we will discuss the $\mathcal{E}_u^I$ doublet in detail below, while the Irreps $\mathcal{E}_u^{II}$ and $\mathcal{E}_u^{III}$ are discussed in Appendix A.6.

$\mathcal{E}_u^I$ Doublet

We rewrite the mass matrix (Eq. 3.3) as

$$m^{\mathcal{E}_u^I}(\mathbf{d}) = \Delta^{\mathcal{E}_u^1}\left(d_1^{\mathcal{E}_u^I} m_1^{\mathcal{E}_u^I} + d_2^{\mathcal{E}_u^I} m_2^{\mathcal{E}_u^I}\right) = |\Delta^{\mathcal{E}_u^I}|\ \mathbf{d}\cdot\mathbf{m}^{\mathcal{E}_\mathbf{u}^\mathbf{I}}, \tag{4.33}$$

where

$$\mathbf{d} = e^{i\tilde{\phi}}\left(\cos\theta,\ \sin\theta\, e^{i\tilde{\gamma}}\right) \tag{4.34}$$

is a two-component complex vector and $|\Delta^{\mathcal{E}_u^I}|$ is the magnitude of the pairing. Checking for unitarity, we have

$$\left[\mathbf{\Delta}^{\mathcal{E}_u^I}\cdot\mathbf{m}^{\mathcal{E}_\mathbf{u}^\mathbf{I}}\right]\cdot\left[\mathbf{\Delta}^{\mathcal{E}_u^I}\cdot\mathbf{m}^{\mathcal{E}_\mathbf{u}^\mathbf{I}}\right]^\dagger = |\mathbf{\Delta}^{\boldsymbol{\mathcal{E}}_\boldsymbol{u}^\mathbf{I}}|^2\left(\Sigma_0\tau_0\sigma_0 + \frac{i}{2}\sin(2\theta)\sin(\tilde{\gamma})\left[m_1^{\mathcal{E}_u^1}, m_2^{\mathcal{E}_u^1}\right]\right), \tag{4.35}$$
$$\text{where } \frac{1}{2i}[m_1^{\mathcal{E}_u^1}, m_2^{\mathcal{E}_u^1}] = \Sigma_{45}\tau_0\sigma_0.$$

The two distinct eigenvalues (represented by $\lambda_\pm^{\mathcal{E}_u^I}$) of the matrix in eq. 4.35 are given by

$$\lambda_\pm^{\mathcal{E}_u^I} = (\Delta^{\mathcal{E}_u^I})^2\left(1 \pm \sin(\tilde{\gamma})\sin(2\theta)\right), \tag{4.36}$$

(with each being 8-fold degenerate) such that for the TR invariant (breaking) manifold, $\tilde{\gamma} = 0$ ($\theta, \tilde{\gamma} \neq 0$), and we get a unitary (non-unitary) SC and consequently a single (double) gap structure. Interestingly, on the isolated points within the TR breaking manifold of SCs, when $\theta = \pm\pi/4, \pm 3\pi/4$ and $\tilde{\gamma} = \pm\pi/2$, corresponding to

$$\sin(\tilde{\gamma})\sin(2\theta) = \pm 1, \tag{4.37}$$

when one of the eigenvalues vanishes, leading to the collapse of the smaller of the two pairing gaps, we have 8-fold gapless (nodal) Bogoliubov excitations.

The above low-energy theory is obtained from a mean field lattice Hamiltonian in the global basis of the form similar to Eq. 4.6 with onsite pairing between the $j = 3/2$ electrons given by

$$\sum_\mathbf{r} f(\mathbf{r})\left(\left(\Delta_{lat,1}^{\mathcal{E}_u^I}\right)^* \Psi^T(\mathbf{r})\,\Sigma_{24}\,\Psi(\mathbf{r}) + \left(\Delta_{lat,2}^{\mathcal{E}_u^I}\right)^* \Psi^T(\mathbf{r})\,\Sigma_{25}\,\Psi(\mathbf{r})\right). \tag{4.38}$$

Here, $f(r)$ ($= \pm 1$) is a function defined on the lattice sites $\mathbf{r}$ (see Fig. 4.5). This modulation $f(\mathbf{r})$ breaks the point group symmetry while preserving the translational sym-

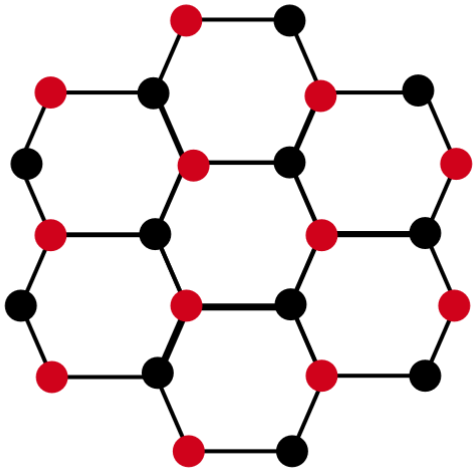

Figure 4.5: Schematic figure for the pairing amplitude of the $\mathcal{E}_u^I$ on the lattice in the global basis (Eq. 4.38). Black dots represents onsite pairing with pairing matrix $\Sigma_i \in (\Sigma_{24}, \Sigma_{25})$ and Red dots represents onsite pairing with pairing matrix $-\Sigma_i$ with $\{\Sigma_{24}, \Sigma_{25}\}$ being the two members of the doublet. The relative negative sign of the pairings on the two sublattices ensures that the SC is odd under inversion.

metry of the honeycomb lattice, and corresponds to staggered on-site pairing.

The corresponding anti-symmetric spin wave function of the Cooper pair is given by Eqs. 4.23 and 4.26 respectively for the two components. Thus, the Cooper pairs for this doublet are made up of a linear combination of a subset of anti-symmetric $J_T = 2$ ($m_T = 0, \pm 2$) spin multiplet states.

Further insights about the staggered on-site pairing become apparent by going back to the continuum limit, whence using Eq. 4.34 we get

$$\hat{\mathbf{n}} \equiv (n_1, n_2, n_3) = \mathbf{d}^\dagger \vec{\sigma} \mathbf{d} = (\cos\tilde{\gamma} \sin 2\theta, \sin\tilde{\gamma} \sin 2\theta, \cos 2\theta) \tag{4.39}$$

such that (n_1, n_3) transforms as $\mathcal{E}_g^e$, and n_2 transforms as $\mathcal{A}_{2g}^o$ under lattice symmetries and $\vec{\sigma} = (\sigma^x, \sigma^y, \sigma^z)$ are 2×2 Pauli matrices. The TRI sub-manifold is then spanned by $n_2 = 0$, while the pure TR breaking manifold is given by $n_1 = n_3 = 0$, with the latter being an isolated point corresponding to $\theta = \pm\pi/4, \tilde{\gamma} = \pm\pi/2$. Note that at these isolated points, the smaller of the two gaps vanishes, and we get a gapless TR breaking SC (Eq. 4.37). The underlying microscopic symmetries allow for the leading order anisotropic term

$$\lambda_1 n_2^2 + \lambda_2 \left(n_1^2 + n_3^2\right) \tag{4.40}$$

in the Landau free energy, which dictates details of whether the TR invariant/breaking manifold is chosen, depending on the signs of the coupling constants λ_1, λ_2.

Vortex structure: It is interesting to look at the possible topological defects in the presence of this doublet mass. Apart from the usual U(1) vortex in the Nambu sector (texture in the real and imaginary part of superconducting amplitude), we find that there is also another stable vortex defect possible, which we discuss now. This is clear by noting that the order parameter (Eq. 4.34) lives in $(S^1 \times S^2)/Z_2$ manifold, similar to the spinor bosons [17,107,108] which is broken down to $(S^1 \times S^1)/Z_2$ [107,108] in the TRI subspace. Thus, the vortices generically are characterized by $\pi_1((S^1 \times S^2)/Z_2) = Z$ and reduces to $\pi_1((S^1 \times S^1)/Z_2) = Z \times Z$ [17,107,108] in the TRI manifold.

4.2.2 The Gapless Doublet Mass ($\mathcal{E}_g$)

The $\mathcal{E}_g$ doublet masses arise from direct product of the $\mathcal{T}_{2g}$ lattice Irrep in flavour and the $\mathcal{T}_{2g}$ Irrep in valley-subband sector (see Eq. 3.22). The low-energy Hamiltonian in the presence of this doublet mass is given by Eq. 2.21, with the mass matrix, $M^{\mathcal{E}_g}$, given by a form similar to Eq. 3.3 with

$$m_1^{\mathcal{E}_g} = \frac{1}{\sqrt{2}}(\Sigma_0\tau_0\sigma_2 - \Sigma_{12}\tau_3\sigma_2), \tag{4.41}$$

$$m_2^{\mathcal{E}_g} = \frac{1}{\sqrt{6}}(\Sigma_0\tau_0\sigma_2 + \Sigma_{12}\tau_3\sigma_2 + 2\Sigma_{23}\tau_2\sigma_0), \tag{4.42}$$

and

$$\Delta_1^{\mathcal{E}_g} = \langle \chi^T\, m_1^{\mathcal{E}_g}\, \chi \rangle \ , \ \Delta_2^{\mathcal{E}_g} = \langle \chi^T\, m_2^{\mathcal{E}_g}\, \chi \rangle, \tag{4.43}$$

which can be parametrised in a way similar to Eq. 4.32 and gives rise to a non-unitary SC which is TR invariant only for $\gamma = 0, \pi$ and breaks it otherwise. Notably, however the eigenvalues of the matrix $m^{\mathcal{E}_g}(\mathbf{d}).(m^{\mathcal{E}_g}(\mathbf{d}))^\dagger$ is

$$\Bigg(0,\ \frac{8}{3}(\Delta^{\mathcal{E}_g})^2\sin^2(\theta),\ \ \frac{1}{3}(\Delta^{\mathcal{E}_g})^2\left(4 + 2\cos(2\theta) + 2\sqrt{3}\cos(\tilde{\gamma})\sin(2\theta)\right),$$
$$\frac{1}{3}(\Delta^{\mathcal{E}_g})^2\left(4 + 2\cos(2\theta) - 2\sqrt{3}\cos(\tilde{\gamma})\sin(2\theta)\right)\Bigg), \tag{4.44}$$

with each being 4-fold degenerate. Thus, the spectrum of the Bogoliubov quasi-particles is generically gapless, with the degeneracy of the number of gapless nodes varying over the order parameter manifold. The resultant low-energy Bogoliubov spectrum is shown in Fig. 4.6(a) whose origin can be traced back to the Dirac nodes at the Γ-point in the global basis – similar to the case of $\mathcal{A}_{1u}$ and $\mathcal{A}_{2u}$ singlets discussed in Sec. 4.1.2

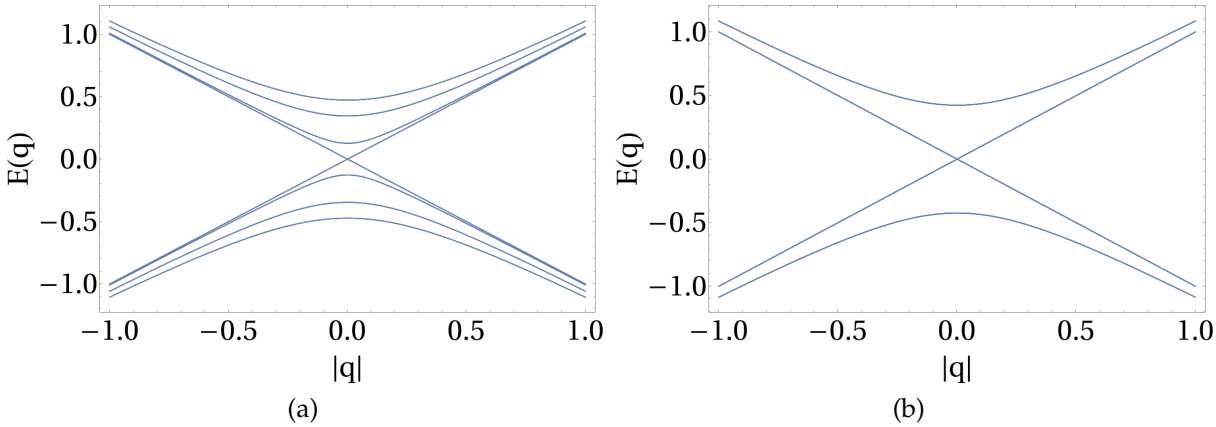

Figure 4.6: Gapless Doublet Spectrum (for $|\Delta^{\mathcal{E}_g}| = 0.30$) (a) For general values of θ (here it is shown for $\theta = \pi/4$), there are 8 bands each of them is 8-fold degenerate. Out of these 8 bands, two bands touch linearly at $\mathbf{q} = \mathbf{0}$, providing 8-gapless modes. (b) For $\theta \in \{\pm\pi/3, \pm 2\pi/3, 0\}$ (here it is shown for $\theta = \pi/3$), Apart from the usual two bands, extra bands are touching each other at $\mathbf{q} = \mathbf{0}$, providing 16-gapless modes.

above (also Appendix A.5). Extra isolated gapless modes can appear on the TRI subspace ($\tilde{\gamma} = 0, \pi$) for $\theta = 0, \pi, \pm\pi/3, \pm 2\pi/3$ as shown in Fig. 4.6(b). On the lattice, these doublet masses correspond to NNN pairing. The equivalent lattice Hamiltonian in this case is similar to that given in Eq. 4.19 with the pairing amplitudes on the NNN bonds (in the global basis) being given by

$$\mathcal{X}_{\mathbf{r}\mathbf{r}'} = f(\mathbf{r}, \mathbf{r}')\Sigma_{13} = -f(\mathbf{r}, \mathbf{r}')\frac{7}{3}\left(J_y - \frac{4}{7}J_y^3\right) \tag{4.45}$$

Here, $f(\mathbf{r}, \mathbf{r}')(= \pm 1)$ is depends on the particular NNN bond. For $\Delta_2^{\mathcal{E}_g} = 0$, $f(\mathbf{r}, \mathbf{r}')$

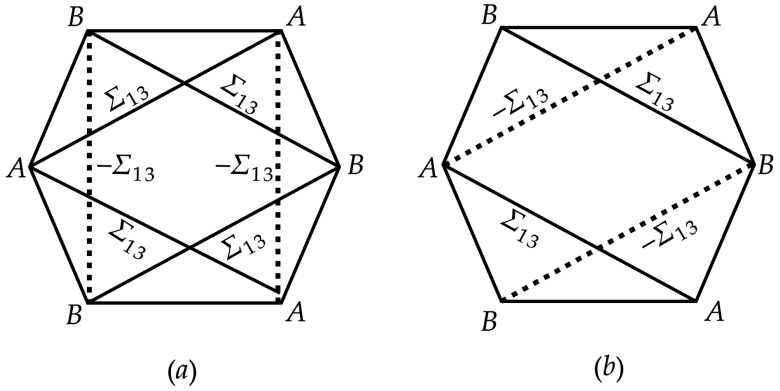

Figure 4.7: Schematics of the pairing for the two components ($m_2^{\mathcal{E}_g}$, $m_1^{\mathcal{E}_g}$) of the $\mathcal{E}_g$ doublet on the lattice in the global basis (Eq. 4.45). The pairing amplitudes are on NNN bonds, and the solid (dashed) lines are related to each other by the change in sign of the pairing matrix as indicated.

is pictorially shown in Fig. 4.7(a). Similarly, Fig. 4.7(b) shows the pairing pattern for $\Delta_1^{\mathcal{E}_g} = 0$. The resultant Cooper-pair wave-function is an anti-symmetric spin singlet and is given by Eq. 4.10, while the spatial part is symmetric with modulation on the NNN bonds, as shown in the figures. Thus, these too correspond to nodal SCs with anisotropic NNN pairing.

With this, our study of singlet and doublet superconductors concludes. The next chapter will focus on triplet superconductors

Chapter 5

Triplet Superconductors

In this chapter, we will complete our discussion of the superconducting phases by discussing the triplet superconductors.

5.1 Triplet Superconductors

Finally, we turn to the triplet SCs. There are eight triplet Irreps (Eqns 3.21 - 3.24) : (3)$\mathcal{T}_{1g}$, (2)$\mathcal{T}_{1u}$, (2)$\mathcal{T}_{2u}$, and $\mathcal{T}_{2g}$. These irreps result in *six* distinct superconducting phases since the two $\mathcal{T}_{1u}$ give rise to a single SC, and so does the two $\mathcal{T}_{2u}$. Specifically, two of the $\mathcal{T}_{1g}$, the $\mathcal{T}_{1u}$, and the $\mathcal{T}_{2u}$ are gapped SCs, while the remaining $\mathcal{T}_{1g}$ and the $\mathcal{T}_{2g}$ are SCs with gapless Dirac nodes. All these SCs correspond to non-unitary pairing generically as we describe below.

5.1.1 The $\mathcal{T}_{1g}$ Triplet superconductors

There are three $\mathcal{T}_{1g}$ triplets corresponding to Eqs. 3.20, 3.21 and 3.22. All three triplets generically break TR, but have extended TRI sub-space. While the first one is a flavour anti-symmetric, the other two are flavour symmetric. However, in the TRI sub-manifold, we find that the three triplets cannot be adiabatically connected without breaking further microscopic lattice symmetries or time reversal. Particularly once TR is broken, the three SCs can be adiabatically connected. Further, while two of them are generically gapped, the third one is a nodal SC. Due to this, we consider them as separate SCs which we denote by $\mathcal{T}_{1g}^{x}$ with $x = I, II, III$. We discuss each of them now separately below.

The low-energy Hamiltonian for these SCs is given in Eqns. 2.21 and 3.3 for $\mathcal{T}_{1g}^{x}$ (for

$x = I, II, III$) with mass matrices of the form

$$\mathcal{T}_{1g}^{I}: \begin{cases} m_1^{\mathcal{T}_{1g}^{I}} = \Sigma_1\tau_1\sigma_0, \\ m_2^{\mathcal{T}_{1g}^{I}} = \Sigma_3\tau_1\sigma_0, \\ m_3^{\mathcal{T}_{1g}^{I}} = i\Sigma_{45}\tau_1\sigma_0. \end{cases} \tag{5.1}$$

$$\mathcal{T}_{1g}^{II}: \begin{cases} m_1^{\mathcal{T}_{1g}^{II}} = \Sigma_2\tau_2\sigma_0, \\ m_2^{\mathcal{T}_{1g}^{II}} = \Sigma_2\tau_3\sigma_2, \\ m_3^{\mathcal{T}_{1g}^{II}} = i\Sigma_2\tau_0\sigma_2. \end{cases} \tag{5.2}$$

and

$$\mathcal{T}_{1g}^{III} = \begin{cases} m_1^{\mathcal{T}_{1g}} = (\Sigma_0\tau_3\sigma_2 - \Sigma_{12}\tau_0\sigma_2)/\sqrt{2} \\ m_2^{\mathcal{T}_{1g}} = (-\Sigma_{23}\tau_0\sigma_2 - \Sigma_0\tau_2\sigma_0)/\sqrt{2} \\ m_3^{\mathcal{T}_{1g}} = i(\Sigma_{12}\tau_2\sigma_0 - \Sigma_{23}\tau_3\sigma_2)/\sqrt{2}. \end{cases} \tag{5.3}$$

The corresponding pairing amplitudes are given by

$$\Delta_i^{\mathcal{T}_{1g}^{x}} = \langle \chi^T m_i^{\mathcal{T}_{1g}^{x}} \chi \rangle \quad (i = 1, 2, 3). \tag{5.4}$$

As discussed in Sec. 3.2, that triplet breaks the microscopic time-reversal symmetry for a general value of the superconducting amplitudes, which, for each triplet, can be generically parametrized as

$$\mathbf{\Delta}^{\mathcal{T}_{1g}^{x}} = |\Delta^{\mathcal{T}_{1g}^{x}}|\, \mathbf{d}^x \tag{5.5}$$

where $\mathbf{d}^x \equiv (d_1^x, d_2^x, d_3^x)$ is a 3-component complex vector that spans the order parameter manifold $(S^1 \times CP^2)/Z_2$ [111, 112] via

$$(d_1^x, d_2^x, d_3^x) = e^{i\tilde{\phi}}(\cos\theta, e^{i\tilde{\gamma}_1}\sin\theta\cos\phi, e^{i\tilde{\gamma}_2}\sin\theta\sin\phi). \tag{5.6}$$

where, $\tilde{\phi}$ is the superconducting phase and $\theta, \tilde{\gamma}_1$ and $\tilde{\gamma}_2$ specify the direction in the triplet space. Note that the TRI sub-manifold is given by $\tilde{\gamma}_1 = \tilde{\gamma}_2 = 0$ or $\theta = 0, \pi$ whence the order parameter manifold reduces to $(S^1 \times S^2)/Z_2$ and corresponding vortices are characterized by $\pi_1((S^1 \times S^2)/Z_2) = Z$.

$\mathcal{T}_{1g}^{I}$ Triplet

A general mass term for this triplet is written as,

$$m^{\mathcal{T}_{1g}^{I}}(\mathbf{d}) = |\Delta^{\mathcal{T}_{1g}^{I}}| \left(d_1^I m_1^{\mathcal{T}_{1g}^{I}} + d_2^I m_2^{\mathcal{T}_{1g}^{I}} + d_3^I m_3^{\mathcal{T}_{1g}^{I}} \right) = \mathbf{\Delta}^{\mathcal{T}_{1g}^{I}} \cdot \mathbf{m}^{\mathcal{T}_{1g}^{I}}, \tag{5.7}$$

such that the unitarity condition leads to

$$\left[\mathbf{\Delta}^{\mathcal{T}_{1g}^{I}} \cdot \mathbf{m}^{\mathcal{T}_{1g}^{I}}\right] \cdot \left[\mathbf{\Delta}^{\mathcal{T}_{1g}^{I}} \cdot \mathbf{m}^{\mathcal{T}_{1g}^{I}}\right]^{\dagger} = |\Delta^{\mathcal{T}_{1g}^{I}}|^2 \times \left(\Sigma_0 \tau_0 \sigma_0 + \frac{1}{2} \left(\mathbf{d}^I \times \mathbf{d}^{I*} \right) \cdot \left(\mathbf{m}^{\mathcal{T}_{1g}^{I}} \times \mathbf{m}^{\mathcal{T}_{1g}^{I}\,\dagger} \right) \right), \tag{5.8}$$

which implies it is unitary provided $\mathbf{d^I} \times \mathbf{d^{I*}} = \mathbf{0}$, *i.e.*, on the TRI manifold. On the other hand, on the TRB manifold, there are two gaps (as can be obtained by diagonalizing Eq. 5.8) generically except at when $|\mathbf{d}^I \times \mathbf{d}^{I*}| = \pm 1$ whence the smaller of the two gaps collapse leading to a nodal SC. However, unlike the doublets (*e.g.*, Eq. 4.37), the above condition of obtaining a node can be satisfied on extended sub-spaces of the order-parameter manifold.

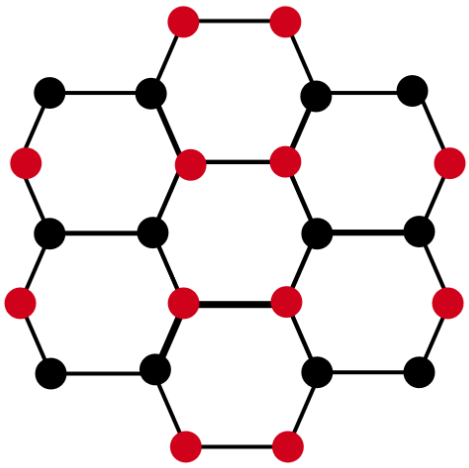

Figure 5.1: Schematics of the pairing for $m_1^{\mathcal{T}_{1g}^{I}}$ (Eq. 5.1) bilinear belonging to the $\mathcal{T}_{1g}^{I}$ triplet in global basis (Eq. 5.9). Here, Black (Red) dots represent on-site pairing in the flavour sector with pairing matrix $\Sigma_1(-\Sigma_1)$. Pairing amplitudes oscillates at momenta corresponding to M_2 point in the BZ(Fig. 2.1). Lattice model for the other two components of the triplets can be generated by acting with $\mathbf{S_6}$ (Table. A.3).

The corresponding lattice Hamiltonian (for mass matrix $m_1^{\mathcal{T}_{1g}^{I}}$) has a form similar to

Eq. 4.6 with on-site pairing term ($\mathcal{Y}_{\mathbf{r}}$) at the lattice site $\mathbf{r}$ is given by

$$\mathcal{Y}_{\mathbf{r}} = \left(\Delta_{lat,1}^{\mathcal{T}_{1g}^{I}}\right)^{*} \left(f(\mathbf{r})\Psi^{T}(\mathbf{r})\Sigma_1\Psi(\mathbf{r})\right), \tag{5.9}$$

where $f(\mathbf{r})(=\pm 1)$ is a function that creates a vertical stripy pattern of pairing on the honeycomb lattice, as illustrated in Fig. 5.1. As is evident from the figure, the pairing breaks translation symmetry in addition to point group symmetries. The pairing amplitude is at a finite momentum corresponding to the M_2 point in the BZ(Fig. 2.1). The spin-wave function of the Cooper pair is anti-symmetric and is given by

$$|\Phi_1\rangle = \frac{1}{\sqrt{2}}\left(|J_T = 2, m_T = 2\rangle + |J_T = 2, m_T = -2\rangle\right) \tag{5.10}$$

which should be contrasted with Eq. 4.26.

The lattice Hamiltonian for the other two masses in this triplet can be obtained by applying $\mathbf{C_3}$ rotations and correspond to the other two stripy patterns on the honeycomb lattice, with $\langle\Psi^{T}\Sigma_3\Psi\rangle$ and $\langle\Psi^{T}\Sigma_{45}\Psi\rangle$ pairings, with the corresponding spin-wave function for the Cooper pair being

$$|\Phi_3\rangle = \frac{1}{\sqrt{2}}\left(|J_T = 2, m_T = 1\rangle - |J_T = 2, m_T = -1\rangle\right), \tag{5.11}$$

and

$$|\Phi_{45}\rangle = \frac{1}{\sqrt{2}}\left(|J_T = 2, m_T = 1\rangle + |J_T = 2, m_T = -1\rangle\right). \tag{5.12}$$

Therefore, these correspond to pair density wave (PDW) SCs [56, 109, 110] (with or without TR) where the pairing amplitude oscillates at finite momentum. The nature of these PDWs and the splitting of their degeneracies can be studied using methods similar to Eq. 4.39, albeit using SU(3) matrices (see Appendix A.7).

$\mathcal{T}_{1g}^{II}$ triplet

The analysis of this triplet (spectrum and unitarity condition) is very similar to $\mathcal{T}_{1g}^{I}$ discussed above, leading to a PDW SC with a two-gap structure on the TRB manifold, which reduces to a single gap on the TRI subspace, as before.

The lattice Hamiltonian is similar to that given in Eq. 4.19. For the $m_1^{\mathcal{T}_{1g}^{II}}$ mass of this triplet, the pairing amplitude on the NNN bond connecting the lattice sites at $\mathbf{r}$

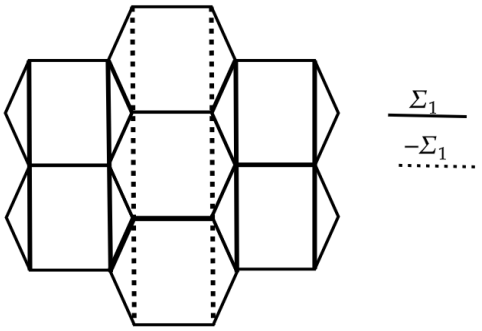

Figure 5.2: Schematic of NNN pairing for the bilinear $m_1^{\mathcal{T}_{1g}^{II}}$ (Eq. 5.2) component of $(\mathcal{T}_{1g}^{II})$ in global basis (Eq. 5.13). Here dotted (Solid) line represents pairing in the flavour sector with Pairing matrix $\Sigma_1(-\Sigma_1)$. Pairing amplitudes oscillate at momenta corresponding to the M_2 point in the BZ(Fig. 2.1).Pairings for the two other components of the triplet can be obtained by acting with $\mathbf{S_6}$ on the present one (Table. A.3).

and $\mathbf{r}'$ is given by

$$\mathcal{X}_{\mathbf{r}\mathbf{r}'} = f(\mathbf{r}, \mathbf{r}')\Sigma_1. \tag{5.13}$$

Here, $f(\mathbf{r}, \mathbf{r}')(= \pm 1)$ is such that it forms a vertical stripy pattern on the honeycomb lattice (see Fig. 5.2). The lattice model for other masses of the triplet can be obtained by action of $\mathbf{S_6}$, which leads to NNN pairing with stripy pattern along M_1 and M_3 momenta (Fig. 2.1). Thus, this is a NNN version of the $\mathcal{T}_{1g}^{I}$ triplet.

$\mathcal{T}_{1g}^{III}$ triplet

Finally, we turn to the $\mathcal{T}_{1g}^{III}$ triplet that arises from the direct product of the flavour and valley sub-band triplets (Eq. 3.22). This results in a nodal PDW SC with excitation spectrum given in Fig. 5.3.

The structure of the Bogoliubov spectrum is best understood by writing the generic mass matrix (using Eqs. 5.4 and 5.3) in the global basis (see Eq. 4.17), whence its structure reduces to a form similar to Eq. 4.18. Therefore, like the $\mathcal{A}_u$ singlets discussed above and the Γ-DSM of Ref. [40], the mass matrix here too has a zero block corresponding to the Dirac fermions at the BZ center, leading to the nodal PDW SC.

Interestingly, on the TRI manifold ($\mathbf{d} \times \mathbf{d}^* = \mathbf{0}$), there are extra gapless modes in the spectrum for some special linear combinations of the masses. We find that in the parameter space of TRI points, on the great circles (Fig. 5.4), two of the gapped bands in Fig. 5.5(a) touch each other at $\mathbf{q} = 0$ and the degeneracy of the gapless bands becomes 16 (also see the related discussion in Ref. [40]). The masses in this triplet correspond to the lattice Hamiltonian of the form given in Eq. 4.19. For the first mass

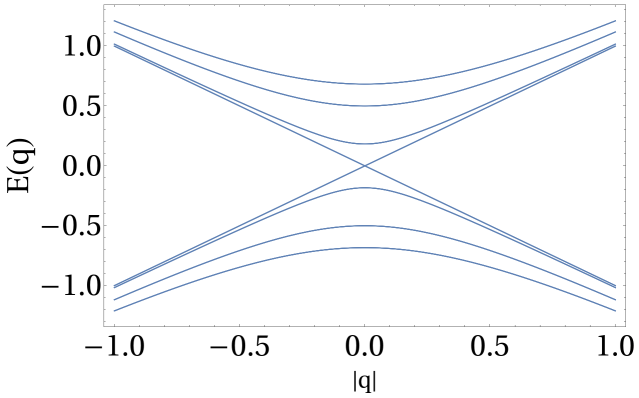

Figure 5.3: Spectrum for gapless triplet $\mathcal{T}_{1g}$ on TRI manifold, for general (θ, ϕ) and (for $|\Delta^{\mathcal{T}_{1g}}| = 0.31$). There are two bands which touch each other linearly at $\mathbf{q} = 0$; each is four-fold degenerate. For values of (θ, ϕ) on the Great circle (Fig. 5.4), the number of bands touching each other at $\mathbf{q} = \mathbf{0}$ increases and the two bands touching linearly at $\mathbf{q} = \mathbf{0}$, each one is 8-fold degenerate.

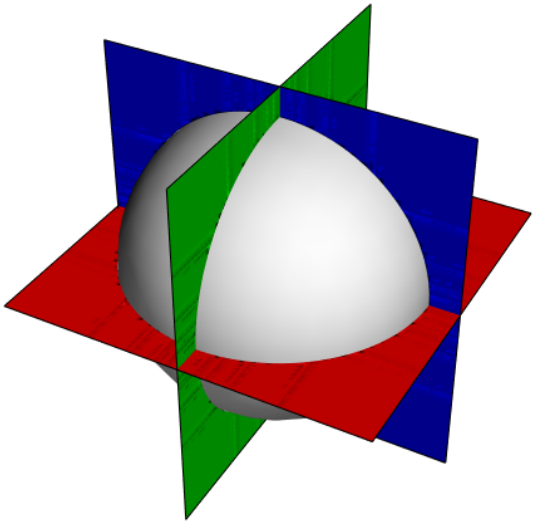

Figure 5.4: Schematic diagram for parameter space of Triplets on TRI manifold represented by Sphere. Circles obtained from the intersection of sphere with the blue-, green- and red-plane (representing $d_1 = 0$,$d_2 = 0$ and $d_3 = 0$ planes respectively) correspond to the Great circle discussed for $\mathcal{T}_{1g}$ triplet.

in this triplet, the pairing matrix $\mathcal{X}_{\mathbf{r}\mathbf{r}'}$ (in the global basis) on the NNN bonds is shown pictorially in Fig. 5.5 with

$$\Sigma_a = i\Sigma_{23} = i\frac{7}{3}\left(J_x - \frac{4}{7}J_x^3\right), \tag{5.14}$$

$$\Sigma_b = -i\Sigma_{23}. \tag{5.15}$$

This leads to a symmetric spin wave function for the Cooper pairs

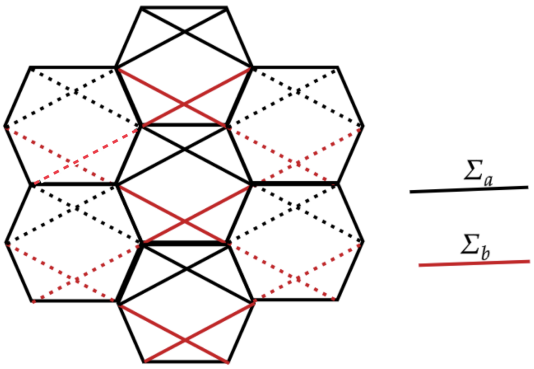

Figure 5.5: Lattice model for mass $m_1^{\mathcal{T}_{1g}}$ of the same triplet with NNN pairing indicated by connecting lines with the colors of lines red (black) representing the pairing matrices $\Sigma_a(\Sigma_b)$ whose forms are mentioned in Eq. 5.14. Momenta at which the pairing amplitudes oscillates corresponds to M_2 point in the BZ(Fig. 2.1).

$$|\Phi_{23}\rangle = \frac{1}{\sqrt{5}}\left(2|J_T = 3, m_T = 0\rangle + |J_T = 1, m_T = 0\rangle\right), \tag{5.16}$$

with an antisymmetric real-space part. The other two masses can be obtained by acting with $\mathbf{S_6}$, and the resultant mass matrices are Σ_{12} and Σ_0 respectively.

5.1.2 The $\mathcal{T}_{2g}$ triplet superconductor

The single $\mathcal{T}_{2g}$ SC arises from the direct product of triplets in both the flavour and the valley sub-band sectors (Eq. 3.22) and correspond to nodal SC.

The pairing amplitude is similar to Eq. 5.4, which can be parametrized using Eq. 5.5, and the mass matrices are given by

$$\begin{aligned} m_1^{\mathcal{T}_{2g}} &= \frac{1}{\sqrt{2}}(\Sigma_0\tau_3\sigma_2 + \Sigma_{12}\tau_0\sigma_2), \\ m_2^{\mathcal{T}_{2g}} &= \frac{1}{\sqrt{2}}(-\Sigma_{23}\tau_0\sigma_2 + \Sigma_0\tau_2\sigma_0), \\ m_3^{\mathcal{T}_{2g}} &= \frac{i}{\sqrt{2}}(\Sigma_{12}\tau_2\sigma_0 + \Sigma_{23}\tau_3\sigma_2), \end{aligned} \tag{5.17}$$

such that the mass matrix (Eq. 3.3 in the global basis (Eq. 4.17), $M_{global}^{\mathcal{T}_{2g}}$, has the generic

form

$$\left(\begin{array}{cc|cc|cc|cc} 0_{4\times4} & 0_{4\times4} & 0_{4\times4} & \mathcal{R}_A & 0_{4\times4} & \mathcal{R}_B & 0_{4\times4} & \mathcal{R}_C \\ 0_{4\times4} & 0_{4\times4} & \mathcal{R}_A^\dagger & 0_{4\times4} & \mathcal{R}_B^\dagger & 0_{4\times4} & \mathcal{R}_C^\dagger & 0_{4\times4} \\ \hline 0_{4\times4} & \mathcal{R}_A & 0_{4\times4} & 0_{4\times4} & 0_{4\times4} & 0_{4\times4} & 0_{4\times4} & 0_{4\times4} \\ \mathcal{R}_A^\dagger & 0_{4\times4} & 0_{4\times4} & 0_{4\times4} & 0_{4\times4} & 0_{4\times4} & 0_{4\times4} & 0_{4\times4} \\ \hline 0_{4\times4} & \mathcal{R}_B & 0_{4\times4} & 0_{4\times4} & 0_{4\times4} & 0_{4\times4} & 0_{4\times4} & 0_{4\times4} \\ \mathcal{R}_B^\dagger & 0_{4\times4} & 0_{4\times4} & 0_{4\times4} & 0_{4\times4} & 0_{4\times4} & 0_{4\times4} & 0_{4\times4} \\ \hline 0_{4\times4} & \mathcal{R}_C & 0_{4\times4} & 0_{4\times4} & 0_{4\times4} & 0_{4\times4} & 0_{4\times4} & 0_{4\times4} \\ \mathcal{R}_C^\dagger & 0_{4\times4} & 0_{4\times4} & 0_{4\times4} & 0_{4\times4} & 0_{4\times4} & 0_{4\times4} & 0_{4\times4} \end{array}\right) \tag{5.18}$$

such that in the global basis it corresponds to inter-valley pairing between the three M-valleys with the Γ-valley. The structure of the mass matrix is similar to the M-DSM phase of Ref [40] and yields 8-fold degenerate gapless nodes as can be seen from the eigenvalues of $\left[\mathbf{\Delta}^{\mathcal{T}_{2g}} \cdot \mathbf{m}^{\mathcal{T}_{2g}}\right] \cdot \left[\mathbf{\Delta}^{\mathcal{T}_{2g}} \cdot \mathbf{m}^{\mathcal{T}_{2g}}\right]^\dagger$. The resultant spectrum is shown in Fig. 5.6. The gapless manifold has an effective SU(4) symmetry at low energy. It would be interesting to understand the nature of phases that can be obtained by breaking this emergent SU(4) [10].

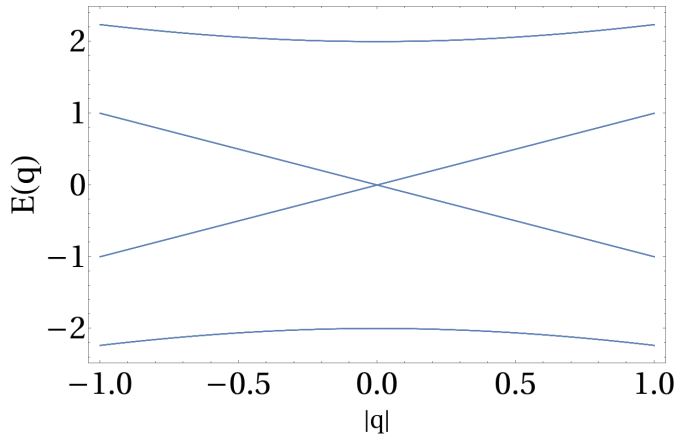

Figure 5.6: Spectrum for gapless triplet $\mathcal{T}_{2g}$ on the TRI manifold for all (θ, ϕ) with $|\Delta^{\mathcal{T}_{2g}}| = 1$. There are four bands, each 8-fold degenerate. Two bands touch at $\mathbf{q} = 0$, and the number of gapless modes remains the same for all TRI parameters.

On the lattice, in the global basis, the first mass of this triplet corresponds to NNN pairing of the form given in Eq. 4.19, where the NNN pairing matrices $(\mathcal{X}_{\mathbf{r}\mathbf{r}'})$ given by Eq. 5.14 , albeit with a different hopping structure as shown in Fig. 5.7, and corresponds to a finite momentum ordering with the spin wave function of the Cooper pair given by Eq. 5.16. Thus, this corresponds to a non-unitary nodal PDW SC.

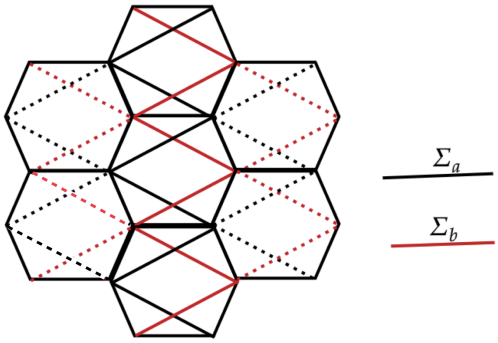

Figure 5.7: Lattice model for mass $m_1^{\mathcal{T}_{2g}}$ of the same triplet with NNN pairing shown by connecting lines: red (black) for Σ_a (Σ_b) as in Eq. 5.14. Pairing oscillates at momenta corresponding to M_2 in the BZ (Fig. 2.1).

5.1.3 The $\mathcal{T}_{2u}$ Triplet superconductors

These two ($\mathcal{T}_{2u}^I$ and $\mathcal{T}_{2u}^{II}$) SCs arise from flavour symmetric spaces (Eqs. 3.23 and 3.24). An analysis similar to that performed in Sec. 4.1.1 for the $\mathcal{A}_{1g}$ singlets demonstrate that these two irreducible representations give rise to the same superconducting phase as both Irreps can be adiabatically connected via one-parameter interpolation without closing spectrum gap and also not breaking any further microscopic symmetries.

The mass matrices for the $\mathcal{T}_{2u}^x$ (for $x = I, II$) triplets are given by Eq. 3.3 with $d = 3$, with

$$\Delta_i^{\mathcal{T}_{2u}^x} = \left\langle \chi^T m_i^{\mathcal{T}_{2u}^x} \chi \right\rangle, \quad (i = 1,2,3) \tag{5.19}$$

where

$$\begin{aligned}
m_1^{\mathcal{T}_{2u}^I} &= \frac{1}{\sqrt{2}}\left[\left(\frac{\sqrt{3}\Sigma_{34}}{2} - \frac{\Sigma_{35}}{2}\right)\tau_0\sigma_2 - \left(\frac{\Sigma_4}{2} - \frac{\sqrt{3}\Sigma_5}{2}\right)\tau_3\sigma_2\right], \\
m_2^{\mathcal{T}_{2u}^I} &= \frac{1}{\sqrt{2}}\left(\frac{1}{2}\Sigma_4 - \frac{\sqrt{3}}{2}\Sigma_5\right)\tau_2\sigma_0 + \frac{1}{\sqrt{2}}\Sigma_{15}\tau_0\sigma_2, \\
m_3^{\mathcal{T}_{2u}^I} &= \frac{i}{\sqrt{2}}\left(\frac{\sqrt{3}}{2}\Sigma_{34} - \frac{1}{2}\Sigma_{35}\right)\tau_2\sigma_0 - \frac{i}{\sqrt{2}}\Sigma_{15}\tau_3\sigma_2,
\end{aligned} \tag{5.20}$$

for $\mathcal{T}^{I}_{2u}$, and

$$
\begin{aligned}
m_1^{\mathcal{T}^{II}_{2u}} &= \frac{1}{\sqrt{2}}\left[(\frac{\sqrt{3}\Sigma_{35}+\Sigma_{34}}{2})\tau_0\sigma_2 + (\frac{\Sigma_5+\sqrt{3}\Sigma_4}{2})\tau_3\sigma_2\right], \\
m_2^{\mathcal{T}^{II}_{2u}} &= \frac{1}{\sqrt{2}}(\frac{1}{2}\Sigma_5 + \frac{\sqrt{3}}{2}\Sigma_4)\tau_2\sigma_0 + \frac{1}{\sqrt{2}}\Sigma_{14}\tau_0\sigma_2, \\
m_3^{\mathcal{T}^{II}_{2u}} &= -\frac{i}{\sqrt{2}}(\frac{\sqrt{3}}{2}\Sigma_{35} + \frac{1}{2}\Sigma_{34})\tau_2\sigma_0 + \frac{i}{\sqrt{2}}\Sigma_{14}\tau_3\sigma_2,
\end{aligned} \tag{5.21}
$$

for $\mathcal{T}^{II}_{2u}$. Using the parametrization similar to Eq. 5.6, it is straightforward to show that both the triplets ($\mathcal{T}^{x}_{2u}$, $x \in (I, II)$) correspond to non-unitary PDW SCs that break TR, provided $\mathbf{d}^x \times \mathbf{d}^{x*} \neq 0$. However, unlike the triplets discussed above, the present ones are non-unitary even within the TRI subspace and exhibit a multi-gap structure, with the gap magnitudes dependent on $\mathbf{d}^x$. In fact, at isolated points on the TRI

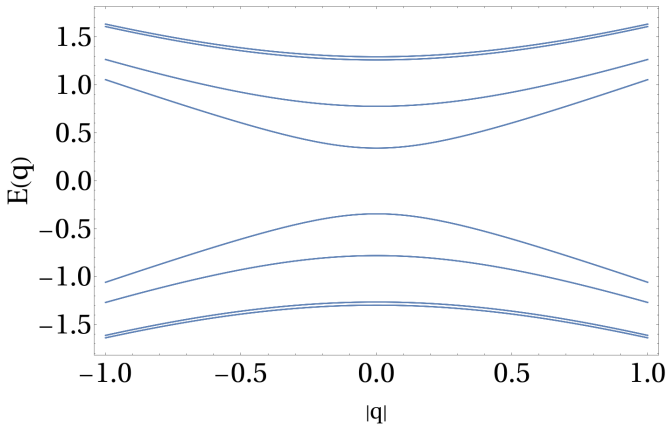

Figure 5.8: Spectrum for $\mathcal{T}_{1u}$ and $\mathcal{T}_{2u}$ Irreps on TRI manifold (for $(|\Delta^{\mathcal{T}_{1u}}| = 1$ or $|\Delta^{\mathcal{T}_{2u}}| = 1)$ for general $\mathbf{d}$ on the TRI manifold, the spectrum is gapped. Shown for $\mathbf{d} = (1/\sqrt{6}, 1/\sqrt{6}, 2/\sqrt{6})$. Eigenvalues depend on $\mathbf{d}$.

sub-space $\mathbf{d}^x = \left(\pm\frac{1}{\sqrt{3}}, \pm\frac{1}{\sqrt{3}}, \pm\frac{1}{\sqrt{3}}\right)$, the smaller of the two gaps go to zero to yield a nodal SC (Fig. 5.8 and 5.9) with the gapless nodes arising from the mixing of the Γ and the M valleys allowed by finite momentum pairing. On moving away from the TRI sub-space, the above isolated gapless points appear to bifurcate, but the full analysis of the fate of these isolated nodal SCs needs to be explored further.

The mean field lattice Hamiltonian has the form similar to Eq. 4.19, with NNN pairing as shown in Fig. 5.10, where the pairing matrices, $\mathcal{X}_{\mathbf{r}\mathbf{r}'}$, corresponding to $m_1^{\mathcal{T}^{I}_{2u}}$ and $m_1^{\mathcal{T}^{II}_{2u}}$ are given by (with reference to Fig. 5.10)

$$
\Sigma_b = i\left(\frac{\sqrt{3}}{2}\Sigma_{14} - \frac{1}{2}\Sigma_{15}\right), \quad \Sigma_a = i\left(\frac{\sqrt{3}}{2}\Sigma_{14} + \frac{1}{2}\Sigma_{15}\right), \tag{5.22}
$$

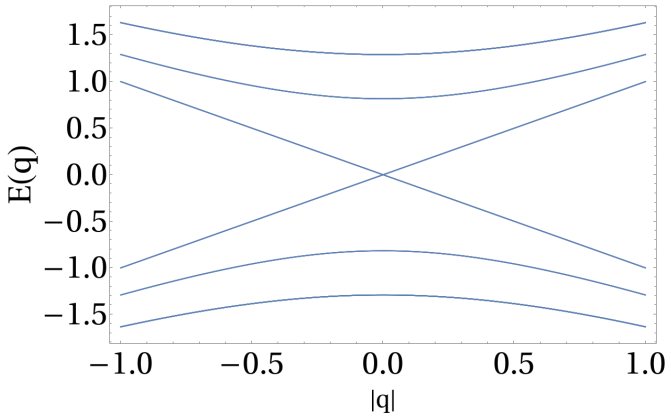

Figure 5.9: Spectrum for $\mathcal{T}_{1u}$ and $\mathcal{T}_{2u}$ Irreps on TRI manifold (for $(|\Delta^{\mathcal{T}_{1u}}| = 1$ or $|\Delta^{\mathcal{T}_{2u}}| = 1)$ where Gapless modes appear at special points $\left(\mathbf{d} = \left(\pm\frac{1}{\sqrt{3}}, \pm\frac{1}{\sqrt{3}}, \pm\frac{1}{\sqrt{3}}\right)\right)$ on the TRI manifold (S^2 in this case).

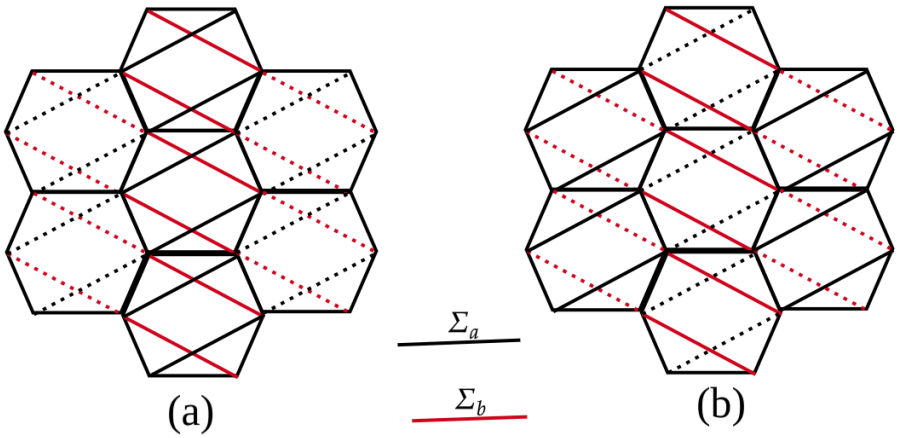

Figure 5.10: (a) Schematic for the NNN pairing for $m_1^{\mathcal{T}_{2u}^I}$ ($m_1^{\mathcal{T}_{2u}^{II}}$) bilinears of the Triplets $\mathcal{T}_{2u}^I$ ($\mathcal{T}_{2u}^{II}$) in global basis. The black (red) colour of connecting lines represents the pairing matrix Σ_a (Σ_b) mentioned in Eq. 5.22 (Eq. 5.23) while dashed lines correspond to -ve of the matrices. (b) Schematic for the NNN pairing for $m_1^{\mathcal{T}_{1u}^I}$ ($m_1^{\mathcal{T}_{1u}^{II}}$) bilinears of the Triplets $\mathcal{T}_{1u}^I$ ($\mathcal{T}_{1u}^{II}$) in global basis with the notation and form of matrices (Σ_a, Σ_b) being same as used in (a) subfigure. For both lattice models, momenta at which the pairing amplitudes oscillate corresponding to M_2 point in the BZ(Fig. 2.1).

and

$$\Sigma_b = i\left(\frac{\sqrt{3}}{2}\Sigma_{15} + \frac{1}{2}\Sigma_{14}\right), \quad \Sigma_a = -i\left(\frac{\sqrt{3}}{2}\Sigma_{15} - \frac{1}{2}\Sigma_{14}\right), \tag{5.23}$$

respectively. The corresponding spin-wave function for the Cooper pair is symmetric and given by

$$\begin{aligned}|\Phi_b\rangle =& \sqrt{\frac{3}{5}}|J_T = 1, m_T = 0\rangle - \sqrt{\frac{3}{20}}|J_T = 3, m_T = 0\rangle \\ &+ \frac{1}{2\sqrt{2}}\left(|J_T = 3, m_T = 2\rangle + |J_T = 3, m_T = -2\rangle\right), \end{aligned} \tag{5.24}$$

$$\begin{aligned}|\Phi_a\rangle =& \sqrt{\frac{3}{5}}|J_T = 1, m_T = 0\rangle - \sqrt{\frac{3}{20}}|J_T = 3, m_T = 0\rangle \\ &- \frac{1}{2\sqrt{2}}\left(|J_T = 3, m_T = 2\rangle + |J_T = 3, m_T = -2\rangle\right), \end{aligned} \tag{5.25}$$

for $\mathcal{T}_{2u}^{I}$, and

$$\begin{aligned}|\Phi_b\rangle =& \frac{2\sqrt{2}}{5}|J_T = 1, m_T = 0\rangle - \frac{\sqrt{2}}{5}|J_T = 3, m_T = 0\rangle \\ &- \sqrt{\frac{3}{5}}\left(|J_T = 3, m_T = 2\rangle + |J_T = 3, m_T = -2\rangle\right), \end{aligned} \tag{5.26}$$

$$\begin{aligned}|\Phi_a\rangle =& \frac{2\sqrt{2}}{5}|J_T = 1, m_T = 0\rangle - \frac{\sqrt{2}}{5}|J_T = 3, m_T = 0\rangle \\ &+ \sqrt{\frac{3}{5}}\left(|J_T = 3, m_T = 2\rangle + |J_T = 3, m_T = -2\rangle\right), \end{aligned} \tag{5.27}$$

for $\mathcal{T}_{2u}^{II}$. The other two components are obtained by symmetry transformations given in Table A.3.

5.1.4 The $\mathcal{T}_{1u}$ triplet superconductors

There are two $\mathcal{T}_{1u}$ ($\mathcal{T}_{1u}^{I}$ and $\mathcal{T}_{1u}^{II}$) triplets that arise in Eq. 3.23 and 3.24, which can be adiabatically connected without breaking further symmetries, and hence represent the same SC. The pairing amplitudes are given by expressions similar to Eq. 5.4 with mass

matrices

$$
\begin{aligned}
m_1^{\mathcal{T}_{1u}^I} &= \frac{1}{\sqrt{2}}\left[(\frac{\sqrt{3}\Sigma_{34}}{2}-\frac{\Sigma_{35}}{2})\tau_0\sigma_2+(\frac{\Sigma_4}{2}-\frac{\sqrt{3}\Sigma_5}{2})\tau_3\sigma_2\right],\\
m_2^{\mathcal{T}_{1u}^I} &= \frac{1}{\sqrt{2}}(\frac{1}{2}\Sigma_4-\frac{\sqrt{3}}{2}\Sigma_5)\tau_2\sigma_0-\frac{1}{\sqrt{2}}\Sigma_{15}\tau_0\sigma_2,\\
m_3^{\mathcal{T}_{1u}^I} &= \frac{i}{\sqrt{2}}(\frac{\sqrt{3}}{2}\Sigma_{34}-\frac{1}{2}\Sigma_{35})\tau_2\sigma_0+\frac{i}{\sqrt{2}}\Sigma_{15}\tau_3\sigma_2.
\end{aligned}
\tag{5.28}
$$

for $\mathcal{T}_{1u}^I$, and

$$
\begin{aligned}
m_1^{\mathcal{T}_{1u}^{II}} &= \frac{1}{\sqrt{2}}\left[(\frac{\sqrt{3}\Sigma_{35}}{2}+\frac{\Sigma_{34}}{2})\tau_0\sigma_2-(\frac{\Sigma_5}{2}+\frac{\sqrt{3}\Sigma_4}{2})\tau_3\sigma_2\right],\\
m_2^{\mathcal{T}_{1u}^{II}} &= \frac{1}{\sqrt{2}}(\frac{1}{2}\Sigma_5+\frac{\sqrt{3}}{2}\Sigma_4)\tau_2\sigma_0-\frac{1}{\sqrt{2}}\Sigma_{14}\tau_0\sigma_2,\\
m_3^{\mathcal{T}_{1u}^{II}} &= -\frac{i}{\sqrt{2}}(\frac{\sqrt{3}}{2}\Sigma_{35}+\frac{1}{2}\Sigma_{34})\tau_2\sigma_0-\frac{i}{\sqrt{2}}\Sigma_{14}\tau_3\sigma_2,
\end{aligned}
\tag{5.29}
$$

for $\mathcal{T}_{1u}^{II}$. The spectrum (on TRI manifold) for this triplet is the same as that of the $\mathcal{T}_{2u}$ triplets in the sense that the number of bands and the gap structure is the same. It should be noticed that for general points in the parameter space, each of the $\mathcal{T}_u$ SC has 8 bands, each band is 4-fold degenerate. Out of them, 8 of the bands become gapless on the special points $\left(\mathbf{d}=\left(\pm\frac{1}{\sqrt{3}},\pm\frac{1}{\sqrt{3}},\pm\frac{1}{\sqrt{3}}\right)\right)$ on TRI manifold. This similarity in the spectrum is also extended to the TRB manifold. The resultant PDW SCs are very similar to the $\mathcal{T}_{2u}$ ones just discussed, albeit with a different lattice symmetry-breaking pattern as indicated by the Irrep. It is evident from the lattice model for $m_1^{\mathcal{T}_{1u}^I}(m_1^{\mathcal{T}_{1u}^{II}})$ shown in Fig. 5.10(b).

5.2 Summary

In the first part of this thesis, we have presented the superconducting phases (Tables 2.1, 2.2 and 2.3) that are naturally proximate the SU(8) DSM that may be realized in honeycomb lattice materials with strong SOC at 1/4th filling. The resultant unconventional SCs differ from the usually studied ones in two aspects– (1) the larger spin representation stemming from the $j=3/2$ orbitals, and (2) non-trivial implementation of the microscopic symmetries due to the SOC-induced mixing of spin and real spaces. As a result, the different SC phases proximate to the SU(8) DSM are very different from

that of graphene [114] even though the microscopic symmetries and the lattice structures are the same. Indeed, the larger spin representation facilitates substantially generalizes (compared to $S = 1/2$ [10, 115], and the discussion of $j = 1/2$ spin-orbit coupled fermions presented in Appendix. A.8) the scope of the interplay between the *spin* and superconducting pairing channels to realize various unconventional SCs. While superconductivity in higher spin-representations, arising due to strong SOC, is well known in several rare earth and actinide compounds [10, 96–99, 116], the SOC concomitantly is responsible for lowering the symmetry in such materials distinguishing them from the present study.

Chapter 6

Z_2 Fractionalized Phases

This chapter is based on our work that is to be submitted for publication. This was done in collaboration with Subhro Bhattacharjee and Sergej Moroz.

6.1 Introduction

After examining the symmetry implementation for spin-orbit coupled systems, we now turn to a setting in which electrons are fractionalized. Fractionalization offers a framework for describing long-range entangled phases such as quantum spin liquids [5], the fractional quantum Hall effect [12], and orthogonal metals [61]. Among the various ways electrons can fractionalize, a particularly insightful and tractable scenario occurs when the electron fractionalizes into a fermion and an Ising spin degree of freedom [61–64, 117]. This fractionalization scheme provides a useful framework to explore the interplay between fermionic statistics and discrete gauge structures in long-range entangled phases. A central example of such fractionalized phases is the orthogonal metal [61] phase, a paradigmatic fractionalized metallic phase in which the electron decomposes into a fermion and an Ising spin [61, 118]. In this phase, the gauge-invariant fermion is gapped, yet transport persists via the fractionalized fermions [61, 62].

This fractionalization leads to a Z_2 gauge structure in the theory, resulting in the projective implementation of microscopic symmetries. In the first part of this chapter, we will look at the projective realization of microscopic symmetries for such Z_2 fractionalized metal. Specifically, we consider a model of Ising spins and fermions minimally coupled to a Z_2 gauge field on the square lattice, which arises from the fractionalization of the electron. We focus on the regime corresponding to the deconfined phase of the gauge field. In this regime, the Ising sector corresponds to the frustrated transverse-field Ising model on the square lattice, which undergoes an order-

to-disorder transition described by the 3D XY^* universality class. Meanwhile, the fermionic sector reduces to fermions hopping on a square lattice with a background π-flux. At half-filling of fermions, the resulting low-energy description is given by Dirac theory. We analyze this low-energy theory to identify the leading gauge-invariant, symmetry-allowed couplings between the fermionic and Ising fields, which determine the fate of the fermions once the Ising spins condense in the ordered phase. This requires understanding how the low-energy degrees of freedom transform under the microscopic symmetries of the square lattice.

6.2 Model

We begin with the following fractionalization,

$$c_{i\alpha} = \tau_i^x f_{i\alpha} \tag{6.1}$$

where the fermions, $f_{i\alpha}^\dagger$ create both electronic charge and spin, the Ising field, τ_i^z counts the parity of electron occupancy at the ith site such that it detects the presence of spin moments [119]. This role of the Ising field is clear from the constraint given by

$$(n_i - 1)^2 = \frac{1 + \tau_i^z}{2}, \tag{6.2}$$

where n_i is the electron occupancy at the ith site. Therefore, τ_i^x changes the fermion parity. Under the global electronic charge U(1) and spin SU(2) transformations, we get

$$f_{i\alpha} \to e^{i\theta} f_{i\alpha} \quad \text{and} \quad f_{i\alpha} \to \mathcal{U}_{\alpha\beta} f_{i\beta} \quad \text{where } \mathcal{U} \in \text{SU(2)} \tag{6.3}$$

while,

$$\tau_i^\zeta \to \tau_i^\zeta, \ \ \zeta \in (x, y, z) \tag{6.4}$$

under both. The above parton representation is invariant under Z_2 gauge transformation :

$$\tau_i^x \to \epsilon_i \tau_i^x \qquad f_{i\alpha} \to \epsilon_i f_{i\alpha} \qquad \text{with} \quad \epsilon_i = \pm 1 \tag{6.5}$$

Therefore, both τ^x and f_α carry a Z_2 gauge charge and hence minimally couple to the Z_2 gauge field, $\sigma_{ij}^z = \pm 1$ defined on the links of the lattice. For this thesis, we will be considering the fractionalization of spinless fermions (c_i) on the square lattice, so we will not be keeping the spin index on the fermions. The low energy effective theory of

the fractionalized degree of freedom minimally coupled [1]

to Z_2 gauge field is given by [61,64],

$$\mathcal{H} = \mathcal{H}_\tau + \mathcal{H}_f + \mathcal{H}_\sigma \tag{6.6}$$

where

$$\mathcal{H}_\tau = -J \sum_{\langle ij \rangle} \tau_i^x \sigma_{ij}^z \tau_j^x - \Gamma \sum_i \tau_i^z \tag{6.7}$$

This term corresponds to Ising spin minimally coupled to Z_2 gauge field with a transverse field.

$$\mathcal{H}_f = -t \sum_{\langle ij \rangle} f_i^\dagger \sigma_{ij}^z f_j - \mu \sum_i f_i^\dagger f_i \tag{6.8}$$

This term corresponds to fermions hopping on square lattice and minimally coupled to Z_2 gauge fields.

$$\mathcal{H}_\sigma = -\kappa \sum_\square \prod_{\langle ij \rangle \in \square} \sigma_{ij}^z - h \sum_{\langle ij \rangle} \sigma_{ij}^x \tag{6.9}$$

This term represents the Z_2 gauge theory which captures the dynamics of the gauge fields (σ^α) [65]. The first term is the product of σ^z operators around a plaquette of the square lattice (Fig. 6.1), and σ_{ij}^x corresponds to the electric field. The Gauss's law is given by

$$\prod_{j \in i} \sigma_{ij}^x = (-1)^{\frac{1-\tau_i^z}{2} + f_i^\dagger f_i}, \tag{6.10}$$

where the product is over the bonds connected to ith site (Fig. 6.1). Above Hamiltonian can also be written using gauge invariant degree of freedom. Introduce the gauge invariant degrees of freedom :

$$Z_{ij} = \tau_i^x \sigma_{ij}^z \tau_j^x; \qquad X_{ij} = \sigma_{ij}^x \tag{6.11}$$

[1] Minimal coupling of a Z_2 gauge field refers to the lowest-order gauge-invariant term that introduces a discrete Z_2 gauge coupling to matter. For a matter field ψ_i on lattice sites i and a Z_2 gauge field $\sigma_{ij} = \pm 1$ on links $\langle ij \rangle$, this typically replaces a hopping term $t\psi_i^\dagger \psi_j$ with $t\psi_i^\dagger \sigma_{ij} \psi_j$, ensuring invariance under the local gauge transformation $\psi_i \to \eta_i \psi_i$, $\sigma_{ij} \to \eta_i \sigma_{ij} \eta_j$ with $\eta_i = \pm 1$.

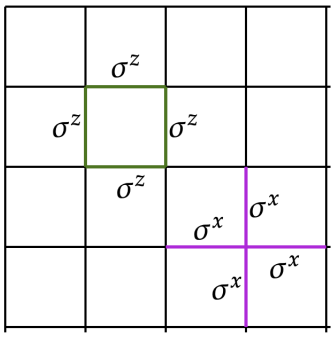

Figure 6.1: Schematic diagram representing the plaquette term $\prod_{\langle ij\rangle\in\square}\sigma^z_{ij}$ and Star term $\prod_{j\in i}\sigma^x_{ij}$,

on the bonds along with the electrons in Eq. 6.1 to re-write Eq. 6.6 as :

$$\mathcal{H}_\tau = -J\sum_{\langle ij\rangle} Z_{ij} - \Gamma\sum_i \left[\prod_{j\in i} X_{ij}\right](-1)^{c_i^\dagger c_i} \tag{6.12}$$

where we have used the Gauss's law (Eq. 6.10) and

$$\mathcal{H}_f = -t\sum_{\langle ij\rangle} c_i^\dagger Z_{ij} c_j - \mu\sum_i c_i^\dagger c_i \tag{6.13}$$

$$\mathcal{H}_\sigma = -\kappa\sum_{\square}\prod_{\langle ij\rangle\in\square} Z_{ij} - h\sum_{\langle ij\rangle} X_{ij} \tag{6.14}$$

Now that we have defined the model, we focus on a particular limit corresponding to the deconfined phase of the Z_2 gauge theory, which will be discussed in the following section.

6.3 Deconfined Phase

We are interested in the regime that corresponds to the deconfined phase of the Z_2 gauge theory (Eq. 6.9). This phase is accessed by setting $h = 0$ in Eq. 6.9, which leads to the following Hamiltonian,

$$\mathcal{H} = -J\sum_{\langle ij\rangle}\tau_i^x\sigma_{ij}^z\tau_j^x - \Gamma\sum_i\tau_i^z - t\sum_{\langle ij\rangle} f_i^\dagger\sigma_{ij}^z f_j - \mu\sum_i f_i^\dagger f_i - \kappa\sum_{\square}\prod_{\langle ij\rangle\in\square}\sigma_{ij}^z \tag{6.15}$$

along with the Gauss's law given by Eq. 6.10. It's gauge invariant form is

$$\mathcal{H} = -J\sum_{\langle ij\rangle} Z_{ij} - \Gamma\sum_i \left[\prod_{j\in i} X_{ij}\right](-1)^{c_i^\dagger c_i} - t\sum_{\langle ij\rangle} c_i^\dagger Z_{ij} c_j - \mu\sum_i c_i^\dagger c_i - \kappa\sum_{\square}\prod_{\langle ij\rangle\in\square} Z_{ij} \tag{6.16}$$

In this case, the product of Z_{ij}, around a plaquette, $B_p = \prod_{\langle ij\rangle\in\square_p} Z_{ij} = \prod_{\langle ij\rangle\in\square_p}\sigma^z_{ij}$, is conserved and is static, *i.e.*,

$$[\mathcal{H}, B_p] = 0 \quad \forall B_p. \tag{6.17}$$

Phrased in the modern language, the model enjoys magnetic 1-form symmetry generated by closed Wilson loops $W = \prod_C Z$. For $J = 0$ and $t = 0$, all states that comprise the same $\{B_p\}$ sector are degenerate. In this case, the ground state lies in

$$B_p = \begin{cases} +1 & \forall\ p \quad \text{If } \kappa > 0 \\ -1 & \forall\ p \quad \text{If } \kappa < 0 \end{cases} \tag{6.18}$$

The former corresponds to 0-flux while the latter corresponds to π-flux. For $\kappa > 0$ and $J = 0$, this is exactly solvable [61] with the ground state being given by [64, 117],

$$|\Psi_{GS}\rangle = \prod_i \frac{1+\tilde{A}_i}{2}|0\rangle \otimes |FS, \nu\rangle \tag{6.19}$$

where $|0\rangle$ denotes all bond spins pointing up, $Z_{ij} = +1 \quad \forall\langle ij\rangle$ and $|FS, \nu\rangle$ is the free fermi surface state for the c-fermions corresponding to the all up state at filling ν. The above construction can be extended to arbitrary flux sectors as indicated in Ref. [117]. Also, $\tilde{A}_i = \left[\prod_{j\in i} X_{ij}\right](-1)^{c_i^\dagger c_i}$ is the modified projection operator for the zero $e-$charge sector [2]. For the above wave function, $\langle\Psi_{GS}|\tau_i^x|\Psi_{GS}\rangle = 0 \quad \forall\ i$ whereas one can create a set of gapless fermionic excitations. This state therefore represents the orthogonal metal [61, 64]. As one tunes J, there is transition from orthogonal metal phase to metal phase which are studied a lot in recent years [61–64]. We are interested in the limit $\kappa \to -\infty$, in which $B_p = -1$. In Eq. 6.15, this leads to a frustrated transverse-field Ising model for the Ising spins and a background π-flux for fermions hopping on the square lattice. In this case, the disordered phase of the frustrated transverse-field Ising model corresponds to the orthogonal semi-metal phase [64, 117]. We investigate what happens to fermions as we tune the Ising model from the disor-

[2] at ν=0, it reduces to the ground state of Toric code, where zero electric charge sector is defined as $\prod_{j\in i} X_{ij}|\Psi_{GS}\rangle = |\Psi_{GS}\rangle \quad \forall\ i$ [5].

dered to the ordered phase. For that, we examine the corresponding low-energy field theory of the model, which we discuss below.

6.4 Field Theory Analysis

In this section, we perform a field-theoretic analysis of the model given in Eq. 6.15 in the limit $\kappa \to -\infty$ and $h = 0$, which fixes the π-flux background for the fermions (f) and Ising spin (τ^x).

6.4.1 Fermionic Field Theory

Let us start with the fermionic hopping term at half filling ($\mu = 0$),

$$H_f = -t \sum_{\langle ij \rangle} f_i^\dagger \sigma_{ij}^z f_j \tag{6.20}$$

To incorporate the π-flux constraint, we will work with the following gauge choice

$$\sigma_{i,i+\hat{x}}^z = 1 \quad , \quad \sigma_{i,i+\hat{y}}^z = (-1)^{i_x}. \tag{6.21}$$

Hamiltonian in Eq. 6.20 becomes,

$$H_f = -t \sum_i \left(f_i^\dagger f_{i+\hat{x}} + (-1)^{i_x} f_i^\dagger f_{i+\hat{y}} + h.c. \right). \tag{6.22}$$

Working with a particular gauge choice results in a projective implementation of microscopic symmetries, that is, microscopic symmetries accompanied by a gauge transformation keep the Hamiltonian invariant. In momentum space, Hamiltonian has the form,

$$H_f = -t \sum_{\mathbf{k}} \begin{bmatrix} f_{\mathbf{k}}^\dagger & f_{\mathbf{k}+\pi\hat{x}}^\dagger \end{bmatrix} \begin{bmatrix} 2\cos(k_x) & 2\cos(k_y) \\ 2\cos(k_y) & -2\cos(k_x) \end{bmatrix} \begin{bmatrix} f_{\mathbf{k}} \\ f_{\mathbf{k}+\pi\hat{x}} \end{bmatrix} \tag{6.23}$$

Here, $k_x \in (-\pi/2, \pi/2)$ and $k_y \in (-\pi, \pi)$[3] and band dispersion is given by,

$$E_f(\mathbf{k})_\pm = \pm 2t \sqrt{\cos^2(k_x) + \cos^2(k_y)} \tag{6.24}$$

[3] we are taking lattice spacing, a=1

The two band touches linearly at the two Dirac points in the brillouin zone at,

$$\mathbf{k}_L = (\pi/2, \pi/2) \quad , \quad \mathbf{k}_R = (\pi/2, -\pi/2) \tag{6.25}$$

At half filling, the low energy theory derived in the vicinity of Dirac cones takes the following form,

$$H_f^{linearize} = -2t \int d^2\mathbf{x} \;\; \psi^\dagger(\mathbf{x}) \left(\alpha_x(-i\partial_x) + \alpha_y(-i\partial_y)\right) \psi(\mathbf{x}) \tag{6.26}$$

where, the Dirac spinor has the following form,

$$\psi(\mathbf{x}) = \begin{bmatrix} \psi_{\mathbf{k_L},1} & \psi_{\mathbf{k_L},2} & \psi_{\mathbf{k_R},1} & \psi_{\mathbf{k_R},2} \end{bmatrix}^T \tag{6.27}$$

here, $\mathbf{k_L}$ and $\mathbf{k_R}$ are the valley indices whereas $(1, 2)$ are the subband indices. The form of Dirac matrices (α_x, α_y) is given by

$$\alpha_x = \tau_0\sigma_3 \quad , \quad \alpha_y = \tau_3\sigma_1 \tag{6.28}$$

here, τ and σ are 2-dimensional Identity and Pauli matrices which acts on valley and subband sector respectively.

6.4.2 Ising Field Theory

Now we consider the Ising part of the Hamiltonian,

$$H_\tau = -J \sum_{\langle ij \rangle} \tau_i^x \sigma_{ij}^z \tau_j^x + \Gamma \sum_i \tau_i^z. \tag{6.29}$$

For this, we choose the same gauge fixing as mentioned in Eq. 6.21. We are working with a 2-site unit cell as shown in Fig. 6.2, such that in momentum space, the interaction part of the Hamiltonian has the following form,

$$H_\tau = J \sum_{\mathbf{k}} \begin{bmatrix} \tau_A(\mathbf{k}) & \tau_B(\mathbf{k}) \end{bmatrix} \begin{bmatrix} -2\cos(k_y) & -(1+e^{2ik_x}) \\ -(1+e^{-2ik_x}) & 2\cos(k_y) \end{bmatrix} \begin{bmatrix} \tau_A(-\mathbf{k}) \\ \tau_B(-\mathbf{k}) \end{bmatrix}, \tag{6.30}$$

where $k_x \in (-\pi/2, \pi/2)$ and $k_y \in (-\pi, \pi)$.

The eigenvalues of the above Hamiltonian are given by,

$$E_\tau(\mathbf{k})_\pm = \pm 2J\sqrt{\cos^2(k_x) + \cos^2(k_y)}. \tag{6.31}$$

Extremal eigenvalues occur at $(k_x, k_y) = (0, 0)$ and $(0, \pi)$.

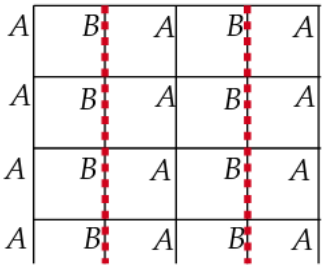

Figure 6.2: Schematic diagram for the choice of gauge to implement the π-flux condition (Eq. 6.45). The dashed (solid) red (black) bonds correspond to $\sigma^z_{ij} = -1$ $(+1)$.

The soft mode expansion about these momenta provides us with two soft mode fields (ϕ_1,ϕ_2) (see [120, 121]) and the soft mode expansion is given by,

$$\begin{bmatrix} \tau_A(x,y) \\ \tau_B(x,y) \end{bmatrix} = \phi_1 \begin{bmatrix} 1+\sqrt{2} \\ 1 \end{bmatrix} + \phi_2\, e^{i\pi y} \begin{bmatrix} 1 \\ 1+\sqrt{2} \end{bmatrix}. \tag{6.32}$$

The low-energy effective field theory governing the order-to-disorder transition is captured by the 3D XY model [67]:

$$H_\tau = \int d^2\mathbf{x} \Big[(\partial_\mu \phi)^T (\partial_\mu \phi) + m^2 \phi^T \phi + u_2 (\phi^T \phi)^2 + u_3 (\phi^T \phi)^3 + u_4 (\phi^T \phi)^4 + \lambda (\phi^T \beta_3 \phi)^2 (\phi^T \beta_1 \phi)^2 \Big]. \tag{6.33}$$

Here, $\phi = (\phi_1, \phi_2)^T$, the λ term is dangerously irrelevant [122] and $\beta_{\alpha=1,3}$ are two-dimensional Pauli matrices. Section. 6.7.1 discusses the order-to-disorder transition using the Gauge-Invariant form of the Hamiltonian (Eq. 6.16).

6.4.3 Coupling term

The leading order gauge-invariant coupling between the Ising modes and Dirac fermions is given by

$$H_{f\tau} = \int d^2\mathbf{x} \left(\sum_{\alpha,\gamma} \left(\phi^T \beta_\alpha \phi \right) \left(\psi^\dagger M^\gamma \psi \right) \right), \tag{6.34}$$

where β_α are the two-dimensional Pauli matrices (for our case, β_1 and β_3) and M^γ are 4×4 matrices. If M^γ anticommutes with the Dirac matrices (Eq. 6.28), condensation of ϕ would gap out the Dirac fermions in the presence of the quartic interactions described above. To analyze this, we examined the symmetry transformations of Dirac bilinears of the form $\psi^\dagger M^\gamma \psi$, where M^γ is a mass matrix. We also considered the same

for the Ising soft modes, whose quadratic terms take non-zero expectation values in the ordered phase when the Ising field condenses; these are $\phi^T \beta_1 \phi$ and $\phi^T \beta_3 \phi$.

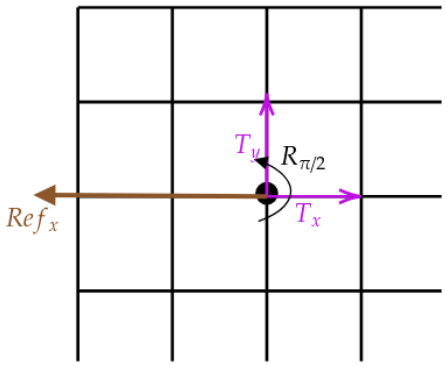

Figure 6.3: Lattice transformation: Transformation $R_{\pi/2}$ is the rotation by $\pi/2$ amount about the origin. T_x (and T_y) are translations by unit lattice distance in x-(and y-) direction respectively. Ref_x corresponds to reflection about y=0 axis.

The symmetry group considered in this analysis consists of translations on the square lattice (T_x, T_y), the point-group symmetries of the square lattice (Fig. 6.3), and time-reversal symmetry. Due to gauge fixing, these symmetries act projectively on the Dirac spinors. Knowing the transformation properties of the spinors, discussed in detail in Appendix B.1, we then determine the corresponding transformation properties of the Dirac bilinears. Table 6.1 shows the symmetry analysis of the mass terms.

	$\psi^\dagger M \psi$	T_x	T_y	$R_{\pi/2}$	Ref_x	Time Reversal
M_1	$\psi^\dagger (\tau_0 \sigma_2) \psi$	-M_1	M_1	-M_2	M_1	M_1
M_2	$\psi^\dagger (\tau_2 \sigma_1) \psi$	M_2	-M_2	M_1	-M_2	M_2
M_3	$\psi^\dagger (\tau_3 \sigma_2) \psi$	M_3	M_3	M_3	-M_3	-M_3
M_4	$\psi^\dagger (\tau_1 \sigma_1) \psi$	-M_4	-M_4	M_4	M_4	M_4

Table 6.1: **Classification of Mass:** This table presents the classification of four mass terms. There is one two-dimensional representation, (M_1, M_2), which corresponds to stripy ordering of fermions on the lattice. There are also two singlets: M_3, which describes a Chern insulator, and M_4, which corresponds to a staggered charge density wave on the lattice.

For the Ising case, we examined the transformation properties of the following quadratic operators, which correspond to order parameters that acquire non-zero values in the ordered phase of the frustrated Ising model:

$$(O_1^\tau, O_2^\tau) = \left(\phi^T \beta_1 \phi,\ \phi^T \beta_3 \phi\right). \tag{6.35}$$

These operators correspond to the columnar/plaquette ordering of dimers on the lattice, as discussed in Sec. 6.7.1. Knowing the symmetry transformations of the soft

modes (ϕ_1, ϕ_2), as listed in Table B.1, we derived the corresponding symmetry transformations of these order parameters, which are summarized in the following table 6.2. There does not exist any gauge-invariant, symmetry-allowed quartic cou-

O^τ	T_x	T_y	$R_{\pi/2}$	Ref_x	Time Reversal
O_1^τ	O_1^τ	-O_1^τ	O_2^τ	O_1^τ	O_1^τ
O_2^τ	- O_2^τ	O_2^τ	O_1^τ	O_2^τ	O_2^τ

Table 6.2: Table of symmetry transformations of the order parameters for the frustrated transverse field Ising model, which corresponds to columnar ordering of dimers on the dual lattice [3].

pling that generates a mass term for the Dirac fermions as the Ising field condenses. This implies that the fermions remain gapless in the ordered phase of the frustrated Ising model, resulting in a semi-metallic phase that breaks lattice symmetries [64]. One way to understand this is through the gauge-invariant form of the Hamiltonian (Eq. 6.16): in the limit where the Ising spins are ordered, the fermions hop on the lattice in the background of a dimer configuration. The hopping amplitude is provided by Z_{ij}, which depends on the underlying configuration. Due to this symmetry-broken background, the fermions also break lattice symmetry. To characterize the symmetry breaking of the fermions, we construct order parameters for the gauge-invariant fermions, which acquire non-zero expectation values in the ordered phase of the Ising model. For this purpose, we define the following operators:

$$O^c(\mathbf{n}, \mathbf{q}) = \sum_{\mathbf{r_i}} \left(e^{i\mathbf{r}\cdot\mathbf{q}} c_{\mathbf{r}}^\dagger c_{\mathbf{r}+\mathbf{n}} + h.c. \right) \tag{6.36}$$

In momentum space, the operator takes the form

$$O^c(\mathbf{n}, \mathbf{q}) = \sum_{\mathbf{k}} \left(e^{i\mathbf{n}\cdot(\mathbf{q}+\mathbf{k})} c_{\mathbf{k}}^\dagger c_{\mathbf{k}+\mathbf{q}} + \text{h.c.} \right). \tag{6.37}$$

These operators are constructed analogously to the order parameters for the ordered phase of the frustrated transverse-field Ising model [123]. We now examine the order parameters that characterize the symmetry breaking of the fermions in the ordered phases of the Ising model. These operators transform under the microscopic symmetries in the same way as the Ising order parameters and are defined as:

$$O_1^c = O^c(\mathbf{n} = (0,1), \mathbf{q} = (\pi, 0)) = \sum_{\mathbf{k}} \left(e^{ik_y} c_{\mathbf{k}}^\dagger c_{\mathbf{k}+\pi\hat{\mathbf{x}}} + \text{h.c.} \right) \tag{6.38}$$

$$O_2^c = O(\mathbf{n} = (1,0), \mathbf{q} = (0, \pi)) = \sum_{\mathbf{k}} \left(e^{ik_x} c_{\mathbf{k}}^\dagger c_{\mathbf{k}+\pi\hat{\mathbf{y}}} + \text{h.c.} \right). \tag{6.39}$$

Examining the symmetry table for O_1^c and O_2^c (see Appendix B.3 for details), their transformation properties are summarized as

O^c	T_x	T_y	$R_{\pi/2}$	Ref_x	Time Reversal
O_1^c	$-O_1^c$	O_1^c	O_2^c	O_1^c	O_1^c
O_2^c	O_2^c	$-O_2^c$	O_1^c	O_2^c	O_2^c

(6.40)

Both order parameters transform identically to the Ising order parameters and develop non-zero expectation values in the ordered phase, as illustrated in Fig. 6.4 [4]. An-

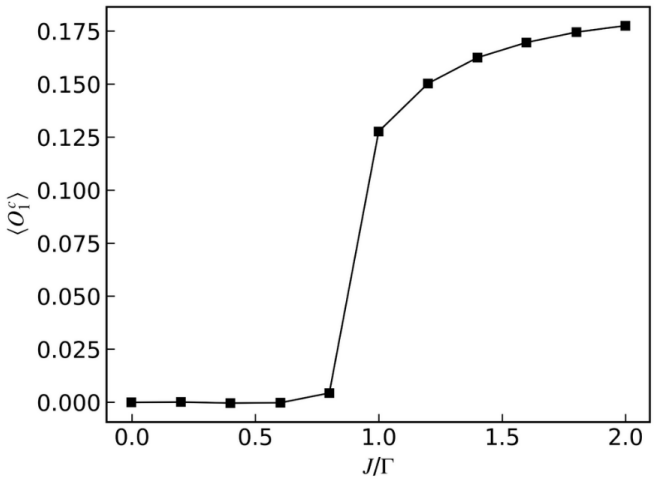

Figure 6.4: Plot of the expectation value of the order parameter O_1^c, obtained from iDMRG simulations on a cylinder of circumference four sites with bond dimension $\chi = 410$, $\kappa = -4$, $\Gamma = 0.50$, and $t = 0.20$. This order parameter takes a non-zero value in the ordered phase of the Ising model, which corresponds to large J/Γ. For a detailed discussion of the order-disorder transition in the frustrated transverse field Ising model, see Section 6.7.1.

other way to understand why this semimetal breaks lattice symmetries in this phase is via the Luttinger theorem. Tuning Γ such that $\Gamma/J \gg 1$ drives a transition to a semi-metallic phase with topological order, known as an orthogonal semimetal [64]. According to the theorem, the phase with $\Gamma/J \ll 1$ can remain semimetallic only if it breaks translational symmetry by doubling the unit cell [64]. This provides insight into the phase and completes our discussion of the implementation of microscopic symmetries in the case of fractionalized metals.

However, if we consider the gauge-invariant form of the model in Eq. 6.16, the model provides an avenue to realize both the physics of dimers and that of topologically ordered phases. We analyzed the model in the absence of fermions and supplemented it with a term that yields the phase diagram shown in Fig. 6.7. Before presenting those results, we start with a general introduction to dimer physics and

[4] *This plot was generated by Sergej Moroz.*

topologically ordered phases, and then show how Eq. 6.16 forms an ultimate platform to realize these phases.

6.5 Dimer Model and Toric Code

Quantum Dimer Models (QDMs) on lattices provide paradigmatic examples of unconventional phases and phase transitions, including long-range entangled liquid phases [124–127]. They are expected to arise in frustrated spin-1/2 antiferromagnets, where the spins locally minimize energy by forming spin singlets (dimers) such that the low-energy physics is dominated by the quantum dynamics of these dimers [5, 128]. Central to the richness of QDMs is the fact that the dimer Hilbert space does not have a tensor product structure, arising from the constraint that each spin can be part of only one dimer at a time, *i.e.*, if $n_{IJ}(=0,1)$ denotes the dimer number on a bond connecting sites I and J on a lattice, then we must have

$$\sum_{J\in I} n_{IJ} = 1, \quad \forall\, I, \tag{6.41}$$

where $J \in I$ refers to the summation over all sites J connected to I on the lattice under consideration. The typical dimer dynamics maintaining these constraints are encapsulated in the intensely studied paradigmatic Rokhsar-Kivelson (RK) type QDM Hamiltonians [71]

$H_{\text{Dimer}} = -\Gamma \sum$ 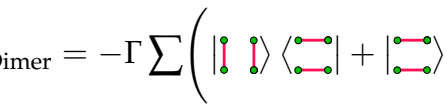 $+\, \Omega \sum$. (6.42)

Here, the first (second) term provides kinetic (potential) energy to the dimers. The phase diagram of RK Hamiltonians has been intensely studied on various lattices; in two dimensions, they typically feature an extended Z_2 topological liquid phase on non-bipartite lattices along with dimer crystal phases (valence bond solids) [124]. On bipartite lattices, the liquid phase is fine-tuned to the special RK point, $\Gamma = \Omega$, where the ground state is given by an equal superposition of all dimer coverings [124]. Indeed, the constraint in Eq. 6.41 is akin to Gauss's law of electrodynamics, albeit for Ising variables, and forms the starting point for mapping the RK Hamiltonian to an odd Ising gauge theory [129], where the liquid phase corresponds to the deconfined (Coulomb) phase of the gauge theory, while the dimer crystals correspond to confined (magnetic-Higgs) phases.

A somewhat different microscopic setting that realizes the Z_2 topological liquid in two dimensions is the Toric code Hamiltonian [1], which, unlike the dimer model, is

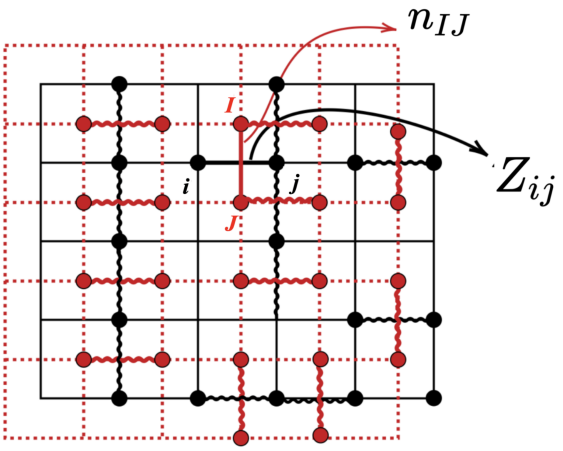

Figure 6.5: Schematic diagram of direct square lattice (lattice represented by dotted red bonds) and dual square lattice (lattice represented by solid black bonds). The black curly (solid) bonds represents value of Ising variable $Z = -1(Z = +1)$ on that bond of dual lattice. The red bonds with curly(or dotted) lines represents presence(or absence) of dimer that bond of direct square lattice. The relation between the dimer occupancy(n_{IJ}) and value of Z are related, considering the $\langle ij \rangle$ (and $\langle IJ \rangle$) bonds as shown in figure on dual (or direct) square lattice, the dimer occupancy (n_{IJ}) is related to value of Ising variable Z_{IJ} on dual lattice by the relation, $n_{IJ} = \frac{1}{2}(1 - Z_{ij})$.

described in terms of spin-1/2s living on the bonds of the square lattice and described by the Hamiltonian

$$\mathcal{H}_{\text{TC}} = -\kappa \sum_{\square} \prod_{\langle ij \rangle \in \square} Z_{ij} - \Gamma \sum_{i} \left[\prod_{j \in i} X_{ij} \right], \tag{6.43}$$

where Z_{ij}, X_{ij}, and Y_{ij} are bond spins obeying the Pauli algebra. While the system no longer has spin-rotation symmetry, the ground state can be obtained exactly since the two sets of terms (stabilizers) in the above Hamiltonian commute. The two kinds of gapped bosonic excitations—magnetic and electric—are obtained by violating the first and second stabilizers respectively [5]. These excitations see each other as sources of π-flux.

6.6 The generalized Hamiltonian

We obtain the generalized model starting from the Quantum Dimer Model (QDM) in Eq. 6.42 on a square lattice — in particular, considering the dimer model on the square lattice drawn with red dotted lines in Fig. 6.5. To each bond (where the dimer resides) we assign an Ising spin $Z_{ij} = \pm 1$, where ij refers to the uniquely associated bond of

the dual square lattice (in black) with sites i and j, such that

$$n_{IJ} = \frac{1 - Z_{ij}}{2}. \tag{6.44}$$

The single dimer constraint (Eq. 6.41), in terms of the Ising fields, becomes

$$\sum_{\langle ij \rangle \in \square} Z_{ij} = 2, \tag{6.45}$$

where the sum is over each dual square plaquette enclosing one site of the direct lattice.

The QDM Hamiltonian (Eq. 6.42), expressed in terms of the Ising spins with the constraint Eq. 6.45, reads (see appendix B.4)

$$\mathcal{H}_{Dimer} = -\Gamma \sum_i \left[\prod_{j \in i} X_{ij} \right] + \frac{\Omega}{4} \sum_i \left[(1 - Z_{i-\hat{x},i})(1 - Z_{i+\hat{x},i}) + (1 - Z_{i-\hat{y},i})(1 - Z_{i+\hat{y},i}) \right], \tag{6.46}$$

where X_{ij} (as defined below Eq. 6.43) anticommutes with Z_{ij} and causes spin flips.

The constraint in Eq. 6.45 is implemented by adding an energy-cost term to the Hamiltonian:

$$\mathcal{H}_{\text{constraint}} = -\kappa \sum_{\square} \prod_{\langle ij \rangle \in \square} Z_{ij} - J \sum_{\langle ij \rangle} Z_{ij}, \tag{6.47}$$

where the first term, in the limit $\kappa \to -\infty$, enforces

$$\prod_{\langle ij \rangle \in \square} Z_{ij} = -1, \tag{6.48}$$

per plaquette of the dual lattice, which, via Eq. 6.44, corresponds to having one or three dimers per site of the direct lattice. The second term, with $J > 0$, lifts the degeneracy in favor of one dimer per site. Note that it is important to keep the ratio $\kappa/J \to -\infty$, and thus the order of limits matters.

This leads to the generic spin-1/2 Hamiltonian

$$\begin{aligned} \mathcal{H} = H_{Dimer} + H_{\text{constraint}} = &-\kappa \sum_{\square} \prod_{\langle ij \rangle \in \square} Z_{ij} - \Gamma \sum_i \left[\prod_{j \in i} X_{ij} \right] - J \sum_{\langle ij \rangle} Z_{ij} \\ &+ \frac{\Omega}{4} \sum_i \left[(1 - Z_{i-\hat{x},i})(1 - Z_{i+\hat{x},i}) + (1 - Z_{i-\hat{y},i})(1 - Z_{i+\hat{y},i}) \right], \end{aligned} \tag{6.49}$$

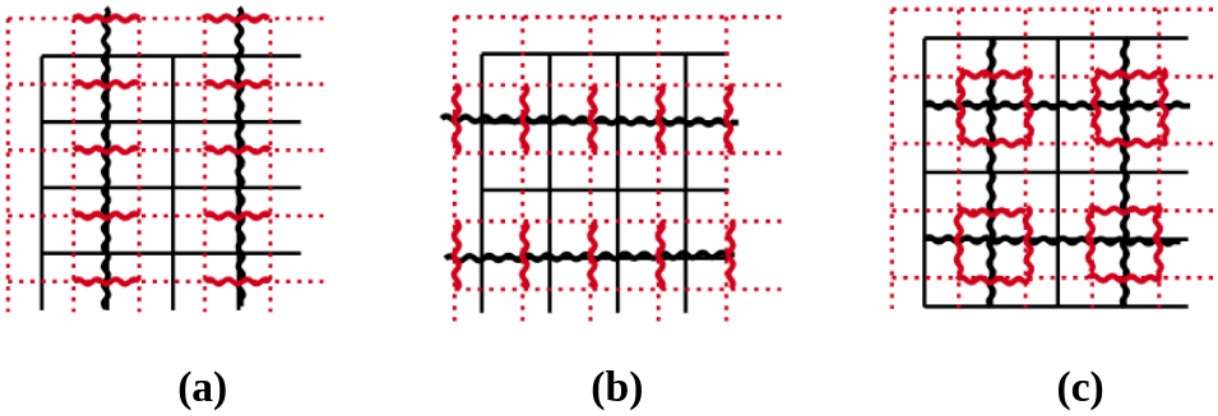

Figure 6.6: Schematic diagram of possible columnar and plaquette configurations: The black solid (red dotted) lattice denotes the dual (direct) lattice, while red (black) curly bonds indicates that the expectation value of dimer occupancy, $\langle n_{IJ} \rangle$ (and $\langle Z_{ij} \rangle$ on associate bond of dual lattice) is different from that on other bonds, and results in (a) Vertical columnar ordering of dimer order. (b) Horizontal columnar ordering of dimer order. (c) Plaquette ordering of dimers.

which interpolates between the dimer limit discussed above and the Toric code, with the latter obtained in the limit $J = \Omega = 0$. Here, we emphasize that for $\Omega = 0$, this Hamiltonian reduces to that given in Eq. 6.16 at zero fermion filling. Notably, in the dimer limit ($J \to \infty, \kappa \to -\infty$), the point $\Gamma = \Omega = 0$ corresponds to the classical dimer model with a macroscopically degenerate ground state manifold.

The Toric code, however, unlike the normally discussed case, is described by the ground state conditions

$$\prod_{\langle ij \rangle \in \square} Z_{ij} = -1, \quad \forall \square, \tag{6.50}$$

and

$$\prod_{j \in i} X_{ij} = +1, \quad \forall i, \tag{6.51}$$

where for the remainder of this chapter, we take $\Gamma > 0$. We call this the *odd* Toric code [64], since each electric charge experiences a π-flux when traversing a closed contour enclosing an odd number of plaquettes.

We shall study the above Hamiltonian in the limit $\kappa \to -\infty$, while relaxing the constraint of large J, keeping it positive along with Ω and Γ. In this limit, the general topology of the phase diagram, schematically plotted in Fig. 6.7 as a function of Γ/J and Ω/J, becomes clear. The $\Omega/J, \Gamma/J \ll 1$ region reflects the dimer physics. In this regime, for $\Gamma/\Omega > 1$, the kinetic term of the dimer model dominates, resulting in the

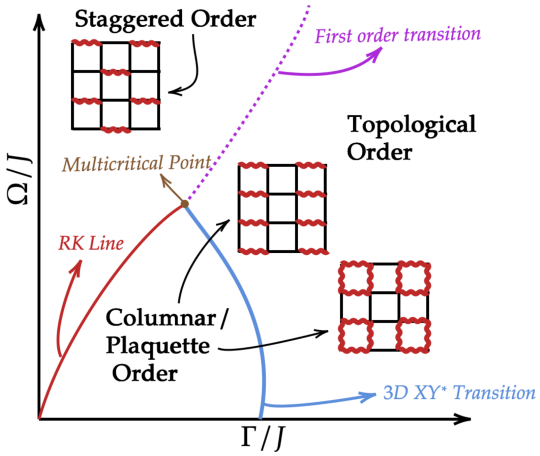

Figure 6.7: Schematic Phase diagram: There are three phases: Topological Ordered (TO), Columnar/Plaquette ordered and Staggered ordered phases, separated by three phase boundary chracterized by 3D XY^* criticality, RK criticality and first order transition and all these boundary meets at a multicritical point.

columnar/plaquette dimer crystal (Fig. 6.6), while for the potential-dominated case $\Gamma/\Omega < 1$, a staggered dimer crystal (Fig. 6.12) is obtained. Finally, the $\Omega = \Gamma \neq 0$ line corresponds to the extension of the RK point emanating from the classical dimer point $\Gamma = \Omega = 0$. In fact, the entire $\Gamma = 0$ line is classical, where $\Omega \neq 0$ selects locally staggered configurations. Notably, the entire RK line corresponds to a fine-tuned $U(1)$ liquid that describes a deconfined quantum phase transition between the two distinct dimer crystals.

On the other hand, along the $\Omega = 0$ line, we obtain the odd Toric code Hamiltonian in a longitudinal Zeeman field, where the magnetic charges are infinitely costly ($\kappa \to -\infty$), while the electric charges have a finite energy cost ($\sim \Gamma$). The Zeeman term renders the electric charges dynamic, resulting in a dispersion with a bandwidth $\sim J$, such that for $\Gamma \sim J$, the electric charges condense. Due to the background π-flux experienced by the electric charges, two finite-momentum soft modes develop, leading to a translation-symmetry-broken phase—the columnar/plaquette dimer crystal—upon condensation. The critical theory (see below), obtained following Blanckstein *et al.* [67], belongs to the 3D XY universality class and describes, once again, a Landau-forbidden continuous phase transition between a topologically ordered Z_2 liquid phase and a translation-symmetry-broken plaquette/columnar phase.

The gapped topological phase is, of course, stable to the inclusion of small Ω/J. However, deep within the topological ordered (or Z_2 liquid phase), increasing Ω/J eventually leads to a potential-energy-dominated staggered phase through a first-order phase transition. The remarkable stability of the staggered crystal at large Ω/J for all values of Γ/J, as well as its eventual first-order transition to the topological or-

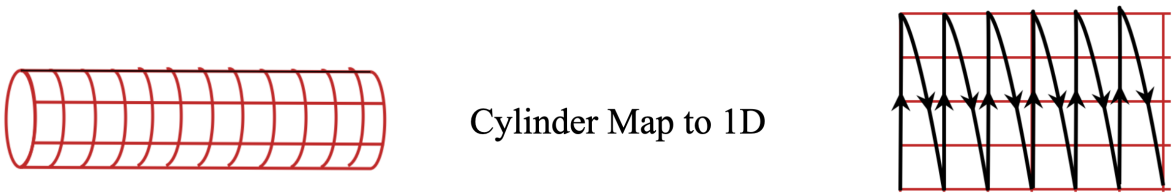

Figure 6.8: Schematic illustration of mapping a two-dimensional cylinder to a one-dimensional infinite lattice by snaking. The sites on the cylinder are ordered sequentially in a snake-like pattern around the circumference, thereby converting the 2D geometry into a 1D chain suitable for iDMRG simulations.

dered, can be traced to the absence of perturbation-induced (by Γ/J) local dynamics within the staggered phase. The two Landau-forbidden phase transition lines and the first-order line possibly meet at a multicritical point.

Having established the limiting regimes and the general topology of the phase diagram, we now turn to numerical calculations to obtain quantitative confirmation of the phases and the associated phase transition lines.

6.7 Numerical Calculations

We performed iDMRG calculations on the infinite-cylinder geometry using the tensor network Python (TeNPy) library [130]. We used it to obtain the ground state of the Hamiltonian in the form of matrix product states (MPS), employing an efficient truncation scheme based on a parameter χ, known as the bond dimension [5]. In this approach, the two-dimensional lattice on a cylinder is mapped onto a one-dimensional infinite chain by wrapping the cylinder around its circumference, as illustrated in Fig. 6.8. This mapping allows us to exploit the efficiency of the density matrix renormalization group (DMRG) in one dimension, while still capturing the essential two-dimensional physics of a cylinder with finite circumference. The infinite DMRG (iDMRG) algorithm is a variant of DMRG designed for systems in the thermodynamic limit. The method iteratively grows the unit cell of the matrix product state (MPS) until convergence is reached, thereby providing access to ground states of infinite cylinders with fixed circumference [130].

A key advantage of iDMRG is the ability to extract quantities directly from the MPS representation. One such quantity is the correlation length ξ, which can be obtained from the eigenvalue spectrum of the MPS transfer matrix [130]. The MPS is normalized such that the largest eigenvalue of the transfer matrix is $\lambda_1 = 1$. In this normalization, the correlation length is determined from the ratio of the largest and

[5]The amount of maximum entanglement that can be captured by the MPS approximation of the quantum state is determined by the bond dimension χ.

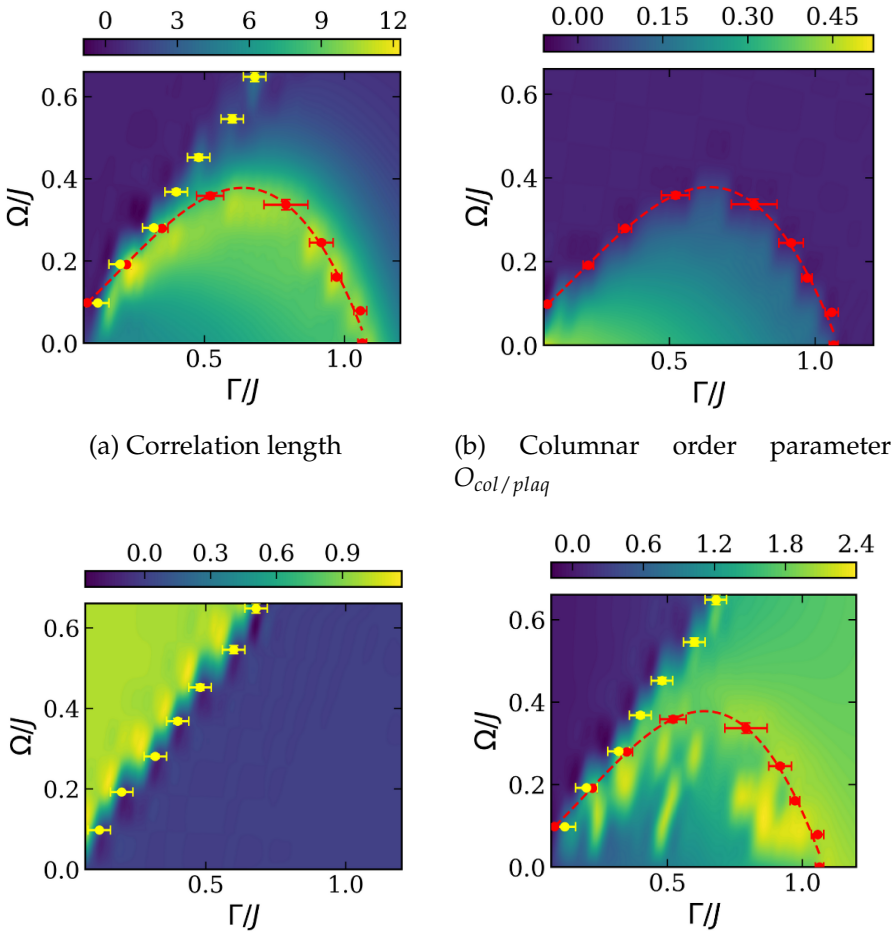

(a) Correlation length

(b) Columnar order parameter $O_{col/plaq}$

(c) Staggered order parameter O_{stag}

(d) Entanglement entropy

Figure 6.9: Contour plot of (a) correlation length, (b) columnar order parameter (O_{col}), and (c) staggered order parameter (O_{stag}) in the Ω/J–Γ/J plane, where $L_y = 4$, $\kappa = -10$, $J = 1$, and bond dimension $\chi = 300$. The red dots indicate points where the columnar order parameter vanishes, while yellow dots denote discontinuities in the staggered order parameter. (d) Contour plot of entanglement entropy for $L_y = 4$, $\kappa = -10$, $J = 1$, and $\chi = 300$. The red dots indicate where the columnar order parameter vanishes, and yellow dots denote discontinuities in the staggered order parameter.

next-largest eigenvalues as

$$\xi = -1/\ln(\lambda_2), \tag{6.52}$$

where λ_2 denotes the second-largest eigenvalue of the transfer matrix [130]. The correlation length diverges with increasing bond dimension (χ) [130] at gapless points such as phase transitions, whereas it saturates in gapped phases, thereby serving as a useful probe to detect phase transitions.

For our simulations, we considered an infinite cylinder with a circumference of

four sites ($L_y = 4$). We set $\kappa = -10$ as the largest coupling constant in order to impose a π-flux per square plaquette [see Eq. 6.48]. The interaction strength was fixed at $J = 1$, while the parameters $\Gamma \in (0, 5)$ and $\Omega \in (0, 5)$ were varied. To construct the numerical phase diagram, we scanned along straight lines in the (Γ, Ω)-plane, defined by

$$\Omega = \frac{\Omega_{\max}}{5}(5 - \Gamma), \tag{6.53}$$

where $\Omega_{\max}$, is the value of Ω where this line intersects $\Gamma = 0$ axis. Along each such line, we computed several observables of the ground state, including the correlation length, entanglement entropy, columnar order parameter, staggered order parameter, and the mean value of the star operator.

For the columnar/plaquette and staggered order parameters, we defined the following operator

$$O(\mathbf{q}, \mathbf{n}) = \frac{1}{N}\sum_{\vec{\mathbf{r}}} e^{i\mathbf{q}\cdot\mathbf{r}}\langle Z_{\mathbf{r},\mathbf{r}+\mathbf{n}}\rangle \tag{6.54}$$

For staggered order parameter, we computed,

$$\begin{aligned} O_1 &= O(\mathbf{q} = (\pi, \pi), \quad \mathbf{n} = \mathbf{x}) \\ O_2 &= O(\mathbf{q} = (\pi, \pi), \quad \mathbf{n} = \mathbf{y}) \\ O_{stag} &= \sqrt{O_1^2 + O_2^2}. \end{aligned} \tag{6.55}$$

For columnar/plaquette order parameter, we computed,

$$\begin{aligned} O_3 &= O(\mathbf{q} = (0, \pi), \quad \mathbf{n} = \mathbf{x}) \\ O_4 &= O(\mathbf{q} = (\pi, 0), \quad \mathbf{n} = \mathbf{y}) \\ O_{col/plaq} &= \sqrt{O_3^2 + O_4^2}. \end{aligned} \tag{6.56}$$

Note that for columnar order we have $O_3 \neq 0$ and $O_4 = 0$ or the other way while for plaquette order $O_3 = O_4 \neq 0$.

For the star operator, we computed,

$$O_{star} = \frac{1}{N}\sum_i \langle \prod_{j\in i} X_{ij}\rangle. \tag{6.57}$$

The summation is carried out over a 4×4 unit cell, with N denoting the number of sites in the unit cell, which is 16 in our case. The entanglement entropy obtained from iDMRG represents the half-cylinder entropy, i.e., the entanglement between the two

halves of a cylinder.

The results of this analysis are summarized in Fig. 6.9. Figure 6.9(a) shows a contour plot of the correlation length in the Ω/J–Γ/J plane, revealing three distinct phases separated by phase boundaries. In the regime $\Gamma/J \ll 1$ and $\Omega/J \ll 1$, the system corresponds to the Rokhsar–Kivelson limit, where tuning Ω/J at small Γ/J drives a transition from the columnar to the staggered phase. These two phases are characterized by the order parameters O_{stag} and $O_{\text{col/plaq}}$, corresponding respectively to the staggered and columnar orders. As shown in Figs. 6.9(b) and 6.9(c), these order parameters take nonzero expectation values in their respective phases and vanish in the topological ordered phase. Figure 6.9(d) presents the entanglement entropy, which further distinguishes the three phases. Its value saturates to (L_y-1)log 2 [131] in large Γ/J limit further confirming the presence of toplogical ordered phase.

Having summarized the numerically obtained phase diagram, we now delve into the details of various parts of the phase diagram in the subsections below in further detail.

6.7.1 $\Omega/J = 0$ Line

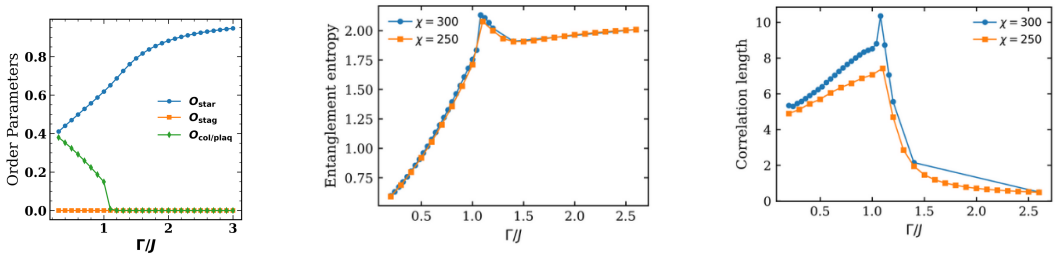

(a) (b) (c)

Figure 6.10: Plots along the $\Omega = 0$ line for an infinite cylinder with circumference $L_y = 4$, $\kappa = -10$, $J = 1$, and bond dimension $\chi = 250$: (a) columnar, staggered, and star order parameters; (b) entanglement entropy; (c) correlation length.

We start with the $\Omega = 0$ line, whence the Hamiltonian reduces to the odd Toric code in the presence of a longitudinal Zeeman field. This corresponds to the frustrated transverse field Ising model discussed in Section 6.4.2, which, when expressed in terms of gauge-invariant degrees of freedom and in the absence of fermions (i.e., filling $\nu = 0$), corresponds to the $\Omega = 0$ line. Figure 6.10(a) shows the behavior of the columnar/plaquette (Eq. 6.56) and staggered (Eq. 6.55) order parameters: the columnar order parameter takes a non-zero value in the small Γ/J regime, signaling the columnar phase, and vanishes at larger Γ/J, indicating a phase transition. The

staggered order parameter, on the other hand, remains zero throughout the parameter range.

To gain insight into the large Γ/J phase, we also plot the expectation value of the vertex operator, O_{star} (Eq. 6.57), where, deep inside the topological ordered phase ($\Gamma/J \gg 1$), the expectation saturates to 1, indicating the absence of electric charges. As Γ/J decreases, the expectation value decreases, indicating the proliferation of electric charges; however, since Eq. 6.57 counts the uniform density of such charges, it does not go to zero.

The non-trivial many-body entangled nature of the topological ordered ground state is further evident in Fig. 6.10(b), where we plot the bipartite von Neumann entanglement entropy as a function of Γ/J, with the peak marking the transition and the saturation at large Γ approaching the topological entanglement entropy, $(L_y - 1)\log 2$ [131, 132].

Finally, in Fig. 6.10(c), we plot the correlation length, ξ (Eq. 6.52), as a function of Γ/J. The peak signals a phase transition from the columnar/plaquette dimer crystal to the topological ordered state, where the peak value increases with bond dimension, indicating the divergence of the correlation length.

The transition between the Z_2 topological ordered and the columnar/plaquette dimer crystal can be understood in terms of the condensation of the electric charges. Indeed, the Zeeman term gives dynamics to the electric charges, eventually leading to their condensation. To obtain the critical field theory, it is useful to introduce the Z_2 electric charge field manifestly; this can be achieved by casting the Hamiltonian (Eq. 6.16) in terms of an Ising gauge theory with dynamic electric matter, as discussed in Section 6.4.2.

The resultant fully frustrated transverse field nearest-neighbor Ising model, upon coarse-graining, leads to a 3D-XY field critical theory where the $O(2)$ field is composed of the two soft electric matter modes [67] (Eq. 6.32):

$$(\phi_1, \phi_2) \tag{6.58}$$

Thus, the transition from the topological ordered to the columnar/plaquette ordered phase lies in the 3D XY* universality class (Eq. 6.33), where the asterisk denotes that the $O(2)$ field is not an observable but a fractionalized degree of freedom — the Ising electric charge. On the other hand, the columnar/plaquette order parameter (Eq. 6.56) is given by

$$(O_3, O_4) \sim (2\phi_1\phi_2, \;\; \phi_1^2 - \phi_2^2) \tag{6.59}$$

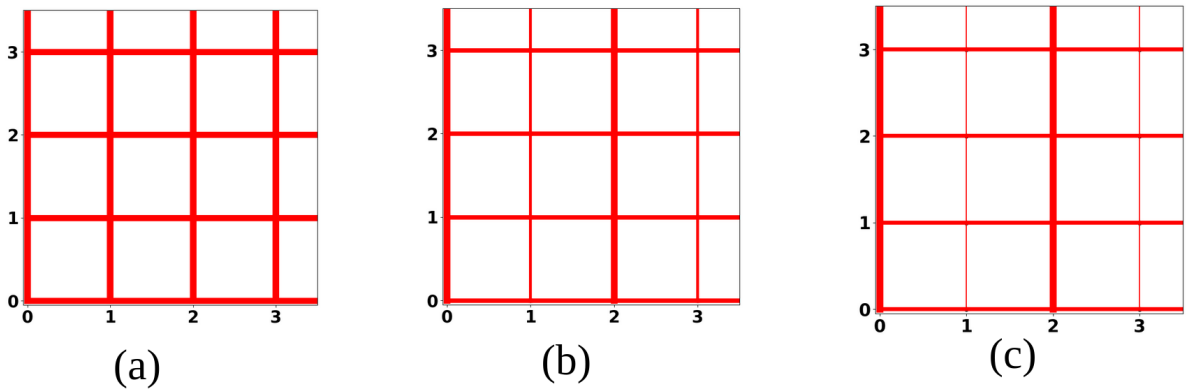

Figure 6.11: Plot of configuration of $\langle Z_{ij} \rangle$ for a 4×4 unit cell with periodic boundary conditions along the y-direction and repeating in the x-direction with a periodicity of four sites shown for $\Omega = 0$, J=1 and bond dimension $\chi = 300$ at (a) $\Gamma = 2.6$, (b) $\Gamma = 0.88$ and (c) $\Gamma = 0.36$. Thickness of the bond is proportional to the value of $\langle Z_{ij} \rangle$.

The emergent $O(2)$ symmetry is broken by an 8th-order term

$$\sim -\lambda \cos(8\theta) \tag{6.60}$$

where $\phi_1 + i\phi_2 = |\Phi| e^{i\theta}$ and θ is the phase of the $O(2)$ field. This term is irrelevant at the critical point but selects the exact dimer pattern between columnar ($\lambda > 0$) and plaquette ($\lambda < 0$) ordering. Within our finite-size calculation, we tentatively conclude that columnar order is chosen (which is only twofold degenerate on the cylinder), as evident from the plot of $\langle Z_{ij} \rangle$ in Fig. 6.11 for different Γ/J.

6.7.2 The classically frustrated system on $\Gamma = 0$ line.

Turning to the other limit, $\Gamma = 0$, of the Hamiltonian (Eq. 6.49), the $\Omega/J = 0$ line selects the classical dimer manifold in the limit $\kappa = -\infty$. Upon turning on a finite Ω/J, the extensively degenerate classical dimer manifold splits energetically, favoring the staggered configurations (Fig. 6.12), locally characterized by

$$\prod_{\langle ij \rangle \in \square} Z_{ij} = -1, \quad \forall \quad \square, \tag{6.61}$$

and

$$(1 - Z_{i,i-\mathbf{n}})(1 - Z_{i,i+\mathbf{n}}) = 0, \quad \mathbf{n} \in \{\mathbf{x}, \mathbf{y}\}, \quad \forall \quad i, \tag{6.62}$$

However, in this classical limit, the domain walls of such staggered arrangements are free of energy cost, leading to a sub-extensively degenerate staggered manifold char-

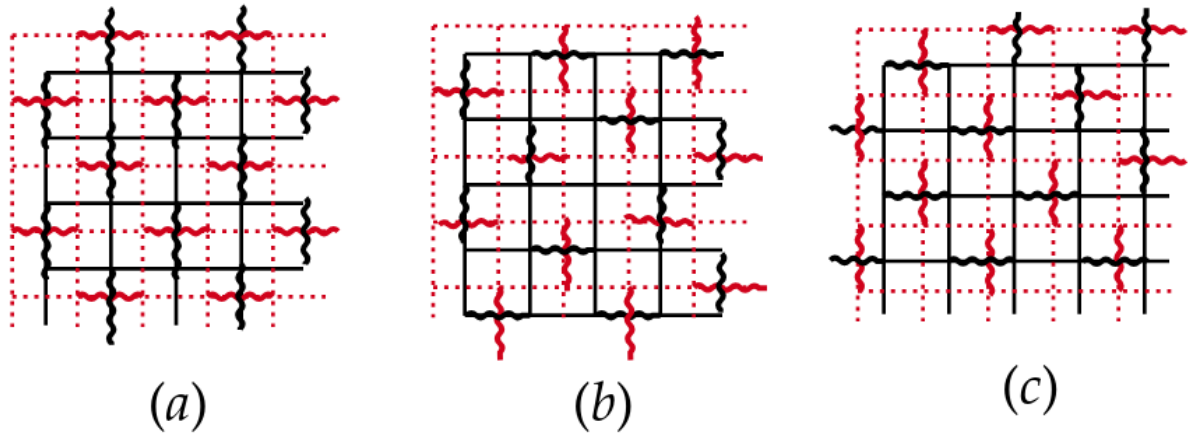

Figure 6.12: Schematic diagram of possible staggered configurations on open boundary, satisfying the condition in Eq. 6.62. The black solid (red dotted) lattice denotes the dual (direct) lattice, while red (black) curly bonds indicates that the expectation value of dimer occupancy, $\langle n_{IJ} \rangle$ (and $\langle Z_{ij} \rangle$ on associate bond of dual lattice) is different from that on other bonds, and results in (a) Staggered dimer order without vortices or domain walls. (b) Staggered order with a vortex. (c) Staggered order with a domain wall.

acterized by uniform staggered dimer order (Fig. 6.12(a)) as well as by configurations with domain walls (Fig. 6.12(c)).

On the bipartite lattice, the dimer model is a $U(1)$ gauge theory; hence, quantum fluctuations are expected to lead to a confining state via the order-by-disorder mechanism, resulting in the staggered state, as seen in our numerical calculations.

6.7.3 The RK limit: $\Omega/J \ll 1, \Gamma/J \ll 1$

As discussed above, this corresponds to the dimer limit of the phase diagram. Sitting on the classical line $(\Gamma/J = 0)$ and turning on a small Γ/J selects the staggered dimer order. Conversely, the columnar dimer crystal, obtained along the $\Omega/J = 0$ line (see above), remains stable upon turning on a small Ω/J. This behavior aligns with expectations from Rokhsar-Kivelson (RK) physics on the square lattice, which suggests the existence of an intermediate RK transition line separating these two phases (see Fig. 6.7). Our numerical results support this scenario, as demonstrated in Figs. 6.9(b,c).

Performing a perturbative calculation in the limits $\Gamma/J \ll 1$ and $\Omega/J \ll 1$ yields the Rokhsar-Kivelson (RK) Hamiltonian of Eq. 6.42, discussed in detail in Appendix B.4. Consequently, there is a transition in this limit from the columnar/plaquette phase to the staggered phase, as shown in Fig. 6.9. The correlation length data in Fig. 6.9(a), along with cuts in the $\Omega/J - \Gamma/J$ plane (Figs. 6.13(a) and 6.13(b)), reveal two peaks. The peak at small Γ marks the transition from the columnar/plaquette order to the staggered phase. Furthermore, Fig. 6.14 illustrates that moving away from this limit

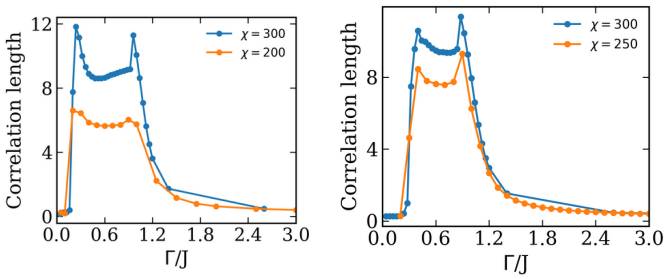

Figure 6.13: Correlation length obtained from iDMRG performed on an infinite cylinder of circumference of 4-sites for different bond dimensions(χ), along different directions in the Ω/J–Γ/J plane with $J = 1$ and (a) $\Omega = 0.04(5-\Gamma)$ and (b) $\Omega = 0.06(5-\Gamma)$.

reduces the extent of the columnar phase, ultimately leading to a transition from a topologically ordered phase to a staggered ordered phase. The entanglement entropy shown in Fig. 6.9(d) also displays a sudden drop at the RK transition, reflecting the change from a columnar/plaquette ordered state to a staggered phase, which is a product state.

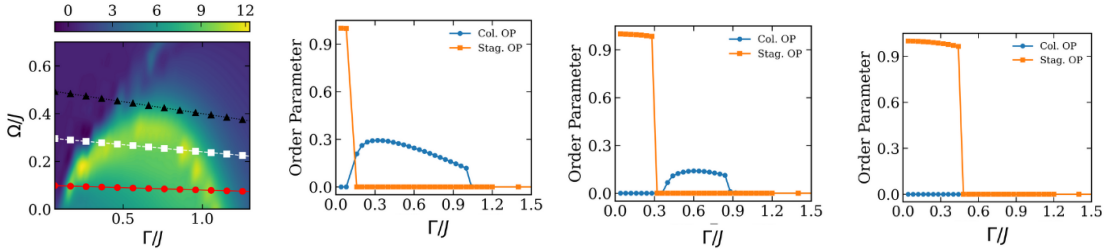

Figure 6.14: (a) Contour plot of the correlation length in the Ω/J–Γ/J plane, for $L_y = 4$, $\kappa = 10$, $J = 1$, and bond dimension $\chi = 300$. (b) Plot of Columnar and staggered order parameters along the red line $\Omega = 0.02(5-\Gamma)$ in (a). (c) The same order parameters along the white line $\Omega = 0.06(5-\Gamma)$ in (a). (d) The order parameters along the black line $\Omega = 0.1(5-\Gamma)$ in (a).

6.7.4 $\Omega/J \gg 1$, $\Gamma/J \gg 1$

The staggered phase, stabilized at large Ω/J, is particularly robust against turning on Γ/J due to the absence of local dynamics. Eventually, however, the staggered phase at large Ω/J becomes energetically unstable as Γ/J is increased and directly gives way to the topological ordered via a phase transition, which appears to be first order as evidenced by the discontinuity of the staggered order parameter. The analysis for this limit is shown in Fig. 6.15 and Fig. 6.16, where scans along the lines $\Omega = 5 - \Gamma$ (in

Fig. 6.15) and $\Omega = 1.25(5 - \Gamma)$ (in Fig. 6.16) for $J = 1$ are presented. It can be concluded that the columnar/plaquette order parameter $O_{\text{col/plaq}}$ vanishes throughout, whereas the staggered order parameter shown in Fig. 6.15(a) and Fig. 6.16(a) takes non-zero values in the staggered ordered phase and vanishes in the topological ordered, with a discontinuity at the transition. Furthermore, the peak in the correlation length shown in Fig. 6.15(b) and Fig. 6.16(b) marks the transition, accompanied by a sharp increase in the entanglement entropy at the transition point as Γ is tuned from the staggered ordered limit to the topological ordered limit.

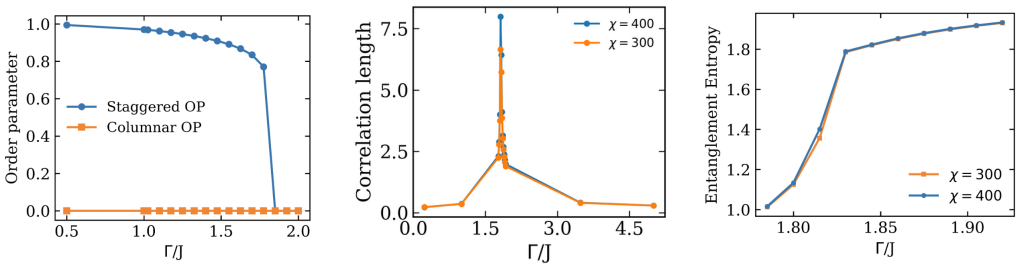

(a) (b) (c)

Figure 6.15: Analysis along the line $\Omega = 5 - \Gamma$ for $J = 1$ and $L_y = 4$. (a) Plot of staggered order parameter O_{stag} and columnar/plaquette order parameter $O_{\text{col/plaq}}$, computed for bond dimension $\chi = 400$. (b) Correlation length ξ for various bond dimensions χ. (c) Entanglement entropy S for the same set of parameters (shown for values of Γ in the vicinity of transition point).

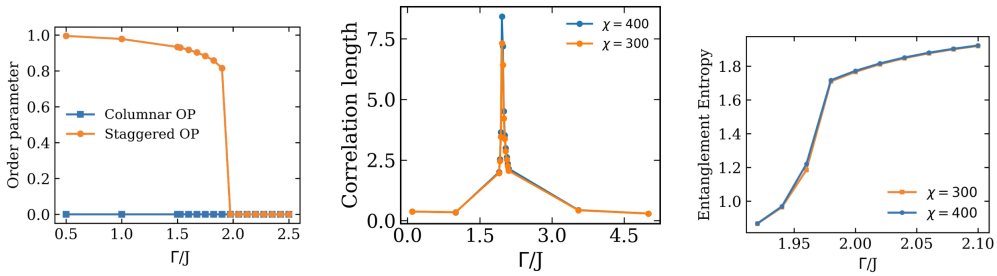

(a) (b) (c)

Figure 6.16: Analysis along the line $\Omega = 1.25(5 - \Gamma)$ for $J = 1$ and $L_y = 4$. (a) Plot of staggered order parameter O_{stag} and columnar/plaquette order parameter $O_{\text{col/plaq}}$, computed for bond dimension $\chi = 400$. (b) Correlation length ξ for various bond dimensions χ. (c) Entanglement entropy S for the same set of parameters (shown for values of Γ in the vicinity of transition point).

6.7.5 Interpolating the two limits

The RK line corresponding to the transition from the plaquette/columnar and the staggered dimer crystals via the fine-tuned critical $U(1)$ liquid evolves continuously in the

$(\Gamma/J, \Omega/J)$ plane. On the other hand, the line corresponding to the transition between the topological ordered and the columnar/dimer order bends towards smaller Γ/J at finite Ω/J to approach the RK line. This is evident in Fig. 6.9(a), scanning along the line $\Omega = \frac{\Omega_{\rm max}}{5}(5-\Gamma)$, where $\Omega_{\rm max}$ corresponds to the value of Ω at which this line intersects the Ω-axis at $\Gamma = 0$. This structure is further revealed in the line cuts presented in Fig. 6.17(a) (for $\Omega_{\rm max} = 0.2$), which exhibit two peaks: the peak at decreasing Γ corresponds to the transitions from the toplogical ordered phase to the columnar phase, and then from the columnar to the staggered phase—consistent with the behaviors of the columnar and staggered order parameters shown in Fig. 6.9(b) and 6.9(c). Increasing $\Omega_{\rm max}$ causes the two peaks to move closer together, as illustrated in Figs. 6.17(b) (for $\Omega_{\rm max} = 0.3$) and 6.17(c) (for $\Omega_{\rm max} = 0.75$). Finally, for even larger $\Omega_{\rm max} = 1.75$, there is a direct transition between the Z_2 liquid and the staggered crystal with a single peak in the correlation length, as shown in Fig. 6.17(d) (for $\Omega_{\rm max} = 1.75$)- consistent with the onset of the staggered order parameter in that limit as shown in Fig. 6.15(a)($\Omega_{\rm max} = 5$) and Fig. 6.16(a)($\Omega_{\rm max} = 6.25$). This analysis suggests the possibility of a multicritical point where the two Landau-forbidden transition lines meet the first-order transition line.

This compeletes our study of the phase diagram. Our present numerical calculations, while too limited by system sizes to detect the nature of the phase transitions, do not reveal any other phases other than the two crystals and the Z_2 liquid (toplogical ordered). This is strongly indicative of the possible interesting structure of the phase diagram as sketched schematically in Fig. 6.7 – the RK, the 3D-XY* transition and the first order lines meeting at a multi-critical point. Notably, since both the RK and the XY* lines correspond to Landau forbidden deconfined quantum phase transitions, the nature of such multi-critical point could be rather interesting.

6.8 Summary

In this chapter, we examined the case of Z_2 fractionalization of spinless fermions, wherein the implementation of microscopic symmetries becomes projective. Our analysis focused on the limit corresponding to the deconfined phase of the emergent Z_2 gauge field. In this regime, the model reduces to gauge-invariant fermions hopping on a dimer background defined by Ising variables residing on the lattice links. The symmetry analysis presented in this chapter reveals that, in this phase, the fermions realize a semimetallic state that breaks lattice symmetries. Furthermore, by employing iDMRG computations, we identified order parameters that characterize the symmetry breaking exhibited by the fermions in this phase.

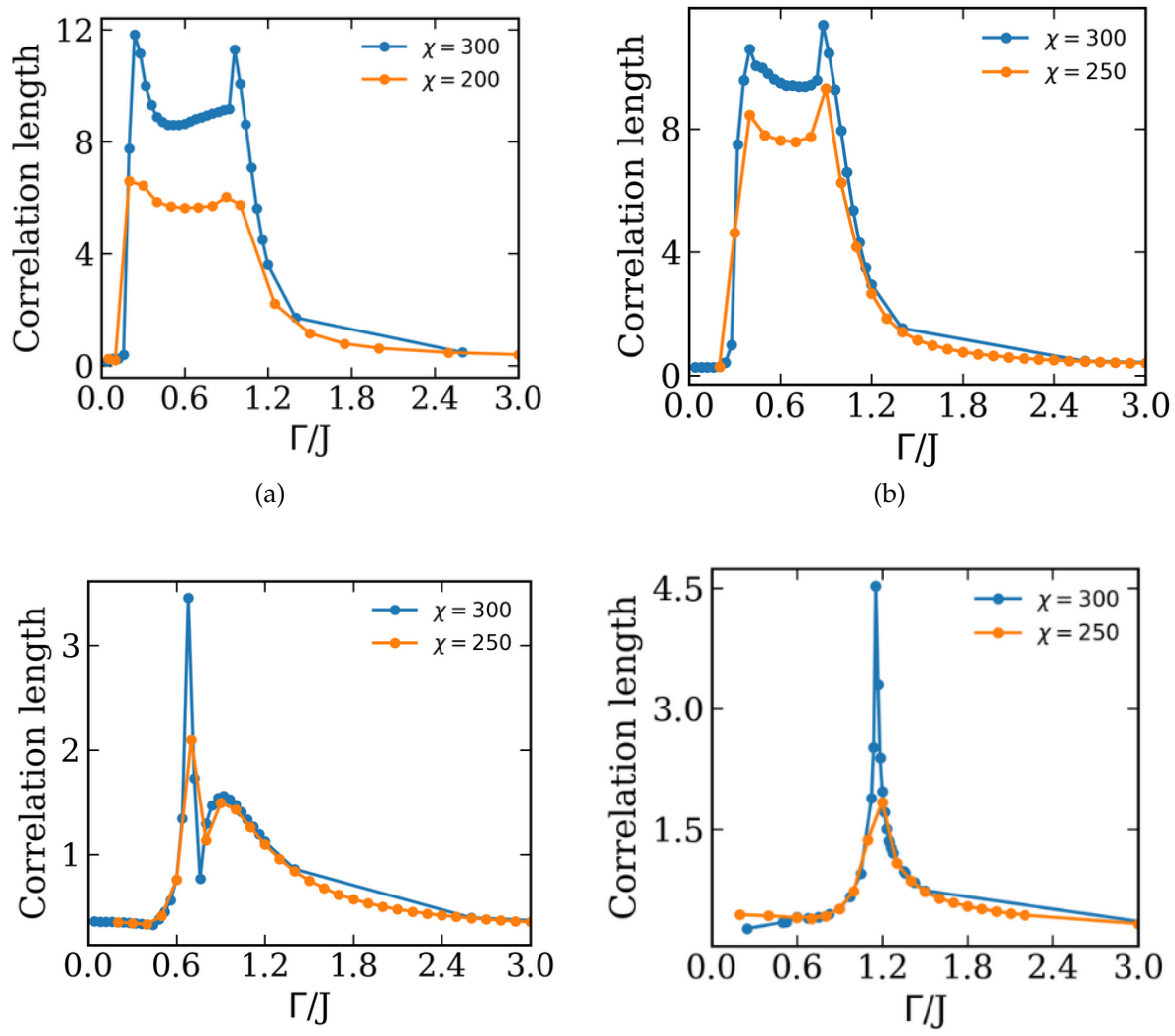

Figure 6.17: Correlation length obtained from iDMRG performed on an infinite cylinder of circumference of 4-sites for different bond dimensions(χ), along different directions in the Ω/J–Γ/J plane with $J = 1$ and (a) $\Omega = 0.04(5 - \Gamma)$, (b) $\Omega = 0.06(5 - \Gamma)$, (c) $\Omega = 0.15(5 - \Gamma)$, (d) $\Omega = 0.35(5 - \Gamma)$.

In the absence of fermions, the model—when supplemented with a potential term for dimers [71]—provides a framework for interpolating between the dimer and topological ordered limits within the same phase diagram. Through iDMRG analysis, we identified three distinct phases: the columnar (or plaquette) phase, the staggered phase, and the topological ordered phase. Our present analysis indicates the possibility that these three phase boundaries meet at a multicritical point. It is intriguing to investigate the nature of this multicritical point, where two Landau-forbidden transitions—the $3D\ XY^*$ transition and the RK transition—converge and possibly intersect a first-order line.

Chapter 7

Trial Wave functions for Correlated Metals

This chapter is based on our paper (Ref. [78]), which was done in collbaoration with Harsh Nigam, Subhro Bhattacharjee and Krishnendu Sengupta. The numerics of exact diagonalization results discussed in Section 7.2 were performed by Harsh Nigam.

Our understanding of metallic phases squarely rest on the idea of Fermi-surface (FS) and long-lived fermionic quasi-particles (the so called Landau quasi-particles) about it at low energies [36, 133, 134] . For non-interacting fermions, these are easily determined by the single particle eigenstates in momentum space, $n_{\mathbf{k}}$, which in turn depends on the single-particle energy $\varepsilon_{\mathbf{k}} - \mu$ where μ is the chemical potential, and $\varepsilon_{\mathbf{k}}$ is the single-particle dispersion. The shape and volume of the FS are determined by the underlying symmetry and filling respectively [135]. The corresponding ground state (GS) wave-function has a product structure in momentum space corresponding to non-trivial entanglement in real space [136].

In the presence of a moderate short-ranged four fermion interaction, the above description survives and forms the backbone of Landau-Fermi liquid (FL) theory [36,133, 134] in spatial dimensions $d > 1$. Indeed the single particle residue, $Z_{\mathbf{k}}$, obtained from the jump in $\langle n_{\mathbf{k}} \rangle$ at the FS, and the associated Luttinger theorem [137, 138] provides a definition for the long-lived gapless electron-like Landau quasi-particles near the FS in such a FL which then can be described via an effectively weakly interacting framework. In a FL, $0 < Z_{\mathbf{k}_F} < 1$, such that the FS remains sharply defined via the position of the jump in occupation inspite of fluctuations in $n_{\mathbf{k}}$ near the FS. One then expects that the corresponding GS is very well approximated via short-range entangled states in the momentum space across the non-interacting FS such that the real-space entanglement signatures are similar to that of the non-interacting case [139].

In this chapter, we show that *quantum fluctuations* arising from the coherent superposition of wave-functions with different momenta occupation $\{n_{\mathbf{k}}\}$ can result in loss of Landau quasi-particle while the FS remains defined. We explicitly construct wave-functions for such *quantum fluctuating* FS, which, we note, is different from the dynamical fluctuation of a classical membrane. Instead, in the former, the location of the membrane (the FS) has a uncertainty in the momentum space. This superposition is then closely related to the dimer coverings in Rokhsar-Kivelson (RK) models [71], but applied to momentum space for the FS. These wave-functions form a starting point for understanding the loss of the Landau quasi-particle leading to a so-called non-Fermi liquid (NFL) phase. Such phases are generically known to arise in one dimensional (1D) interacting fermion systems and are collectively known as Tomonaga Luttinger liquids (TLL) [2, 140]. The quasi-particle residue, for these TLLs, vanish at the FS and is replaced by a point of inflection with $\langle n_{\mathbf{k}} \rangle \sim |\mathbf{k} - \mathbf{k}_{\mathrm{F}}|^p$ near the FS with $0 < p < 1$ being related to the Luttinger parameter [2] (also see below). Thus while the Landau quasi-particle is lost, the FS is still well defined in accordance with the Luttinger theorem [141]. In higher dimensions ($d > 1$) similar phenomena, *i.e.*, loss of quasi-particles can occur with a well defined *critical FS* [142–144] which arises at fermionic quantum critical point [142, 145–147] between the large and small FSs in heavy fermion systems [147–151] or Mott transition in correlated metals [152, 153] where the entire FS disappears on approaching from the metallic side [142, 143].

For $d > 1$, effective field theory calculations [48] of fermions (at finite density) interacting with gapless boson near a metallic quantum critical point or in a gapless phase (such as in the U(1) quantum spin liquid with a spinon-FS [154, 155]) indicate that due to the presence of the tangential scattering with the bosons, even at ultra-low energies, the Landau quasi-particle is killed possibly leading to a NFL [75, 147, 156–158] particularly in 2D [48, 155, 159–165]. However, the fate of the infra-red (IR) fixed point of such theories is not quite settled due to lack of control over re-summation procedures; this is the case even in large-N_f limit with N_f being the flavour of fermions. This calls for new ideas in understanding such a NFL state which is parent to a large number of diverse strongly correlated phenomena; this is the central motivation for the trial wave-function approach that we study here.

The wave-functions that we propose here explicitly capture the partial or complete loss of the single-fermion residue signalling the loss of the Landau quasi-particle at low energies. In 1D, we show that we can re-interpret the existing numerical and field-theoretic understanding for the 1D TLL [2] for spinless fermions within the above trial wave-functions (Figs. 7.1 and 7.2). This can be achieved by re-writing such wave-functions in the basis of fluctuating $\{n_{\mathbf{k}}\}$ and comparing the average occupation, $\langle n_{\mathbf{k}} \rangle$

with predictions from bosonization. In addition, the entanglement signatures can also be shown to match with those computed from TLL. Interestingly, following RK construction of dimer models, we can construct minimal projector Hamiltonians, albeit in momentum space, where the GS allows large fluctuations, both in 1D and 2D, in the occupation $\{n_{\mathbf{k}}\}$. These wave-functions, at partial filling, do not break any symmetry and are devoid of sharp FS like signatures in momentum space. Therefore, in accordance with Lieb-Schultz-Mattis (LSM) [141, 166] theorem in 1D or their higher dimensional extensions [138, 167], they possibly correspond to GSs of gapless phases of correlated metals (in higher dimensions, in principle, gapped topological order is also allowed). We study the generic properties of such wave-functions in 2D that correspond to smooth deformation of the FS as an example of fixed-point wave-functions for correlated metals with and without Landau quasi-particles and isotropically or anisotropically blurred FS. In particular, the anisotropic loss of the single-particle residue leads to Fermi-arc like features, albeit at zero temperature, similar to underdoped cuprates and direction dependent Friedel oscillations.

In the rest of this chapter, we provide the details of the construction of the trial wave-functions starting with the single particle distribution in momentum space and use it to provide initial insights into their nature via selected examples in 1D and 2D. In section 7.1 we provide the details of construction of the trial wave-function which is a straightforward extension of superposing single-particle Slater determinants. Such superposition generically leads to fluctuations in momentum space occupation $\{n_{\mathbf{k}}\}$ and this forms the right basis (Eq. 7.1) to capture the quantum fluctuation of the FS (Eq. 7.3) as is evident from the generic interacting fermionic Hamiltonian, when written (Eq. 7.7) in this basis. In Sec. 7.2 we show that the new basis provides a useful momentum-space truncation scheme to understand the physics of TLL in a system of spinless Fermions in 1D. In particular, we characterize the relation between the fluctuations of the FS and the loss of the fermionic quasi-particle residue by quantitatively comparing with bosonization for larger system sizes for a momentum space Hamiltonian (Figs. 7.2, 7.3 and 7.4). Having obtained a description of the TLL in $d = 1$, we turn to the general properties of the wave-functions of the type in Eq. 7.3. We mainly restrict ourselves to description of a class of effective projector models in Sec. 7.3 whose GSs allow *equal* superposition of various $\{n_{\mathbf{k}}\}$ distributions; we note that these wave-functions are qualitatively different from those describing a free Fermi gas GS. This naturally leads to possible fixed-point fermion wave-functions in Sec. 7.4 that are GSs similar to that of suitable RK-type projector Hamiltonians that describe strongly correlated NFLs; such NFL may be obtained near a metallic phase transition due to the Yukawa interactions with gapless bosons as discused above. Our study in Secs. 7.3

and 7.4 may be relevant for some of these systems. We discuss various properties of a selected class of such wave-functions emphasising their NFL features. Various technical details and supporting plots are given in the different appendices.

7.1 The trial wave-function

In order to define the wave-function, we consider a finite lattice of linear size N with periodic boundary conditions. In d-dimensions, the Brillouin zone (BZ) is d-tori with a grid of spacing $2\pi/N$ along each direction. For concreteness we restrict ourselves to $d = 1, 2$ while extension to higher dimensions are straightforward. With such a discretized momentum grid, we can now re-write the N_p-particle occupation states in the momentum-space occupation basis (equivalent to Slater determinants [168]) by defining an Ising variable $\theta_{\mathbf{k}} = \pm 1$ and using them to obtain

$$|\Psi[\theta]\rangle = (c^\dagger_{\mathbf{k_B}})^{(1+\theta_{\mathbf{k}_B})/2} \cdots (c^\dagger_{\mathbf{k_1}})^{(1+\theta_{\mathbf{k}_1})/2} |0\rangle, \tag{7.1}$$

where the momenta are arranged from smallest to largest by assigning a particular ordering in which $\mathbf{k}_1 < \cdots < \mathbf{k}_B$ over the entire BZ. Here $c^\dagger_{\mathbf{k}}$ are spinless fermion creation operators following usual fermion algebra $\{c_{\mathbf{k}}, c^\dagger_{\mathbf{k}'}\} = \delta_{\mathbf{k},\mathbf{k}'}$ and $\{c_{\mathbf{k}}, c_{\mathbf{k}'}\} = 0$. In the above wave-function modes where $\theta_{\mathbf{k}} = +1$ are occupied while $\theta_{\mathbf{k}} = -1$ are empty. The above set of wave-functions form an orthonormal basis, *i.e.* $\langle \Psi[\theta]|\Psi[\theta']\rangle = \delta_{[\theta],[\theta']}$. The Slater-determinant form of the corresponding real-space representation and matrix elements of various many-body operator is easily represented in this basis and are shown in Appendix C.1 for completeness. In particular, the total particle number and the net momenta are given by

$$N_p = \sum_{\mathbf{k}\in \mathrm{BZ}} \frac{1+\theta_{\mathbf{k}}}{2}, \quad \text{and} \quad \mathbf{k}_\mathrm{T} = \sum_{\mathbf{k}\in \mathrm{BZ}} \mathbf{k} \frac{1+\theta_{\mathbf{k}}}{2}. \tag{7.2}$$

Note that the second relation in Eq. 7.2 automatically implies that the momentum of a empty/filled band is zero. Generically, for a given filling ($\nu = N_p/N^d$), the number of above basis states increases as ${}^{N^d}C_{N_p}$ with N and is therefore of little value for numerical calculations. However, it provides an alternate way to visualize the N_p-particle Fock space basis states. In terms of the new variables $\theta_{\mathbf{k}}$, a single FS stands for a closed volume in BZ separed by the domain-wall of the Ising variable separating the $\theta_{\mathbf{k}} = +1$ (occupied) and $\theta_{\mathbf{k}} = -1$ (unoccupied) regions such that we recover the familiar FS wave function.

Using the N_p-particle basis states in Eq. 7.1, we can write down the the most generic

state for N_p-fermions as

$$|\psi\rangle = \sum_{[\theta]|\sum_{\mathbf{k}}\theta_{\mathbf{k}}/N^d=\nu} \psi[\theta]|\Psi[\theta]\rangle, \tag{7.3}$$

where $\psi[\theta]$ is the amplitude for the state with the occupancy distribution $[\theta]$ and each basis state obeys Eq. 7.2. In this sense, Eq. 7.3 is a momentum space *wave-functional* which is equivalent to superposing Slater determinants. The above wave-functional (Eq. 7.3) is very generic and can captures *all* fermionic phases in presence and absence translation symmetries. In this work, we however, consider a particular subset of such wave-functionals that are candidate ground states of correlated metals, which, we discuss below, captures the physics of quantum fluctuation of the FS. In particular we show that such fluctuations consisting of *smooth* (in 2D) deformations of the FS capture the low energy properties of strongly correlated metals – the so-called non-fermi liquids without Landau quasi-particles. Our present construction therefore does not capture correlated or disorder driven insulators which are more readily accessed starting from basis localized in real-space and hence require drastic superpositions in momentum space and hence the FS ceases to be well defined.

To this end, we consider an interacting four (spinless) fermion Hamiltonian

$$H = H_0 + H_I \tag{7.4}$$

where

$$H_0 = \sum_{\mathbf{k}} E_{\mathbf{k}} c^\dagger_{\mathbf{k}} c_{\mathbf{k}} \tag{7.5}$$

is the free fermion Hamiltonian with $E_{\mathbf{k}} = (\varepsilon_{\mathbf{k}} - \mu)$ being the single-particle dispersion and

$$H_I = \sum_{\mathbf{k}_1,\mathbf{k}_2,\mathbf{q}\neq 0} V_{\mathbf{q}}\ c^\dagger_{\mathbf{k}_1} c^\dagger_{\mathbf{k}_2} c_{\mathbf{k}_2-\mathbf{q}} c_{\mathbf{k}_1+\mathbf{q}}, \tag{7.6}$$

represents four-fermion interactions with strength $V_{\mathbf{q}}$. Note that the $\mathbf{q} = 0$ term is removed from the summation because of the neutralizing background due to the ions [168]. In the basis of Eq. 7.1, the above Hamiltonian can be written in the N_p-particle sector as

$$\begin{aligned} H &= \sum_{\{\theta\}}\sum_{\{\theta'\}} |\Psi[\theta]\rangle \Big[E[\theta]\delta_{[\theta],[\theta']} + E_I([\theta],[\theta'])(1-\delta_{[\theta],[\theta']})\Big] \langle\Psi[\theta']|, \\ E[\theta] &= \langle\Psi[\theta]|H|\Psi[\theta]\rangle \quad , \quad E_I([\theta],[\theta']) = \langle\Psi[\theta]|H_I|\Psi[\theta']\rangle, \end{aligned} \tag{7.7}$$

where the first term on the right hand side denotes the diagonal element of H in the momentum space occupation basis. The details of the form of $E[\theta]$ is given by Eq. C.13 in Appendix C.2. The diagonal contribution of H_0 in Eq. 7.7 is a direct consequence of the structure of the the free particle Hamiltonian such that the ground state is given by the $[\theta]$ configuration which yields minimum energy (within the constraint of Eq. 7.2), *i.e.*, Min $(E[\theta])$. The corresponding distribution $[\theta]$ gives rise to the FS of the free electron gas whose shape is dictated by the microscopic symmetries and energetics via the form of $E_{\mathbf{k}}$. The second term in Eq. 7.7 corresponds to the four-fermion interaction which has both diagonal and off-diagonal contributions. It's explicit form is given by Eq. C.12 and Eq. C.14. Thus interactions lead to generic superposition of distributions of $[\theta]$ having the same filling and total momentum (Eq. 7.2). It is easy to see that in the case of the four fermion interactions, the off-diagonal matrix elements of H_I are non-zero only between two distributions of $[\theta]$ that differ by occupation at four momenta (up to overall momentum conservation); this has been shown explicitly in Appendix C.2. The ${}^{N^d}C_{N_p} \times {}^{N^d}C_{N_p}$ matrix, in this basis, corresponding to H_I therefore generically sparse.

Other possible alternative forms of the interaction stem from the electrons interacting with a gapless bosonic mode, $\phi_{\mathbf{q}}$, (phonon/gauge field/collective modes) via typically a Yukawa type interaction $\sim \sum_{\mathbf{k},\mathbf{q}} V(\mathbf{q})\phi_{\mathbf{q}} c^\dagger_{\mathbf{k}+\mathbf{q}} c_{\mathbf{k}}$; these interacting Hamiltonians also have a sparse off-diagonal structure once the bosons are integrated out. Such Yukawa interactions are renormalization group (RG) relevant and can lead to NFLs in d=2 [48, 155, 159–165]. The central distinguishing feature of such Yukawa interactions in comparison to the short range four-fermion interactions is the presence of tangential scatterings; their RG relevance indicates the collective effect of such scattering which would necessarily change the fermion distribution about the non-interacting FS. This leads to the quantum fluctuation of the FS as suggested by the form of Eq. 7.7.

Below, we explore different forms of $\langle \Psi[\theta]|H_I|\Psi[\theta']\rangle$ and understand the nature of the resultant GSs. We note that the simplest case where the four-fermion interactions can already lead to a TLL [2, 140] in $d = 1$. Indeed, in this case we show that in the TLL, the GS wave-function can be very efficiently described using the form of Eq. 7.3 with non-zero amplitudes, $\psi[\theta]$, only for configurations that allow for $[\theta]$-configurations corresponding to low energy particle-hole excitations. Note however, in $d = 1$, fluctuations in the occupancy necessarily leads to disconnected segments of $\{n_{\mathbf{k}}\}$ which is not the generic case in higher dimensions (see Sec. 7.4).

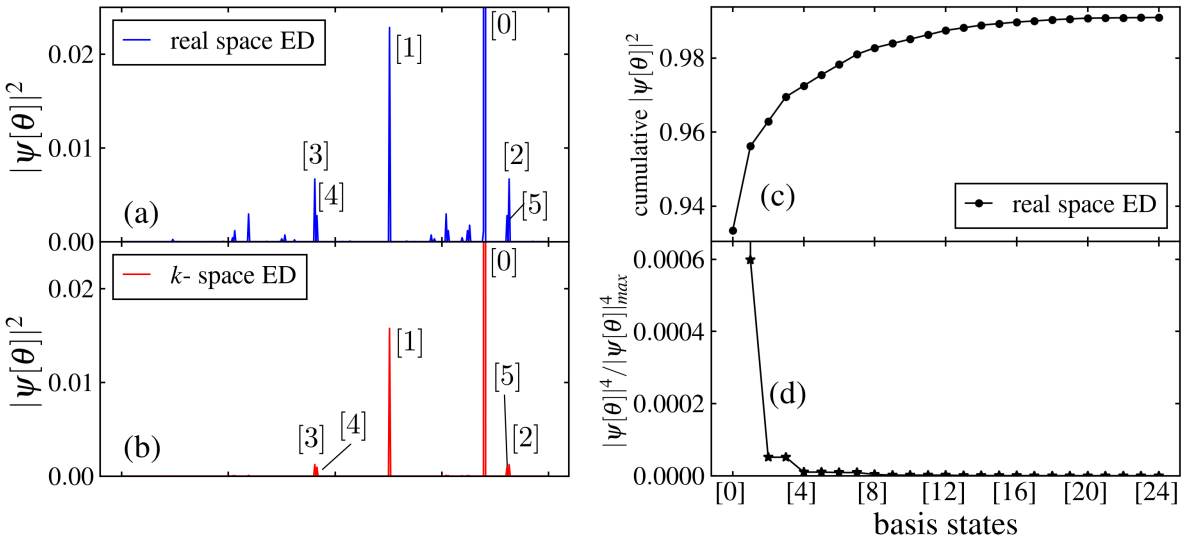

Figure 7.1: **The contribution of the different basis states, $|\Psi[\theta]\rangle$ (Eq. 7.1) to the ground states of the TLL :** (a) The weights, $|\psi[\theta]|^2$ (Eq. 7.3), of different basis states, $|\Psi[\theta]\rangle$ (horizontal axis), for the GS wave-function obtained from (real-space) ED for spinless fermions at the half filling with nearest neighbour density-density interactions (Eq. C.24) for $N = 14, t = 1$ and $V_0 = 0.3$ whence the system is in a TLL phase (see main text and Appendix C.3 for details). The relevant momenta in the first BZ are denoted by $k = -\pi + \alpha\pi/7$ with $\alpha = 0, 1, \cdots, 13$. In this labelling scheme, the six states with leading contributions are shown as $[0] \equiv [00001111111000]$ being the non-interacting GS and the rest corresponding to the particle-hole excitations above it. These are $[1] = [00010111110100]$, $[2] = [00011011110010]$, $[3] = [00100111101100]$, $[4] = [00011101110001]$ and $[5] = [01000111011100]$. The states are arranged in terms of the increasing number of particle-hole excitations which can also be quantified via their root mean square momenta deviation from the FS as defined in Table C.1 in Appendix C.3. Note that the vertical scale has been truncated for improved visibility of the contributing basis states. The normalised weights are given in Table C.1. (b) The same plot as in (a) for ED in momentum space for Hamiltonian in Eq. 7.4 with $V(\mathbf{q})$ given by Eq. 7.9 done using the momentum space cut-off ($n_c = 3$ $\left(q_c = \frac{2\pi}{N} n_c\right)$, $n_0 = 1.5$ $\left(q_0 = \frac{2\pi}{N} n_0\right)$ (see main text for details) for ($N = 14, t = 1$ and $\frac{\tilde{V}_0}{N} = 0.3$. (c) The cumulative weights of the different basis states corresponding to the plot (a). (d) The inverse participation ratio (IPR), defined as $|\psi[\theta]|^4/|\psi[\theta]|^4_{\max}$, for the different basis states corresponding to (a). The IPR has been normalized with respect to the maximum contribution (vertical axis truncated for better visibility) from $[0]$.

7.2 Interacting fermions in 1D: The TLL

To understand the physics of the TLL, we start from Eq. 7.4 and note that the system, for moderate short ranged (in real space) four-fermion interactions, $V_{\mathbf{q}}$, is expected to support a TLL. In particular, $E_{\mathbf{k}} = -2t\cos k$ and $V_{\mathbf{q}} = \frac{\tilde{V}_0}{N} e^{-q^2/(2q_0^2)}$ corresponds to spinless fermions with nearest neighbour hopping (with amplitude t) and short-range density density interactions at half-filling with the Hamiltonian in real space of the form

$$H = -t\sum_i \left(c_i^\dagger c_{i+1} + \text{h.c.}\right) + \sum_{ij} V_{|i-j|} n_i n_j \tag{7.8}$$

where i, j denotes the real-space lattice sites for a one dimensional system with N sites and $n_i = c_i^\dagger c_i$ are the corresponding on-site densities of spinless fermions created by $c_i^\dagger$. As shown in Appendix C.3, the resultant form for the interaction in real space is given by $V(x) = V_0 \exp[-x^2/(2x_0^2)]$ where $x_0 \sim 1/q_0$ controls the spatial extent of the interaction in real space and $V_0 = \tilde{V}_0 q_0/\sqrt{2\pi}$.

For $x_0 \sim a$ (lattice spacing), the nearest-neighbor interactions predominate. In that case, truncating to nearest neighbor interactions, reduces it to the Hamiltonian (Eq. C.24) of spinless fermions at half filling ($N_p/N = \nu = 1/2$) with nearest-neighbor (NN) density-density interactions. We use exact diagonalization (ED) technique to study the GS properties of such fermions interacting with NN density-density interactions ($V_0 \sum_i n_i n_{i+1}$) at half filling (for details, see Appendix C.3). The numerically obtained GS for a finite chain of N sites can indeed be written as a superposition of slater determinants and hence the fermionic wave-functions as envisaged in Eq. 7.3. This is shown in Fig. 7.1 for $N = 14$ and $\nu = 1/2$ where we plot the overlap probabilities and inverse participation ratios (IPRs) of various basis states (slater determinants), $|\Psi[\theta]\rangle$ contributing to the GS wave-function obtained using ED.

Fig. 7.1(a) shows the the six leading order contributions, $|\psi(\theta)|^2$ to the GS. These states, as expected, consist of the non-interacting GS and particle-hole excitations above it. Further details of the weight of these overlaps and the nature of the particle-hole excitation are shown in Table C.1 in Appendix C.3 which include up to 25 basis states ordered in terms of their increasing root-mean square (RMS) momenta and indicating number of particle-hole excitations about the FS. The cumulative weights of these states and their inverse participation ratios are shown in Fig. 7.1(c) and (d) respectively.

It is clear from Fig. 7.1(a,c,d) that, in accordance with expectations [36], only the basis states $|\Psi[\theta]\rangle$ whose distribution in $[\theta]$ differs from that of the non-interacting FS (denoted by $[0]$ in Fig. 7.1) only near its FS has appreciable overlap with the interacting

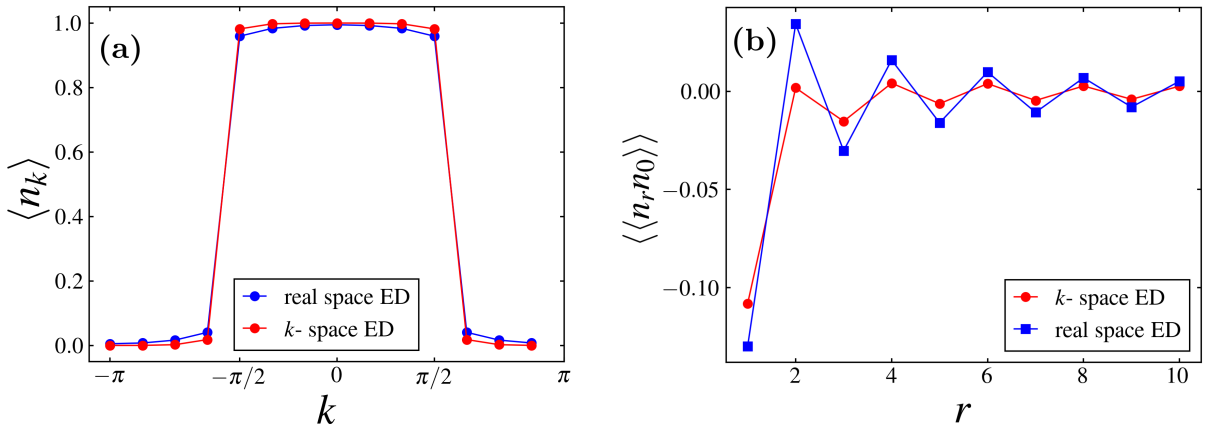

Figure 7.2: **Comparison of the correlation functions in TLL obtained from the real-space and momentum space models :** (a) $\langle n_{\mathbf{k}} \rangle$ calculated from real space ED and k-space ED ($N = 14$) and (b) the two-point connected correlator $\langle\langle n_{\mathbf{r}} n_0 \rangle\rangle$ in real space ($N = 22$). The other parameters are t=1.0, for real space ED $V_0 = 0.3$ (Eq. C.27) and for k-space ED $\frac{\tilde{V}_0}{N} = 0.3$ (Eq. 7.9), $n_c = 3$ $\left(q_c = \frac{2\pi}{N} n_c\right)$, $n_0 = 1.5$ $\left(q_0 = \frac{2\pi}{N} n_0\right)$.

GS wave-function. In fact Figs. 7.1(c) and (d) show that the weight of the GS wave-function is saturated appreciably solely by basis states with particle-hole excitations near the non-interacting FS. Taking cue from this, we consider an effective low energy model in momentum space which accounts for the interactions between the fermions (at half filling) within a window of $\mathbf{k}_F \pm \mathbf{q}_c$. This is obtained by choosing

$$V(\mathbf{q}) = \begin{cases} \frac{\tilde{V}_0}{N} e^{\frac{-q^2}{2q_0^2}} & \forall |\mathbf{q}| \leq |\mathbf{q}_c|, \\ 0 & \text{otherwise.} \end{cases} \tag{7.9}$$

in Eq. 7.6. We performed the ED in momentum space on this Hamiltonian directly in the occupation basis (Eq. 7.1) in momentum space (for details, see Appendix C.3). This is analogous to momentum-space ED adapted to the FS with a soft ($\mathbf{q_0}$) as well as a hard cutoff ($\mathbf{q}_c$) for H (Eq. 7.4). We expect this momentum space model to reproduce the low energy features of the real space nearest neighbor model in the TLL regime as it contains similar low energy physics – scattering of the fermions near the FS.

The contributions of the basis states to the numerically obtained GS of the momentum space model is shown in Fig. 7.1(b). This indicates that the momentum space model indeed correctly captures the dominant basis states contributing to the TLL GS as obtained via the real-space diagonalisation of the nearest neighbor model. This serves as a benchmark of the momentum space ED in terms of the weights of different configurations since they can be compared with their real-space counterparts. We can further benchmark the momentum space ED by comparing different correlators with those obtained from the real space ED for TLL phase of the related models. In this

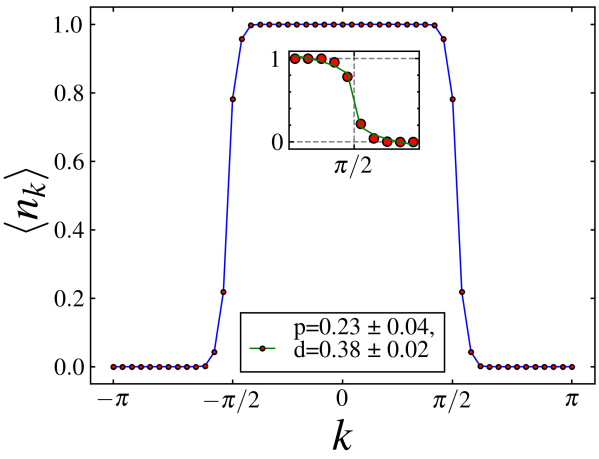

Figure 7.3: A plot of the Fermi distribution function $\langle n_{\mathbf{k}} \rangle$ as a function of k from momentum space ED. The inset shows the curve fitting of $\langle n_{\mathbf{k}} \rangle$ (near the Fermi point) with known bosonization result : $\langle n_{\mathbf{k}} \rangle = d\ \mathrm{sign}(k_f - k)|k - k_f|^p + 1/2$ with $p = (K + K^{-1})/2 - 1$ [2] where K is the Luttinger parameter and d is a constant). For this plot, $t = 1.0$, $\frac{\tilde{V}_0}{N} = 0.6$ (Eq. 7.9), $n_0 = 1.5$, $n_c = 5$ $\left(q_c = \frac{2\pi}{N} n_c\right)$ and $N = 50$.

work we calculate the average momentum occupation, $\langle n_{\mathbf{k}} \rangle$, the two-point connected correlator,

$$\langle\langle n_{\mathbf{r}} n_0 \rangle\rangle \quad = \quad \langle n(\mathbf{r}) n(0) \rangle - \langle n(\mathbf{r}) \rangle \langle n(0) \rangle, \tag{7.10}$$

and the bipartite von-Neumann entanglement entropy, S_{vN}.

The plot of $\langle n_{\mathbf{k}} \rangle$, shown in Fig. 7.2 (a), provides a comparison between the two models and methods of doing ED. The results are in agreement with each other with Fig. 7.2(b) indicating the presence of the FS in both the cases. For the two-point correlator (Eq. 7.10) plotted in Fig. 7.2(b), there is qualitative agreement and the oscillations are dominated by the same length-scale, $2k_f = \pi$. However, the amplitudes of the oscillations are different due to difference in the microscopic details of the two models. Notably, in a TLL the FS does not have a sharp jump, but a point of inflection [2] in the thermodynamic ($N \to \infty$) limit which is cut-off by finite momentum grid in Fig. 7.2(a). While extending the real-space ED to larger systems is numerically quite expensive, the momentum space calculations with the cut-off, $\mathbf{q}_c$ about the FS can be more easily extended to larger system sizes to reveal the form of $\langle n_{\mathbf{k}} \rangle$ as expected from low energy theory of TLL. This is shown in Fig. 7.3 for $N = 50$ and $q_c = 2\pi/10$.

This, therefore, can be compared with the standard bosonization results for $\langle n_{\mathbf{k}} \rangle$ which is devoid of a jump and has a form $\langle n_{\mathbf{k}} \rangle \sim |\mathbf{k} - \mathbf{k}_{\mathrm{F}}|^p$ with $p = (K + 1/K)/2 - 1$ with K being the Luttinger parameter [2]. An estimation of the point of inflection, obtained from such a comparison, is in accordance with the Luttinger theorem. Thus the

basis in Eq. 7.1 effectively captures the TLL GS which has a sharp FS denoted by the point of inflection, but no Landau quasi-particle. This further confirms some advantage in using the basis in Eq. 7.1 and validates the fact that the low energy physics is dominated by FS fluctuations. Finally, we calculate the bi-partite von-Neumann entanglement for both the models and this is shown in Fig. 7.4 as a function of subsystem size. For both the models the entanglement entropy fits well to the Cardy-Calabrese formula (Eq. C.34) [169] for $(1+1)D$ conformal field theory with central charge, $c = 1$ indicating that for the respective parameter values, both the systems are in the TLL phase. However, in this case (also in case of the two-point correlator in real space (Fig. 7.2(b))), the advantage of the momentum space calculations are less evident at this point. This is due to the fact that we are still restricted to smaller sizes due to calculational costs for entanglement entropy. In addition, the estimation of the central charge (Fig. 7.4(b)) is somewhat crude due to the presence of the finite cut-off. On the other hand, while the two-point correlator can be calculated for larger system sizes, it suffers from spurious oscillations arising due to the cut-off, $\mathbf{q}_c$, for parameters similar to Fig. 7.3. Therefore, while promising, our momentum-space ED scheme with cut-off around the FS requires more systematic investigation in future.

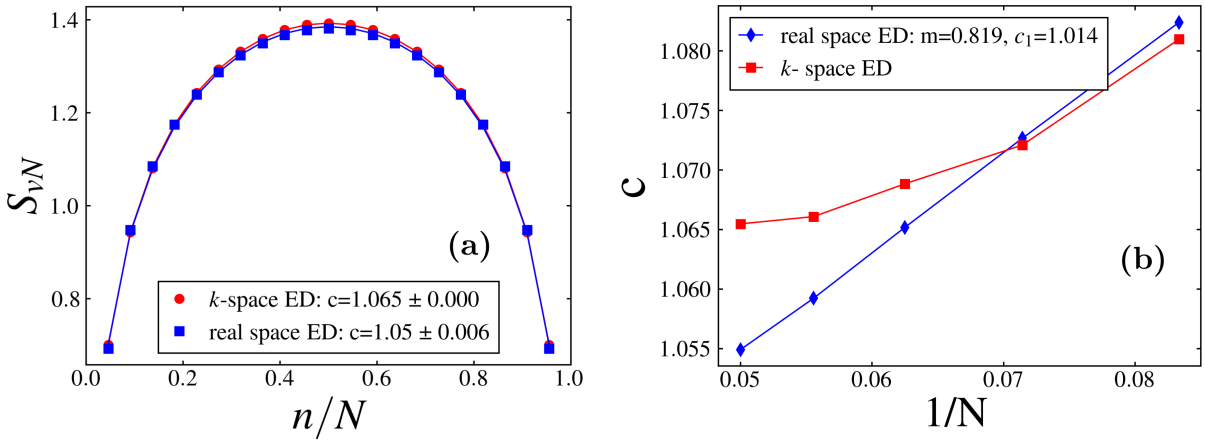

Figure 7.4: **Comparsion of the entanglement entropy for the TLL of the real space and momentum space models :** (a) entanglement entropy from k-space ED and real-space ED, with both datasets (red and blue points) fitted (red and blue lines) to the Cardy-Calabrese formula (b) central charge variation with $1/N$ (we have done linear curve fit ($c = m(1/N) + c_1$) for real space data) for the two ED methods. The system parameters are $t = 1.0$, V_0=0.3 (Eq. C.27), $\frac{\tilde{V}_0}{N} = 0.3$ (Eq. 7.9), $n_c = 3$ $\left(q_c = \frac{2\pi}{N} n_c\right)$, $n_0 = 1.5$ $\left(q_0 = \frac{2\pi}{N} n_0\right)$ and $N = 22$.

7.3 Exactly solvable toy model for GS with FS superposition

Having shown that the basis in Eq. 7.1 may be useful to capture the physics of TLL in 1D, in this section, we study another particularly useful question– are there parent Hamiltonians which allows massive FS fluctuation in the GS ? The positive answer is provided in a simple limit of the Hamiltonian in Eq. 7.7. This is obtained when, for a particular filling $\nu(= N_{\rm P}/N^d)$,

$$\frac{E[\theta]}{E_I([\theta],[\theta'])} = -2\left({}^{N^d}C_{N_p} - 1\right), \tag{7.11}$$

where $E[\theta]$ and $E_I([\theta'],[\theta])$ are respectively the diagonal and off-diagonal matrix elements (Eq. 7.7). In this limit, the Hamiltonian then can be re-written as a sum of projectors $h([\theta],[\theta'])$ as

$$H_{\rm RK} = \mathcal{C} \sum_{[\theta],[\theta'],[\theta]\neq[\theta']} h([\theta],[\theta']), \tag{7.12}$$

where $\mathcal{C} > 0$ is a filling dependent positive constant and

$$h([\theta],[\theta']) = \left(\frac{(|\Psi[\theta]\rangle - |\Psi[\theta']\rangle)}{\sqrt{2}}\right)\left(\frac{(\langle\Psi[\theta]| - \langle\Psi[\theta']|)}{\sqrt{2}}\right), \tag{7.13}$$

with $h^2([\theta],[\theta']) = h([\theta],[\theta'])$ a projector. We note that the condition in Eq. 7.11 may be obtained in systems with all-to-all-interactions.

The Hamiltonian in Eq. 7.12 can be solved in the same spirit as the projector dimer model Hamiltonians by Rokhsar and Kivelson (RK) [71]. The difference between the two models comes from the fact that in the present case the $[\theta]$ basis is orthonormal unlike the hardcore dimer-covering basis of the quantum dimer models with the dimers being spin singlets. The GS wave-function is then easily read off; it is given by the state which are annihilated by $h([\theta],[\theta'])$ for all pairs of $([\theta],[\theta'])$ and constitutes an equal and completely symmetric superposition

$$|\psi_{\rm RK}\rangle = \frac{1}{\sqrt{N_{\rm RK}}}\sum_{[\theta]}|\Psi[\theta]\rangle, \tag{7.14}$$

with $N_{\rm RK}$ being the number of states in the superposition. Notably $\langle\psi_{\rm RK}|\hat{n}_{\mathbf{k}}|\psi_{\rm RK}\rangle = \nu$ for all $\mathbf{k} \in$ BZ. Thus, an equal superposition of all $|\psi(\theta)\rangle$ in momentum space leads to loss of any sharp structure and hence the FS. In fact, this is not very surprising because

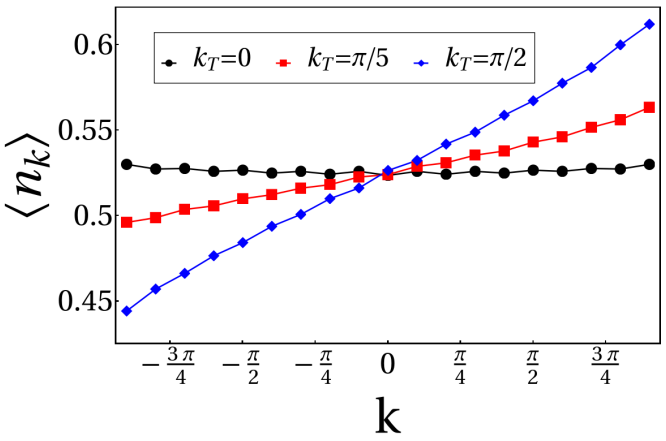

Figure 7.5: Plot of $\langle n_{\mathbf{k}} \rangle$ as a function of k for the constrained RK type projector GSs ($|\psi_{\rm RK}^{\mathbf{k}_T}\rangle$), here we have taken 20 sites for different $\mathbf{k}_T$ for periodic boundary conditions (PBC). Note that n_π(=0) is not shown as in the plot.

the condition in Eq. 7.11 mixes distributions of $[\theta]$ belonging to different momentum sectors and hence the resultant Hamiltonian does not have translation symmetry.

Hence, while it is interesting to study the properties of the generic projector Hamiltonian in Eq. 7.12 (*e.g.*, we plot $\langle n_{\mathbf{r}} \rangle = \langle \psi_{\rm RK} | \hat{n}_{\mathbf{r}} | \psi_{\rm RK} \rangle$ in Fig. C.5 in Appendix C.4 along with few other details), we shall consider a sub-class of Hamiltonian in Eq. 7.12 which conserves total momentum, $\mathbf{k}_T$, at a constant filling, ν (Eq. 7.2) having the form

$$\tilde{H}_{\rm RK} = \sum_{\mathbf{k}_T} H_{\rm RK}^{\mathbf{k}_T} \tag{7.15}$$

where

$$H_{\rm RK}^{\mathbf{k}_T} = \mathcal{C}_{\mathbf{k}_T} \sum_{[\theta],[\theta'] \in \mathbf{k}_T, [\theta] \neq [\theta']} h([\theta],[\theta']) \tag{7.16}$$

with $\mathcal{C}_{\mathbf{k}_T} > 0$ is now dependent on the momentum sector and the sum over $[\theta]$ is restricted to the single $\mathbf{k}_T$ sector.

The lowest energy wave-function in each $\mathbf{k}_T$ sector, $|\psi_{\rm RK}^{\mathbf{k}_T}\rangle$, is now an equal superposition, similar to Eq. 7.14, but with basis states within the $\mathbf{k}_T$ sector. It is fairly easy to show that $\langle \psi_{\rm RK}^{\mathbf{k}_T} | n_{\mathbf{r}} | \psi_{\rm RK}^{\mathbf{k}_T} \rangle = \nu$, *i.e.*, constant (Eq. C.37); moreover, such a constrained RK wavefunctions are translation invariant unlike Eq. 7.14. The average momentum-space occupation, $\langle n_{\mathbf{k}} \rangle$, for such such states in different $\mathbf{k}_T$ sectors are plotted as a function of k in Fig. 7.5 for a 1D fermion system with $N = 20$ and $N_p = 10$, *i.e.*, $\nu = 1/2$ for different k_T (we also put in an extra constraint that $\theta_{\mathbf{k}=\pi} = -1$, *i.e.*, the $\mathbf{k} = \pi$ mode is always empty for convenience – see discussion in Appendix C.4). The slope of $\langle n_{\mathbf{k}} \rangle$ is proportional to $\mathrm{k_T}$; in particular it is flat for the zero momentum sector

with a value tending to ν for large N. For finite systems $\langle n_{\mathbf{k}} \rangle$ shows oscillations (see Appendix C.4), but the amplitude of these oscillations vanishes with increasing system size. This indicates absence of sharp FS-like signature for $|\psi_{\mathrm{RK}}^{\mathbf{k}_{\mathrm{T}}}\rangle$ for large N even in presence of translation symmetry. This is due to the large number of basis states, $|\Psi[\theta]\rangle$, with very different $[\theta]$ distribution contributing to $|\psi_{\mathrm{RK}}^{\mathbf{k}_{\mathrm{T}}}\rangle$ at least for small k_T.

The lowest energy sector of $\tilde{H}_{\mathrm{RK}}$ is macroscopically degenerate. This degeneracy is easily lifted on adding the centre of mass momentum kinetic energy which chooses the $\mathbf{k}_T = 0$ sector. Notably such symmetric wave-function with zero net momentum is not expected to be unique at fractional filling due to Lieb-Schultz-Mattis (LSM) theorem [166] and hence the above RK wavefunctions most likely corresponds to the GS of a gapless phase. It would be interesting to explore the nature of such possible gapless phase without a sharp FS.

7.4 Fixed-point wave-functions: fermi surface superposition in two dimensions

The RK construction of the superposition of FS provides important clues to generating the trial wave-functions in higher dimensions. It shows that a generic superposition completely destroys the central feature of the metallic GS – the FS. This raises an interesting question – can we superpose FS but still partially retain properties of metals– both weakly and strongly correlated ones? In this section we investigate this question by constructing a series of trial wave-functions in 2D which interpolates between non-fluctuating FS in the free Fermi-gas limit and the systematically superposing $|\Psi[\theta]\rangle$ corresponding to smooth distortions of the FS (subset of Eq. 7.3). We expect it to capture the phenomenology of correlated metals. We note here that it is possible to write appropriate RK-like parent projector Hamiltonians for which some of the wave-functions (those with equal superposition) that we discuss below are exact GSs. Such wave-functions can be thought as a IR fixed-point wave-functions describing the GS of correlated metals.

One way to obtain such wave-functions is by choosing $\psi[\theta]$ such that various microscopic symmetries beyond translation are implemented manifestly via $[\theta_{\mathbf{k}}]$. For example, under time reversal $\theta_{\mathbf{k}} \to \theta_{-\mathbf{k}}$ while for a generic spatial symmetry $\mathcal{R}$, we get $\theta_{\mathbf{k}} \to \theta_{\mathcal{R}[\mathbf{k}]}$. To incorporate the symmetries we then need to choose $\psi[\theta]$ in Eq. 7.3 such that the distribution of $[\theta]$ and $[\theta']$ that are connected by symmetry transformation are weighted equally, i.e. $\psi[\theta] = \psi^*[\theta']$ for TR and $\psi[\theta] = \psi[\theta']$ with spatial symmetries. We shall focus on the case of TR symmetric systems which is achieved by

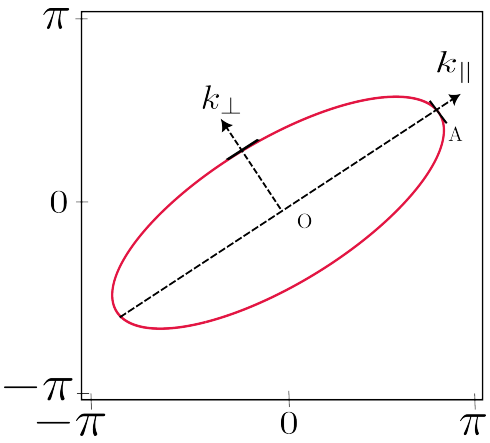

Figure 7.6: Schematic Figure of an elliptical FS (Eq. C.38) with major axis along $k_{||}$ and eccentricity ϵ.

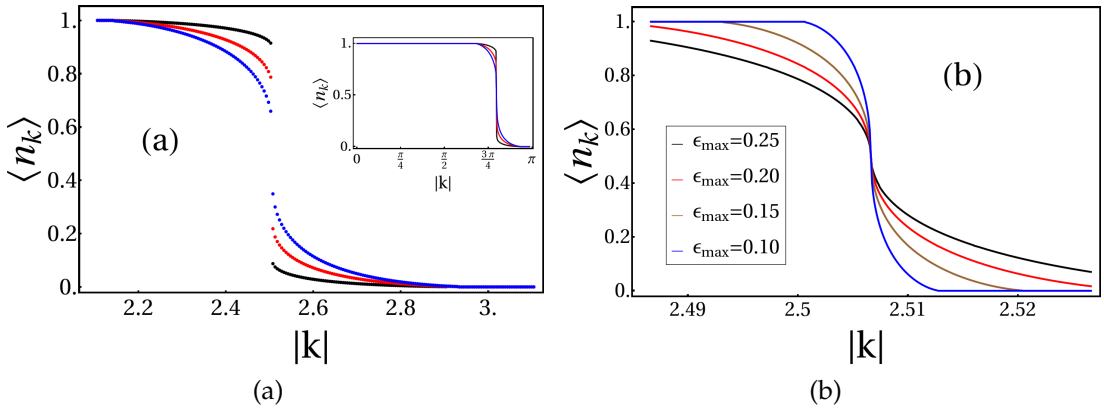

Figure 7.7: (a) $\langle n_{\mathbf{k}} \rangle$ (in the vicinity of FS) vs. k for Eq. 7.20 with $\epsilon_0 = 0$, $\epsilon_{\max} = 0.7$, and $Z_{\epsilon_0,\hat{\mathbf{k}}_0} = 0.8$ (black), 0.5 (red), 0.2 (blue). Inset: $\langle n_{\mathbf{k}} \rangle$ for $k \in (0, \pi)$. The jump in $\langle n_k \rangle$ equals $Z_{\epsilon_0,\hat{\mathbf{k}}_0}$.(b) $n_{\mathbf{k}}$ vs. k for the isotropic NFL (Eq. 7.21) near the FS ($k_F = \sqrt{2\pi}$).

considering $[\theta]$ to be symmetric about $\mathbf{k} = 0$ and $\psi[\theta]$ to be real. Other symmetries are implemented in a similar manner. We focus on two situations– (1) isotropic, and, (2) square lattice which have different spatial symmetries.

Finally, Eq. 7.1 contains arbitrary distributions of $\{n_{\mathbf{k}}\}$ over the entire BZ subject to the constraints given by Eq. 7.2. We note that at low energies, various interaction terms can only cause scattering near the FS [36] similar to the case of TLL in the previous section. In contrast, in higher dimensional systems with Yukawa interactions that hosts NFLs, the RG relevant tangential scatterings [155] around the FS lead to a large number of fermion-hole excitations. These excitations ultimately lead to the breakdown of the Landau quasi-particle. However, the proliferation of the such fermion-hole excitation, particularly on integrating out the boson, would lead to change in the distribution of $\{n_{\mathbf{k}}\}$ via low energy processes. For the rest of this chapter, we assume that these low energy processes lead to smooth deformation of the FS and basis states of the form in

Eq. 7.1 which represents such smooth deformation have non-zero amplitude in the GS wave-function that we focus on.

Noting this, we consider the basic fluctuations of an elliptic distribution of $[\theta]$ which describes an elliptic FS centered around origin ($\mathbf{k}_T = 0$ in Eq. 7.2), at filling, ν, with eccentricity ϵ and major axis along $\hat{\mathbf{k}}$ in the 2D momentum space. An example is shown in Fig. 7.6. We denote such a sub-set of these basis state wave-function (Eq. 7.1) as $|\epsilon, \nu, \hat{\mathbf{k}}\rangle$ (see Appendix C.5 for details). The generic wave-function for superposition of such *elliptical* FS is given by

$$|\Psi_\nu\rangle = \int_0^{\epsilon_{\max}} d\epsilon \int_0^{\pi} d\hat{\mathbf{k}}\ \psi(\epsilon, \hat{\mathbf{k}}) |\epsilon, \nu, \hat{\mathbf{k}}\rangle, \tag{7.17}$$

where the first integral is over the eccentricity between $[0, \epsilon_{\max}(\leq 1)]$ for the elliptical distribution with major axis along $\hat{\mathbf{k}}$ and the second integral denotes the sum over all possible directions of the major axis. To impose the filling constraint, all the participating ellipses for which the amplitude $\psi(\epsilon, \hat{\mathbf{k}})$ is non-zero, have same area and for the rest of this work we set $\nu = 1/2$.

It is fairly easy to show that such wave-functions have uniform fermion density in real space, *i.e.*, $\langle \Psi_e | n_{\mathbf{r}} | \Psi_e \rangle = \nu$, unlike the generic RK wave-functions (Eq. 7.14) (see Appendix C.5). However, not surprisingly, depending on the form of $\psi(\epsilon, \hat{\mathbf{k}})$, its single particle signatures can be rather different from that of a FL. This is seen by calculating the single particle residue, $Z_{\epsilon, \hat{\mathbf{k}}}$, defined via the single particle correlator [170] for an elliptical FS, *i.e.*, a basis state $|\epsilon, \nu = 1/2, \hat{\mathbf{k}}\rangle \equiv |\epsilon, \hat{\mathbf{k}}\rangle$ (details in Appendix C.5),

$$Z_{\epsilon, \mathbf{k}} = \lim_{\delta \to 0^+} \frac{\delta^2}{\left(\frac{k_\parallel^2}{a^2} + \frac{k_\perp^2}{a^2(1-\epsilon^2)} - \mu \right)^2 + \delta^2}, \tag{7.18}$$

where μ fixes the filling, ν, for the elliptic FS of eccentricity ϵ and area $A = \pi \mu a^2 \sqrt{1-\epsilon^2}$ and $k_\parallel (k_\perp)$ are momentum components resolved along (perpendicular to) the major axis along $\hat{\mathbf{k}}$ as shown in Fig. 7.6. For a single elliptic FS, the residue shows a jump at the perimeter of the ellipse as expected (Fig. C.8), signaling the presence of the FS which can then be used to define long-lived low energy quasi-particles. For the superposed elliptical FS (Eq. 7.17) then, the *averaged* residue is given by

$$Z = \int_0^{\epsilon_{\max}} d\epsilon \int_0^{\pi} d\hat{\mathbf{k}} |\psi(\epsilon, \hat{\mathbf{k}})|^2 Z_{\epsilon, \hat{\mathbf{k}}}. \tag{7.19}$$

Importantly, Eq. 7.19 recovers the FL form for

$$\psi(\epsilon, \hat{\mathbf{k}}) = \sqrt{Z_{\epsilon_0,\hat{\mathbf{k}}_0}}\, \delta(\epsilon - \epsilon_0)\, \delta(\hat{\mathbf{k}} - \hat{\mathbf{k}}_0) + \sqrt{\frac{1 - Z_{\epsilon_0,\hat{\mathbf{k}}_0}}{\pi \epsilon_{\max}}}, \tag{7.20}$$

for $Z_{\epsilon_0,\hat{\mathbf{k}}_0} \in [0,1]$. The resultant momentum space occupancy of the fermions $\langle n_{\mathbf{k}} \rangle$ is shown in Fig. 7.7 where we chose $\epsilon_0 = 0$ (*i.e.*, circular FS) for convenience. The quasi-particle residue, by construction, is $Z_{\epsilon_0,\hat{\mathbf{k}}_0}$ and represents the non-interacting limit for $Z_{\epsilon_0,\hat{\mathbf{k}}_0} = 1$. Further details are given in Appendix C.5.2.

The above form of the wave-function (Eq. 7.20) naturally leads us to investigate the case where the weight of the δ-function goes to zero such that

$$\psi(\epsilon, \hat{\mathbf{k}}) = \frac{1}{\sqrt{\epsilon_{\max}}} \frac{1}{\sqrt{\pi}}. \tag{7.21}$$

The resultant plot of $\langle n_{\mathbf{k}} \rangle$ is shown in Fig. 7.7 for different extent of superposition of eccentricities obtained by changing $\epsilon_{\max}$ (further details in Appendix C.5.2). Notably for finite $\epsilon_{\max}$, the jump in the occupancy is systematically smeared out as is evident by comparing the two panels of Fig. 7.7. This is further confirmed by calculating the residue using Eqs. 7.18 and 7.19 as shown in C.10(b) for various $\epsilon_{\max} \neq 0$ which shows that $Z = 0$. However, instead the residue is replaced by a point of inflection (see Fig. C.9d in Appendix C.5.2) somewhat similar to the TLL in 1D. The position of the point of inflection as well as the finite resolution jump of $\langle n_{\mathbf{k}} \rangle$ is shown in Fig. 7.8. Notably the contour of the inflection point encloses an area in accordance with the Luttinger theorem in spite of the single particle residue being zero. Thus the presence of the inflection point sharply defines the position of the FS, while $Z = 0$ indicates the absence of Landau quasi-particles similar to the critical FS [142] or marginal FLs [171,172]. Similar to the TLL, the average momentum mode occupancy is a power-law, *i.e.*, $\langle n_{\mathbf{k}} \rangle \sim |\mathbf{k}_F - \mathbf{k}|^p$ with $p \geq 0$ (see Fig. C.11) and p increases monotonically with $\epsilon_{\max}$. This power-law form is consistent with the scaling form suggested in Ref. [142]. Fig. 7.9 shows the two-point connected correlator $W(\mathbf{r}, 0) = \langle\langle n_{\mathbf{r}} n_0 \rangle\rangle$ as a function of $r = |\mathbf{r}|$(see Appendix C.5.3 for detailed expressions) for the wave-functions given by Eq. 7.20 for $\epsilon_{\max} = 0.75$ and different $Z_{\epsilon_0,\hat{\mathbf{k}}_0}$ (including $Z_{\epsilon_0,\hat{\mathbf{k}}_0} = 0$ whence we get Eq. 7.21). The only difference between the non-interacting limit ($Z_{\epsilon_0,\hat{\mathbf{k}}_0} \to 1$) and the completely superposed limit ($Z_{\epsilon_0,\hat{\mathbf{k}}_0} \to 0$) seems to be in the amplitude of oscillations while other features survive the loss of single-fermion quasi-particle as signalled by the vanishing residue. Notably the similarity of the forms and the decaying oscillations shows that even for the fully superposed case, the density correlations decay, albeit as a power-law, to zero such that the superposed wave-function obeys cluster

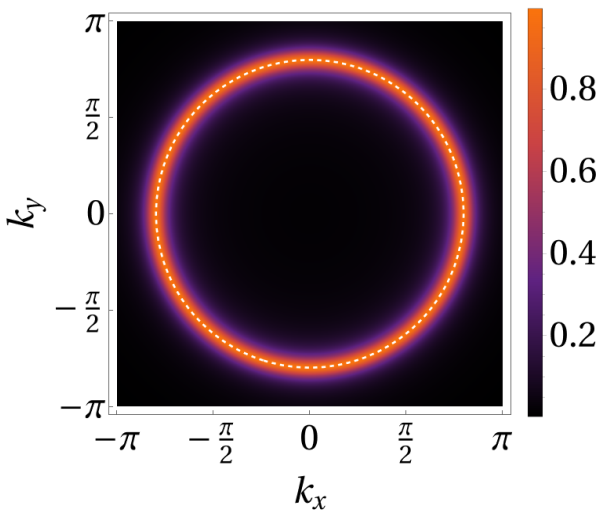

Figure 7.8: Plot of the single particle residue Z as a function of k_x and k_y for the superposed FS corresponding to the wave-function in Eq. 7.21 for $\epsilon_{\max} = 0.2$ and $\delta = 0.12$. Note that the residue is uniform and is ≤ 1; it $\to 0$ as $\delta \to 0$ for $\epsilon_{\max} \neq 0$. The maximum value of Z (for finite δ) is at the perimeter of circle of radius=$\sqrt{2\pi}$ (dashed contour) that also marks the position of the point of inflection of $n_{\mathbf{k}}$. See text for details.

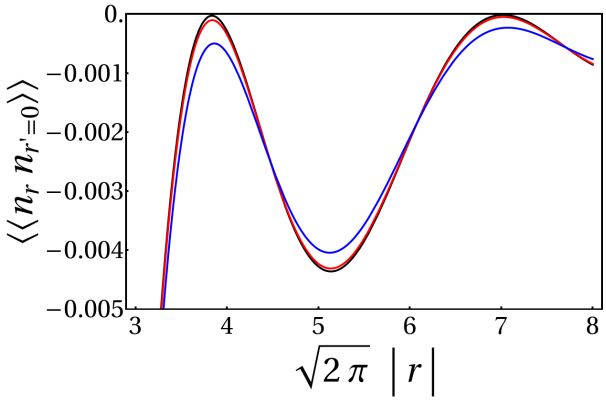

Figure 7.9: Plot of the density-density correlation $W(\mathbf{r}, \mathbf{0}) = \langle\langle n_{\mathbf{r}} n_0 \rangle\rangle$ as a function of $r = |\mathbf{r}|$ corresponding to state Eq. 7.20 for $\epsilon_{\max} = 0.75$ and different values of $Z_{\epsilon_0, \hat{\mathbf{k}}_0} = 0.95$ (black), 0.80(red) and 0.00 (blue).

decomposition principle as is expected from a physical state [44].

Finally, we move to the case of the square lattice where we only have a four-fold rotational symmetry. This should be reflected in the choice of the amplitudes in Eq. 7.17 via constraining them for different ellipses related by a four-fold rotation as discussed above. For illustrative purposes, in this case, we choose the major axis of the ellipses to lie along the Cartesian directions $\hat{\mathbf{x}}$ and $\hat{\mathbf{y}}$ such that we now have

$$\psi[\epsilon, \hat{\mathbf{k}}] = \sum_{\boldsymbol{\alpha}=\hat{\mathbf{x}},\hat{\mathbf{y}}} \psi(\epsilon)\delta(\hat{\mathbf{k}} - \hat{\boldsymbol{\alpha}}), \tag{7.22}$$

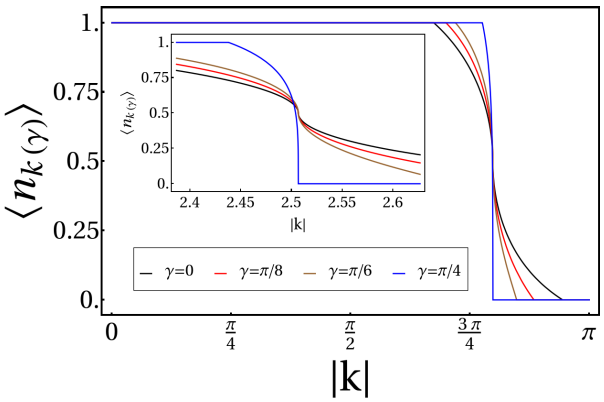

Figure 7.10: Plot of $\langle n_{\mathbf{k}} \rangle$ as a function of k, where $\mathbf{k} = (k\cos\gamma\ ,\ k\sin\gamma)$ for the superposed state mentioned in Eq. 7.23 for different γ and $\epsilon_{\max} = 0.7$. The inset shows $\langle n_{\mathbf{k}} \rangle$ as a function of k in the vicinity of the FS.

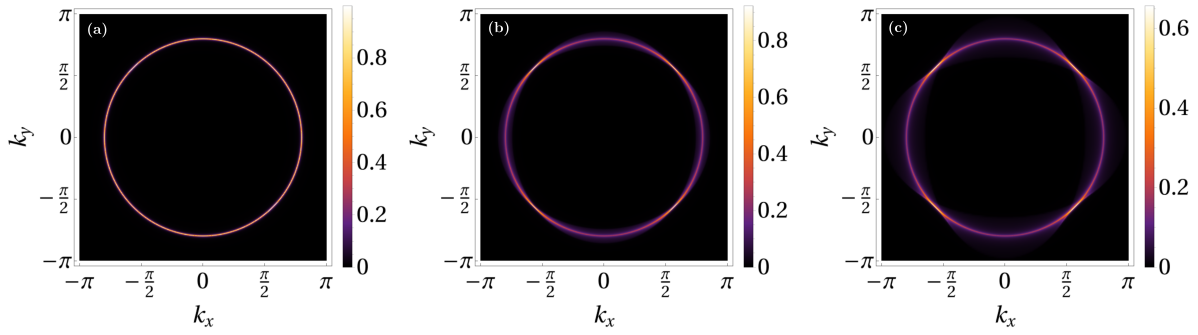

(a) $\epsilon_{\max} = 0.10$ (b) $\epsilon_{\max} = 0.50$ (c) $\epsilon_{\max} = 0.75$

Figure 7.11: Plot of Z as a function of k_x and k_y for the superposed states (Eq. 7.23) with $\delta = 0.01$. Panels show results for (a) $\epsilon_{\max} = 0.10$, (b) $\epsilon_{\max} = 0.50$, and (c) $\epsilon_{\max} = 0.75$. Variations of Z with δ are shown in Fig. C.12.

where $\psi(\epsilon)$ is a smooth real (to ensure TR) function of ϵ such that Eq. 7.17 reduces to

$$|\Psi_s\rangle = \int_0^{\epsilon_{\max}} d\epsilon\ \psi(\epsilon) \frac{(|\epsilon, \hat{\mathbf{x}}\rangle + |\epsilon, \hat{\mathbf{y}}\rangle)}{\sqrt{2}}. \tag{7.23}$$

This is nothing but equally superposing ellipses of eccentricity up to $\epsilon_{\max}$, but with major axis only restricted to horizontal and vertical directions with equal amplitude for any given ϵ. We note that dynamic lattice nematic fluctuations of the type discussed in context of cuprate superconductors [173] can possibly lead to such superpositions of the FS. Choosing different functions $\psi(\epsilon)$ result in superposing the above set of ellipses with varying amplitudes and leads to different wave-functions with manifest TR and lattice symmetries. Consider, for example, $\psi(\epsilon) = \frac{1}{\sqrt{\epsilon_{\max}}}$ that correspond to an equal superposition of all such ellipses (see Appendix C.5.2 for further details).

The momentum space occupation is shown in Fig. 7.10 for different directions γ (the angle with respect to k_x). As can be seen from the figure (see inset), in contrast

to Fig. 7.7, both the position of the rapid change of $\langle n_{\mathbf{k}} \rangle$ and its form depends on γ (being sharpest for $\gamma = \pm\pi/4$). This is reflected in the finite resolution quasi-particle residue (Eq. 7.19) plotted in Fig. 7.11 for different extent of superposition of eccentricities, $\epsilon_{\max}$ and finite resolution, δ (Eq. 7.18). Notably, on taking $\delta \to 0$ (see Fig. C.10(c) in Appendix C.5.2) the residue goes to zero for all momentum points. However, unlike the isotropic case, it goes to zero anisotropically with the contrast of the anisotropy increasing with $\epsilon_{\max}$; this is revealed by comparing the finite resolution leftmost ($\epsilon_{\max} = 0.1$) and the rightmost ($\epsilon_{\max} = 0.75$) plots of Fig. 7.11. In other words, now we get $\langle n_{\mathbf{k}} \rangle \sim |\mathbf{k_F} - \mathbf{k}|^{p(\gamma)}$ such that for a given $\epsilon_{\max}$, the exponent $p(\gamma)$ depends on the angle; this is in accordance with the scaling form expected in Ref. [142]. However, we note that the above simple power-law breaks down very close to the $\gamma = \pi/4$ (and equivalent points).

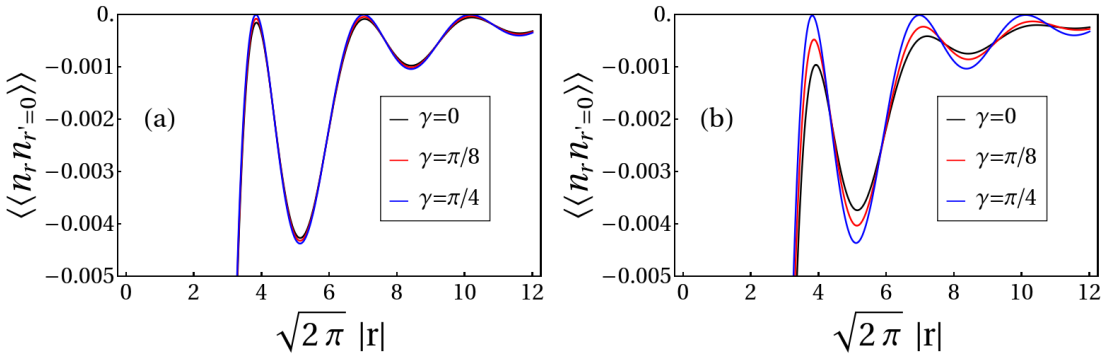

(a) $\epsilon_{\max} = 0.5$ (b) $\epsilon_{\max} = 0.75$

Figure 7.12: Plot of $\langle\langle n_{\mathbf{r}} n_{\mathbf{r}'=0} \rangle\rangle$ ($W(\mathbf{r}, \mathbf{0})$) as a function of $r = |\mathbf{r}|$ for the superposition of elliptical FSs (Eq. 7.23) in different directions ($\tan\gamma = \frac{y}{x}$): (a) $\epsilon_{\max} = 0.5$ and (b) $\epsilon_{\max} = 0.75$.

Concentrating on Fig. 7.11(c), we find that the largest residue at finite resolution, $Z_{\max}(\delta)$, always occur along the $k_x = \pm k_y$ lines with the maximum at $(\sqrt{\pi}, \sqrt{\pi})$ (Fig. C.15) for all $\epsilon_{\max}$ (Figs. 7.11 and C.13) and goes to zero parametrically more slowly compared to the other directions such that at finite resolution we get a smeared residue around these directions as shown in Fig. 7.11.

One can ascribe a *length* to such segments of finite resolution residue as a function of both δ and $\epsilon_{\max}$ as mentioned in Fig. C.16 of Appendix C.5.2. Finally turning to the density-density-correlator, $\langle\langle n_{\mathbf{r}} n_{\mathbf{r}'} \rangle\rangle$, the Friedel oscillations now become highly direction dependent as shown in Fig. 7.12, but still decays with a power-law in accordance with the expectation from the cluster decomposition principle [44]. This completes the phenomenology of the one and two particle static correlations of the many-fermion wave-function obtained by superposition of ellipses.

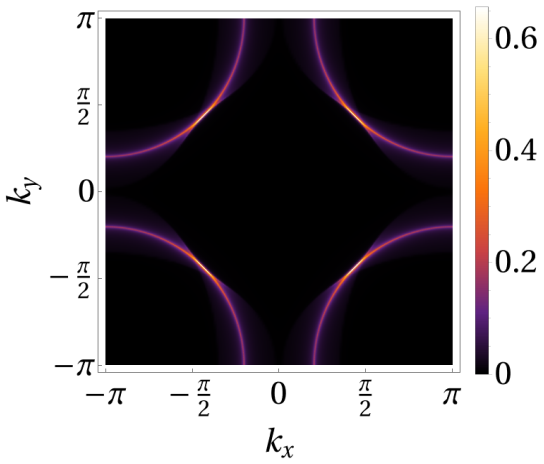

Figure 7.13: Plot of Z as a function of k_x and k_y for superposed states (Eq. 7.23) for a hole FS centered around $\mathbf{k} = (\pi, \pi)$.

7.5 Summary and outlook

Having described the construction of many-fermion trial wave-functions via superposition of FS that can possibly describe correlated metals including NFLs, we now summarize our main results.

The trial wave-function of the form in Eq. 7.3 provide interesting insights into the two basic phenomenology of NFL metals– (1) the lack of Landau quasi-particles, and (2) the well defined FS– that are obtained from quantum superposition of momentum space occupation. In view of the anisotropic loss of Landau quasi-particles on square lattice, it is interesting to re-plot Fig. 7.11 for the hole FS centered around $\mathbf{k} = (\pi, \pi)$. This is shown in Fig. 7.13 where the similarity with Fermi-arcs in underdoped cuprates [174] is apparent. However in cuprates such phenomena is observed at finite temperature while the present construction is strictly for the GS, *i.e.*, $T = 0$; in underdoped cuprates, a superconductor is obtained at lower temperatures. It has been suggested [142] that Fermi arcs can arise as a finite temperature effect of critical FS with angle-dependent scaling exponents. It would indeed be promising to investigate if similar low energy phenomenology can be obtained starting from the wave-function presented here.

Turning back to structure of the basis (Eq. 7.1), consider a distribution $[\theta]$ representing a fully filled FS, $|\Psi[\theta]\rangle$, at filling ν. Now consider a related state, $|\Psi[\theta']\rangle$, at the same filling obtained from $[\theta]$ by taking a particle at $\mathbf{k}_1$ from inside the FS and putting it at an empty mode at $\mathbf{k}_2$. Then, superposing the above two results in a EPR (Einstein Podolsky Rosen) pair in momentum space for a particle and hole at the two specified momenta in the background of the rest of the fermions. At low energies, both $\mathbf{k}_1$ and $\mathbf{k}_2$ lie within an annulus around the FS– hence local in momentum space.

Thus, the GSs obtained by superposing the FS may be roughly thought as made up of *local* (in momentum space) particle-hole EPR pairs across the FS. It would be interesting to explore if this point provides advantage in understanding metallic phases using density-matrix-renormalization-group (DMRG) methods in momentum space [175].

At low energies, both $\mathbf{k}_1$ and $\mathbf{k}_2$ lie within an annulus around the FS– hence local in momentum space. Thus, the GSs obtained by superposing the FS may be roughly thought as made up of *local* (in momentum space) particle-hole EPR pairs across the FS. It would be interesting to explore if this point provides advantage in understanding metallic phases using density-matrix-renormalization-group (DMRG) methods in momentum space [175].

Extending the present formulation to spinful fermions can be obtained by defining a augmented momentum-space grid $\{\mathbf{k}, \sigma\}$ with $\sigma = \uparrow\downarrow$. Finally, the present ground-states immediately lead to questions pertaining to the low energy spectrum both within and beyond the RK type Hamiltonians. At this point we note that the trial wave-functions (Eq. 7.3 or 7.17), after implementing the symmetries, represent symmetric wave-functions at fractional filling, ν. Application of LSM theorem [141, 166] would suggest that this corresponds to the GS of a gapless phase as is indeed the case of the half filled spinless fermions with nearest neighbour interactions as our calculations explicitly show. In higher dimensions, application of flux threading arguments of Ref. [138] indicate that it is possible to generate orthogonal states with momentum difference $2\pi\nu N^{d-1}$. For Hamiltonians which are short ranged (in real space) two dimensional generalization of LSM theorem [138,167] would lead to a similar conclusion as in 1D about the fate of the present wave-functions in regards to them being valid GSs of gapless phases. Addressing these issues would decide the feasibility of the present approach to understand the physics of correlated metals.

Chapter 8

"Every new beginning comes from some other beginning's end."

- Lucius Annaeus Seneca

Summary and Outlook

This thesis investigates the interplay between microscopic symmetries and many-body entanglement in the low-energy theory for two cases: spin–orbit-coupled SU(8) Dirac fermions on the honeycomb lattice and Z_2 fractionalized phases.

For the spin–orbit–coupled system, we investigated the possible superconducting phases that can be realized for spin–orbit–coupled SU(8) Dirac fermions on the honeycomb lattice. Our analysis identifies 12 distinct superconducting phases, broadly classified into four lattice singlets, two lattice doublets, and six lattice triplets. All of these are multiband superconductors, encompassing non-unitary (multi-gapped) superconductors, nodal superconductors, and pair-density-wave superconductors. We provide a detailed characterization of these phases, including their spectra, vortex structures, and possible lattice realizations.

One of the central outcomes of this study is the identification of multiple-gap superconductors whose gap magnitudes can be tuned via the direction of the superconducting order parameter, thereby enabling a transition from a gapped superconductor to a nodal one. This tuning gives rise to a variety of unconventional superconductors, including a particularly notable case: an unconventional even-parity non-unitary superconductor. Moreover, the ability to control pairing gaps and the associated relative phases motivates interesting questions about the corresponding Leggett modes [104, 113] for future investigation. The catalogue of unconventional superconductors presented in this thesis raises several open questions. Given the diversity of unconventional phases discussed here, an important avenue for future study is the classification of their topological properties [93, 176–180] and the implications for various tunnel junctions [181] involving these superconductors [182]. Another question concerns the nature of unconventional quantum phase transitions [183] between these superconducting phases and the corresponding normal phases, which are intimately connected at low energies via an emergent SO(16) symmetry. We hope that

these results will stimulate experimental efforts on candidate materials [49], providing concrete platforms to explore such phenomena. Finally, a similar analysis applies to systems with an even number of surface Dirac cones in weak topological insulators, which are also stabilized by strong spin–orbit coupling, although the symmetry of the corresponding low-energy Dirac theory differs from SU(8).

For the case of Z_2 fractionalization of spinless fermions, we considered a particular regime of the model in which the fractionalized degrees of freedom are frustrated. Understanding this regime through the projective implementation of microscopic symmetries proves to be a powerful approach for exploring the behavior of fermions as the Ising spins undergo a transition from the ordered to the disordered phase. The symmetry analysis forbids any quartic coupling between the Ising field and Dirac fermions that could generate a mass term for the fermions, thereby ensuring that they remain gapless. Although our results indicate that such terms are not allowed by symmetry, a systematic understanding of the underlying reason for this prohibition remains an open question. In the absence of fermions, when the model is supplemented with a potential term for dimers [71], it provides a pathway to interpolate between the physics of dimers and topologically ordered phases, leading to a rich phase diagram. Using iDMRG, we investigated this phase diagram—our finite-size numerics indicate the presence of three distinct phases: the columnar/plaquette-ordered phase, the staggered-ordered phase, and the topological liquid phase. These are separated by three phase boundaries corresponding respectively to the RK transition between the staggered and columnar/plaquette-ordered phases, the $3D\ XY^*$ transition between the topological liquid and the columnar/plaquette-ordered phase, and a first-order transition between the topological liquid and staggered-ordered states. Our numerical results suggest the possibility that these three phase boundaries meet at a multicritical point. Exploring the nature of this multicritical point—where two Landau-forbidden transitions intersect a first-order line—poses an intriguing question. Another interesting direction concerns the reintroduction of fermions: how do they influence or modify the nature of these transitions?

In the third part of this thesis, we introduce a trial wavefunction approach that captures the phenomenology of both Fermi-liquid and non-Fermi-liquid phases. We examined various observables in these ground states; however, an interesting direction for future study is to compute the bipartite entanglement of these states. In addition, the present ground states naturally motivate questions concerning the low-energy spectrum, both within and beyond Rokhsar–Kivelson (RK)–type Hamiltonians. .

Appendix A

Appendix for Superconductivity in Spin-Orbit coupled system

A.1 Summary of the low-energy Dirac theory in the global basis

The low-energy Hamiltonian in the global basis (Fig. 2.1) is obtained by performing a unitary transformation on the Dirac spinors in the local basis, χ (Eq. 2.10),

$$\chi_g = U_{global} \ \chi. \tag{A.1}$$

where U_{global} is a 16×16 unitary matrix whose explicit form is given in Ref. [40] and χ_g is the spinor in the global basis, *i.e.*,

$$\chi_g = (\chi_{g\Gamma}, \chi_{gM_1}, \chi_{gM_2}, \chi_{gM_3})^T \tag{A.2}$$

where each χ_{gv} corresponds to a 4-component spinor corresponding to the Dirac fermions at the four valleys $v = (\Gamma, M_1, M_2, M_3)$ in the global basis (Fig. 2.1). The low-energy Hamiltonian (Eq. 2.1) in the global basis is then given by

$$H_D = iv_F \int d^2\mathbf{x}\, \chi_g^\dagger \left[\left(\Sigma_0 \tilde{\Sigma}_{23}\right) \partial_1 + \left(-\Sigma_0 \tilde{\Sigma}_{24}\right) \partial_2 \right] \chi_g. \tag{A.3}$$

Here, Σ_0 represents the four Dirac valleys in the global basis. The $\tilde{\Sigma}_i$ are 4×4 Hermitian matrices which are of the same form as the Σ_i matrices (appendix C of Ref. [40]), but, unlike the Σ_i matrices, they do not exclusively act on the flavour space.

A.2 The BdG Hamiltonian and the pairing amplitudes for the Dirac superconductors

The BdG Hamiltonian for the SU(8) Dirac fermions is given by [85,87]

$$H_{MF} = \int d^2\mathbf{q}\, \tilde{\chi}_N^\dagger(\mathbf{q})\, \mathcal{H}_{BdG}(\mathbf{q})\, \tilde{\chi}_N(\mathbf{q}) \tag{A.4}$$

where

$$\tilde{\chi}_N(\mathbf{q}) = [\chi(\mathbf{q}), (\mathcal{T}\chi(\mathbf{q}))^*]^T \tag{A.5}$$

is the Nambu spinor with χ given by Eq. 2.10 and $\mathcal{T}$ is the TR symmetry operator such that [40]

$$\mathcal{T}\chi(\mathbf{q}) = i\Sigma_{13}\tau_1\sigma_0\mathcal{K}\chi(-\mathbf{q}) = i\Sigma_{13}\mathcal{K}[\tau_1\chi_1, \tau_1\chi_2, \tau_1\chi_3, \tau_1\chi_4]^T \tag{A.6}$$

with $\mathcal{K}$ being the complex conjugation operator and

$$\tau_1\chi_f = (\chi_{f1-}, \chi_{f2-}, \chi_{f1+}, \chi_{f2+}) \tag{A.7}$$

where χ_f is given by Eq. 2.7. Putting everything together, Eq. A.5 becomes

$$\tilde{\chi}_N(\mathbf{q}) = \begin{pmatrix} \mathbb{I}_{16} & 0 \\ 0 & i\Sigma_{13}\tau_1\sigma_0\mathcal{K} \end{pmatrix} \begin{pmatrix} \chi(\mathbf{q}) \\ \chi^*(-\mathbf{q}) \end{pmatrix} \equiv \mathcal{Y}\cdot\chi_N \tag{A.8}$$

where χ_N is defined in Eq. 2.18. Finally,

$$\mathcal{H}_{BdG}(\mathbf{q}) = \begin{pmatrix} \hat{\varepsilon}_\mathbf{q} & \hat{\Delta}_\mathbf{q} \\ \hat{\Delta}_\mathbf{q}^\dagger & -\hat{\varepsilon}_\mathbf{q} \end{pmatrix} \tag{A.9}$$

with $\hat{\varepsilon}_\mathbf{q} = \frac{v_F}{2}\Sigma_0(\alpha_1 q_x + \alpha_2 q_y)$ being the free Dirac Hamiltonian and $\hat{\Delta}_\mathbf{q}$ being the pairing matrix.

The relation between the form of H_{MF} in Eq. A.4 and that of Eq. 2.21 is obtained via the transformation

$$\mathcal{Y}^{-1}\cdot\mathcal{H}_{BdG}\cdot\mathcal{Y} = \frac{v_F}{2}(\tilde{\alpha}_1 q_x + \tilde{\alpha}_2 q_y) + M^{SC} \tag{A.10}$$

where the two terms in the RHS are given by Eqs. 2.19 and 3.3 respectively. Note that under the above transformation, $\hat{\Delta}\cdot\hat{\Delta}^\dagger$ remains invariant.

Eq. A.4 is diagonalized [10] via Bogoliubov transformations

$$\tilde{\chi}_N(\mathbf{q}) = \mathcal{W}_{\mathbf{q}}\Gamma(\mathbf{q}) \tag{A.11}$$

where $\Gamma(\mathbf{q})$ is the 32-component Bogoliubov fermions while $\mathcal{W}_{\mathbf{q}}$ is a 32×32 unitary matrix (*i.e.* $\mathcal{W}_{\mathbf{q}} \cdot \mathcal{W}_{\mathbf{q}}^{\dagger} = 1$) of the form

$$\mathcal{W}_{\mathbf{q}} = \begin{pmatrix} u_{\mathbf{q}} & v_{\mathbf{q}} \\ v_{-\mathbf{q}}^{*} & u_{-\mathbf{q}}^{*} \end{pmatrix} \tag{A.12}$$

with each of u and v being 16×16 matrix. The energy spectrum is then obtained from

$$E_{\mathbf{q}} = \mathcal{W}_{\mathbf{q}}^{\dagger} \cdot \mathcal{H}_{BdG} \cdot \mathcal{W}_{\mathbf{q}} \quad \Rightarrow \quad \mathcal{W}_{\mathbf{q}} \cdot E_{\mathbf{q}} = \mathcal{H}_{BdG} \cdot \mathcal{W}_{\mathbf{q}} \tag{A.13}$$

where $E_{\mathbf{q}}$ is the diagonalized form having the structure

$$E_{\mathbf{q}} = \begin{pmatrix} \mathcal{E}_{\mathbf{q}} & 0 \\ 0 & -\mathcal{E}_{\mathbf{q}} \end{pmatrix} \tag{A.14}$$

with $\mathcal{E}_{\mathbf{q}}$ being a 16×16 diagonal matrix with entries $\mathcal{E}_{\mathbf{q},a}$ $(a = 1, 2, \cdots, 16)$. The second form of Eq. A.13 is expanded to get

$$u_{\mathbf{q}}\mathcal{E}_{\mathbf{q}} = \hat{\varepsilon}_{\mathbf{q}}u_{\mathbf{q}} + \hat{\Delta}_{\mathbf{q}}v_{-\mathbf{q}}^{*} \tag{A.15}$$

$$v_{-\mathbf{q}}^{*}\mathcal{E}_{\mathbf{q}} = \hat{\Delta}_{\mathbf{q}}^{\dagger}u_{\mathbf{q}} - \hat{\varepsilon}_{\mathbf{q}}v_{-\mathbf{q}}^{*} \tag{A.16}$$

For Dirac dispersion, since $\hat{\varepsilon}_{\mathbf{q}}^2 \propto \mathbb{I}$, generalizing the methods outlined in Ref. [10], we get

$$u_{\mathbf{q}}\left(\mathcal{E}_{\mathbf{q}}^2 - \hat{\varepsilon}_{\mathbf{q}}^2\right) = \hat{\Delta}_{\mathbf{q}}\hat{\Delta}_{\mathbf{q}}^{\dagger}u_{\mathbf{q}} \tag{A.17}$$

The solution then depends on whether the pairing is unitary ($\hat{\Delta} \cdot \hat{\Delta}^{\dagger} = |\Delta|^2\mathbb{I}_{16\times16}$) or non-unitary ($\hat{\Delta} \cdot \hat{\Delta}^{\dagger} = \sum_{\alpha\beta\gamma} A_{\alpha\beta\gamma}\Sigma_{\alpha}\tau_{\beta}\sigma_{\gamma}$).

Note that a similar analysis is applicable in principle to the lattice theory. This may be slightly easier in the local basis where the SU(4) flavour symmetry is manifest, however, the actual solutions of the eigenvectors are substantially complicated in practice.

Knowing the transformation from the basis in Eq. 2.17 to that in Eq. A.5, the general

pairing matrix M^{Sc} (Eq. 3.3) transforms as

$$M^{Sc} \rightarrow \mathcal{Y} M^{Sc} \mathcal{Y}^{\dagger} \tag{A.18}$$

A.3 The Majorana representation

As a first step to obtain the Majorana representation, we perform a unitary transformation on the spinors, χ as

$$\tilde{\chi} = \tilde{U}\,\chi. \tag{A.19}$$

Here, $\tilde{U} = \tilde{U}_2\tilde{U}_1$ is a product of 16-dimensional unitary matrices which are given by

$$\tilde{U}_1 = \frac{1}{2}\Big(\Sigma_0(\tau_0+\tau_3)\sigma_0 + \Sigma_0(\tau_0-\tau_3)\sigma_2\Big). \tag{A.20}$$

and

$$\tilde{U}_2 = I_{8\times 8} \otimes \exp\left[\mathrm{i}\pi\sigma_1^{maj}/4\right] \tag{A.21}$$

where σ_i^{maj} (for $i = 0, \cdots, 3$) are the Pauli matrices acting in the mixed valley-subband sector. The free Hamiltonian in $\tilde{\chi}$ basis has the following form,

$$H_D = -iv_F \int d^2\mathbf{x}\, \tilde{\chi}^{\dagger}(\mathbf{x})(\alpha_1'\partial_x + \alpha_2'\partial_y)\tilde{\chi}(\mathbf{x}) \tag{A.22}$$

with

$$\alpha_1' = \tilde{U}.\alpha_x.\tilde{U}^{\dagger} = I_{8\times 8} \otimes \sigma_1^{maj}, \tag{A.23}$$
$$\alpha_2' = \tilde{U}.\alpha_y.\tilde{U}^{\dagger} = I_{8\times 8} \otimes \sigma_3^{maj}. \tag{A.24}$$

Performing the basis rotation mentioned in Eq. A.19 mixes the valley and subband sectors. Now we define the Majorana fermions, η, as

$$\eta = \Big(\eta_r, \eta_I\Big)^T = \left(\frac{1}{2}(\tilde{\chi}+\tilde{\chi}^{\dagger}), \frac{1}{2i}(\tilde{\chi}-\tilde{\chi}^{\dagger})\right)^T. \tag{A.25}$$

The Hamiltonian in Eq. A.22 has the following form in the Majorana basis,

$$H_D = -i\frac{v_F}{2}\int d^2\mathbf{x}\, \eta^T\left(\alpha_1^m\partial_1 + \alpha_2^m\partial_2\right)\eta, \tag{A.26}$$

Irrep	mass	$\mathbf{T_1}$	$\mathbf{T_2}$	$\mathbf{C_2}'$	$\mathbf{C_3}$	$\mathbf{S_6}$	$\mathbf{I}$	$\sigma_\mathbf{d}$
$\mathcal{A}_{1g}$	M	M	M	M	M	M	M	M
$\mathcal{A}_{2g}$	M	M	M	-M	M	M	M	M
$\mathcal{A}_{1u}$	M	M	M	M	M	-M	-M	-M
$\mathcal{A}_{2u}$	M	M	M	-M	M	-M	-M	M

Table A.1: Table for one-dimensional Irreps of microscopic symmetries

where

$$\alpha_1^m = \begin{pmatrix} \alpha_1' & 0 \\ 0 & \alpha_1' \end{pmatrix} = I_{16\times 16} \otimes \sigma_1^{maj},$$
$$\alpha_2^m = \begin{pmatrix} \alpha_2' & 0 \\ 0 & \alpha_2' \end{pmatrix} = I_{16\times 16} \otimes \sigma_3^{maj}. \tag{A.27}$$

The form of the Hamiltonian in Eq. A.26 has manifest SO(16) symmetry, where generators of the SO(16) are of the form

$$g_{majorana} \otimes \sigma_0^{maj} \tag{A.28}$$

where $g_{majorana}$ are 16-dimensional real anti-symmetric matrices, i.e., $g_{majorana}^T = -g_{majorana}$, and are formed out of the 4 flavours, 2 Majorana and 2 mixed valley-subband components.

As shown in Eq. A.26, the matrices $\{\alpha_1^m, \alpha_2^m\}$, when written in the notation introduced in Eq. 2.25, are of the form $\{X_{0001}, X_{0003}\}$. Thus, the matrices that anticommute with $\{\alpha_1^m, \alpha_2^m\}$ has the form $X_{\alpha\beta\gamma 2}$, for which there are 256 possibilities. Furthermore, in the Majorana basis, the particle-hole constraint (Eq. 2.23) is equivalent to the condition that $X_{\alpha\beta\gamma 2}$ is anti-symmetric. This requires that

$$(\mu_\alpha \Sigma_\beta \tau_\gamma)^T = \mu_\alpha \Sigma_\beta \tau_\gamma. \tag{A.29}$$

i.e., all 16×16 symmetric matrices which are 136 in number. Note that $136 = 1 \oplus 135$, where 1 is the SO(16) singlet and 135 is the irreducible representation of SO(16) made up of the rank-2 traceless symmetric SO(16) tensor.

A.4 Transformation of Irreps under lattice.

The symmetry transformations of the different Irreps [40] are summarized in the following tables A.1, A.2 and A.3 for completeness.

Irrep	mass	$\mathbf{T_1}$	$\mathbf{T_2}$	$\mathbf{C_2'}$	$\mathbf{C_3}$	$\mathbf{S_6}$	$\mathbf{I}$	$\sigma_\mathbf{d}$
$\mathcal{E}_\mathrm{u}$	M_1	M_1	M_1	M_1	$\frac{1}{2}\left(-M_1-\sqrt{3}M_2\right)$	$\frac{1}{2}\left(M_1-\sqrt{3}M_2\right)$	$-M_1$	$-M_1$
	M_2	M_2	M_2	$-M_2$	$\frac{1}{2}\left(\sqrt{3}M_1-M_2\right)$	$\frac{1}{2}\left(\sqrt{3}M_1+M_2\right)$	$-M_2$	M_2
$\mathcal{E}_\mathrm{g}$	M_1	M_1	M_1	$-M_1$	$\frac{1}{2}\left(\sqrt{3}M_2-M_1\right)$	$\frac{1}{2}\left(-M_1-\sqrt{3}M_2\right)$	M_1	$-M_1$
	M_2	M_2	M_2	M_2	$\frac{1}{2}\left(-\sqrt{3}M_1-M_2\right)$	$\frac{1}{2}\left(\sqrt{3}M_1-M_2\right)$	M_2	M_2

Table A.2: Table for two-dimensional Irreps of microscopic symmetries

Irrep	mass	$\mathbf{T_1}$	$\mathbf{T_2}$	$\mathbf{C_2}'$	$\mathbf{C_3}$	$\mathbf{S_6}$	$\mathbf{I}$	$\sigma_\mathbf{d}$
$\mathcal{T}_{1\mathrm{g}}$	M_1	-M_1	-M_1	M_1	M_3	M_2	M_1	M_1
	M_2	M_2	-M_2	M_3	M_1	M_3	M_2	M_3
	M_3	-M_3	M_3	M_2	M_2	M_1	M_3	M_2
$\mathcal{T}_{2\mathrm{g}}$	M_1	-M_1	-M_1	-M_1	M_3	M_2	M_1	- M_1
	M_2	M_2	- M_2	- M_3	M_1	M_3	M_2	-M_3
	M_3	-M_3	M_3	-M_2	M_2	M_1	M_3	-M_2
$\mathcal{T}_{1\mathrm{u}}$	M_1	-M_1	-M_1	M_1	M_3	-M_2	-M_1	-M_1
	M_2	M_2	- M_2	M_3	M_1	- M_3	- M_2	- M_3
	M_3	- M_3	M_3	M_2	M_2	- M_1	- M_3	- M_2
$\mathcal{T}_{2\mathrm{u}}$	M_1	-M_1	- M_1	- M_1	M_3	- M_2	- M_1	M_1
	M_2	M_2	- M_2	- M_3	M_1	- M_3	- M_2	M_3
	M_3	- M_3	M_3	- M_2	M_2	- M_1	- M_3	M_2

Table A.3: Table for three-dimensional Irreps of microscopic symmetries

A.5 Gapless Protection: Symmetry Analysis for Γ-DSM

The Bogoliubov spectrum for the two gapless non-unitary singlet SCs in Sec. 4.1.2 has a two-gap structure with one gap exactly zero, as explained in the main text. The gapless sector in both cases is four-fold degenerate with the Hamiltonian for the gapless sector (in the local basis) given by

$$H_{Gapless} = \int d^2\mathbf{q}\left(\chi_G^\dagger\left(\tilde{\zeta}_1\, q_1 + \tilde{\zeta}_2\, q_2\right)\chi_G\right) \tag{A.30}$$

where (not to be confused with Eq. 2.11)

$$\tilde{\zeta}_1 = \begin{pmatrix} \tilde{\beta}_3\tilde{\gamma}_1 & 0_{4\times4} \\ 0_{4\times4} & \tilde{\beta}_3\tilde{\gamma}_1 \end{pmatrix},\ \tilde{\zeta}_2 = \begin{pmatrix} -\tilde{\beta}_0\tilde{\gamma}_2 & 0_{4\times4} \\ 0_{4\times4} & \tilde{\beta}_0\tilde{\gamma}_2 \end{pmatrix} \tag{A.31}$$

with $\tilde{\beta}_i$ and $\tilde{\gamma}_i$ are the 2-dimensional Identity and the Pauli matrices and χ_G is a 8-component Nambu spinor obtained from an unitary transformation of Eq. 2.18 and is

given by

$$\chi_G = (\eta_G, \left[\eta_G^\dagger\right]^T) \tag{A.32}$$

where η_G is a 4-component Dirac spinor capturing the gapless sector of Fig. 4.3 that is given by

$$\eta_G = \begin{pmatrix} \frac{\chi(q)_{31-}}{\sqrt{2}} + \frac{\chi(q)_{42+}}{\sqrt{2}} \\ \frac{\chi(q)_{41+}}{\sqrt{2}} - \frac{\chi(q)_{32-}}{\sqrt{2}} \\ \frac{\chi(q)_{22-}}{\sqrt{2}} - \frac{\chi(q)_{11+}}{\sqrt{2}} \\ \frac{\chi(q)_{21-}}{\sqrt{2}} + \frac{\chi(q)_{12+}}{\sqrt{2}} \end{pmatrix} \tag{A.33}$$

The Hamiltonian in Eq. A.30 has a SO(4) symmetry which becomes manifest in terms of a Majorana representation.

Notably, these gapless fermions can be gapped out via a mass term similar to that discussed in the main text (Eq. 2.15), albeit with an 8-dimensional mass-matrix of the form

$$\tilde{\Updownarrow}_{abc} = \mu_a \tilde{\beta}_b \tilde{\gamma}_c \qquad a, b, c = 0, 1, 2, 3 \tag{A.34}$$

where μ still acts in the Nambu space. The lattice symmetry transformations of 10 different allowed mass terms are given in Table A.4, and it shows that most of them are not allowed without further lattice symmetry breaking. However, the three masses given by the matrices $\{\tilde{\Updownarrow}_{021}, \tilde{\Updownarrow}_{202}, \tilde{\Updownarrow}_{102}\}$ which does not break any lattice symmetries, but are forbidden by the emergent SO(4) symmetry of Eq. A.30. The mass term $\tilde{\Updownarrow}_{021}$ is the projection of bilinear $\chi^\dagger \Sigma_{45}\tau_3\sigma_3\chi$ which is quantum Spin-octupole Hall insulator($\mathcal{A}_{1g}^e$). while the two components of superconducting mass ($\tilde{\Updownarrow}_{202}$, $\tilde{\Updownarrow}_{102}$) are respectively the projections of the singlet ($\mathcal{A}_{1g}$) SC $\chi^T \Sigma_{13}\tau_1\sigma_0\chi$ discussed in the main text (Sec. 4.1.1).

A.6 Summary of the two other gapped doublets $\mathcal{E}_u$

While, $\mathcal{E}_u^I$ is discussed in detail in the main text (Sec. 4.2.1), here we summarize the other two ($\mathcal{E}_u^{II}$ and $\mathcal{E}_u^{III}$) which are adiabatically connected to the first one. Using the parametrization in Eq. 4.32, spectrum of $\left[\mathbf{\Delta}^{\mathcal{E}_u^x} \cdot \mathbf{m}^{\mathcal{E}_u^x}\right] \cdot \left[\mathbf{\Delta}^{\mathcal{E}_u^x} \cdot \mathbf{m}^{\mathcal{E}_u^x}\right]^\dagger$ for $x \in (I, II)$, has the form,

$$|\Delta^{\mathcal{E}_u^x}|^2 \left(\frac{1 \pm \sin(\tilde{\gamma}) \sin(2\theta)}{2} \,,\, \frac{1}{6}\left(5 \pm 3\sin(\tilde{\gamma})\sin(2\theta) - 4\cos(2\theta)\right) \right) \tag{A.35}$$

Mass	$\mathbf{T_1}$	$\mathbf{T_2}$	$\mathbf{C_2'}$	$\mathbf{C_3}$	TR
$\tilde{\Updownarrow}_{021}$	Yes	Yes	Yes	Yes	Yes
$\tilde{\Updownarrow}_{102}$	Yes	Yes	Yes	Yes	No
$\tilde{\Updownarrow}_{120}$	Yes	Yes	No	No	No
$\tilde{\Updownarrow}_{132}$	Yes	Yes	Yes	No	No
$\tilde{\Updownarrow}_{202}$	Yes	Yes	Yes	Yes	Yes
$\tilde{\Updownarrow}_{220}$	Yes	Yes	No	No	Yes
$\tilde{\Updownarrow}_{232}$	Yes	Yes	Yes	No	Yes
$\tilde{\Updownarrow}_{303}$	Yes	Yes	No	No	No
$\tilde{\Updownarrow}_{311}$	Yes	Yes	Yes	No	No
$\tilde{\Updownarrow}_{333}$	Yes	Yes	No	Yes	No

Table A.4: Table of mass terms. The notation used is mentioned in Eq. A.34. Yes(No) implies corresponding symmetry is not broken(broken) by mass term.

such that there are 4 distinct eigenvalues and each one is 4-fold degenerate. As it can be concluded from the spectrum even on TRI ($\tilde{\gamma} = 0$ or π), these SC are always gapped but not unitary. However, they develop nodes at isolated points on the TRB manifold.

As mentioned in the main text, these two doublets correspond to the same phase as $\mathcal{E}_u^I$ discussed before. It can be shown by considering the following deformation from $\mathcal{E}_u^I$ to $\mathcal{E}_u^{II}$ doublets, carried through parameter p

$$\tilde{M}_1(p) = \mathrm{p}\ \mu_1 \otimes m_1^{\mathcal{E}_u^I} + (1-\mathrm{p})\mu_1 \otimes (m_1^{\mathcal{E}_u^{II}} + m_2^{\mathcal{E}_u^{II}}) \tag{A.36}$$

and further deformation to $\mathcal{E}_u^{III}$ in the following way,

$$\tilde{M}_2(p) = \mathrm{p}\ \mu_1 \otimes m_1^{\mathcal{E}_u^{II}} + (1-\mathrm{p})\mu_1 \otimes m_1^{\mathcal{E}_u^{III}}. \tag{A.37}$$

Spectrum of $\tilde{M}_1$ and $\tilde{M}_2$ shows that none of the eigenvalues go to zero during deformation, and also no extra microscopic symmetries were broken.

The lattice model for $m_1^{\mathcal{E}_u^{II}}$ and $m_1^{\mathcal{E}_u^{III}}$ have NNN pairing as shown in Fig. A.1, with the corresponding pairing matrices,
For $m_1^{\mathcal{E}_u^{II}}$,

$$\Sigma_a = -\Sigma_{25}\ ,\ \Sigma_b = \frac{\sqrt{3}\Sigma_{24} + \Sigma_{25}}{4}\ ,\ \Sigma_c = \frac{\sqrt{3}\Sigma_{24} - \Sigma_{25}}{4} \tag{A.38}$$

and for $m_1^{\mathcal{E}_u^{III}}$,

$$\Sigma_a = \Sigma_{24}\ ,\ \Sigma_b = \frac{\sqrt{3}\Sigma_{25} - \Sigma_{24}}{4}\ ,\ \Sigma_c = \frac{\sqrt{3}\Sigma_{25} + \Sigma_{24}}{4} \tag{A.39}$$

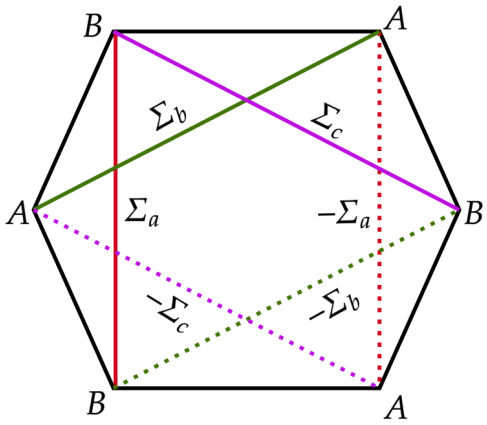

Figure A.1: Schematics of the pairing for the two components $m_{II}^{\mathcal{E}_u}$ and $m_{III}^{\mathcal{E}_u}$ with the corresponding pairing matrices mentioned in Eq. A.38 and A.39 respectively. The pairing amplitudes are on NNN bonds, and the solid (dashed) lines are related to each other by the change in sign of the pairing matrix as indicated.

A.7 The analysis of Triplet PDW

To understand the symmetry-breaking pattern for the triplets $\mathcal{T}_{1g}$, here we will be looking at the secondary order parameter in the same spirit as done in Eq. 4.39, but using SU(3) Gell-Mann matrices [84]. There are 8 possible independent secondary order parameters defined as,

$$\mathbf{\Lambda}_i = \mathbf{d}^\dagger \Lambda_i \mathbf{d} \text{ where } i \in (1,..,8) \tag{A.40}$$

where Λ_i are 3-dimensional Gell-Mann matrices [84]. In terms of parameters $(\theta, \phi, \tilde{\gamma}_1, \tilde{\gamma}_2)$, $\mathbf{\Lambda}$ has the following form:

$$\mathbf{\Lambda} = \begin{pmatrix} \mathbf{\Lambda_1} \\ \mathbf{\Lambda_2} \\ \mathbf{\Lambda_3} \\ \mathbf{\Lambda_4} \\ \mathbf{\Lambda_5} \\ \mathbf{\Lambda_6} \\ \mathbf{\Lambda_7} \\ \mathbf{\Lambda_8} \end{pmatrix} = \begin{pmatrix} \cos(\tilde{\gamma}_1)\sin(2\theta)\cos(\phi) \\ \sin(\tilde{\gamma}_1)\sin(2\theta)\cos(\phi) \\ \frac{1}{4}\left(1 - 2\sin^2(\theta)\cos(2\phi) + 3\cos(2\theta)\right) \\ \cos(\tilde{\gamma}_2)\sin(2\theta)\sin(\phi) \\ \sin(\tilde{\gamma}_2)\sin(2\theta)\sin(\phi) \\ \cos(\tilde{\gamma}_1 - \tilde{\gamma}_2)\sin^2(\theta)\sin(2\phi) \\ -\sin(\tilde{\gamma}_1 - \tilde{\gamma}_2)\sin^2(\theta)\sin(2\phi) \\ \frac{1}{4}\left(6\sin^2(\theta)\cos(2\phi) + 3\cos(2\theta) + 1\right) \end{pmatrix} \tag{A.41}$$

These 8 breaks into $3 \oplus 3 \oplus 2$ under lattice symmetries, such that $(\mathbf{\Lambda_1}, \mathbf{\Lambda_4}, \mathbf{\Lambda_6})$ and $(\mathbf{\Lambda_2}, \mathbf{\Lambda_5}, \mathbf{\Lambda_7})$ corresponds to $\mathcal{T}_{1g}^e$ and $\mathcal{T}_{2g}^o$ respectively and $(\mathbf{\Lambda_3}, \mathbf{\Lambda_8})$ corresponds to $\mathcal{E}_g^e$. As mentioned before, $|\mathbf{d} \times \mathbf{d}^*| = 0$ is the condition for TRI, which implies $\mathcal{T}_{2g}^o$ should

be zero. The leading order anisotropic term in the free energy, which is allowed by lattice symmetries, is of the form,

$$\lambda_1(\mathbf{\Lambda_1}^2+\mathbf{\Lambda_4}^2+\mathbf{\Lambda_6}^2)+\lambda_2(\mathbf{\Lambda_2}^2+\mathbf{\Lambda_5}^2+\mathbf{\Lambda_7}^2)+\lambda_3\left(\mathbf{\Lambda_3}^2+\mathbf{\Lambda_8}^2\right) \tag{A.42}$$

where signs of λ_1, λ_2 and λ_3 dictates symmetry breaking pattern of the SC. Also, this analysis is the same for other triplets discussed in the main text.

A.8 Superconductivity in system with $j = 1/2$ orbitals

In this appendix, we present our results for the same problem as studied in the main text, but for two orbitals *i.e.*, a $j = 1/2$ doublet per site (in contrast with four orbitals per site for $j = 3/2$ (Eq. 2.4) discussed in the main text) of the honeycomb lattice (fig. 2.2).The Hamiltonian of the system is the same as Eq. 2.3 with $\mathcal{U}^{global}_{\mathbf{rr'}}$ are 2×2 Pauli matrices acting on the $j = 1/2$ orbitals whose directed product around the hexagon is equal to $-\mathbb{I}_{2\times2}$, as in the main text, indicating the π-flux. The system has (fig. 2.2) lattice translations $\mathbf{T_1}$ and $\mathbf{T_2}$, $\mathbf{C_3}$ rotations, $\boldsymbol{\sigma_d}$ dihedral reflection and time reversal (TR) $\mathbb{T}$, with, as in the main text, $\mathbb{T}^2 = -1$.

Working in the global basis (see main text), this system has four non-degenerate bands. At quarter filling, two bands touch "linearly" at four points Γ, M_1, M_2, M_3 in the BZ leading to a low-energy description in terms of 2-component Dirac spinors χ_ν where $\nu \in \{\Gamma, M_1, M_2, M_3\}$ at the four valleys. The low-energy theory, analogous to Eq. 2.1, for this case is

$$H = -iv_F \int \mathrm{d}^2x \chi^\dagger(x)(\alpha_1\partial_1 + \alpha_2\partial_2)\chi(x), \tag{A.43}$$

a Dirac theory where $\chi(x)$ is now an 8-component Dirac spinor made up by stacking two-component Dirac spinors, χ_ν, from the four valleys. The 8×8 matrices α_i can be chosen as

$$\alpha_i = \sigma_0\sigma_0\sigma_i$$

Where σs are Pauli matrices, and v_F is a microscopic velocity scale (Note that for this appendix, we use σ to denote the spin, valley and the band spaces, unlike in the main text). To prepare for the analysis of the superconducting masses, we recast this Hamiltonian in Nambu formulation (analogous to Eq. 2.19) as

$$H_N = -i\frac{v_F}{2}\int \mathrm{d}^2x\, \chi_N^\dagger(x)\,(\tilde{\alpha}_1\partial_1 + \tilde{\alpha}_2\partial_2)\,\chi_N(x) \tag{A.44}$$

where $\chi_N^\dagger(x) = (\chi^\dagger(x) \quad \chi^T(x))$. Here,

$$\tilde{\alpha}_1 = M_{0001}, \quad \tilde{\alpha}_2 = M_{3002}$$

Where we have introduced a convenient notation

$$M_{\alpha\beta\gamma\delta} = \sigma_\alpha \sigma_\beta \sigma_\gamma \sigma_\delta$$

For the set of all 256 16×16 matrices obtained by Kronecker products of Pauli matrices which act on the Nambu, spin, valley and band spaces.

Matrices of the type $M_{\alpha\beta\gamma\delta}$ that anticommute with $\tilde{\alpha}_1$ and $\tilde{\alpha}_2$, and satisfy the conjugacy condition (analogous to Eq. 2.23)

$$M_{\alpha\beta\gamma\delta} + M_{1000} M_{\alpha\beta\gamma\delta}^T M_{1000} = 0$$

are the allowed masses. Among these, masses of the from $M_{0\beta\gamma\delta}$ and $M_{3\beta\gamma\delta}$ are normal (non-superconducting) masses, while those of the type $M_{1\beta\gamma\delta}$ and $M_{2\beta\gamma\delta}$ are superconducting masses describing pairing fields between the fermions. There are 16 matrices of the normal type, which result in seven distinct phases as shown in [40]. Here we focus on the superconducting masses of which 20 matrices, 10 each of the type $M_{1\beta\gamma\delta}$ and $M_{2\beta\gamma\delta}$ which can be interpreted and the matrices that couple respectively to real and imaginary parts of the pairing amplitudes.

The superconducting masses form an adjoint representation of the group generated by the symmetry elements of the system discussed above. This representation is broken down into irreducible components. We find that there are five superconducting phases, two of which are singlets, one doublet, and two triplets. We will only show the $M_{2\beta\gamma\delta}$ terms in the discussion below.

A.8.1 $\mathcal{A}_1$ Unitary Singlet Superconductor

This phase breaks the $\sigma_{\mathbf{d}}$ symmetry, with a mass term

$\mathcal{A}_1^I$	
1	(1) M_{2002}

This fully gapped superconductor has 8-fold-degenerate Bogoliubov quasi-particle bands and corresponds to the regular s-wave SC for $j = 1/2$ electrons. While this phase is analogous to the $\mathcal{A}_{1g}^I$ phase in the system with $j = 3/2$ discussed in the main text (see sec. 4.1.1), the crucial difference is the absence of the extra pairing in the $j = 3/2$ sector with a π-phase. This state is characterized by a uniform pairing (same

at all sites) between the time-reversed $j = 1/2$ fermions.

A.8.2 $\mathcal{A}_1^{II}$ Non-unitary Double-Gapped Singlet Superconductor

This double gapped superconductor breaks the $\sigma_{\mathbf{d}}$ symmetry with a mass term

$\mathcal{A}_1^{II}$	
1	$\left(\frac{1}{\sqrt{3}}\right) M_{2032} + \left(\frac{1}{\sqrt{3}}\right) M_{2302} + \left(\frac{1}{\sqrt{3}}\right) M_{2332}$

The pairing matrix is non-unitary. The Bogoliubov bands break up into 2-fold degenerate bands around the Γ point and 6-fold degenerate bands around the M points. The pairing is an extended s-wave type similar to the $\mathcal{A}_{1g}^{II}$ phase found in the system discussed in the main text (see sec. 4.1.1).

A.8.3 $\mathcal{E}$ Non-unitary Gapless Doublet Superconductor

This superconducting phase breaks $\mathbf{C_3}$ and $\sigma_{\mathbf{d}}$ symmetries. The doublet mass components are

$\mathcal{E}$	
1	$\left(\frac{1}{\sqrt{2}}\right) M_{2032} + \left(-\frac{1}{\sqrt{2}}\right) M_{2332}$
2	$\left(\frac{1}{\sqrt{6}}\right) M_{2032} + \left(-\sqrt{\frac{2}{3}}\right) M_{2302} + \left(\frac{1}{\sqrt{6}}\right) M_{2332}$

This nodal superconductor has a quasi-particle band (doubly degenerate) at the Γ point and three sets of doubly degenerate gapped quasi-particle bands. The gapped bands undergo crossings depending on the values of the components of the pairing amplitudes, multiplying the two masses. The pairing pattern includes anisotropic next-neighbour pairing (thus breaking the $\mathbf{C_3}$ symmetry), similar to the $\mathcal{E}_g$ doublet mass of sec. 4.2.2. The order parameter manifold is also $(S^1 \times S^2)/Z_2$.

A.8.4 $\mathcal{T}_2$ Non-unitary Gapless Triplet Superconductor

This non-unitary superconductor breaks all the lattice symmetries, with mass components:

$\mathcal{T}_2$	
1	$\left(\frac{1}{\sqrt{2}}\right) M_{2112} + \left(-\frac{1}{\sqrt{2}}\right) M_{2222}$
2	$\left(-\frac{1}{\sqrt{2}}\right) M_{2102} + \left(-\frac{1}{\sqrt{2}}\right) M_{2132}$
3	$\left(-\frac{1}{\sqrt{2}}\right) M_{2012} + \left(-\frac{1}{\sqrt{2}}\right) M_{2312}$

There is a four-fold degenerate Dirac cone quasi-particle band at the Γ point, and a four-fold degenerate gapped quasi-particle band. Each of the mass components

represents a pairing between the Γ-point states and M_i point states, denoting a finite momentum pairing corresponding to the $\mathbf{K}_{M_i}$ wave-vectors of the BZ. This phase is analogous to the $\mathcal{T}_{2g}$ phase found in sec. 5.1.2. The order parameter manifold is $(S^1 \times CP^2)/Z_2$. The quasi-particle dispersion does not change its structure when the order parameter is varied on this manifold. Note, however, that the wavefunctions of the Dirac quasi-particles do change upon changing the order parameter on the said manifold.

A.8.5 $\mathcal{T}_1$ Non-unitary Gapless Triplet Superconductor

All lattice symmetries are broken in this superconducting phase, which carries a distinct three-dimensional representation (compared to the triplet discussed in the previous section) of the symmetry group of the system. The mass components are:

$\mathcal{T}_1$	
1	$\left(\frac{1}{\sqrt{2}}\right) M_{2112} + \left(\frac{1}{\sqrt{2}}\right) M_{2222}$
2	$\left(-\frac{1}{\sqrt{2}}\right) M_{2102} + \left(\frac{1}{\sqrt{2}}\right) M_{2132}$
3	$\left(-\frac{1}{\sqrt{2}}\right) M_{2012} + \left(\frac{1}{\sqrt{2}}\right) M_{2312}$

For a generic set of pairing amplitudes, there is always a two-fold degenerate Dirac code quasi-particle band and three other gapped quasi-particle bands that are each two-fold degenerate. Here the pairing occurs between the states near the M points in the BZ, *i.e.*, the triplet corresponds to pairing between M_1-M_2, M_2-M_3 and M_3-M_3, which gives the same vectors for the pair density as in the triplet phase discussed in the previous section. This phase is similar to the $\mathcal{T}_{1g}^{III}$ phase discussed in sec. 5.1.1. The order parameter manifold is again $(S^2 \times CP^2)/Z_2$, and just as in sec. 5.1.1, there are points on the order parameter manifold where there are additional gapless modes. Interestingly, the states in the proximity of Γ points are always gapless. Thus, the nature of gapless states at two generic points on the order parameter manifold remains unchanged; this is to be contrasted with the physics seen in the triplet superconducting phase discussed in the previous section.

Appendix B

Appendix for Z_2 Fractionalization

B.1 Symmetry Transformation of Fermionic spinors

We considered the following symmetry transformations, which are also discussed in Fig. 6.3.

- T_y: Translation by one unit along y-direction
- T_x: Translation by one unit along x-direction
- $R_{\pi/2}$: Rotation by $\frac{\pi}{2}$ about origin
- Ref_x: Reflection about x-axis
- TR: Time reversal

The choice of the Z_2 gauge field σ^z_{ij} on the lattice in Eq. 6.21 makes it appear that translation by one unit along the x-direction and rotation by $\frac{\pi}{2}$ are no longer symmetries. Under these operations, the Hamiltonian transforms into a gauge-equivalent configuration. By combining the lattice transformations $\hat{U}$ with an appropriate gauge transformation $\hat{G}$ (Fig. B.1 and B.2), we can recover a symmetry operation.

$$(\hat{G}\hat{U})\hat{H}(\hat{G}\hat{U})^{-1} = \hat{H}\,. \tag{B.1}$$

In terms of the fermion operators,

$$f^\dagger_{\mathbf{r}} \xrightarrow{\hat{U}} f^\dagger_{\mathbf{r}'} \xrightarrow{\hat{G}} \epsilon_{\mathbf{r}'} f^\dagger_{\mathbf{r}'}\,. \tag{B.2}$$

Due to Z_2 gauge structure, at every site $\epsilon_{\mathbf{r}'}$ can take value ± 1. Now we will discuss the symmetry transformation of Dirac spinors.

Translation by one unit along y-direction Under this operation, the lattice comes back to itself and no additional gauge transformation is required.

$$\hat{U} f^{\dagger}_{\mathbf{r}} \hat{U}^{-1} = f^{\dagger}_{\mathbf{r}+\hat{y}} \tag{B.3}$$
$$\hat{U} f^{\dagger}_{\mathbf{k}} \hat{U}^{-1} = e^{-i\mathbf{k}\cdot\hat{y}} f^{\dagger}_{\vec{k}} \tag{B.4}$$

Evaluating this for the soft mode momenta gives:

$$\hat{U}\ \psi(\mathbf{x})\ \hat{U}^{-1} = (\tau_3 \otimes \sigma_0)\psi(\mathbf{x}) \tag{B.5}$$

Translation by one unit along x-direction Under this operation, a gauge transformation is required following the operation of lattice transformation by one unit along x. The process is depicted in Fig.B.1. The sites highlighted by light blue have $\epsilon_{\vec{r}_i} = -1$ and all others have $+1$. The gauge choice is -1 at all sites with odd y-coordinate can be written as $\epsilon_{\vec{r}_i} = e^{i(\pi\hat{y}).\vec{r}_i}$.

$$\hat{G}\hat{U} f^{\dagger}_{\mathbf{r}} (\hat{G}\hat{U})^{-1} = \epsilon_{\mathbf{r}_i+\hat{x}} f^{\dagger}_{\mathbf{r}+\hat{x}} \tag{B.6}$$
$$\hat{G}\hat{U} f^{\dagger}_{\mathbf{k}} (\hat{G}\hat{U})^{-1} = e^{-i\mathbf{k}.\hat{x}} f^{\dagger}_{\mathbf{k}+\pi\hat{y}} \tag{B.7}$$

Evaluating this for the soft mode momenta gives:

$$\hat{G}\hat{U}\psi(\mathbf{x})(\hat{G}\hat{U})^{-1} = (\tau_1 \otimes \sigma_3)\psi(\mathbf{x}) \tag{B.8}$$

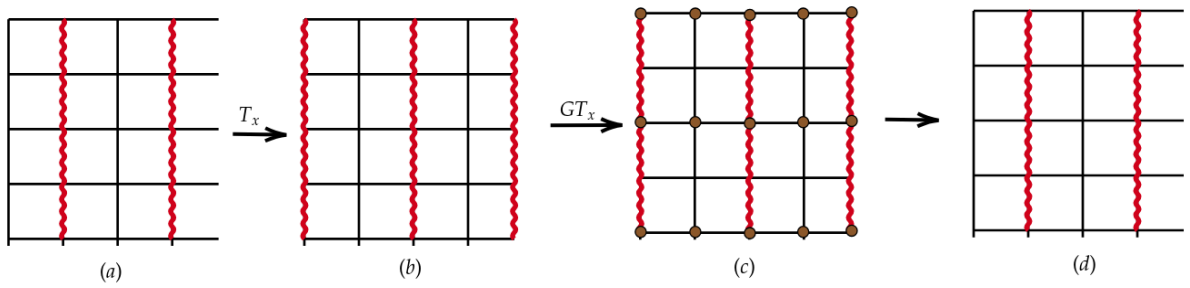

Figure B.1: Schematic figure representing the translation by one unit along the x-direction. (a) shows the gauge choice mentioned in Eq. 6.21, where the red curly bonds correspond to $\sigma^z_{ij} = -1$ and the black solid bonds correspond to $\sigma^z_{ij} = +1$. Under the action of T_x, the original configuration of σ^z_{ij} shown in (a) transforms to the configuration shown in (b). However, by performing a gauge transformation $\epsilon_{\mathbf{r}} = -1$ on the fermions at the sites highlighted by brown dots, we can recover the original configuration, as illustrated in (d).

Rotation by $\frac{\pi}{2}$ about origin Under this operation, a gauge transformation is required following the operation of rotating the lattice by $\frac{\pi}{2}$ in clockwise direction keeping the site at the origin fixed. The process is depicted in Fig.B.2. The sites highlighted by light blue have $\epsilon_{\vec{r}_i} = -1$ and all others have $+1$. The gauge choice has to be -1 at sites which have both the coordinates odd. It can be written as $\epsilon_{\vec{r}_i} = \frac{1}{2}(1 + e^{i(\pi\hat{x}).\vec{r}_i} + e^{i(\pi\hat{y}).\vec{r}_i} - e^{i(\pi\hat{x}+\pi\hat{y}).\vec{r}_i})$.

$$\hat{G}\hat{U}f^\dagger_{\mathbf{r}}(\hat{G}\hat{U})^{-1} = \epsilon_{\mathbf{r}'}f^\dagger_{\mathbf{r}'}, \tag{B.9}$$

$$\hat{G}\hat{U}f^\dagger_{\mathbf{k}}(\hat{G}\hat{U})^{-1} = \frac{1}{2}(f^\dagger_{\mathbf{k}'} + f^\dagger_{\mathbf{k}'+\pi\hat{x}} + f^\dagger_{\mathbf{k}'+\pi\hat{y}} - f^\dagger_{\mathbf{k}'+\pi\hat{x}+\pi\hat{y}}), \tag{B.10}$$

where $\mathbf{r}' = n_y\hat{x} - n_x\hat{y}$ and $\mathbf{k}' = k_y\hat{x} - k_x\hat{y}$.

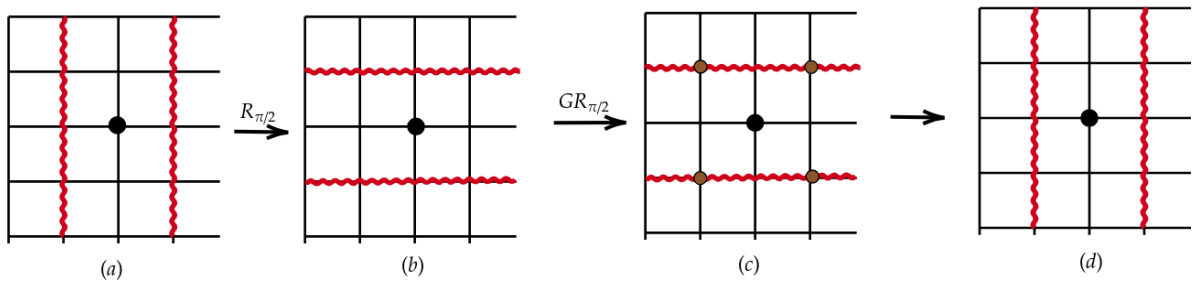

Figure B.2: Schematic figure representing the translation by one unit along the x-direction. (a) shows the gauge choice mentioned in Eq. 6.21, where the red curly bonds correspond to $\sigma^z_{ij} = -1$ and the black solid bonds correspond to $\sigma^z_{ij} = +1$. Under the action of $R_{\pi/2}$ about the origin (shown by black dot), the original configuration of σ^z_{ij} shown in (a) transforms to the configuration shown in (b). However, by performing a gauge transformation $\epsilon_{\mathbf{r}} = -1$ on the fermions at the sites highlighted by brown dots, we can recover the original configuration, as illustrated in (d).

Evaluating this for the soft mode momenta gives:

$$\hat{G}\hat{U}\psi(\mathbf{x})(\hat{G}\hat{U})^{-1} = \frac{1}{2}((\tau_0 \otimes \sigma_0) + i(\tau_2 \otimes \sigma_3) - i(\tau_3 \otimes \sigma_2) + (\tau_1 \otimes \sigma_1))\psi(R^{-1}_{\pi/2}\mathbf{x}). \tag{B.11}$$

Reflection about x axis Under this operation, a gauge transformation is not required.

$$\hat{U}f^\dagger_{\mathbf{r}}\hat{U}^{-1} = f^\dagger_{\mathbf{r}'}, \tag{B.12}$$

$$\hat{U}f^\dagger_{\mathbf{k}}\hat{U}^{-1} = f^\dagger_{\mathbf{k}'}, , \tag{B.13}$$

where $\mathbf{r}_i^{'} = n_x\hat{x} - n_y\hat{y}$ and $\mathbf{k}^{'} = k_x\hat{x} - k_y\hat{y}$. Evaluating this for the soft mode momenta gives:

$$\hat{U}\psi(\mathbf{x})\hat{U}^{-1} = (\tau_1 \otimes \sigma_0)\psi(\mathrm{Ref}_x^{-1}\mathbf{x}) \tag{B.14}$$

Time reversal Under time reversal $\vec{k}$ goes to $-\vec{k}$ and there is complex conjugation(K) of the matrix element.

$$\hat{\Theta}\psi(\mathbf{x})\hat{\Theta}^{-1} = (\tau_1 \otimes \sigma_1)K\psi(\mathbf{x})\ . \tag{B.15}$$

B.2 Symmetry Transformation for Ising Soft modes

As done for the fermionic case, the symmetries for the Ising spins are also supplemented with gauge transformations. However, in this case, the gauge transformations act on the Ising spins. The required gauge transformations are the same as those required for the fermions. The soft mode in Eq. 6.32, together with the gauge transformations, yields the following symmetry table for the Ising soft modes.

ϕ	T_x	T_y	$R_{\pi/2}$	R_π	Ref_x	Time Reversal
ϕ_1	ϕ_2	ϕ_1	$(\phi_1+\phi_2)/\sqrt{2}$	ϕ_1	ϕ_1	ϕ_1
ϕ_2	ϕ_1	-ϕ_2	$(\phi_1-\phi_2)/\sqrt{2}$	ϕ_2	ϕ_2	ϕ_2

Table B.1: The transformation of the two soft modes under square lattice symmetries. $T_x(T_y)$ is unit lattice translation along the $x(y)$ direction; R_π represents a rotation by π about site, and Ref_x corresponds to a reflection about the y axis.

B.3 Transformation of order parameter under lattice symmetries

In this section, we examine the transformation properties of $O^c(\mathbf{n},\mathbf{q})$, introduced in Eq. 6.37, under microscopic symmetries. Since we are considering correlators of physical electrons, the symmetry implementation is not projective, unlike the case for the gauge fermions f.

1. Translation in x-direction (T_x): $x \to x + a$:
   Under Translation,

$$c_{\mathbf{k}} \to e^{i\mathbf{k}\cdot\mathbf{r}}c_{\mathbf{k}},$$
$$O^c(\mathbf{n},\mathbf{q}) \to e^{i\mathbf{q}\cdot\mathbf{r}}O^c(\mathbf{n},\mathbf{q}) = e^{iq_x a}O^c(\mathbf{n},\mathbf{q}) \tag{B.16}$$

2. Translation in y-direction (T_y): $y \to y + a$:

$$O^c(\mathbf{n}, \mathbf{q}) \to e^{i\mathbf{q}\cdot\mathbf{r}} O^c(\mathbf{n}, \mathbf{q}) = e^{iq_y a} O^c(\mathbf{n}, \mathbf{q}) \tag{B.17}$$

3. Reflection about x-axis (Ref_x) :

$$\begin{aligned} c_{\mathbf{k}=(k_x,k_y)} &\to c_{\mathbf{k}'=(k_x,-k_y)}, \\ O^c(\mathbf{n}, \mathbf{q}) = \sum_{\mathbf{k}} \left(e^{i\mathbf{n}\cdot(\mathbf{q}+\mathbf{k})} c^\dagger_{\mathbf{k}} c_{\mathbf{k}+\mathbf{q}} + h.c. \right) &\to \sum_{\mathbf{k}} \left(e^{i\mathbf{n}\cdot(\mathbf{q}+\mathbf{k})} c^\dagger_{\mathbf{k}'} c_{\mathbf{k}'+\mathbf{q}'} + h.c. \right) \\ \sum_{\mathbf{k}} \left(e^{i\mathbf{n}\cdot(\mathbf{q}+\mathbf{k})} c^\dagger_{\mathbf{k}'} c_{\mathbf{k}'+\mathbf{q}'} + h.c. \right) = \sum_{\mathbf{k}'} \left(e^{i\mathbf{n}'\cdot(\mathbf{q}'+\mathbf{k}')} c^\dagger_{\mathbf{k}'} c_{\mathbf{k}'+\mathbf{q}'} + h.c. \right) &= O^c(\mathbf{n}', \mathbf{q}') \\ \text{where, } \mathbf{n}' = (n_x, -n_y),\ \mathbf{q}' &= (q_x, -q_y) \end{aligned} \tag{B.18}$$

4. Rotation by $\frac{\pi}{2}$ about origin ($R_{\pi/2}$):

$$\begin{aligned} c_{\mathbf{k}=(k_x,k_y)} &\to c_{\mathbf{k}'=(k_y,-k_x)} \\ O^c(\mathbf{n}, \mathbf{q}) &\to O^c(\mathbf{n}', \mathbf{q}') \\ \text{where, } \mathbf{n}' = (-n_y, n_x),\ \mathbf{q} &= (-q_y, q_x) \end{aligned} \tag{B.19}$$

5. Time Reversal (TR) :

$$\begin{aligned} c_{\mathbf{k}} \to K c_{-\mathbf{k}}, \quad K\text{: Complex Conjugation} \\ O^c(\mathbf{n}, \mathbf{q}) \to O^*(\mathbf{n}, \mathbf{q}) = O^c(\mathbf{n}, -\mathbf{q}) \end{aligned} \tag{B.20}$$

B.4 Perturbative Calculation for RK Hamiltonian

Consider the Hamiltonian in Eq. 6.16. In the dimer limit, we impose the constraints $\kappa \to -\infty$ and $J \to \infty$, while keeping $\kappa/J \to \infty$. For $\Gamma = 0$ and $\Omega = 0$, the ground state corresponds to configurations of dimers on the dual lattice with a local constraint on the number of dimers attached to a given site:

$$\sum_{J \in I} n_{IJ} = 1, \tag{B.21}$$

which, on the direct lattice, translates into Eq. 6.45 for Ising spins on links of the direct lattice. We now perturb the system by turning on Γ and Ω and examine their action on the dimer configuration. Since these terms act locally, their effect can be understood by

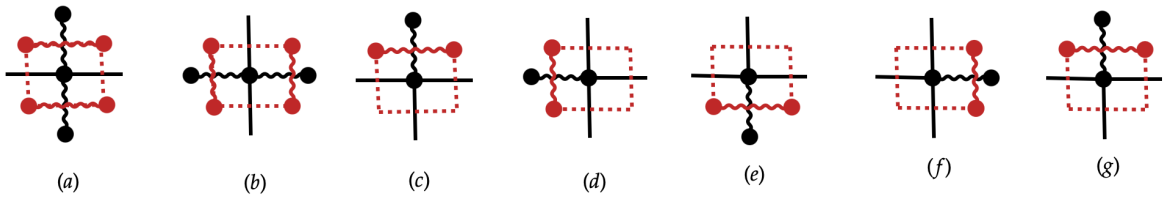

Figure B.3: Possible configurations of Z_{ij} (and dimer occupancy n_{IJ}) in the dimer limit around a single site, on both direct and dual lattices. Black curly (solid) bonds indicate Ising variable values $Z = -1$ ($Z = +1$) on bonds of the direct lattice. Red curly (or dotted) bonds represent the presence (or absence) of a dimer on the corresponding bond of the dual square lattice, as in Fig. 6.5. The dimer occupancy n_{IJ} is related to the Ising variable Z_{ij} by $n_{IJ} = \frac{1}{2}(1 - Z_{ij})$.

considering the possible dimer configurations around a single site shown in Fig. B.3.

To first order in perturbation theory, let us examine the action of the Γ term:

$$-\Gamma \prod_{j\in i} X_{ij} \left| \right\rangle = -\Gamma \left| \right\rangle ,$$

$$-\Gamma \prod_{j\in i} X_{ij} \left| \right\rangle = -\Gamma \left| \right\rangle .$$

For other configurations, this operator scatters the state into ones not belonging to the ground-state sector.

Now, consider the action of the Ω term:

$$\frac{\Omega}{4}\left[(1 - Z_{i-\hat{x},i})(1 - Z_{i+\hat{x},i}) + (1 - Z_{i-\hat{y},i})(1 - Z_{i+\hat{y},i})\right] \left| \right\rangle = \Omega \left| \right\rangle ,$$

$$\frac{\Omega}{4}\left[(1 - Z_{i-\hat{x},i})(1 - Z_{i+\hat{x},i}) + (1 - Z_{i-\hat{y},i})(1 - Z_{i+\hat{y},i})\right] \left| \right\rangle = \Omega \left| \right\rangle .$$

For all other cases, the matrix element vanishes. To leading (first) order in perturbation theory, the effective Hamiltonian is the Rokhsar-Kivelson Hamiltonian discussed in Eq. 6.42.

Appendix C

Appendix for Trial wavefunction for correlated metals

C.1 The details of the $[\theta]$ basis

In this section, we chart out several properties of the $|\Psi[\theta]\rangle$ (Eq. 7.1) basis. The real-space representation of the many-body state in Eq. 7.1, $\Psi[\theta]\left(\{\mathbf{r}\}\right) = \langle\{\mathbf{r}\}|\Psi[\theta]\rangle$, can be obtained from the determinant of the matrix

$$\begin{pmatrix} s_{\mathbf{k}_1}\phi_{\mathbf{k}_1}(\mathbf{r}_1) & s_{\mathbf{k}_2}\phi_{\mathbf{k}_2}(\mathbf{r}_1) & \cdots & \cdots & s_{\mathbf{k}_B}\phi_{\mathbf{k}_B}(\mathbf{r}_1) \\ s_{\mathbf{k}_1}\phi_{\mathbf{k}_1}(\mathbf{r}_2) & s_{\mathbf{k}_2}\phi_{\mathbf{k}_2}(\mathbf{r}_2) & \cdots & \cdots & s_{\mathbf{k}_B}\phi_{\mathbf{k}_B}(\mathbf{r}_2) \\ \cdots & \cdots & \cdots & \cdots & \cdots \\ \cdots & \cdots & \cdots & \cdots & \cdots \\ s_{\mathbf{k}_1}\phi_{\mathbf{k}_1}(\mathbf{r}_{N_p}) & s_{\mathbf{k}_2}\phi_{\mathbf{k}_2}(\mathbf{r}_{N_p}) & \cdots & \cdots & s_{\mathbf{k}_B}\phi_{\mathbf{k}_B}(\mathbf{r}_{N_p}) \end{pmatrix}, \tag{C.1}$$

where $s_{\mathbf{k}} = (1+\theta_{\mathbf{k}})/2$, $\{\mathbf{r}\} \equiv (\mathbf{r}_1, \mathbf{r}_2, \cdots, \mathbf{r}_{N_p})$ is the position basis for particles corresponding to filling ν, and $\phi_{\mathbf{k}}(\mathbf{r})$ are the corresponding single-particle wave-functions. Note that the above matrix is in general a rectangular one (for $\nu \neq 1$) and in that case, for a given ν, only N_p columns have non-zero entries with the rest of $(N - N_p)$ being identically zero. Determinant of such type of matrices, A, can be defined via the Gramian determinant calculated as $\sqrt{\mathrm{Det}\left[\mathrm{A}\cdot\mathrm{A}^{\mathrm{T}}\right]}$ where A^T is the transpose of A. This is equivalent to removing all the columns of zeros whence we get a $N_p \times N_p$ square matrix and taking its determinant. The above procedure can be checked to give the right antisymmetric Slater-determinant wave-function.

Turning to the various many-body operators, consider the action of $c^\dagger_{\mathbf{q}}$ on this state,

$$c^\dagger_{\mathbf{q}}|\Psi[\theta]\rangle = c^\dagger_{\mathbf{q}}\prod_{\mathbf{k}}(c^\dagger_{\mathbf{k}})^{\frac{1+\theta_{\mathbf{k}}}{2}}|0\rangle = \delta_{\theta_{\mathbf{q}},-1}\left(\prod_{\mathbf{k}'\neq\mathbf{q}}\delta_{\theta_{\mathbf{k}'},\theta'_{\mathbf{k}'}}\right)\delta_{\theta_{\mathbf{q}},-\theta'_{\mathbf{q}}}(-1)^{\sum_{\mathbf{k}>\mathbf{q}}\frac{1+\theta_{\mathbf{k}}}{2}}|\Psi[\theta']\rangle.$$

Similarly

$$c_{\mathbf{q}}|\Psi[\theta]\rangle \;=\; \delta_{\theta_{\mathbf{q}},1}\left(\prod_{\mathbf{k}'\neq\mathbf{q}}\delta_{\theta_{\mathbf{k}'},\theta'_{\mathbf{k}'}}\right)\delta_{\theta_{\mathbf{q}},-\theta'_{\mathbf{q}}}\times(-1)^{\sum_{\mathbf{k}>\mathbf{q}}\frac{1+\theta_{\mathbf{k}}}{2}}|\Psi[\theta']\rangle. \tag{C.2}$$

Therefore the matrix elements are given by

$$\left(c^{\dagger}_{\mathbf{q}}\right)_{[\theta],[\theta']}=\left(\prod_{\mathbf{k}'\neq\mathbf{q}}\delta_{\theta_{\mathbf{k}'},\theta'_{\mathbf{k}'}}\right)\delta_{\theta_{\mathbf{q}},-\theta'_{\mathbf{q}}}\times\left(\frac{1-\theta_{\mathbf{q}}}{2}\right)\exp\left[i\pi\sum_{\mathbf{k}>\mathbf{q}}\frac{1+\theta_{\mathbf{k}}}{2}\right], \tag{C.3}$$

and

$$\left(c_{\mathbf{q}}\right)_{[\theta],[\theta']}=\left(\prod_{\mathbf{k}'\neq\mathbf{q}}\delta_{\theta_{\mathbf{k}'},\theta'_{\mathbf{k}'}}\right)\delta_{\theta_{\mathbf{q}},-\theta'_{\mathbf{q}}}\times\left(\frac{1+\theta_{\mathbf{q}}}{2}\right)\exp\left[i\pi\sum_{\mathbf{k}>\mathbf{q}}\frac{1+\theta_{\mathbf{k}}}{2}\right]. \tag{C.4}$$

These results are easily extended to matrix elements of multiple creation and annihilation operators. For two particles, represented by corresponding fermion creation operators,

$$\begin{aligned}\left(c^{\dagger}_{\mathbf{q}_1}c^{\dagger}_{\mathbf{q}_2}\right)_{[\theta],[\theta']}=&\left(\prod_{\mathbf{k}'\neq\mathbf{q}_1,\mathbf{q}_2}\delta_{\theta_{\mathbf{k}'},\theta'_{\mathbf{k}'}}\right)\delta_{\theta_{\mathbf{q}_1},-\theta'_{\mathbf{q}_1}}\,\delta_{\theta_{\mathbf{q}_2},-\theta'_{\mathbf{q}_2}}\times\mathrm{sign}(\mathbf{q}_1,\mathbf{q}_2)\left(\prod_{i=1}^{2}\frac{1-\theta_{\mathbf{q}_i}}{2}\right)\\&\times\prod_{i=1}^{2}\exp\left[i\pi\sum_{\mathbf{k}>\mathbf{q}_i}\frac{1+\theta_{\mathbf{k}}}{2}\right],\end{aligned} \tag{C.5}$$

where in the same ordering as used in Eq. 7.1, $\mathrm{sign}(\mathbf{q_1},\mathbf{q_2})$ reads

$$\mathrm{sign}(\mathbf{q}_1,\mathbf{q}_2)=\begin{cases}+1 & \forall\ \mathbf{q}_1>\mathbf{q}_2\\ 0 & \forall\ \mathbf{q}_1=\mathbf{q}_2\\ -1 & \forall\ \mathbf{q}_1<\mathbf{q}_2.\end{cases} \tag{C.6}$$

This shows that the matrix elements encode the sign structure associated with the anticommutation of fermion operators. Continuing for N-particle, we have

$$\left(\prod_{i=1}^{N}c^{\dagger}_{\mathbf{q_i}}\right)=c^{\dagger}_{\mathbf{q_1}}c^{\dagger}_{\mathbf{q_2}}.....c^{\dagger}_{\mathbf{q_{N-1}}}c^{\dagger}_{\mathbf{q_N}}, \tag{C.7}$$

$$\left(\prod_{i=1}^{N} c^{\dagger}_{\mathbf{q_i}}\right)_{[\theta],[\theta']} = \left(\prod_{\mathbf{k'}\neq\mathbf{q_i}\forall\mathbf{i}} \delta_{\theta_{\mathbf{k'}},\theta'_{\mathbf{k'}}}\right)\left(\prod_{i=1}^{N}\delta_{\theta_{\mathbf{q_i}},-\theta'_{\mathbf{q_i}}}\right)\times\prod_{i,j,i>j}^{N}\mathrm{sign}(\mathbf{q}_j,\mathbf{q}_i)\left(\prod_{i=1}^{N}\frac{1-\theta_{\mathbf{q_i}}}{2}\right)$$
$$\times\prod_{i=1}^{N}\exp\left[i\pi\sum_{\mathbf{k}>\mathbf{q}_i}\frac{1+\theta_{\mathbf{k}}}{2}\right]. \tag{C.8}$$

We note that the above matrix elements are valid provided both $[\theta]$ and $[\theta']$ obey the constraint relation of Eq. 7.2 with $0 \leq \nu \leq 1$. For particle-hole bilinears in momentum space the matrix elements are given by

$$\left(c^{\dagger}_{\mathbf{k+q}}c_{\mathbf{k}}\right)_{[\theta],[\theta']} = \left(\prod_{\mathbf{k'}\neq\mathbf{k+q},\mathbf{k}}\delta_{\theta_{\mathbf{k'}},\theta'_{\mathbf{k'}}}\right)\delta_{\theta_{\mathbf{k+q}},-\theta'_{\mathbf{k+q}}}\delta_{\theta_{\mathbf{k}},-\theta'_{\mathbf{k}}}\times\mathrm{sign}(\mathbf{k}+\mathbf{q},\mathbf{k})\left(\frac{1-\theta_{\mathbf{k+q}}}{2}\right)\left(\frac{1+\theta_{\mathbf{k}}}{2}\right)$$
$$\times\exp\left[i\pi\sum_{\mathbf{k+q}>\mathbf{k'}>\mathbf{k}}\frac{1+\theta_{\mathbf{k'}}}{2}\right]+\delta_{\mathbf{q},0}\left(\prod_{\mathbf{k'}}\delta_{\theta_{\mathbf{k'}},\theta'_{\mathbf{k'}}}\right)\frac{1+\theta_{\mathbf{k}}}{2}, \tag{C.9}$$

where the last term gives the diagonal contribution for the momentum space occupation $n_{\mathbf{k}} = c^{\dagger}_{\mathbf{k}}c_{\mathbf{k}}$.

C.2 Hamiltonian in the $[\theta]$ basis

Having constructed the wave-function in the $[\theta]$ basis, we now consider the action of interacting fermionic Hamiltonian H (Eq. 7.4) on these wave-functions. The matrix elements of the non-interacting part, H_0, in this basis is given by

$$\langle\Psi[\theta']|H_0|\Psi[\theta]\rangle = \left(\sum_{\mathbf{k}}E_{\mathbf{k}}\left(\frac{1+\theta_{\mathbf{k}}}{2}\right)\right)\langle\Psi[\theta']|\Psi[\theta]\rangle. \tag{C.10}$$

Thus H_0 is diagonal in the $[\theta]$ basis, as discussed in the main text. For interacting part H_I of Eq. 7.4, putting $\mathbf{k_1} = \mathbf{k_2} - \mathbf{q}$, we get

$$\begin{aligned} H_I(\mathbf{k_1} = \mathbf{k_2} - \mathbf{q}) &= \sum_{\mathbf{k_1}}\sum_{\mathbf{q}\neq\mathbf{0}} V_{\mathbf{q}}c^{\dagger}_{\mathbf{k_1}}c^{\dagger}_{\mathbf{k_1+q}}c_{\mathbf{k_1}}c_{\mathbf{k_1+q}} \\ &= -\sum_{\mathbf{k_1}}\sum_{\mathbf{q}\neq\mathbf{0}} V_{\mathbf{q}}\left(c^{\dagger}_{\mathbf{k_1}}c_{\mathbf{k_1}}\right)\left(c^{\dagger}_{\mathbf{k_1+q}}c_{\mathbf{k_1+q}}\right) \\ &= -\sum_{\mathbf{k_1}}\sum_{\mathbf{q}\neq\mathbf{0}} V_{\mathbf{q}}n_{\mathbf{k_1}}n_{\mathbf{k_1+q}} \end{aligned} \tag{C.11}$$

where $n_{\mathbf{k}} = c^{\dagger}_{\mathbf{k}} c_{\mathbf{k}}$ is the density operator. In the $[\theta]$ basis, it follows that

$$\begin{aligned}\langle \Psi[\theta'] | H_I(\mathbf{k_1} = \mathbf{k_2} - \mathbf{q}) | \Psi[\theta] \rangle &= -\sum_{\mathbf{k_1}} \sum_{\mathbf{q}\neq 0} V_{\mathbf{q}} \langle \Psi[\theta'] | n_{\mathbf{k_1}} n_{\mathbf{k_1}+\mathbf{q}} | \Psi[\theta] \rangle \\ &= -\sum_{\mathbf{k_1}} \sum_{\mathbf{q}\neq 0} V_{\mathbf{q}} \left(\frac{1+\theta_{\mathbf{k_1}}}{2}\right) \left(\frac{1+\theta_{\mathbf{k_1}+\mathbf{q}}}{2}\right) \delta_{[\theta'][\theta]} \end{aligned} \tag{C.12}$$

and is also a diagonal term. This implies $E[\theta]$ (in Eq. 7.7) has the form,

$$E[\theta] = \sum_{\mathbf{k}} \left(E_{\mathbf{k}} \left(\frac{1+\theta_{\mathbf{k}}}{2}\right) - \sum_{\mathbf{q}\neq 0} V_{\mathbf{q}} \left(\frac{1+\theta_{\mathbf{k}}}{2}\right) \left(\frac{1+\theta_{\mathbf{k}+\mathbf{q}}}{2}\right) \right) \tag{C.13}$$

Next, we consider the non-diagonal matrix elements for interacting part H_I, given by the second term of Eq. 7.4. These matrix elements can be written as

$$\begin{aligned}\langle \Psi[\theta'] | H_I | \Psi[\theta] \rangle &= E_I([\theta'], [\theta]) \\ &= \sum_{\mathbf{k}_1} \sum_{\mathbf{k}_2} \sum_{\mathbf{q}\neq 0} V(\mathbf{q}) \left(\prod_{\mathbf{k}\neq \mathbf{k}_1, \mathbf{k}_2, \mathbf{k}_1+\mathbf{q}, \mathbf{k}_2-\mathbf{q}} \delta_{\theta_{\mathbf{k}} \theta'_{\mathbf{k}}} \right) \\ &\times \left(\delta_{\theta_{\mathbf{k}_1}, -\theta'_{\mathbf{k}_1}} \delta_{\theta_{\mathbf{k}_2}, -\theta'_{\mathbf{k}_2}} \delta_{\theta_{\mathbf{k}_1+\mathbf{q}}, -\theta'_{\mathbf{k}_1+\mathbf{q}}} \delta_{\theta_{\mathbf{k}_2-\mathbf{q}}, -\theta'_{\mathbf{k}_2-\mathbf{q}}} \right) \\ &\times \left(\frac{1-\theta_{\mathbf{k}_1}}{2}\right) \left(\frac{1-\theta_{\mathbf{k}_2}}{2}\right) \left(\frac{1+\theta_{\mathbf{k}_1+\mathbf{q}}}{2}\right) \left(\frac{1+\theta_{\mathbf{k}_2-\mathbf{q}}}{2}\right) \\ &\times \text{sign}(\mathbf{k}_1, \mathbf{k}_2)\, \text{sign}(\mathbf{k}_2 - \mathbf{q}, \mathbf{k}_1 + \mathbf{q}) \times \exp\left[i\pi \left(\chi_{\mathbf{k}_1} + \chi_{\mathbf{k}_2} + \chi_{\mathbf{k}_2-\mathbf{q}} + \chi_{\mathbf{k}_1+\mathbf{q}} \right) \right] \end{aligned} \tag{C.14}$$

$$\begin{aligned} &= \sum_{\mathbf{k}_1} \sum_{\mathbf{k}_2} \sum_{\mathbf{q}\neq 0} V(\mathbf{q}) \left(\prod_{\mathbf{k}\neq \mathbf{k}_1, \mathbf{k}_2, \mathbf{k}_1+\mathbf{q}, \mathbf{k}_2-\mathbf{q}} \delta_{\theta_{\mathbf{k}} \theta'_{\mathbf{k}}} \right) \\ &\times \left(\delta_{\theta_{\mathbf{k}_1}, -\theta'_{\mathbf{k}_1}} \delta_{\theta_{\mathbf{k}_2}, -\theta'_{\mathbf{k}_2}} \delta_{\theta_{\mathbf{k}_1+\mathbf{q}}, -\theta'_{\mathbf{k}_1+\mathbf{q}}} \delta_{\theta_{\mathbf{k}_2-\mathbf{q}}, -\theta'_{\mathbf{k}_2-\mathbf{q}}} \right) \\ &\quad \times \left(\frac{1-\theta_{\mathbf{k}_1}}{2}\right) \left(\frac{1-\theta_{\mathbf{k}_2}}{2}\right) \left(\frac{1+\theta_{\mathbf{k}_1+\mathbf{q}}}{2}\right) \left(\frac{1+\theta_{\mathbf{k}_2-\mathbf{q}}}{2}\right) \\ &\quad \times \exp\left[i\pi \left(\tilde{\chi}_{\mathbf{k}_1} + \tilde{\chi}_{\mathbf{k}_2} + \tilde{\chi}_{\mathbf{k}_2-\mathbf{q}} + \tilde{\chi}_{\mathbf{k}_1+\mathbf{q}} \right) \right], \end{aligned} \tag{C.15}$$

where, $\chi_{\mathbf{k_i}} = \sum_{\mathbf{k}>\mathbf{k_i}} \frac{1+\theta_{\mathbf{k}}}{2}$ for $\mathbf{k_i} \in \{\mathbf{k_1}, \mathbf{k_2}, \mathbf{k_2}-\mathbf{q}, \mathbf{k_1}+\mathbf{q}\}$ and

$$\tilde{\chi}_{\mathbf{k_1}+\mathbf{q}} = \sum_{\mathbf{k_i}>\mathbf{k_1}+\mathbf{q}} \frac{1+\theta_{\mathbf{k_i}}}{2}, \;\; \tilde{\chi}_{\mathbf{k_2}-\mathbf{q}} = \sum_{\mathbf{k_i}>\mathbf{k_2}-\mathbf{q}} \frac{1+\theta_{\mathbf{k_i}}}{2} - \frac{(1-\text{sign}\,((\mathbf{k_2}-\mathbf{q}),(\mathbf{k_1}+\mathbf{q})))}{2},$$
$$\tilde{\chi}_{\mathbf{k_2}} = \sum_{\mathbf{k_i}>\mathbf{k_2}} \frac{1+\theta_{\mathbf{k_i}}}{2} - \frac{(1-\text{sign}\,(\mathbf{k_2},(\mathbf{k_2}-\mathbf{q})))}{2} - \frac{(1-\text{sign}\,(\mathbf{k_2},(\mathbf{k_1}+\mathbf{q})))}{2},$$
$$\tilde{\chi}_{\mathbf{k_1}} = \sum_{\mathbf{k_i}>\mathbf{k_1}} \frac{1+\theta_{\mathbf{k_i}}}{2} - \frac{(1-\text{sign}\,(\mathbf{k_1},\mathbf{k_2})))}{2} - \frac{(1-\text{sign}\,(\mathbf{k_1},(\mathbf{k_2}-\mathbf{q})))}{2} - \frac{(1-\text{sign}\,(\mathbf{k_1},(\mathbf{k_1}+\mathbf{q})))}{2}. \tag{C.16}$$

In Eq. C.16, all the sign factors neutralize the effects of each other in the contribution. So we have,

$$\sum_{i=1}^{4} \tilde{\chi}_{\mathbf{k_i}} = \sum_{i=1}^{4} \chi_{\mathbf{k_i}} - \frac{(1-\text{sign}\,((\mathbf{k_2}-\mathbf{q}),(\mathbf{k_1}+\mathbf{q})))}{2} - \frac{(1-\text{sign}\,(\mathbf{k_1},\mathbf{k_2})))}{2} \tag{C.17}$$

which implies

$$\begin{aligned}(-1)^{\sum_{i=1}^{4}\tilde{\chi}_{\mathbf{k_i}}} =& \text{sign}\,((\mathbf{k_2}-\mathbf{q}),(\mathbf{k_1}+\mathbf{q})) \\ & \times \text{sign}\,(\mathbf{k_1},\mathbf{k_2}))\,(-1)^{\sum_{i=1}^{4}\chi_{\mathbf{k_i}}}.\end{aligned} \tag{C.18}$$

Eq. C.14 thus provides matrix elements for H_I. The full Hamiltonian can now be written as in Eq. 7.7 which can be put into a more concise form as

$$H = \sum_{[\theta],[\theta']} M\left([\theta],[\theta']\right) |\Psi[\theta]\rangle\langle\Psi[\theta']|, \tag{C.19}$$
$$M([\theta],[\theta']) = E[\theta]\,\delta_{[\theta],[\theta']} + E_I([\theta],[\theta'])\left(1-\delta_{[\theta],[\theta']}\right).$$

C.3 Details of the Exact diagonalization in one spatial dimension.

As explained in the main text, consider, in Eq. 7.6, using

$$V(\mathbf{q}) = \frac{\tilde{V}_0}{N} e^{-\frac{\mathbf{q}^2}{2q_0^2}} \tag{C.20}$$

where q_0 is the momentum scale at which the interactions decay in momentum space. Then the (four fermion) interacting part of the Hamiltonian is given by

$$H_{int}| = \sum_{\mathbf{k_1},\mathbf{k_2},\mathbf{q}} V(\mathbf{q}) \mathbf{c}^\dagger_{\mathbf{k_1}} \mathbf{c}^\dagger_{\mathbf{k_2}} \mathbf{c}_{\mathbf{k_2}-\mathbf{q}} \mathbf{c}_{\mathbf{k_1}+\mathbf{q}} \tag{C.21}$$

$$= \frac{\tilde{V}_0}{N} \sum_{\mathbf{r_1},\mathbf{r_2}} \left(\sum_{\mathbf{q}} e^{-\frac{\mathbf{q}^2}{2q_0^2}} e^{i(\mathbf{q}\cdot(\mathbf{r_1}-\mathbf{r_2}))} \right) \left(c^\dagger_{\mathbf{r_1}} c^\dagger_{\mathbf{r_2}} c_{\mathbf{r_2}} c_{\mathbf{r_1}} \right) \tag{C.22}$$

The Fourier transform over $\mathbf{q}$ can now be done (most conveniently by transforming the sum to an integral, *i.e.*, $\frac{1}{N}\sum_{\mathbf{q}} \to \frac{1}{2\pi}\int dq$) to obtain the real-space form

$$H_{int} = \sum_{\mathbf{r_1},\mathbf{r_2}} \tilde{V}_0 \left(\frac{q_0}{\sqrt{2\pi}} \exp\left(-\frac{q_0^2 |\mathbf{r_1}-\mathbf{r_2}|^2}{2} \right) \right) c^\dagger_{\mathbf{r_1}} c^\dagger_{\mathbf{r_2}} c_{\mathbf{r_2}} c_{\mathbf{r_1}} \tag{C.23}$$

which is similar to the density-density interaction (up to a chemical potential which is tuned to a value to ensure half filling) in Eq. 7.8.

On truncating the interactions in Eq. 7.8 to nearest neighbour, the Hamiltonian becomes

$$H = -t \sum_i \left(c^\dagger_i c_{i+1} + \text{h.c.} \right) + V_0 \sum_i n_i n_{i+1}. \tag{C.24}$$

Alternatively we can obtain Eq. C.24 from Eqs. 7.4 and 7.6 for $V(\mathbf{q}) = \frac{V_0}{N} e^{iqa}$.

For our real space ED calculations we use Eq. C.24. In fact using the well-known transformation to the XXZ spin Hamiltonian [184] via Jordan-Wigner transformation :

$$S^z_i = \frac{1}{2} - c^\dagger_i c_i, \;\; S^+_i = \frac{1}{2} \tilde{K}_i c_i, \;\; S^-_i = \frac{1}{2} c^\dagger_i \tilde{K}_i, \tag{C.25}$$

where S^α_i ($\alpha = x, y, z$) are spin-1/2 operators and

$$\tilde{K}_i = \exp\left[i\pi \sum_{j=1}^{i-1} c^\dagger_j c_j \right], \tag{C.26}$$

we get the corresponding XXZ spin Hamiltonian given by

$$H = -2t \sum_i \left(S^x_i \, S^x_{i+1} + S^y_i \, S^y_{i+1} \right) + V_0 \sum_i S^z_i \, S^z_{i+1}. \tag{C.27}$$

We use this spin Hamiltonian for our real-space diagonalisation. For our ED we use numerical linear algebra libraries like *NumPy* in Python (we use sparse matrix techniques).

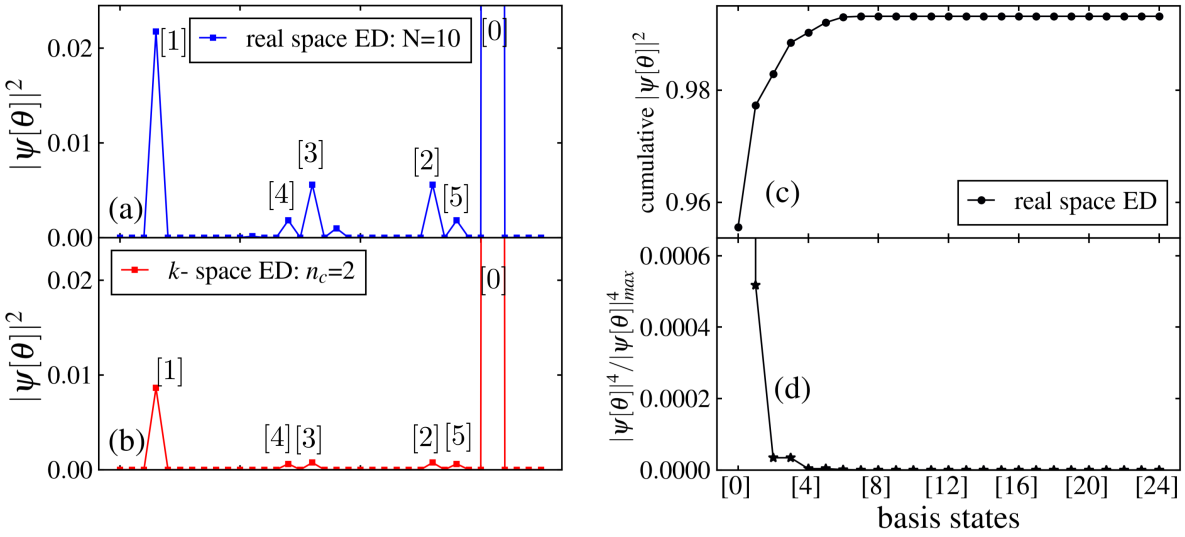

Figure C.1: (a) The probabilities of the GS wave-function obtained from ED of the half filled spinless fermions (Eq. C.24) ($N = 10, t = 1$, for real space ED $V_0 = 0.3$ (Eq. C.27) and for k-space ED $\frac{\tilde{V}_0}{N} = 0.3$ (Eq. 7.9)) for spinless fermions in the basis given by Eq. 7.1 (horizontal axis). The relevant momenta in the first BZ are denoted by $k = -\pi + \alpha\pi/5$ with $\alpha = 0, 1, \cdots, 9$. In this labelling the four states with leading contributions are shown with $[0] \equiv [0001111100]$ being the non-interacting GS and the rest corresponding to the excitations above the non-interacting GS. These are $[1] = [0010111010]$, $[2] = [0011011001]$, $[3] = [0100110110]$, $[4] = [0011010110]$ and $[5] = [0100111001]$. The states are arranged in terms of the increasing number of particle-hole excitations which can also be quantified via their root mean square momenta deviation from the FS. Note that the vertical scale has been truncated for improved visibility of the contributing basis states. (b) The exact diagonalization done using the momentum space cut-off $\mathbf{q}_c$ ($n_c = 2$ $\left(q_c = \frac{2\pi}{N} n_c\right)$, $n_0 = 1.5$ $\left(q_0 = \frac{2\pi}{N} n_0\right)$, see main text for details). (c) The cumulative weights of the different basis states. (4) The IPR for the different basis states. The IPR has been normalised with respect to the maximum contribution (vertical axis truncated for better visibility) from $[0]$.

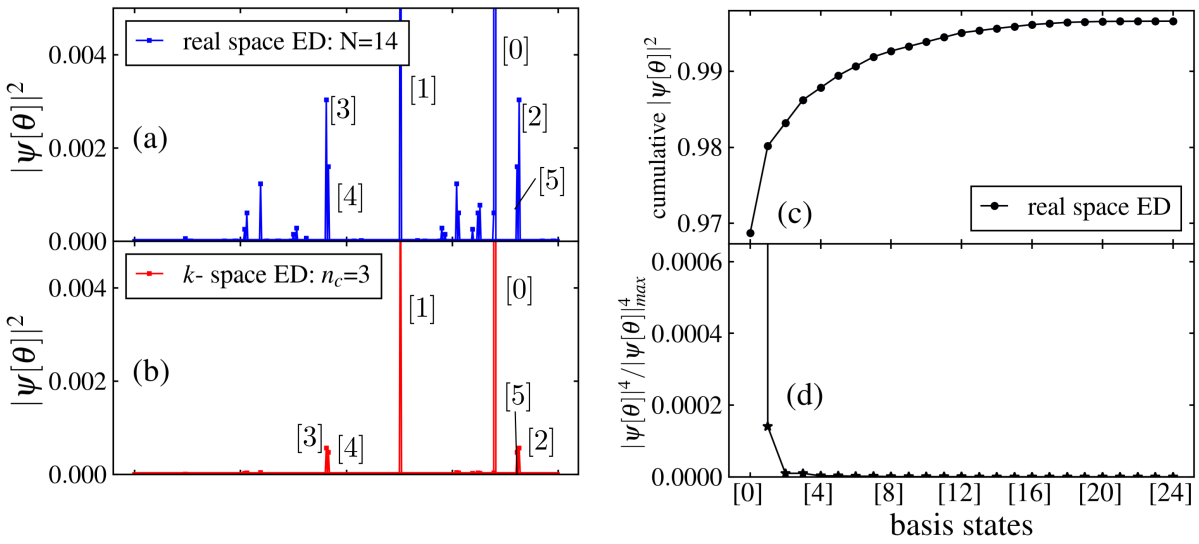

Figure C.2: (a) The probabilities of the GS wave-function obtained from ED of the half filled spinless fermions (Eq. C.24) ($N = 14, t = 1$, for real space ED $V_0 = 0.2$ (Eq. C.27) and for k-space ED $\frac{\tilde{V}_0}{N} = 0.2$ (Eq. 7.9)) for spinless fermions in the basis given by Eq. 7.1 (horizontal axis). The relevant momenta in the first BZ are denoted by $k = -\pi + \alpha\pi/7$ with $\alpha = 0, 1, \cdots, 13$. In this labelling the four states with leading contributions are shown with $[0] \equiv [00001111111000]$ being the non-interacting GS and the rest corresponding to the excitations above the non-interacting GS. These are $[1] = [00010111110100]$, $[2] = [00011011110010]$, $[3] = [00100111101100]$, $[4] = [00011101110001]$ and $[5] = [01000111011100]$. The states are arranged in terms of the increasing number of particle-hole excitations which can also be quantified via their root mean square momenta deviation from the FS. Note that the vertical scale has been truncated for improved visibility of the contributing basis states. (b) The exact diagonalization done using the momentum space cut-off $\mathbf{q}_c$ ($n_c = 3$ $\left(q_c = \frac{2\pi}{N} n_c\right)$, $n_0 = 1.5$ $\left(q_0 = \frac{2\pi}{N} n_0\right)$, see main text for details). (c) The cumulative weights of the different basis states. (4) The IPR for the different basis states. The IPR has been normalised with respect to the maximum contribution (vertical axis truncated for better visibility) from $[0]$.

State	k_{RMS}	$\|\Psi_\theta\|^2_{XXZ}$ (real space ED)	$\|\Psi_\theta\|^2_{q_c}$ (k-space ED)
$\|0\rangle = [0000\mathbf{1}1111\mathbf{1}1000]$	0.00	0.93336	0.97935
$\|1\rangle = [000\mathbf{1}0111\mathbf{1}1\mathbf{0}100]$	0.54	0.02284	0.01575
$\|2\rangle = [000\mathbf{11}01111\mathbf{00}10]$	0.99	0.00669	0.00124
$\|3\rangle = [00\mathbf{1}00111\mathbf{1}01100]$	0.99	0.00669	0.00124
$\|4\rangle = [000\mathbf{111}0111\mathbf{0}001]$	1.38	0.00296	0.00008
$\|5\rangle = [0\mathbf{1}000111\mathbf{011}100]$	1.38	0.00296	0.00008

Table C.1: The probability density corresponding to different basis states representing particle-hole excitations over the FS as obtained through real space (XXZ) (Column 3) and the momentum-space with a fixed q_c (Column 4) ED methods for the system discussed in Fig. 7.1 of the main text. The red numbers in column 1 indicate position of the FS in $|0\rangle$ and chart out the position of the particle-hole excitations near the FS for other states. Column 2 indicates the RMS momenta with respect to FS defined as $k_{RMS} = \sqrt{\langle k^2\rangle} - \sqrt{\langle k^2\rangle}_{FS}$, where ($\sqrt{\langle k^2\rangle} = \sqrt{\sum_k k^2(1+\theta_k)/2}$), which measures deviation from $|0\rangle$ for the corresponding states.

C.3.1 Exact Diagonalization in Real space

For our real space ED results, we used the spin-model in Eq. C.27 for numerical diagonalisation and re-convert our results to the fermion representation using the Jordon-Wigner transformations (Eq. C.25). The ground state (GS) in real space basis is then transformed to the momentum space via Fourier transform of the Slater determinants (for the fermions). This momentum-space GS so obtained can be understood in the $[\theta]$- basis (Eq. 7.1) and can be used to compute the connected correlator and the entanglement entropy; these serve as a benchmark and are shown in Fig. 7.2.

Since we are interested in understanding the role of interaction in the configuration space spanned by $|\Psi[\theta]\rangle$ basis mentioned in Eq. 7.1. We computed the amplitude of various basis states contributing to the GS as shown in Fig. 7.1. The largest peak, as expected, corresponds to the state with non-interacting FS at a given ν. However, due to interaction between fermions, there are other states with non-zero amplitudes. The details of the weights of different $|\Psi[\theta]\rangle$ states with non-zero amplitude in the GS for the system parameters discussed in Fig. 7.1 is given in Table C.1. Results similar to Fig. 7.1 for $N = 10$ is shown in Fig. C.1 and for $N = 14$ and $V_0 = 0.2$ in Fig. C.2.

C.3.2 Exact Diagonalization in momentum space

For the momentum space ED, we use Eq. 7.4 and interactions given by Eq. 7.6 with $V(\mathbf{q})$ given by Eq. C.20. We choose $q_0 = 2\pi n_0/N$ where n_0 the different choices of n_0 are mentioned in captions of respective figures. Taking cue from the TLL ground state wave-function for the nearest neighbour model, as studied in or real space ED,

we expect that at low energy the major contributions arise from mixing of particle-hole excitations near the FS. While keeping intact this low energy physics, we introduce a ultraviolet cut-off in the spirit of renormalisation group approaches for fermions [36], $\mathbf{q}_c = 2\pi n_c/N$ such that for Eq. 7.6 we have the interactions given by Eq. 7.9 in the main text. This reduces the sum over $\mathbf{q}$ in Eq. 7.6 over the window $-|\mathbf{q}_c| < \mathbf{q} < |\mathbf{q}_c|$ around the FS as elaborated in the main text (also see below).

The above form is then used in the Hamiltonian (Eq. 7.4) for our momentum space diagonalization. This starts by writing it in the matrix form in the $|\Psi[\theta]\rangle$ basis using the matrix elements mentioned in Eq. 7.7. For a given n_c ($q_c = 2\pi n_c/N$), the number of states that are kept is given by $N_s = \left({}^{2n_c}C_{n_c}\right)^2$ in 2D; this yields a $N_s \times N_s$ matrix form of the Hamiltonian which is diagonalized using ED.

In 1D, at $\nu = 1/2$, there are two Fermi-points $\mathbf{k_{F1}} = -\frac{\pi}{2}\hat{\mathbf{x}}$ and $\mathbf{k_{F2}} = \frac{\pi}{2}\hat{\mathbf{x}}$. Then to calculate the different elements in Eq. C.14, we note that the three momenta are restricted to the following domain with the possible values of $\mathbf{k_1}, \mathbf{k_2}, \mathbf{q}$ being:

$$\mathbf{k_1} \in \left(\mathbf{k_{F2}} + \frac{2\pi}{N}\hat{\mathbf{x}},\ \ \mathbf{k_{F2}} + \mathbf{q_c}\right), \tag{C.28}$$

$$\mathbf{k_2} \in \left(\mathbf{k_{F1}} - \mathbf{q_c},\ \ \mathbf{k_{F1}} - \frac{2\pi}{N}\hat{\mathbf{x}}\right), \tag{C.29}$$

$$\mathbf{q} \in \left(\frac{2\pi}{N}\hat{\mathbf{x}},\ \ \mathbf{q_c}\right), \tag{C.30}$$

and

$$\mathbf{k_2} \in \left(\mathbf{k_{F2}} + \frac{2\pi}{N}\hat{\mathbf{x}},\ \ \mathbf{k_{F2}} + \mathbf{q_c}\right), \tag{C.31}$$

$$\mathbf{k_1} \in \left(\mathbf{k_{F1}} - \mathbf{q_c},\ \ \mathbf{k_{F1}} - \frac{2\pi}{N}\hat{\mathbf{x}}\right), \tag{C.32}$$

$$\mathbf{q} \in \left(\frac{2\pi}{N}\hat{\mathbf{x}},\ \ \mathbf{q_c}\right). \tag{C.33}$$

The results for weights of different $|\Psi[\theta]\rangle$ states in the momentum-space diagonalization are shown in Fig. 7.1(b), C.1(b) and C.2(b) for comparison.

Details of calculation of entanglement entropy

The TLL is captured by a $(1+1)D$ conformal field theory [2,184] whose bipartite von-Neumann entanglement entropy is captured by the Cardy-Calabrese [169] formula

$$S_{vN} = \frac{c}{3}\log\left(\frac{L}{\pi a}\sin\pi\frac{l}{L}\right) + \text{constant}. \tag{C.34}$$

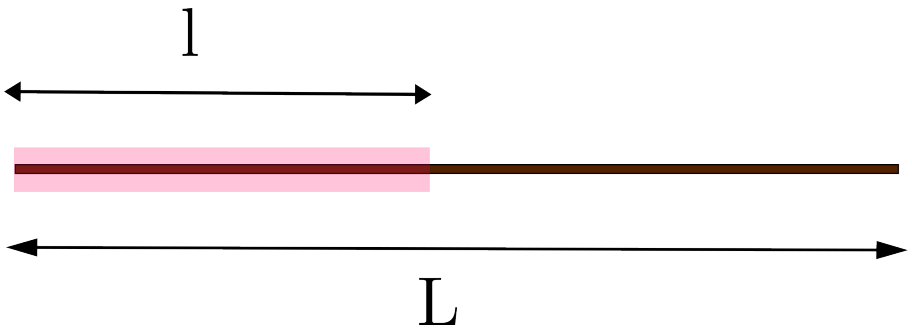

Figure C.3: Schematic diagram for 1D chain : Colored part (of length $l = na$) correspond to subsystem containing n sites integrated out for a system of total length $L = Na$.

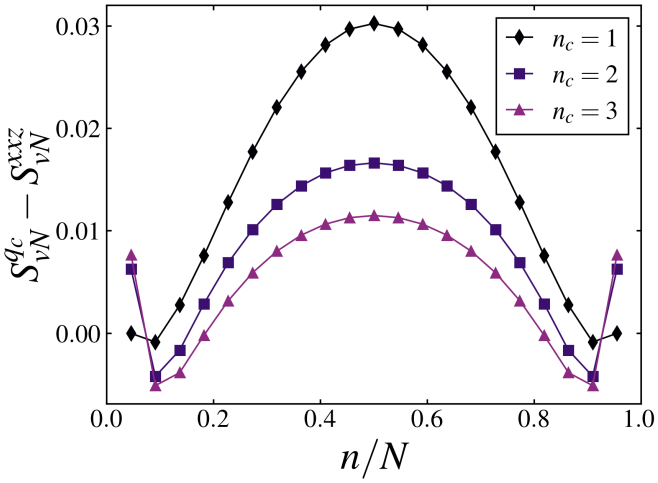

Figure C.4: Difference of S_{vN} calculated from real space ED and k-space ED (for N=22, V_0=0.3 (Eq. C.27), $\frac{\tilde{V}_0}{N}$=0.3 (Eq. 7.9), n_0 = 1.5). As we increase n_c, it approaches zero, which means $S_{vN}^{q_c}$ starts to be in more agreement with S_{vN}^{xxz}.

where c is the central charge of the CFT, $L(= Na)$ is the length of the entire system and $l(= na)$ is that of the sub-system as shown in Fig. C.3.

We numerically calculate bipartite Von-Neumann Entropy

$$S_{vN} = -Tr[\rho_A \ln \rho_A], \tag{C.35}$$

where ρ_A is the reduced density matrix of subsystem A obtained by tracing out the rest of the system ($\bar{A}$). We employed standard singular value decomposition methods (SVD) to calculate the entanglement entropy, S_{vN}, and have used Eq. C.34 to obtain the central charge c as shown in Fig. 7.4.

For comparison, we show, in Fig. C.4, the difference of the entanglement entropy calculated via real space ED and k-space ED for different n_c. As n_c is increased, the entanglement calculated by both methods agrees well showing the efficacy of the momentum-space method.

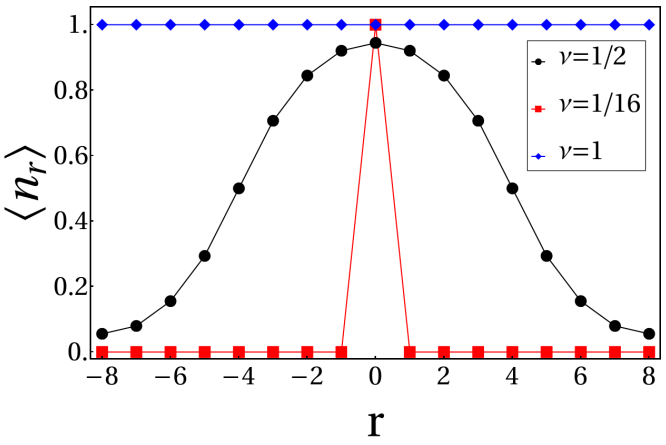

Figure C.5: Plot of $\langle n_{\mathbf{r}} \rangle$ as a function of $\mathbf{r} = r\hat{\mathbf{x}}$ for the RK ground states, where we have taken 16 sites for different fillings ν and used periodic boundary conditions (PBC).

C.4 Different Correlations for the RK state

For Eq. 7.14, we computed the average real space occupation $\langle \Psi_{\mathrm{RK}} | \hat{n}_{\mathbf{r}} | \Psi_{\mathrm{RK}} \rangle$ in 1D for finite systems. This is plotted in Fig. C.5. Useful insights are obtained by considering the single-particle (corresponding to $\nu = 1/16$) RK state (Eq. 7.14) $\sim \sum_{\mathbf{k}} |\mathbf{k}\rangle \sim |\mathbf{r} = 0\rangle$. The expectation value of $n_{\mathbf{r}}$ to be sharply peaked at $\mathbf{r} = 0$ for this state (see Fig. C.5) exhibiting breaking of translation. However, this provides a way to generate Wannier functions centered at other lattice sites by applying the lattice translation operator to the $|\mathbf{r} = 0\rangle$ state. The fully filled ($\nu = 1$) band, on the other hand has a flat average with the intermediate fillings interpolating between the two limits via a distribution of $\langle \Psi_{\mathrm{RK}} | \hat{n}_{\mathbf{r}} | \Psi_{\mathrm{RK}} \rangle$ centered around $\mathbf{r} = 0$. This distribution can be shifted to any lattice site via translation operator as mentioned above. The half-width of the distribution (not shown) increases monotonically with filling. It would be interesting to ask for the spectral properties of H_{RK} which is an interesting future direction.

For the constrained RK state $|\psi_{\mathrm{RK}}^{\mathbf{k}_{\mathrm{T}}}\rangle$, we always choose the momentum $\mathbf{k} = \pi$ to be empty for convenience in the main text. This is because on including this mode, the real space density shows oscillations with wave-vector π irrespective of the filling, ν. We think that this is an artifact of this wave-function. Turning back to $|\psi_{\mathrm{RK}}^{\mathbf{k}_{\mathrm{T}}}\rangle$, we find

$$\langle \psi_{\mathrm{RK}}^{\mathbf{k}_{\mathrm{T}}} | n_{\mathbf{r}} | \psi_{\mathrm{RK}}^{\mathbf{k}_{\mathrm{T}}} \rangle = \frac{1}{N} \sum_{\mathbf{k_1},\mathbf{k_2}} \langle \psi_{\mathrm{RK}}^{\mathbf{k}_{\mathrm{T}}} | c_{\mathbf{k_1}}^{\dagger} c_{\mathbf{k_2}} | \psi_{\mathrm{RK}}^{\mathbf{k}_{\mathrm{T}}} \rangle e^{i(\mathbf{k_1}-\mathbf{k_2})\cdot\mathbf{r}}. \tag{C.36}$$

Since all states in the superposition carries same $\mathbf{k}_{\mathrm{T}}$, this implies $k_1 = k_2$ such that the

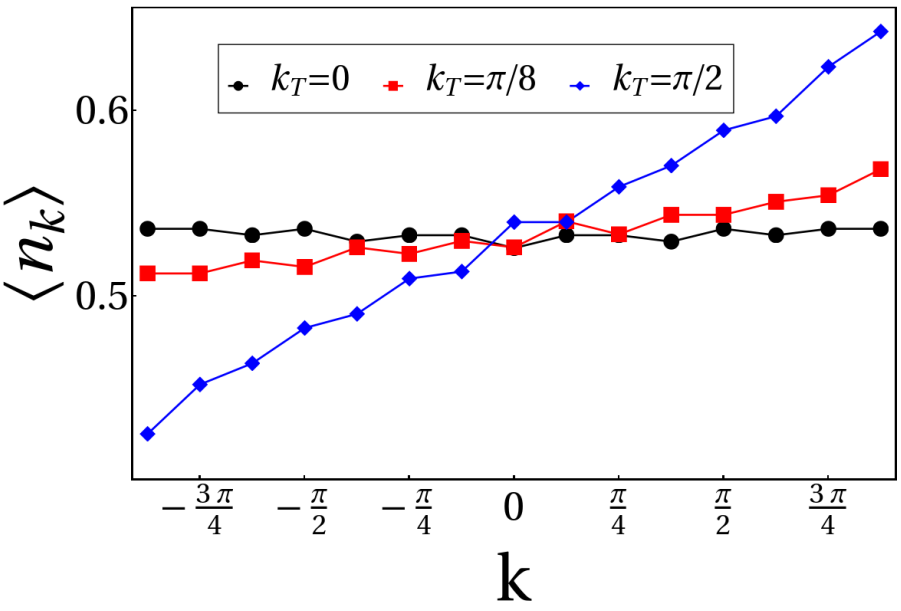

Figure C.6: Plot of $\langle n_{\mathbf{k}} \rangle$ as a function of k for the constrained RK ground states ($|\psi_{\mathrm{RK}}^{\mathbf{k}_\mathrm{T}}\rangle$), where we have taken 16 sites for different $\mathbf{k}_\mathrm{T}$ and used periodic boundary conditions (PBC).

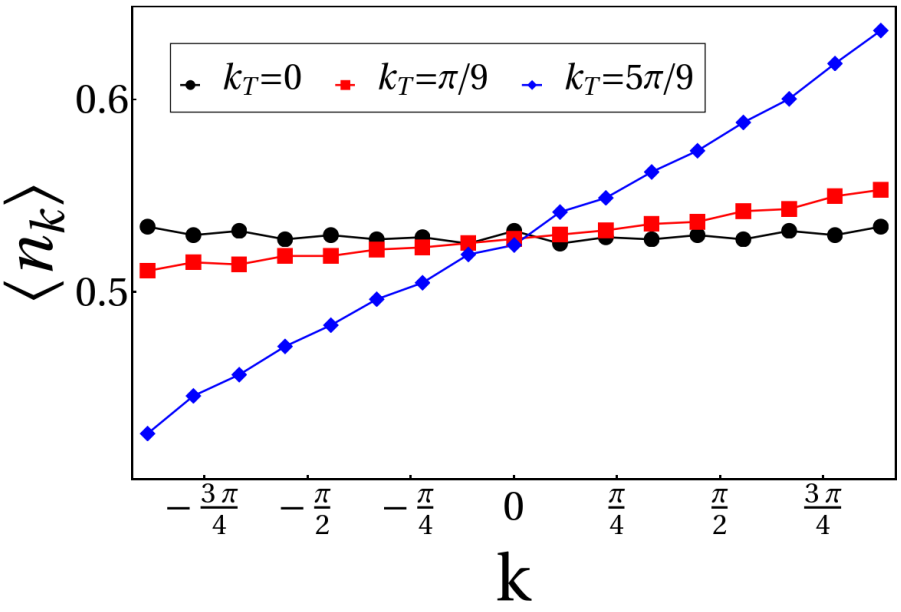

Figure C.7: Plot of $\langle n_{\mathbf{k}} \rangle$ as a function of k for the constrained RK ground states ($|\psi_{\mathrm{RK}}^{\mathbf{k}_\mathrm{T}}\rangle$), where we have taken 18 sites for different $\mathbf{k}_\mathrm{T}$ and used periodic boundary conditions (PBC).

above equation gives

$$\langle \psi^{\mathbf{k}_T}_{RK} | n_{\mathbf{r}} | \psi^{\mathbf{k}_T}_{RK} \rangle = \frac{1}{N} \sum_{\mathbf{k}} \langle \psi^{\mathbf{k}_T}_{RK} | c^{\dagger}_{\mathbf{k}} c_{\mathbf{k}} | \psi^{\mathbf{k}_T}_{RK} \rangle = \nu. \tag{C.37}$$

The average momentum occupancy is shown in Fig. 7.5 in the main text. Similar plots for $N = 16$ and 18 are shown in Fig. C.6 and C.7. As mentioned in the main text, it is concluded that the oscillation in $\langle n_{\mathbf{k}} \rangle$ fades with increasing system size (N) and in the large N limit there is no sharp signature in the momentum space occupation.

C.5 Superposition of Elliptical FS

C.5.1 The Elliptical FS

The area of BZ is $4\pi^2$ and for filling ν, the area of FS therefore is $4\pi^2\nu$. For elliptical FS (Fig. 7.6) with eccentricity ϵ and major axis along $\hat{\mathbf{k}}$, the equal energy contours are given by

$$E_{\epsilon}(\mathbf{k}) = \frac{k_{\parallel}^2}{a^2} + \frac{k_{\perp}^2}{a^2(1-\epsilon^2)} - \mu \tag{C.38}$$

where $k_{\parallel}(k_{\perp})$ are momentum components resolved along (perpendicular) to the major axis along $\hat{\mathbf{k}}$. The equation for the FS (with corresponding state $|\epsilon, \nu, \hat{\mathbf{k}}\rangle$) is $E_{\epsilon}(\mathbf{k}) = 0$ as shown in Fig. 7.6.

For every ellipse (Fig. 7.6) the relation between the major axis (of length $2a$), minor axis (of length $2a\sqrt{1-\epsilon^2}$)for given eccentricity ϵ, such that the relation between the area of the ellipse and the filling is given by

$$\mu\, a^2 \sqrt{1-\epsilon^2} \;\; = \;\; 4\pi\nu, \tag{C.39}$$

where $a < \pi$ for closed FS. For given eccentricity at half filling ($\nu = 1/2$), we have taken

$$\mu = 1, \quad a = \left(\frac{4\pi^2}{1-\epsilon^2} \right)^{1/4}. \tag{C.40}$$

Considering the states mentioned in Eq. 7.20, 7.21 and 7.23, we would like to emphasize that each individual states in the superposition carries same total momenta

($\mathbf{k}_T = 0$ in Eq. 7.2). The average real-space density, $\langle n_{\mathbf{r}} \rangle$, is given by

$$\langle \psi_\nu | n_{\mathbf{r}} | \psi_\nu \rangle = \langle \psi_\nu | c^\dagger_{\mathbf{r}} c_{\mathbf{r}} | \psi_\nu \rangle = \frac{1}{N} \sum_{\mathbf{k_1}, \mathbf{k_2}} \langle \psi_\nu | c^\dagger_{\mathbf{k_1}} c_{\mathbf{k_2}} | \psi_\nu \rangle e^{i(\mathbf{k_1} - \mathbf{k_2}) \cdot \mathbf{r}}. \tag{C.41}$$

Since all states carries same total momentum ($\mathbf{k}_T$), this implies $\mathbf{k_1} = \mathbf{k_2}$ in eq. C.41. Expanding $|\psi_\nu\rangle$ using Eq. 7.17, we finally obtain

$$\begin{aligned} \langle \psi_\nu | n_{\mathbf{r}} | \psi_\nu \rangle =& \frac{1}{N} \sum_{\mathbf{k}} \int_0^\pi d\hat{\mathbf{k}} \int_0^{\epsilon_{\max}} d\epsilon |\psi(\epsilon, \hat{\mathbf{k}})|^2 \langle \epsilon, \nu, \hat{\mathbf{k}} | n_{\mathbf{k}} | \epsilon, \nu, \hat{\mathbf{k}} \rangle \\ =& \int_0^\pi d\hat{\mathbf{k}} \int_0^{\epsilon_{\max}} d\epsilon |\psi(\epsilon, \hat{\mathbf{k}})|^2 \times \nu = \nu. \end{aligned} \tag{C.42}$$

C.5.2 quasi-particle Residue

The quasi-particle residue for an elliptical FS (that can be extended to generic cases), with eccentricity ϵ and major axis $\hat{\mathbf{k}}$, is defined as [170]

$$Z_{\epsilon, \mathbf{K_F}} = n(\mathbf{K_F} - \mathbf{0}^+, \epsilon) - n(\mathbf{K_F} + \mathbf{0}^+, \epsilon), \tag{C.43}$$

where $\mathbf{k_F}$ is the Fermi vector obtained from Eq. C.38 such that $Z_{\epsilon, \mathbf{K_F}}(\epsilon)$ captures the unit discontinuity across the FS for such a state.

Noting that for the above state, $n(\mathbf{k}, \epsilon) = \Theta\left[-E_\epsilon(\mathbf{k})\right]$, where $E_\epsilon(\mathbf{k})$ is given by Eq. C.38 and $\Theta[x]$ is the Heaviside-step function, we can extend above definition of the residue away from the FS as

$$Z_{\epsilon, \mathbf{k}} = \lim_{|\mathbf{q}| \to 0^+} \left[n(\mathbf{k} - \mathbf{q}, \epsilon) - n(\mathbf{k} + \mathbf{q}, \epsilon) \right] \tag{C.44}$$

so that the unit discontinuity only appears when the two momenta are on opposite side of the FS. For small δ, the above equation can be written as

$$\begin{aligned} Z_{\epsilon, \mathbf{k}} &= \lim_{|\mathbf{q}| \to 0} \int_{\mathbf{k}+\mathbf{q}}^{\mathbf{k}-\mathbf{q}} d\mathbf{q}' \cdot \frac{\partial n}{\partial \mathbf{q}'} \\ &= \lim_{|\mathbf{q}| \to 0} \int_{\mathbf{k}+\mathbf{q}}^{\mathbf{k}-\mathbf{q}} d\mathbf{q}' \cdot \frac{\partial E_\epsilon(\mathbf{q}')}{\partial \mathbf{q}'} \frac{\partial n}{\partial E_\epsilon(\mathbf{q}')} \end{aligned} \tag{C.45}$$

The derivative of the Heaviside-step function can be calculated by its integral repre-

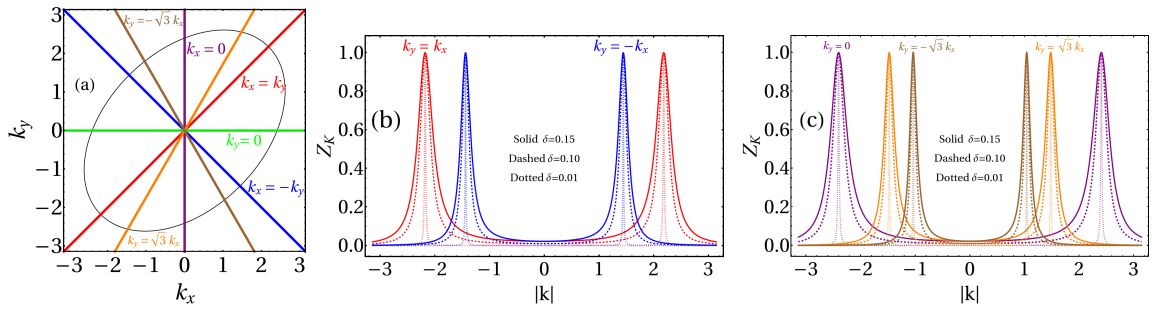

(a) a (b) b (c) c

Figure C.8: (a) Elliptical FS with eccentricity, $\epsilon = 0.75$, aligned along $\hat{\mathbf{k}} = \hat{\mathbf{k}}_\mathbf{x} + \hat{\mathbf{k}}_\mathbf{y}$ and Area = $2\pi^2$ (b) Plot of quasiparticle residue, $Z_{\epsilon,\hat{k}}$(Eq. 7.18) along $k_x = k_y$ and $k_x = -k_y$ corresponding to Red and Blue line in Fig. 21a respectively for different values of δ. (c) $Z_{\epsilon,\hat{k}}$ along $k_y = 0$, $k_y = -\sqrt{3}k_x$ and $k_y = \sqrt{3}k_x$ corresponding to Purple, Brown and Orange line in Fig. 21a for different values of δ. Solid, Dashed and Dotted in the Fig 21b and 21c corresponds to plot with solid line, Dashed line and Dotted line for each color.

sentation $\theta[x] = \frac{1}{2\pi i}\lim_{\tau\to 0}\int_{-\infty}^{\infty} dp e^{ipx}/(p - i\tau)$ to obtain

$$\begin{aligned} Z_{\epsilon,\mathbf{k}} &= \lim_{|\mathbf{q}|\to 0}\int_{\mathbf{k}-\mathbf{q}}^{\mathbf{k}+\mathbf{q}} d\mathbf{q}' \cdot \frac{\partial E_\epsilon(\mathbf{q}')}{\partial \mathbf{q}'}\,\delta\left[E_\epsilon(\mathbf{q}')\right] \\ &= \lim_{|\mathbf{q}|\to 0}\int_{E_\epsilon(\mathbf{k}-\mathbf{q})}^{E_\epsilon(\mathbf{k}+\mathbf{q})} dE'\,\delta\left[E_\epsilon(\mathbf{q}')\right] \end{aligned} \tag{C.46}$$

where $\delta[x]$ is the Dirac-Delta function. Now using the Lorentzian regulator of Dirac-delta function, $\delta[x] = \lim_{\tau\to 0}\frac{1}{\pi}\frac{1}{x^2+\tau^2}$, we get

$$Z_{\epsilon,\mathbf{k}} = \lim_{|\mathbf{q}|\to 0}\int_{E_\epsilon(\mathbf{k}-\mathbf{q})}^{E_\epsilon(\mathbf{k}+\mathbf{q})} dE' \lim_{\tau\to 0}\frac{1}{\pi}\frac{1}{(E_\epsilon(\mathbf{q}'))^2+\tau^2} \tag{C.47}$$

Note that the above integral gets contributions only near the FS as expected, *i.e.*, $E_\epsilon(\mathbf{k}) = 0$. Then an approximate form of the integral can be obtained by setting $E_\epsilon(\mathbf{q}') = E_\epsilon(\mathbf{k})$ and $\pi\delta = E_\epsilon(\mathbf{k}+\mathbf{q}) - E_\epsilon(\mathbf{k}-\mathbf{q})$ which leads to Eq. 7.18 for the residue. Note that Eq. 7.18 has the right limits, *i.e.*, it is equal to unity across the FS and zero otherwise. We find this form easier to use for our numerical calculation. The efficacy of this approximation is shown in Figs. C.8.

Finally, for superposed ellipses, each basis state $|\epsilon, \hat{\mathbf{k}}\rangle$ then produces its own jump with a strength of $|\psi(\epsilon, \hat{\mathbf{k}})|^2$ such that the net *average* residue is given by Eq. 7.19.

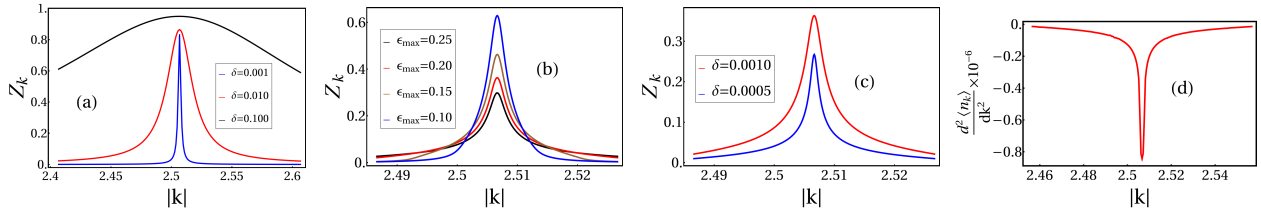

(a) a (b) b (c) c (d) d

Figure C.9: (a)Plot of the residue for FL state (Eq. 7.20) as a function of k, where $\epsilon_0 = 0.0$, $\epsilon_{\max} = 0.7$, and $Z_{\epsilon_0,\hat{\mathbf{k}}} = 0.8$, (b) Plot of $Z_{\mathbf{k}}$ as a function of k for the isotropic NFL case, with different $\epsilon_{\max}$ and δ=0.001, (c) Plot of $Z_{\mathbf{k}}$ as a function of k for the isotropic NFL case with the same $\epsilon_{\max} = 0.2$ and different δ, (d) Plot of $d^2\langle n_{\mathbf{k}}\rangle/dk^2$ corresponding to Fig. 7.7 as a function of k where $\epsilon_{\max} = 0.3$.

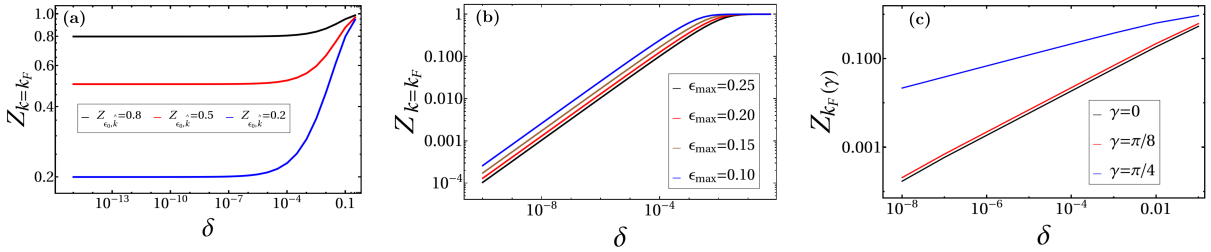

Figure C.10: Plot of $Z_{\mathbf{k}}$ as a function of δ for (a) the FL state (Eq. 7.20) at $k = \sqrt{2\pi}$, $\epsilon_0 = 0.0$ and $\epsilon_{\max} = 0.7$, (b) for the Isotropic NFL (c) for the anisotropic NFL (Eq. 7.23)) for different γ and $\epsilon_{\max} = 0.75$.

The residue for the FL

The residue for the FL (Eq. 7.20) is obtained using Eq. 7.18 numerically for different resolution, δ and taking the limit $\delta \to 0$. This is shown in Fig. C.9a while the variation of the residue at the FS with δ is shown in Fig. C.10(a). Note that the residue is completely isotropic in momentum space.

Isotropic superposition of elliptic FS : Vanishing Residue

For the amplitudes in Eq. 7.21, the quantum state (Eq. 7.17) is given by

$$|\psi_{\nu=1/2}\rangle = \frac{1}{\sqrt{\pi}\sqrt{\epsilon_{\max}}}\int_0^{\pi} d\hat{\mathbf{k}} \int_0^{\epsilon_{\max}} d\epsilon\, |\epsilon, \nu = 1/2, \hat{\mathbf{k}}\rangle, \tag{C.48}$$

such that the expectation value of the occupancy of the momentum modes is given by Fig. 7.7. The corresponding residue calculated using Eq. 7.19 is then shown in Fig. C.9b for a fixed resolution, $\delta = 0.001$ for different $\epsilon_{\max}$ and Fig. C.9c for a fixed $\epsilon_{\max}$ and different resolutions.

The residue, shown in Fig C.9b and C.9c, has its peak (at finite resolution (δ)) at $k = \sqrt{2\pi}$ in all directions. This implies that the area of this circle is $2\pi^2$ which is

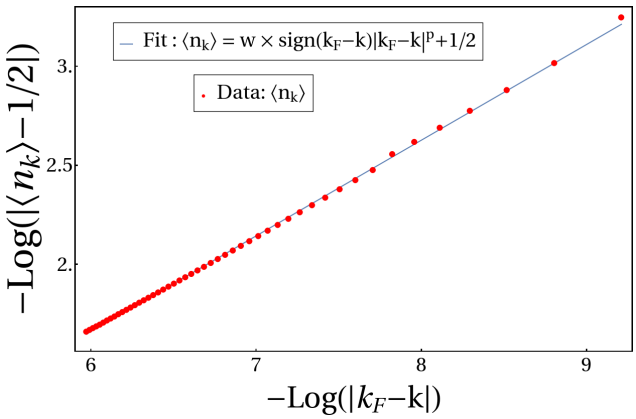

Figure C.11: The scaling of $\langle n_{\mathbf{k}} \rangle \sim |\mathbf{k_F} - \mathbf{k}|^p$ with $p = 0.4828$ near the FS corresponding to Eq. 7.21 with $\epsilon_{\max} = 0.25$.

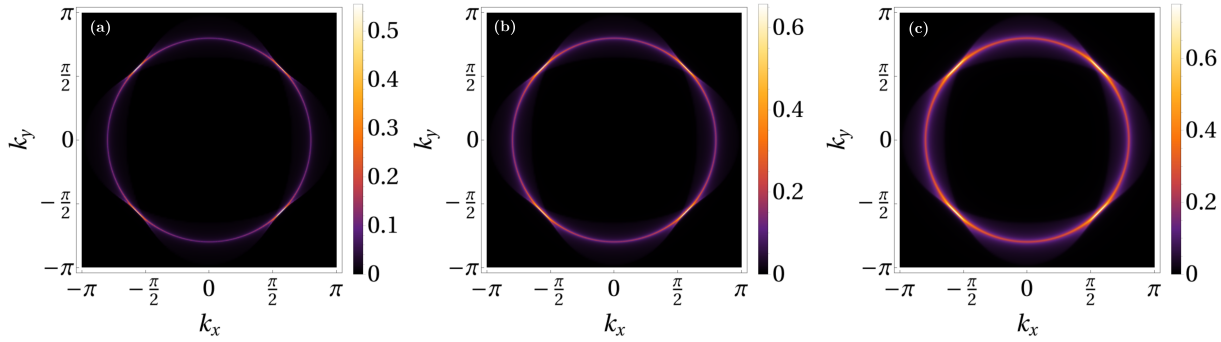

(a) a (b) b (c) c

Figure C.12: Plot of Z as a function of k_x and k_y for the superposed state mentioned in Eq. 7.23 for $\epsilon_{\max} = 0.75$ and (a) $\delta = 0.005$ (b) $\delta = 0.01$ (c) $\delta = 0.02$.

consistent with Luttinger theorem. As shown in Fig. C.10(b), $Z_{\mathbf{k_F}} \to 0$ as $\delta \to 0$. This is also concluded from the $\langle n_{\mathbf{k}} \rangle$ (in Fig 7.7) as the discontinuity at the FS is replaced by the point of inflection. This is shown in Fig. C.9d, where the second derivative of $\langle n_{\mathbf{k}} \rangle$ is showing a jump at the FS($k = \sqrt{2\pi}$) is plotted a s a function of k.

Finally in Fig. C.11 we plot the fitting of the average momentum mode occupation to the power-law form in agreement with the scaling theory of Ref. [142] as discussed in the main text.

Superposition of ellipses on a Square Lattice : Anisotropic residue

For the state in Eq. 7.23, Fig. 7.11 shows that the superposition of FSs led to anisotropy in the quasi-particle residue (at finite resolution δ). Here we present further details of the same as a function of the two parameters $\epsilon_{\max}$ and δ.

From the plot of $\langle n_{\mathbf{k}} \rangle$ as a function of k, shown in Fig. 7.10, we note that for $\gamma = \frac{\pi}{4}$, $\langle n_{\mathbf{k}} \rangle$ vanishes sharply, but smoothly. This is because in $\pi/4$ direction, radius of circle is max distance from origin. For $\epsilon \neq 0$, it lies inside circle where it is smeared; such a

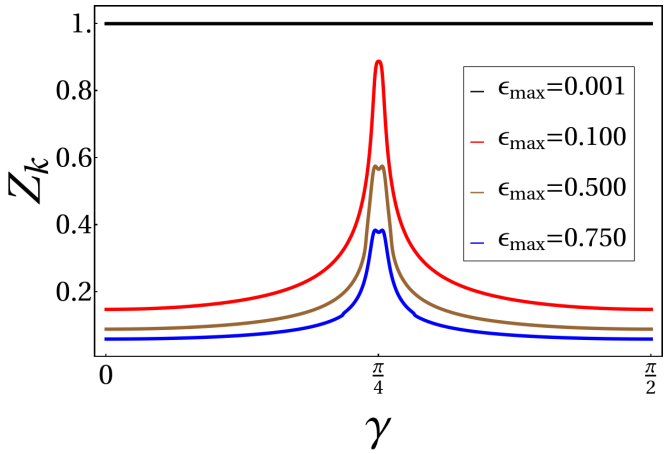

Figure C.13: Plot of $Z_{\mathbf{k}}$(for $\delta = 0.001$) corresponding to state Eq. 7.23 as a function of γ where $\mathbf{k} = (\sqrt{2\pi}\cos(\gamma), \sqrt{2\pi}\sin(\gamma))$ and $\gamma \in \{0, \frac{\pi}{2}\}$.

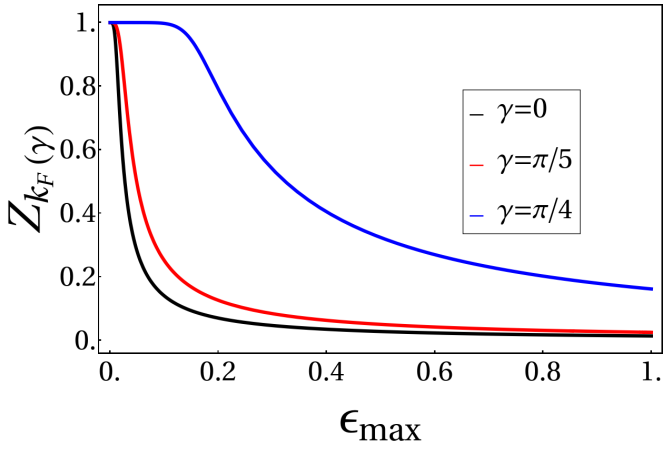

Figure C.14: Plot of $Z_{\mathbf{k_F}(\gamma)}$ for superposed state mentioned in Eq. 7.23, where $\mathbf{k_F}(\gamma) = (\sqrt{2\pi}\cos(\gamma), \sqrt{2\pi}\sin(\gamma)))$ as a function of ϵ_{max} for different γ and $\delta = 10^{-4}$.

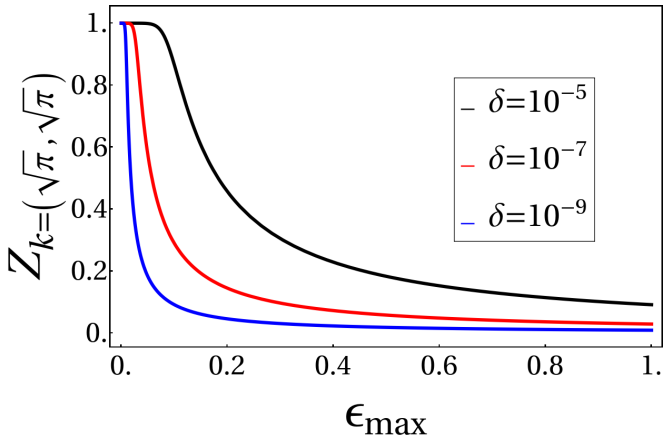

Figure C.15: Plot of $Z_{\mathbf{k}}(\mathbf{k} = (\sqrt{\pi}, \sqrt{\pi}))$ corresponding to Eq. 7.23 as a function of ϵ_{max} for different δ.

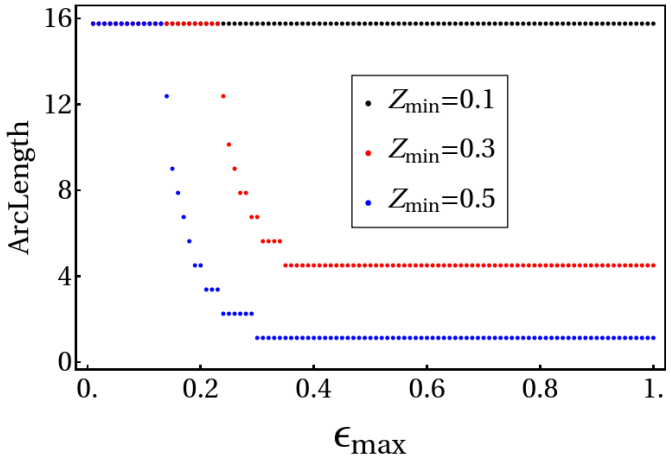

Figure C.16: Plot of the arc length corresponding to Eq. 7.23 as a function of ϵ_{max} with $\delta = 0.001$ and for different Z_{min}.

smearing does not occur outside the circle.

The finite resolution residue (calculated using Eq. 7.19) is plotted in Fig. 7.11 for different ϵ_{max} with a given resolution δ and as a function of δ in Fig. C.12. Fig. C.13 shows a plot of $Z_{\mathbf{k}}(\delta = 0.001)$ as a function of γ for different ϵ_{max} indicating the direction dependence of $Z_{\mathbf{k}}$. As we move away from $\gamma = \frac{\pi}{4}$ direction, the value of the residue decreases rapidly. This is also seen by plotting $Z_{\mathbf{k}}$ as a function of ϵ_{max} for given δ (Fig. C.14). At the momentum of highest smeared jump, we also plot the variation of the magnitude of jump as a function of ϵ_{max} for different resolution in Fig. C.15. The plot shows that for any appreciable superposition, the residue indeed goes to zero. However, it goes to zero much more slowly compared to other angles as shown in Fig. C.10(c).

The *length* of each of the segment of finite resolution residue has been computed as follows. We first normalize $Z_{\text{Norm}} = Z_{\mathbf{k}}/Z_{max}$. Then, while computing the length, we put a lower cut off, Z_{min} on Z_{Norm} and discard all Z_{Norm} below that cutoff. Fig. C.16 shows the width of segment, or the arc length, as a function of ϵ_{max} for same δ but with different lower cutoffs Z_{min}. We find that the maximum arc length is that of the perimeter of circle ($2\pi\sqrt{2\pi}$).

C.5.3 Density-density Correlation in real space

The connected density-density correlator in real space, $\langle\langle n_{\mathbf{r}_1} n_{\mathbf{r}_2}\rangle\rangle \equiv W(\mathbf{r_1}, \mathbf{r_2})$ is given by

$$\langle\psi_\nu|n_{\mathbf{r}_1} n_{\mathbf{r}_2}|\psi_\nu\rangle - \langle\psi_\nu|n_{\mathbf{r}_1}|\psi_\nu\rangle\langle\psi_\nu|n_{\mathbf{r}_2}|\psi_\nu\rangle, \tag{C.49}$$

for a many-fermion state $|\psi_\nu\rangle$ at filling ν. For an elliptical FS given by $|\epsilon, \nu, \hat{\mathbf{k}}\rangle$ in the main text, we have

$$W(\mathbf{r_1}, \mathbf{r_2}) = \nu\delta^2(\mathbf{r_1} - \mathbf{r_2}) - |F(\epsilon, r, \nu, \hat{\mathbf{k}})|^2, \tag{C.50}$$

where,

$$F(\epsilon, r, \nu, \hat{\mathbf{k}}) = 2\nu \left(\frac{J_1(r t_{\hat{\mathbf{k}}} \sqrt{4\pi\nu})}{(r t_{\hat{\mathbf{k}}} \sqrt{4\pi\nu})} \right), \tag{C.51}$$

and

$$t_{\hat{\mathbf{k}}} = \frac{\sqrt{1 - \epsilon^2 \sin^2(u - \gamma)}}{(1 - \epsilon^2)^{1/4}}, \tag{C.52}$$

with

$$\tan u = \frac{\hat{\mathbf{k}}_y}{\hat{\mathbf{k}}_x}, \;\; r = |\mathbf{r_1} - \mathbf{r_2}|, \; \tan\gamma = \frac{y_2 - y_1}{x_2 - x_1}. \tag{C.53}$$

Next, turning to superposed FS wave-functions (Eq. 7.17) the density-density correlator is given by

$$\begin{aligned} W =& \nu\delta^2(\mathbf{r_1} - \mathbf{r_2}) \\ &+ \int_0^{\epsilon_{\max}} d\epsilon \int_0^{\pi} d\hat{\mathbf{k}} \, |\psi(\epsilon, \hat{\mathbf{k}})|^2 |F(\epsilon, r, \nu, \hat{\mathbf{k}})|^2. \end{aligned} \tag{C.54}$$

This completes our discussion of computation of these correlators.

Publications based on this thesis

1. **Ankush Chaubey**, Basudeb Mondal, Vijay B. Shenoy and Subhro Bhattacharjee. *Superconductivity in spin-orbit coupled SU(8) Dirac fermions on the honeycomb lattice* Phys. Rev. B 112, 085133 (2025)

2. **Ankush Chaubey**, Harsh Nigam, Subhro Bhattacharjee and K.Sengupta , *Variational wave-functions for correlated metals*, arXiv:2408.00834v1(2024).

In-preparation

1. **Ankush Chaubey**, Sergej Moroz, and Subhro Bhattacharjee , *Interpolating between dimer models and Toric code on a square lattice*, manuscript in preparation,

Bibliography

[1] W. Witczak-Krempa, G. Chen, Y. B. Kim and L. Balents, *Correlated quantum phenomena in the strong spin-orbit regime*, *Annual Review of Condensed Matter Physics* **5** (2014) 57–82.

[2] T. Giamarchi, *Quantum Physics in One Dimension*. Oxford University Press, 12, 2003, 10.1093/acprof:oso/9780198525004.001.0001.

[3] S. Wenzel, T. Coletta, S. E. Korshunov and F. Mila, *Evidence for columnar order in the fully frustrated transverse field ising model on the square lattice*, *Phys. Rev. Lett.* **109** (2012) 187202.

[4] N. Wakeham, P. F. S. Rosa, Y. Q. Wang, M. Kang, Z. Fisk, F. Ronning et al., *Low-temperature conducting state in two candidate topological kondo insulators:* smb_6 *and* $ce_3bi_4pt_3$, *Phys. Rev. B* **94** (2016) 035127.

[5] L. Savary and L. Balents, *Quantum spin liquids: a review*, *Reports on Progress in Physics* **80** (2016) 016502.

[6] L. Šmejkal, J. Sinova and T. Jungwirth, *Emerging research landscape of altermagnetism*, *Phys. Rev. X* **12** (2022) 040501.

[7] P. Coleman, *Introduction to Many-Body Physics*. Cambridge University Press, 2015.

[8] X.-G. Wen, *Quantum Field Theory of Many-Body Systems: From the Origin of Sound to an Origin of Light and Electrons*. Oxford University Press, 09, 2007, 10.1093/acprof:oso/9780199227259.001.0001.

[9] M. Tinkham, *Introduction to superconductivity*. Courier Corporation, 2004.

[10] M. Sigrist and K. Ueda, *Phenomenological theory of unconventional superconductivity*, *Rev. Mod. Phys.* **63** (1991) 239.

[11] S. Blundell, *Magnetism in Condensed Matter*, Oxford Master Series in Condensed Matter Physics. OUP Oxford, 2001.

[12] B. I. Halperin and J. K. Jain, *Fractional Quantum Hall Effects: New Developments*. WORLD SCIENTIFIC, Jan., 2020, 10.1142/11751.

[13] H. L. Stormer, D. C. Tsui and A. C. Gossard, *The fractional quantum hall effect*, *Rev. Mod. Phys.* **71** (1999) S298.

[14] L. Pitaevskii and S. Stringari, *527References*. Oxford University Press, 01, 2016, 10.1093/acprof:oso/9780198758884.001.0001.

[15] A. Beekman, L. Rademaker and J. van Wezel, *An introduction to spontaneous symmetry breaking*, *SciPost Physics Lecture Notes* (2019) .

[16] E. A. Rangel, *Density Waves in Solids*.

[17] M. Ueda, *Topological aspects in spinor Bose–Einstein condensates*, *Reports on Progress in Physics* **77** (2014) 122401.

[18] X.-G. Wen, *Colloquium : Zoo of quantum-topological phases of matter*, *Reviews of Modern Physics* **89** (2017) .

[19] M. Z. Hasan and C. L. Kane, *Colloquium: Topological insulators*, *Rev. Mod. Phys.* **82** (2010) 3045.

[20] P. W. Phillips, N. E. Hussey and P. Abbamonte, *Stranger than metals*, *Science* **377** (2022) eabh4273 [https://www.science.org/doi/pdf/10.1126/science.abh4273].

[21] P. W. Anderson, *More is different*, *Science* **177** (1972) 393 [https://www.science.org/doi/pdf/10.1126/science.177.4047.393].

[22] D. Tong, *Statistical field theory*, *Lecture notes, DAMTP, University of Cambridge* (2017) .

[23] E. Fradkin, *Field Theories of Condensed Matter Physics*. Cambridge University Press, 2 ed., 2013.

[24] A. Georges, L. d. Medici and J. Mravlje, *Strong correlations from hund's coupling*, *Annual Review of Condensed Matter Physics* **4** (2013) 137–178.

[25] X. Wan, A. Vishwanath and S. Y. Savrasov, *Computational design of axion insulators based on* 5*d spinel compounds*, *Phys. Rev. Lett.* **108** (2012) 146601.

[26] M. Z. Hasan and J. E. Moore, *Three-dimensional topological insulators*, *Annual Review of Condensed Matter Physics* **2** (2010) 55.

[27] X. Wan, A. M. Turner, A. Vishwanath and S. Y. Savrasov, *Topological semimetal and fermi-arc surface states in the electronic structure of pyrochlore iridates*, *Phys. Rev. B* **83** (2011) 205101.

[28] A. A. Burkov and L. Balents, *Weyl semimetal in a topological insulator multilayer*, *Phys. Rev. Lett.* **107** (2011) 127205.

[29] S. Picozzi, *Spin–orbit coupling in quantum materials: emergent phenomena, their modelling and examples from two-dimensional magnets*, *La Rivista del Nuovo Cimento* (2025) .

[30] U. Mehta, *Postmodern Fermi Liquids*, Ph.D. thesis, Department of Physics, University of Colorado, Boulder, Boulder, CO, USA, GRID:grid.266190.a, 2024. 2307.02536. 10.1007/978-3-031-72403-9.

[31] V. L. Ginzburg and L. D. Landau, *On the theory of superconductivity*, in *On Superconductivity and Superfluidity: A Scientific Autobiography*, (Berlin, Heidelberg), pp. 113–137, Springer Berlin Heidelberg, (2009), DOI.

[32] A. Lopez and E. Fradkin, *Fractional quantum hall effect and chern-simons gauge theories*, *Phys. Rev. B* **44** (1991) 5246.

[33] G. V. Dunne, *Aspects of chern-simons theory*, hep-th/9902115.

[34] G. Giuliani and G. Vignale, *Quantum Theory of the Electron Liquid*. Cambridge University Press, 2005.

[35] L. D. Landau, *The theory of a fermi liquid*, *Sov. Phys. JETP* **3** (1957) 920.

[36] R. Shankar, *Renormalization-group approach to interacting fermions*, *Rev. Mod. Phys.* **66** (1994) 129.

[37] S. Rao and D. Sen, *An introduction to bosonization and aome of its applications*, cond-mat/0005492.

[38] S. Ryu, C. Mudry, C.-Y. Hou and C. Chamon, *Masses in graphenelike two-dimensional electronic systems: Topological defects in order parameters and their fractional exchange statistics*, *Phys. Rev. B* **80** (2009) 205319.

[39] I. F. Herbut, *Interactions and Phase Transitions on Graphene's Honeycomb Lattice*, *Phys. Rev. Lett.* **97** (2006) 146401.

[40] B. Mondal, V. B. Shenoy and S. Bhattacharjee, *Emergent su(8) Dirac semimetal and proximate phases of spin-orbit coupled fermions on a honeycomb lattice*, *Phys. Rev. B* **108** (2023) 245106.

[41] R. Boyack, H. Yerzhakov and J. Maciejko, *Quantum phase transitions in Dirac fermion systems*, *The European Physical Journal Special Topics* **230** (2021) 979.

[42] N. Goldenfeld, *Lectures on Phase Transitions and the Renormalization Group*. CRC Press, 1st ed., 1992, 10.1201/9780429493492.

[43] J. E. T. Ospina, *Emergent symmetries in relativistic Quantum Phase Transitions*, Ph.D. thesis, Universität zu Köln, March, 2019.

[44] D. V. Else, R. Thorngren and T. Senthil, *Non-fermi liquids as ersatz fermi liquids: General constraints on compressible metals*, *Physical Review X* **11** (2021) .

[45] X.-G. Wen, *Quantum orders and symmetric spin liquids*, *Physical Review B* **65** (2002) .

[46] A. J. Schofield, *"non-fermi liquids." contemporary physics 40 (2): 95–115*, .

[47] D. Chowdhury, A. Georges, O. Parcollet and S. Sachdev, *Sachdev-ye-kitaev models and beyond: Window into non-fermi liquids*, *Reviews of Modern Physics* **94** (2022) .

[48] S.-S. Lee, *Recent developments in non-fermi liquid theory*, *Annual Review of Condensed Matter Physics* **9** (2018) 227.

[49] M. Gupta, B. Mondal, S. Bhattacharjee and T. Saha Dasgupta, *Ab initio insights on the fermiology of d^1 transition metals on the honeycomb lattice: Hierarchy of hopping pathways and spin-orbit coupling*, *Phys. Rev. Res.* **5** (2023) 043219.

[50] M. G. Yamada, M. Oshikawa and G. Jackeli, *Emergent* SU(4) *symmetry in* $\alpha-\mathrm{zrcl}_3$ *and crystalline spin-orbital liquids*, *Phys. Rev. Lett.* **121** (2018) 097201.

[51] N. S. Ticea, S. Raghu and Y.-M. Wu, *Pair density wave order in multiband systems*, *Phys. Rev. B* **110** (2024) 094515.

[52] Y.-M. Wu, P. A. Nosov, A. A. Patel and S. Raghu, *Pair density wave order from electron repulsion*, *Phys. Rev. Lett.* **130** (2023) 026001.

[53] J. H. Pixley and P. A. Volkov, *Twisted nodal superconductors*, 2503.23683.

[54] J. J. Cuozzo, W. Yu, P. Davids, T. M. Nenoff, D. B. Soh, W. Pan et al., *Leggett modes in a dirac semimetal*, *Nature Physics* **20** (2024) 1118–1123.

[55] A. Chaubey, B. Mondal, V. B. Shenoy and S. Bhattacharjee, *Superconductivity in spin-orbit coupled su(8) dirac fermions on the honeycomb lattice*, *Phys. Rev. B* **112** (2025) 085133.

[56] D. F. Agterberg, J. S. Davis, S. D. Edkins, E. Fradkin, D. J. Van Harlingen, S. A. Kivelson et al., *The physics of pair-density waves: cuprate superconductors and beyond*, *Annual Review of Condensed Matter Physics* **11** (2020) 231.

[57] T. Senthil and M. P. A. Fisher, *Fractionalization, topological order, and cuprate superconductivity*, *Phys. Rev. B* **63** (2001) 134521.

[58] N. Nagaosa and P. A. Lee, *Ginzburg-landau theory of the spin-charge-separated system*, *Phys. Rev. B* **45** (1992) 966.

[59] C. Kim, *Spin–charge separation in 1d mott-insulators and related systems*, *Journal of Electron Spectroscopy and Related Phenomena* **117–118** (2001) .

[60] M. Hermele, T. Senthil and M. P. A. Fisher, *Algebraic spin liquid as the mother of many competing orders*, *Physical Review B* **72** (2005) .

[61] R. Nandkishore, M. A. Metlitski and T. Senthil, *Orthogonal metals: The simplest non-fermi liquids*, *Phys. Rev. B* **86** (2012) 045128.

[62] C. Chen, X. Y. Xu, Y. Qi and Z. Y. Meng, *Metal to orthogonal metal transition**, *Chinese Physics Letters* **37** (2020) 047103.

[63] T. Senthil and M. P. Fisher, *Z 2 gauge theory of electron fractionalization in strongly correlated systems*, *Physical Review B* **62** (2000) 7850.

[64] E. J. König, P. Coleman and A. M. Tsvelik, *Soluble limit and criticality of fermions in $_2$ gauge theories*, *Phys. Rev. B* **102** (2020) 155143.

[65] S. Sachdev, *Topological order, emergent gauge fields, and fermi surface reconstruction*, *Reports on Progress in Physics* **82** (2018) 014001.

[66] F. J. Wegner, *Duality in generalized ising models*, 1411.5815.

[67] D. Blankschtein, M. Ma and A. N. Berker, *Fully and partially frustrated simple-cubic ising models: Landau-ginzburg-wilson theory*, *Phys. Rev. B* **30** (1984) 1362.

[68] S. Trebst, P. Werner, M. Troyer, K. Shtengel and C. Nayak, *Breakdown of a topological phase: Quantum phase transition in a loop gas model with tension*, *Phys. Rev. Lett.* **98** (2007) 070602.

[69] A. Nanda, K. Dhochak and S. Bhattacharjee, *Phases and quantum phase transitions in an anisotropic ferromagnetic kitaev-heisenberg-■ magnet*, *Phys. Rev. B* **102** (2020) 235124.

[70] U. Borla, A. De and S. Gazit, *"odd" toric code in a tilted field: Higgs-confinement multicriticality, spontaneous self-duality symmetry breaking, and valence bond solids*, 2507.16523.

[71] D. S. Rokhsar and S. A. Kivelson, *Superconductivity and the quantum hard-core dimer gas*, *Phys. Rev. Lett.* **61** (1988) 2376.

[72] A. Banerjee, K. Damle and A. Paramekanti, *Néel to staggered dimer order transition in a generalized honeycomb lattice heisenberg model*, *Physical Review B* **83** (2011) .

[73] M. R. Mahapatra and R. Kumar, *Exact staggered dimer ground state and its stability in a two-dimensional magnet*, *Physical Review B* **110** (2024) .

[74] J. Polchinski, *Effective field theory and the fermi surface*, 1999.

[75] G. R. Stewart, *Non-fermi-liquid behavior in d- and f-electron metals*, *Rev. Mod. Phys.* **73** (2001) 797.

[76] M. R. Norman, H. Ding, M. Randeria, J. C. Campuzano, T. Yokoya, T. Takeuchi et al., *Destruction of the fermi surface in underdoped high-tc superconductors*, *Nature* **392** (1998) 157.

[77] Y. He, Y. Yin, M. Zech, A. Soumyanarayanan, M. M. Yee, T. Williams et al., *Fermi surface and pseudogap evolution in a cuprate superconductor*, *Science* **344** (2014) 608–611.

[78] A. Chaubey, H. Nigam, S. Bhattacharjee and K. Sengupta, *Variational wave-functions for correlated metals*, 2408.00834.

[79] N. B. Kopnin and E. B. Sonin, *BCS Superconductivity of Dirac Electrons in Graphene Layers*, *Phys. Rev. Lett.* **100** (2008) 246808.

[80] B. Uchoa, G. G. Cabrera and A. H. Castro Neto, *Nodal liquid and s-wave superconductivity in transition metal dichalcogenides*, *Phys. Rev. B* **71** (2005) 184509.

[81] A. H. Castro Neto, *Charge Density Wave, Superconductivity, and Anomalous Metallic Behavior in 2D Transition Metal Dichalcogenides*, *Phys. Rev. Lett.* **86** (2001) 4382.

[82] B. Uchoa and A. H. C. Neto, *Comment on "BCS Superconductivity of Dirac Electrons in Graphene Layers"*, *Phys. Rev. Lett.* **102** (2009) 109701.

[83] B. Roy and I. F. Herbut, *Unconventional superconductivity on honeycomb lattice: Theory of Kekule order parameter*, *Phys. Rev. B* **82** (2010) 035429.

[84] R. A. Wilson, *A discrete model for Gell-Mann matrices*, 2024.

[85] C. W. J. Beenakker, *Specular Andreev Reflection in Graphene*, *Phys. Rev. Lett.* **97** (2006) 067007.

[86] S. Bhattacharjee, M. Maiti and K. Sengupta, *Theory of tunneling conductance of graphene normal metal-insulator-superconductor junctions*, *Phys. Rev. B* **76** (2007) 184514.

[87] S. Bhattacharjee and K. Sengupta, *Tunneling conductance of graphene NIS junctions*, *Phys. Rev. Lett.* **97** (2006) 217001.

[88] C. Huang, B. T. Zhou, H. Zhang, B. Yang, R. Liu, H. Wang et al., *Proximity-induced surface superconductivity in Dirac semimetal Cd3As2*, *Nature communications* **10** (2019) 2217.

[89] L. Santos, T. Neupert, C. Chamon and C. Mudry, *Superconductivity on the surface of topological insulators and in two-dimensional noncentrosymmetric materials*, *Phys. Rev. B* **81** (2010) 184502.

[90] S. Kobayashi and M. Sato, *Topological Superconductivity in Dirac Semimetals*, *Phys. Rev. Lett.* **115** (2015) 187001.

[91] L. Zhao, H. Deng, I. Korzhovska, M. Begliarbekov, Z. Chen, E. Andrade et al., *Emergent surface superconductivity in the topological insulator Sb2Te3*, *Nature communications* **6** (2015) 8279.

[92] P. R. Wallace, *The Band Theory of Graphite*, *Phys. Rev.* **71** (1947) 622.

[93] H. Kim, K. Wang, Y. Nakajima, R. Hu, S. Ziemak, P. Syers et al., *Beyond triplet: Unconventional superconductivity in a spin-3/2 topological semimetal*, *Science advances* **4** (2018) eaao4513.

[94] P. Anderson, *Structure of" triplet" superconducting energy gaps*, *Physical Review B* **30** (1984) 4000.

[95] A. Ramires, *Nonunitary superconductivity in complex quantum materials*, *Journal of Physics: Condensed Matter* **34** (2022) 304001.

[96] C. Pfleiderer, *Superconducting phases of f-electron compounds*, *Rev. Mod. Phys.* **81** (2009) 1551.

[97] R. Joynt and L. Taillefer, *The superconducting phases of* UPt_3, *Rev. Mod. Phys.* **74** (2002) 235.

[98] T. Nomoto, K. Hattori and H. Ikeda, *Classification of "multipole" superconductivity in multiorbital systems and its implications*, *Phys. Rev. B* **94** (2016) 174513.

[99] G. Volovik and L. Gor'kov, *Superconducting classes in heavy-fermion systems*, in *Ten Years of Superconductivity: 1980–1990*, pp. 144–155, Springer, (1985).

[100] V. Yarzhemsky and E. Murav'Ev, *Space group approach to the wavefunction of a Cooper pair*, *Journal of Physics: Condensed Matter* **4** (1992) 3525.

[101] P. Dutta, F. Parhizgar and A. M. Black-Schaffer, *Superconductivity in spin-3/2 systems: Symmetry classification, odd-frequency pairs, and Bogoliubov Fermi surfaces*, *Phys. Rev. Res.* **3** (2021) 033255.

[102] E. I. Blount, *Symmetry properties of triplet superconductors*, *Phys. Rev. B* **32** (1985) 2935.

[103] M.-a. Ozaki and K. Machida, *Superconducting classes of heavy-fermion materials*, *Phys. Rev. B* **39** (1989) 4145.

[104] A. Leggett, *Number-phase fluctuations in two-band superconductors*, *Progress of Theoretical Physics* **36** (1966) 901.

[105] I. F. Herbut and S. Mandal, *SO(8) unification and the large-N theory of superconductor-insulator transition of two-dimensional Dirac fermions*, *Phys. Rev. B* **108** (2023) L161108.

[106] A. Nanda, K. Dhochak and S. Bhattacharjee, *Phases and quantum phase transitions in an anisotropic ferromagnetic Kitaev-Heisenberg-■ magnet*, *Physical Review B* **102** (2020) .

[107] F. Zhou, *Spin Correlation and Discrete Symmetry in Spinor Bose-Einstein Condensates*, *Phys. Rev. Lett.* **87** (2001) 080401.

[108] S. Mukerjee, C. Xu and J. E. Moore, *Topological Defects and the Superfluid Transition of the* $s = 1$ *Spinor Condensate in Two Dimensions*, *Phys. Rev. Lett.* **97** (2006) 120406.

[109] A. Himeda, T. Kato and M. Ogata, *Stripe States with Spatially Oscillating d-Wave Superconductivity in the Two-Dimensional $t - t' - J$ Model*, *Phys. Rev. Lett.* **88** (2002) 117001.

[110] E. Berg, E. Fradkin, E.-A. Kim, S. A. Kivelson, V. Oganesyan, J. M. Tranquada et al., *Dynamical Layer Decoupling in a Stripe-Ordered High-T_c Superconductor*, *Phys. Rev. Lett.* **99** (2007) 127003.

[111] W.S.Massey, *The quotient space of the complex projective plane under conjugation is a 4-sphere*, *Geom Dedicata 2, 371–374* (1973) .

[112] N.H.Kuiper, *The quotient space of CP(2) by complex conjugation is the 4-sphere*, *Math. Ann. 208, 175–177* (1974) .

[113] J. J. Cuozzo, W. Yu, P. Davids, T. M. Nenoff, D. B. Soh, W. Pan et al., *Leggett modes in a Dirac semimetal*, *Nature Physics* **20** (2024) 1118.

[114] C. Chamon, C.-Y. Hou, C. Mudry, S. Ryu and L. Santos, *Masses and majorana fermions in graphene*, *Physica Scripta* **2012** (2012) 014013.

[115] D. J. Scalapino, *A common thread: The pairing interaction for unconventional superconductors*, *Reviews of Modern Physics* **84** (2012) 1383.

[116] P. M. R. Brydon, L. Wang, M. Weinert and D. F. Agterberg, *Pairing of $j = 3/2$ Fermions in Half-Heusler Superconductors*, *Phys. Rev. Lett.* **116** (2016) 177001.

[117] K. Roy and E. J. König, *$\mathbb{Z}_n$ lattice gauge theories with matter fields*, *arXiv:2308.13083* (2023) .

[118] L. de'Medici, A. Georges and S. Biermann, *Orbital-selective mott transition in multiband systems: Slave-spin representation and dynamical mean-field theory*, *Phys. Rev. B* **72** (2005) 205124.

[119] A. Rüegg, S. D. Huber and M. Sigrist, *z_2-slave-spin theory for strongly correlated fermions*, *Phys. Rev. B* **81** (2010) 155118.

[120] S. Bhattacharjee, *Quantum destruction of spiral order in two-dimensional frustrated magnets*, *Physical Review B* **84** (2011) .

[121] R. Moessner and S. L. Sondhi, *Ising models of quantum frustration*, *Physical Review B* **63** (2001) .

[122] J. Lou, A. W. Sandvik and L. Balents, *Emergence of u(1) symmetry in the 3d xy model with Z_q anisotropy*, *Phys. Rev. Lett.* **99** (2007) 207203.

[123] R. A. Jalabert and S. Sachdev, *Spontaneous alignment of frustrated bonds in an anisotropic, three-dimensional ising model*, *Phys. Rev. B* **44** (1991) 686.

[124] R. Moessner and K. S. Raman, *Quantum dimer models*, 0809.3051.

[125] Y. Tang, A. W. Sandvik and C. L. Henley, *Properties of resonating-valence-bond spin liquids and critical dimer models*, *Phys. Rev. B* **84** (2011) 174427.

[126] S. A. Kivelson, D. S. Rokhsar and J. P. Sethna, *Topology of the resonating valence-bond state: Solitons and high-T_c superconductivity*, *Phys. Rev. B* **35** (1987) 8865.

[127] M. Levin and T. Senthil, *Deconfined quantum criticality and néel order via dimer disorder*, *Physical Review B* **70** (2004) .

[128] B. Normand, *Frontiers in frustrated magnetism*, *Contemporary Physics* **50** (2009) 533.

[129] R. Moessner, S. L. Sondhi and E. Fradkin, *Short-ranged resonating valence bond physics, quantum dimer models, and ising gauge theories*, *Physical Review B* **65** (2001) .

[130] J. Hauschild and F. Pollmann, *Efficient numerical simulations with Tensor Networks: Tensor Network Python (TeNPy)*, *SciPost Phys. Lect. Notes* (2018) 5.

[131] M. Hermanns, *Entanglement in topological systems*, 1702.01525.

[132] U. Borla, B. Jeevanesan, F. Pollmann and S. Moroz, *Quantum phases of two-dimensional z_2 gauge theory coupled to single-component fermion matter*, *Physical Review B* **105** (2022) .

[133] L. D. Landau and E. M. Lifshit, *Course of theoretical physics (Statistical Physics-2)*. Elsevier, 2013.

[134] J. Polchinski, *Effective field theory and the fermi surface*, *arXiv preprint hep-th/9210046* (1992) .

[135] N. W. Ashcroft and N. D. Mermin, *Solid state physics*, *(No Title)* (1976) .

[136] D. Gioev and I. Klich, *Entanglement entropy of fermions in any dimension and the widom conjecture*, *Phys. Rev. Lett.* **96** (2006) 100503.

[137] J. M. Luttinger and J. C. Ward, *Ground-state energy of a many-fermion system. ii*, *Phys. Rev.* **118** (1960) 1417.

[138] M. Oshikawa, *Topological approach to luttinger's theorem and the fermi surface of a kondo lattice*, *Phys. Rev. Lett.* **84** (2000) 3370.

[139] W. Ding, A. Seidel and K. Yang, *Entanglement entropy of fermi liquids via multidimensional bosonization*, *Phys. Rev. X* **2** (2012) 011012.

[140] F. Haldane, *'luttinger liquid theory'of one-dimensional quantum fluids. i. properties of the luttinger model and their extension to the general 1d interacting spinless fermi gas*, *Journal of Physics C: Solid State Physics* **14** (1981) 2585.

[141] M. Yamanaka, M. Oshikawa and I. Affleck, *Nonperturbative approach to luttinger's theorem in one dimension*, *Phys. Rev. Lett.* **79** (1997) 1110.

[142] T. Senthil, *Critical fermi surfaces and non-fermi liquid metals*, *Phys. Rev. B* **78** (2008) 035103.

[143] W. F. Brinkman and T. M. Rice, *Application of gutzwiller's variational method to the metal-insulator transition*, *Phys. Rev. B* **2** (1970) 4302.

[144] Q. Si, *Quantum criticality and global phase diagram of magnetic heavy fermions*, *physica status solidi (b)* **247** (2010) 476.

[145] F. Krüger and J. Zaanen, *Fermionic quantum criticality and the fractal nodal surface*, *Phys. Rev. B* **78** (2008) 035104.

[146] J. Zaanen, *Quantum critical electron systems: the uncharted sign worlds*, *Science* **319** (2008) 1205.

[147] H. v. Löhneysen, A. Rosch, M. Vojta and P. Wölfle, *Fermi-liquid instabilities at magnetic quantum phase transitions*, *Rev. Mod. Phys.* **79** (2007) 1015.

[148] H. v. Löhneysen, T. Pietrus, G. Portisch, H. G. Schlager, A. Schröder, M. Sieck et al., *Non-fermi-liquid behavior in a heavy-fermion alloy at a magnetic instability*, *Phys. Rev. Lett.* **72** (1994) 3262.

[149] P. Gegenwart, Q. Si and F. Steglich, *Quantum criticality in heavy-fermion metals*, *nature physics* **4** (2008) 186.

[150] J. Custers, P. Gegenwart, H. Wilhelm, K. Neumaier, Y. Tokiwa, O. Trovarelli et al., *The break-up of heavy electrons at a quantum critical point*, *Nature* **424** (2003) 524.

[151] P. Coleman and A. J. Schofield, *Quantum criticality*, *Nature* **433** (2005) 226.

[152] Y. Kurosaki, Y. Shimizu, K. Miyagawa, K. Kanoda and G. Saito, *Mott transition from a spin liquid to a fermi liquid in the spin-frustrated organic conductor* $\kappa-(\mathrm{ET})_2\mathrm{cu}_2(\mathrm{CN})_3$, *Phys. Rev. Lett.* **95** (2005) 177001.

[153] M. Platé, J. D. F. Mottershead, I. S. Elfimov, D. C. Peets, R. Liang, D. A. Bonn et al., *Fermi surface and quasiparticle excitations of overdoped* $\mathrm{tl}_2\mathrm{ba}_2\mathrm{cuo}_{6+\delta}$, *Phys. Rev. Lett.* **95** (2005) 077001.

[154] J. Polchinski, *Low-energy dynamics of the spinon-gauge system*, *Nuclear Physics B* **422** (1994) 617.

[155] S.-S. Lee, *Low-energy effective theory of fermi surface coupled with u(1) gauge field in* $2+1$ *dimensions*, *Phys. Rev. B* **80** (2009) 165102.

[156] J. A. Hertz, *Quantum critical phenomena*, in *Basic Notions of Condensed Matter Physics*, pp. 525–544, CRC Press, (2018), https://link.aps.org/doi/10.1103/PhysRevB.14.1165.

[157] A. J. Millis, *Fluctuation-driven first-order behavior near the* $t = 0$ *two-dimensional stripe to fermi liquid transition*, *Phys. Rev. B* **81** (2010) 035117.

[158] S. Sachdev and J. Ye, *Gapless spin-fluid ground state in a random quantum heisenberg magnet*, *Phys. Rev. Lett.* **70** (1993) 3339.

[159] M. Y. Reizer, *Relativistic effects in the electron density of states, specific heat, and the electron spectrum of normal metals*, *Phys. Rev. B* **40** (1989) 11571.

[160] B. L. Altshuler, L. B. Ioffe and A. J. Millis, *Low-energy properties of fermions with singular interactions*, *Phys. Rev. B* **50** (1994) 14048.

[161] P. A. Lee, *Gauge field, aharonov-bohm flux, and high-*T_c *superconductivity*, *Phys. Rev. Lett.* **63** (1989) 680.

[162] M. A. Metlitski and S. Sachdev, *Quantum phase transitions of metals in two spatial dimensions. ii. spin density wave order*, *Phys. Rev. B* **82** (2010) 075128.

[163] D. F. Mross, J. McGreevy, H. Liu and T. Senthil, *Controlled expansion for certain non-fermi-liquid metals*, *Phys. Rev. B* **82** (2010) 045121.

[164] D. Dalidovich and S.-S. Lee, *Perturbative non-fermi liquids from dimensional regularization*, *Phys. Rev. B* **88** (2013) 245106.

[165] S. Sur and S.-S. Lee, *Chiral non-fermi liquids*, *Phys. Rev. B* **90** (2014) 045121.

[166] E. Lieb, T. Schultz and D. Mattis, *Two soluble models of an antiferromagnetic chain*, *Annals of Physics* **16** (1961) 407.

[167] M. B. Hastings, *Lieb-schultz-mattis in higher dimensions*, *Phys. Rev. B* **69** (2004) 104431.

[168] A. Altland and B. D. Simons, *Condensed matter field theory*. Cambridge university press, 2010.

[169] P. Calabrese and J. Cardy, *Entanglement entropy and conformal field theory*, *Journal of Physics A: Mathematical and Theoretical* **42** (2009) 504005.

[170] L. Landau, E. Lifshitz and L. Pitaevskii, *Course of theoretical physics: Statistical physics, part 2 : by e.m. lifshitz and l.p. pitaevskii*, *(No Title)* (1980) .

[171] P. W. Anderson, *Singular forward scattering in the 2d hubbard model and a renormalized bethe ansatz ground state*, *Phys. Rev. Lett.* **65** (1990) 2306.

[172] C. M. Varma, P. B. Littlewood, S. Schmitt-Rink, E. Abrahams and A. E. Ruckenstein, *Phenomenology of the normal state of cu-o high-temperature superconductors*, *Phys. Rev. Lett.* **63** (1989) 1996.

[173] S. A. Kivelson, E. Fradkin and V. J. Emery, *Electronic liquid-crystal phases of a doped mott insulator*, *Nature* **393** (1998) 550.

[174] M. R. Norman, H. Ding, M. Randeria, J. C. Campuzano, T. Yokoya, T. Takeuchi et al., *Destruction of the fermi surface in underdoped high-t c superconductors*, *Nature* **392** (1998) 157.

[175] T. Xiang, *Density-matrix renormalization-group method in momentum space*, *Phys. Rev. B* **53** (1996) R10445.

[176] C.-K. Chiu, J. C. Teo, A. P. Schnyder and S. Ryu, *Classification of topological quantum matter with symmetries*, *Reviews of Modern Physics* **88** (2016) 035005.

[177] A. P. Schnyder, S. Ryu, A. Furusaki and A. W. Ludwig, *Classification of topological insulators and superconductors*, in *AIP conference proceedings*, vol. 1134, pp. 10–21, American Institute of Physics, 2009, http://dx.doi.org/10.1063/1.3149481.

[178] Y. Hatsugai and S. Ryu, *Topological quantum phase transitions in superconductivity on lattices*, *Phys. Rev. B* **65** (2002) 212510.

[179] Y. Hatsugai, S. Ryu and M. Kohmoto, *Superconductivity and Abelian chiral anomalies*, *Phys. Rev. B* **70** (2004) 054502.

[180] M. Sato and S. Fujimoto, *Topological phases of noncentrosymmetric superconductors: Edge states, Majorana fermions, and non-Abelian statistics*, *Phys. Rev. B* **79** (2009) 094504.

[181] E. Cornfeld, M. S. Rudner and E. Berg, *Spin-polarized superconductivity: Order parameter topology, current dissipation, and multiple-period Josephson effect*, *Phys. Rev. Res.* **3** (2021) 013051.

[182] S.-B. Zhang, L.-H. Hu and T. Neupert, *Finite-momentum Cooper pairing in proximitized altermagnets*, *Nature Communications* **15** (2024) 1801.

[183] T. Grover and T. Senthil, *Topological Spin Hall States, Charged Skyrmions, and Superconductivity in Two Dimensions*, *Physical Review Letters* **100** (2008) .

[184] S. Sachdev, *Quantum Phase Transitions*. Cambridge University Press, 2 ed., 2011.